



Universitat Autònoma de Barcelona

ADVERTIMENT. L'accés als continguts d'aquesta tesi queda condicionat a l'acceptació de les condicions d'ús establertes per la següent llicència Creative Commons:  http://cat.creativecommons.org/?page_id=184

ADVERTENCIA. El acceso a los contenidos de esta tesis queda condicionado a la aceptación de las condiciones de uso establecidas por la siguiente licencia Creative Commons:  <http://es.creativecommons.org/blog/licencias/>

WARNING. The access to the contents of this doctoral thesis it is limited to the acceptance of the use conditions set by the following Creative Commons license:  <https://creativecommons.org/licenses/?lang=en>



Advances on the Synthesis of MOFs at Scale

Ceren Çamur

Doctoral Thesis

PhD in Materials Science

Supervisors:

Prof. Daniel MasPOCH and Dr. Inhar Imaz

Tutor:

Dr. Félix Busqué Sánchez

Catalan Institute of Nanoscience and Nanotechnology

Department of Chemistry- Faculty of Science

2019

Memoria presentada per aspirar al Grau de Doctor per Ceren Çamur.

Ceren Çamur

Vist i plau

Prof. Dr. Daniel Maspoch

Supramolecular Nanochemistry and Materials Group.

Institut Català de Nanociència i Nanotecnologia (ICN2)

Dr. Inhar Imaz

Supramolecular Nanochemistry and Materials Group.

Institut Català de Nanociència i Nanotecnologia (ICN2)

Dr. Félix Busqué Sánchez

Departament de Química

Universidad Autònoma de Barcelona

Bellaterra, 24 de Gener de 2019

Table of Contents

<i>Table of contents</i>	<i>i</i>
<i>Abstract</i>	<i>v</i>
<i>Resumen</i>	<i>vii</i>
<i>Acknowledgements</i>	<i>ix</i>
Chapter 1: Introduction to Metal-Organic Frameworks (MOFs) and Their Synthesis	1
1.1. Porous Materials.....	3
1.2. Metal Organic Frameworks (MOFs).....	4
1.3. Application of MOFs.....	8
1.3.1. Gas storage and separation.....	8
1.3.1.1. CO ₂ sequestration.....	9
1.3.1.2. H ₂ adsorption.....	11
1.3.1.3. CH ₄ adsorption.....	12
1.3.2. Water sorption applications.....	13
1.3.3. Catalysis.....	15
1.4. Synthesis of MOFs at Scale.....	18
1.4.1 Production of MOFs: from laboratory to industrial scale.....	19
1.4.1.1. Electrochemical synthesis.....	21
1.4.1.2. Microwave synthesis.....	28
1.4.1.3. Mechanochemical synthesis.....	31
1.4.1.4. Spray-drying synthesis.....	35
1.4.1.5. Flow chemistry.....	42
1.5. Downstream Processes.....	48
1.6. Perspectives and Commercial Developments.....	54
1.7. References.....	59
Chapter 2: Objectives	73

Chapter 3: Metal Acetylacetonates as a Source of Metals for Aqueous Synthesis of Metal–Organic Frameworks	77
3.1. Introduction.....	79
3.2. Experimental Section.....	81
3.2.1. Materials and methods.....	81
3.2.2. Synthesis of MOFs.....	82
Synthesis of UiO-66-NH ₂ at room temperature.....	82
Synthesis of Zr-Fumarate at room temperature.....	82
Synthesis of UiO-66-(OH) ₂ at room temperature.....	82
Synthesis of UiO-66-(COOH) ₂ at 90 °C.....	82
Synthesis of UiO-66-COOH at 90 °C.....	82
Synthesis of MIL-88A at room temperature.....	83
Synthesis of CAU-10 at 90 °C.....	83
3.3. Results and Discussion.....	83
3.4. Conclusions.....	97
3.5. References.....	98

Chapter 4: Aqueous Production of Spherical Zr-MOF Beads via Continuous-Flow Spray-Drying	101
4.1. Introduction.....	103
4.2. Experimental Section.....	104
4.2.1. Materials and methods.....	104
4.2.2. Optimised aqueous synthesis of UiO-66-NH ₂ by continuous-flow spray-drying.....	105
4.2.3. Optimised aqueous synthesis of Zr-fumarate by continuous-flow spray-drying.....	105
4.3. Results and Discussion.....	106
4.3.1. Aqueous synthesis of UiO-66-NH ₂ beads.....	106
4.3.2. Modulator effects on the synthesis of UiO-66-NH ₂ beads.....	110
4.3.3. Modulated aqueous synthesis of Zr-fumarate beads.....	117
4.3.4. Multi-gram synthesis of UiO-66-NH ₂ beads.....	121

4.4. Conclusion.....	122
4.5. References.....	123
Chapter 5: Systematic Study of the Impact of MOF Densification into Tablets on Textural and Mechanical Properties.....	125
5.1. Introduction.....	127
5.2. Experimental Section.....	129
5.2.1. Synthesis of MOF powders.....	129
5.2.2. Densification method and body characterization.....	130
5.2.3. Structure and porosity characterization.....	132
5.3. Results and Discussion.....	133
5.3.1. Influence of compression on MOF tablet properties.....	133
5.3.2. Comparison with literature data.....	138
5.3.3. Addition of expanded natural graphite as the binder for HKUST-1 powder.....	140
5.3.4. Overtime ageing of tablets in polyethylene bags.....	141
5.4. Conclusion.....	144
5.5. References.....	145
Chapter 6: Conclusions.....	149
Annex.....	155

Abstract

The present PhD Thesis has been dedicated to the development of basic knowledge on aqueous synthesis methodologies of MOFs and their shaping in order to make advances towards the large scale production of MOFs.

The first chapter presents a brief introduction to the porous materials, starting with the examples from nature, which is then followed by a short history of MOFs and their main applications. Additionally, we pay special attention to the current methodologies that are performed for the synthesis of MOFs at scale and downstream processes.

The second chapter consists of general and specific objectives of this Thesis.

In the third chapter, the usage of metal acetylacetonate complexes as an alternative metal salt for the synthesis of MOFs is illustrated in water for several MOFs, including Zr-, Fe- and Al- based MOFs at low temperatures. For each MOF (UiO-66-NH₂, Zr-fumarate, UiO-66-(OH)₂, UiO-66-(COOH)₂, UiO-66-COOH, MIL-88A and CAU-10), critical experimental parameters are defined and optimized to obtain high quality materials with high yields. Finally, the scalability of the methodology is shown with the gram scale synthesis of UiO-66-NH₂ by using optimized parameters in water at room temperature.

The fourth chapter demonstrates the continuous flow spray-drying technique that can be used as a green and scalable method to produce Zr-MOFs in the form of spherical beads. The influences of the important experimental factors are defined and the impact of those parameters on the synthesis of UiO-66-NH₂ and Zr-fumarate is shown. Finally, the scalability of the methodology is proven with the gram scale synthesis of UiO-66-NH₂ by using optimized parameters in water.

In the final chapter, the shaping process of the several MOFs that were synthesized by the spray-drying (HKUST-1 and UiO-66-NH₂) and batch (UiO-66 and UiO-67) synthesis methodologies is demonstrated. Mild pelletization technique is used to shape the MOFs into tablets to study textural and mechanical properties.

Resumen

La presente tesis doctoral ha sido dedicada al desarrollo y optimización de metodologías para la síntesis de MOFs en medio acuoso, así como su conformación y el avance hacia la producción a gran escala de estos materiales.

El primer capítulo presenta una breve introducción a los materiales porosos, empezando por los ejemplos presentes en la naturaleza, a los que luego sigue una breve historia sobre los MOFs y sus principales aplicaciones. Se prestará también especial atención a las metodologías usadas actualmente en la síntesis a gran escala de MOFs y su posterior procesado.

El segundo capítulo presenta los objetivos, generales y específicos, de esta tesis.

En el tercer capítulo se ilustra el uso de complejos metálicos de acetilacetonato como precursores alternativos en la síntesis acuosa a baja temperatura de varios MOFs, entre ellos MOFs basados en Zr, Fe y Al. Para cada material (UiO-66-NH₂, Zr-fumarato, UiO-66-(OH)₂, UiO-66-(COOH)₂, MIL-88A y CAU-10), se definieron y optimizaron diversos parámetros experimentales con el fin de aumentar el rendimiento y la calidad del material final. Finalmente, se confirma la escalabilidad de esta metodología a través de una síntesis optimizada a gran escala de UiO-66-NH₂ en agua a temperatura ambiente.

El cuarto capítulo demuestra el uso de la técnica de secado por atomización, o ‘Spray Drying’, como un método “verde” y escalable para la producción de Zr-MOFs en forma de cuentas esféricas. Se definirá la importancia de diversos factores experimentales, y se demostrará su impacto en la síntesis de UiO-66-NH₂ y Zr-fumarato. Finalmente, la escalabilidad del método será probada a través de una síntesis acuosa optimizada de UiO-66-NH₂ a escala de gramos.

Finalmente, el capítulo final se estudia el proceso de estructuración de varios MOF obtenidos con la técnica de ‘Spray Drying’ (HKUST-1 y UiO-66-NH₂) y de lotes de síntesis (UiO-66 y UiO-67) y su influencia en sus propiedades de adsorción. Tras ser modelados en forma de pastilla a diferentes presiones, se estudiaron sus nuevas propiedades mecánicas y de superficie.

Acknowledgments

First of all, I would like to thank Prof. Dr. Daniel Maspoeh and Dr. Inhar Imaz for their support and patience during my PhD. It has been a great opportunity for me to carry out this thesis under their supervision. I have learned a lot from them. Without their guidance and constant help, this dissertation would not be possible.

Besides my supervisors, I owe special thanks to the postdocs Dr. Javier Troyano, Dr. Javier Perez and Dr. Alexander Legrand for their collaboration during this thesis. They supported me greatly and were always willing to help me not only in lab work but also outside. Thank you for your cooperation in research and sincere friendship.

I would like to thank current and old members of NanoUp, Jordi, Claudia, Amirali, Laura, Blanca, Marta, Heng, Xavi, Natalia, YunHui, Farnoosh, Najmeh, Asier, Cristina and postdocs Sabina, Thais, Vincent and Arnau for sharing all these years with me and making it unforgettable. Special thanks to my current office mates, Luis Carlos, Jorge, Gerard, Anna, Borja, Hossein and Yang with whom I shared and solved many things, not only related to work. I had so much fun working and being with you guys. Thank you for all. Additionally, I want to thank our technicians and project managers, Marta, Jose, Rosa and Raquel for making life easier in the lab for us. It would be much harder without you.

I also thank team “Que trén que trén”, Nuria, Marianna, Kumara, Federico, Dani, and Fabian for their enjoyable accompaniment in Renfe on the way to ICN2 and back home. The time spent in the train would be as dull as dishwater without you guys. Thanks!!!

Many thanks to Turkish crew in Barcelona, Gulçin, Inci, Didem, Basak, Alican, Kutlu, Emre, and Onur. You have been like a family for me. Whenever I needed something, I came to you guys. Besides that, I will never forget our weekends full of fun with drinks, games, concerts, dumplings and many other things. Thank you for your friendship.

I am indebted to my closest friends Tugce & Dielse Inroga, Pinar & Ekin Gokturk and Ece Kizilkaya who have been always there for me. We grew up and spent our most enjoyable and crazy years together. Their support and friendship is very valuable.

My special thanks are for Civan who has been one of my best friends since we met in Bilkent. You were the one who convinced me to do a PhD in Barcelona and was always with me during all the process. Although we couldn't finish together the adventure that we started, I will always appreciate your support and shares as one of the closest person to me during these years.

Last but not least, I have to express my profound gratitude to my parents and my brother for their everlasting love and understanding. I would not be where I am today without them. Love you!!!

CHAPTER 1

Introduction to Metal-Organic
Frameworks (MOFs) and their
Synthesis

1.1. Porous Materials

Nature has always been a source of inspiration that scientists use in order to mimic and create useful materials that lead to an improved daily life. Porous architectures are one of those “natural” structures that benefit from millions of years of trials and errors of design; nowadays being integrated into various functions with many features. Shells of eggs and some seeds, for instance, are very good examples for the natural architecture of amorphous porous materials. Due to their natural semi-permeable membrane structure, these shells protect the inner material of the egg or the seed from the water and help to exchange matters with the environment for some metabolic processes.¹ As for the porous crystalline materials, zeolites are the most well-known naturally available ones. The first zeolite was discovered by a Swedish mineralogist, Axel F. Cronstedt, in the mining area of Kiruna, in northern Sweden. The exciting part of the discovery was the observation of large amounts of steam release from zeolites through the rapid heating of the material itself which opened many new application areas.^{2,3}

Another promising achievement was the dedicated studies for the artificial reproduction of such materials due to their significant sorption properties. The first synthetic porous materials were activated carbons, which were discovered by Egyptians around 3000 B.C. who used charcoal to absorb unpleasant odors. Activated carbons are amorphous porous materials that can be easily produced by the pyrolysis of materials, such as bamboo, coconut husk, willow peat, etc. They are commonly used for water treatment and air purification systems. However, the amorphous character of the activated carbons is a limitation for some applications including gas separation, drug delivery and so on. Other kind of materials and more complex synthesis techniques have been explored to be able to obtain ordered porosity and sharp pore size distribution.⁴

The advent of X-Ray diffraction allowed to determine the internal structure of zeolites. It was understood that they are made of TO_4 tetrahedrons, where TO_4 is $[SiO_4]^{4-}$ and/or $[AlO_4]^{5-}$. These tetrahedrons are bonded with the corner by sharing oxygen atoms to create secondary building units, forming cages and channels inside the structure by connecting each other.⁵ Therefore, zeolites were synthesized by the hydrothermal crystallization of aluminosilicate gels in the presence of alkali hydroxides and/or organic bases, or solutions in a basic environment. Although many people do not realize, these crystalline porous materials are used for many applications in daily life, such as in the removal of harmful gases, dehumidifiers, water purifiers etc. These porous structures have strong lattice stability that makes

them even more interesting for industrial applications including ion exchange,⁶ gas adsorption⁷ and catalysis.⁸

Even though zeolites have a significant place in daily life applications due to their porous nature, their chemistry and composition provide only limited control over the final product. In order to develop a material with a greater degree of flexibility, chemists have used both organic and inorganic components in the preparation of hybrid porous crystals. Tunability of the pore topology and composition of the structures is crucial to design the desired material with required features. In this sense, MOFs have an inherent design advantage making them better candidates for wide range application areas.⁹

1.2. Metal-Organic Frameworks (MOFs)

Metal-Organic Frameworks (MOFs) are hybrid crystalline porous materials produced by the assembly of metal ions or clusters with organic ligands through coordination bonds (Fig.1.1). The crucial step to creating rigid pores in the structure is the coordination of metal cation to organic compounds with at least two available sites to connect the metal parts during the synthesis of these materials.¹⁰

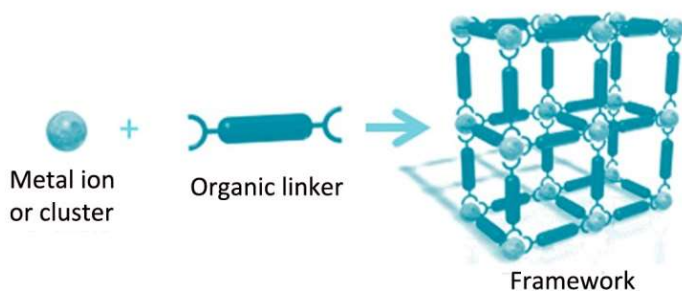


Fig.1.1: Scheme showing creation of MOFs.

Discovery of MOFs is a consequence of an increasing interest on understanding and controlling the assembly of coordination polymers at the beginning of 1990s. In this context, it was Robson who rationalized the formation of the extended networks by taking into account the coordination of metal ions and clusters and the geometry of the bridging ligands for the first time.¹¹ Therefore, Robson was able to describe the first 3-D framework with diamond-like structure

with tetrahedral Cu(I) centers connected to four molecules of tetra(4-cyanotetraphenyl)methane. As a natural evolution of these efforts to rationalize and design the network formation in coordination polymers, Yaghi *et al.* showed the use of a ditopic, rigid and linear molecule, 4,4'-bipyridine (4,4'-bpy) as a ligand to build Cu(4,4'-bpy)(NO₃) and introduce the term Metal-Organic Framework to the literature for the first time in 1995.¹² In this article, a diamond-like three-dimensional structure with voids filled by nitrate anions was reported. Only three years after, the same authors described the first coordination polymer with permanent porosity using a different system. Using bridging carboxylic-based ligands (terephthalic acid (BDC)) and Zn²⁺, they synthesized the Zn(BDC)(DMF)(H₂O) named MOF-2, which contains paddlewheel metal clusters bound by ligands forming 2-D grid networks.¹³ Compared to the previously reported systems, the obtained network was neutral and the channels crossing the structure were only filled by solvent molecules that were evacuated to provide accessible/permanent porosity for other molecules.

Following this route, two main microporous MOFs were subsequently reported in 1999. The first one reported was HKUST-1 (Hong Kong University of Science and Technology), which has the formula of Cu₃(BTC)₂(H₂O)₂ and formed by the assembly of Cu(II) paddlewheel and trimesic acid (BTC). The surface area of this neutral 3-D framework was reported as 692 m² g⁻¹ at that time using the Brunauer-Emmett-Teller (BET) theory.¹⁴ Later, higher values (1800 m² g⁻¹) were achieved with better activation techniques applied for HKUST-1.¹⁵ The second one reported was MOF-5, which consists of the 3-D assembly of octahedral zinc acetate clusters with BDC and has the formula of Zn₄O(BDC)₃. Reported BET surface area for this material was 2900 m² g⁻¹.¹⁶

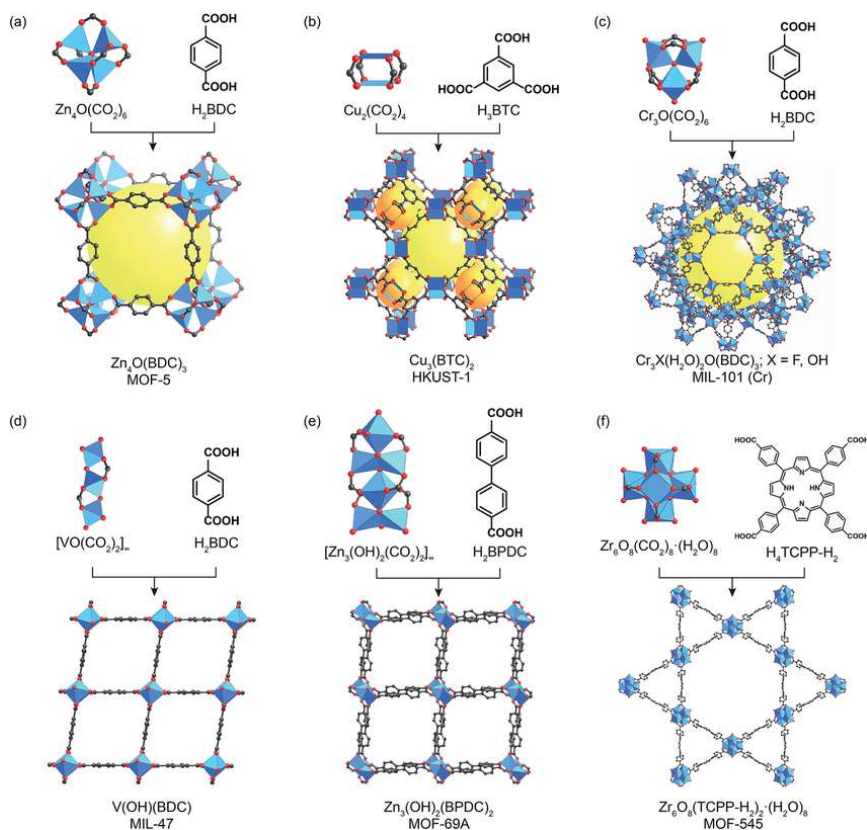


Fig.1.2: Varieties of MOFs synthesized by using different SBUs.¹⁷

Inspired by the previous work from Robson in coordination chemistry and Wells in inorganic chemistry, Yaghi et al. introduced the concept of Secondary Building Unit (SBU) to rationalize the MOF structures. SBUs molecular complexes /clusters in which ligand coordination modes and metal coordination environments can be used in the transformation of these fragments into extended MOFs using polytopic linkers. The consideration of the geometric and chemical attributes of the SBUs and linkers leads to prediction of the framework topology, and turn to the design of a new class of porous materials with robust structures and high porosity. This moment was the triggering point of a new field in science that is still growing nowadays (Fig.1.2).¹⁷

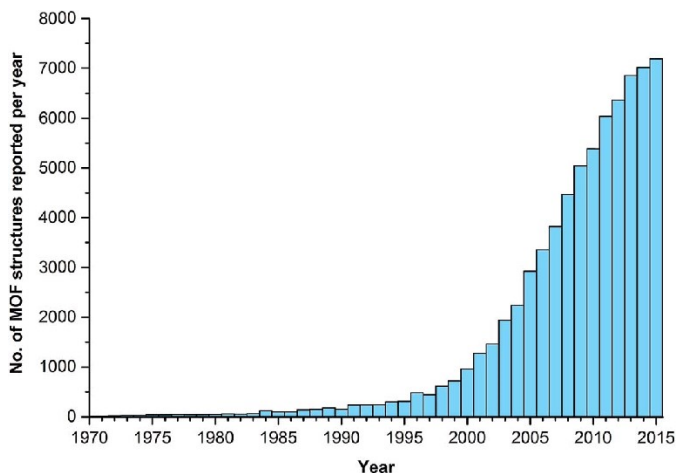


Fig.1.3: Amount of reported MOF structures between 1970 and 2015.¹⁸

Up to date, more than 20,000 MOF structures have been reported and many reviews describing these new porous materials have been published (Fig.1.3).¹⁹ Furthermore, this exponential growing in terms of topology and compositions have been followed by a continuous increase in the porosity performances. Currently, the porosity of the materials synthesized reached up to $7000 \text{ m}^2 \text{ g}^{-1}$.²⁰ This extraordinary result has been exploited in many applications, such as catalysis,²¹ gas storage and separation,²² sensor technology,²³ and drug delivery.²⁴

1.3. Applications of MOFs

MOFs provide unique properties such as high porosity, structural diversity and high stability to be used in wide range of applications (Fig.1.4).¹⁷ In this section, some of these applications will be given as a general overview.



Fig.1.4: Various applications of MOFs.

1.3.1. Gas storage and separation

Mostly, the purposes of gas storage and separation applications are environmental protection, dissemination of clean energy usage and control of toxic gases. In this sense, carbon dioxide separation and capture is very important to control greenhouse effect. In addition to that, hydrogen and methane gases are considered as greener energy sources. However, safe and efficient storage of these gases is still a challenge that has to be overcome before they could be considered a real alternative to oil. In order to solve these problems, MOFs have become a point of focus because of their large surface area compared to other traditional porous materials (Fig.1.5). The potential of the MOFs in gas storage and separation applications is addressed in the following sections.

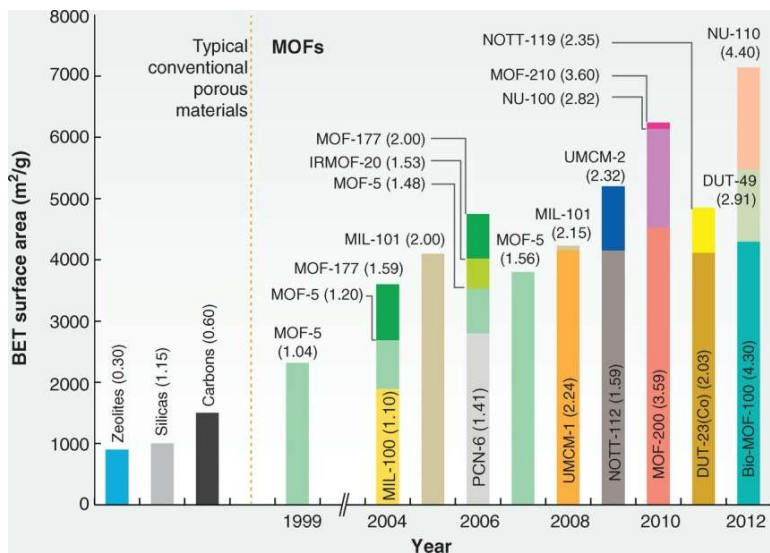


Fig.1.5: Improvement in the porosity of the MOFs during time according to their BET surface area calculation.¹⁸

1.3.1.1. CO₂ sequestration

Atmospheric warming due to greenhouse gases has become a serious global concern. Therefore, there is a need for an immediate-medium term solution to address the CO₂ emission of fossil fuel plants fast and in a cost-effective way. CO₂ capture technologies are recognized as one of the direct answers to this problem. Considering their higher surface area and lower density compared to the aforementioned materials, MOFs have the potential to overcome current challenges in CO₂ sequestration. MOFs are a good candidate to be used in CO₂ capture due to their porosity but also to their chemical tunability.²⁵

Indeed, the adsorbent that is to be used in CO₂ sequestration should exhibit selectivity to CO₂ over the other components including N₂, H₂, and CH₄. This can be the result of the size of the pores combined with the chemical affinity of the framework to CO₂. In this sense, activated MOFs can present unsaturated metals that exhibit Lewis acidity. These coordinately open metal centers act as binding sites where CO₂ molecules can attach and bind to the pore surface by the induction of dipole-quadrupole interactions. Accordingly, Deng *et al.* reported that Mg-MOF-74, with unsaturated magnesium ions, has the highest uptake capacity (27.5 wt %) ever reported under standard conditions (298 K and 1 bar).²⁶ The affinity of MOFs to CO₂ can also be increased introducing, for instance, basic Lewis groups such as

amines, imines, etc., decorating the pores these groups provides the advantage of chemisorptive process since CO_2 interacts with the lone pairs of the nitrogen atoms improving the adsorption of CO_2 . An example of this approach was shown by Hong and Long *et al.* through $\text{Mg}_2(\text{dobpdc})$ ($\text{dobpdc} = 4,4'$ -dioxidobiphenyl-3,3'-dicarboxylate). By the functionalization of the compound with N, N-dimethylethylenediamine (mmen), the CO_2 adsorption capacity increased fifteen times compared to the non-functionalized $\text{Mg}_2(\text{dobpdc})$ with good selectivity to CO_2 even in the presence of moisture (Fig.1.6a-c).²⁷

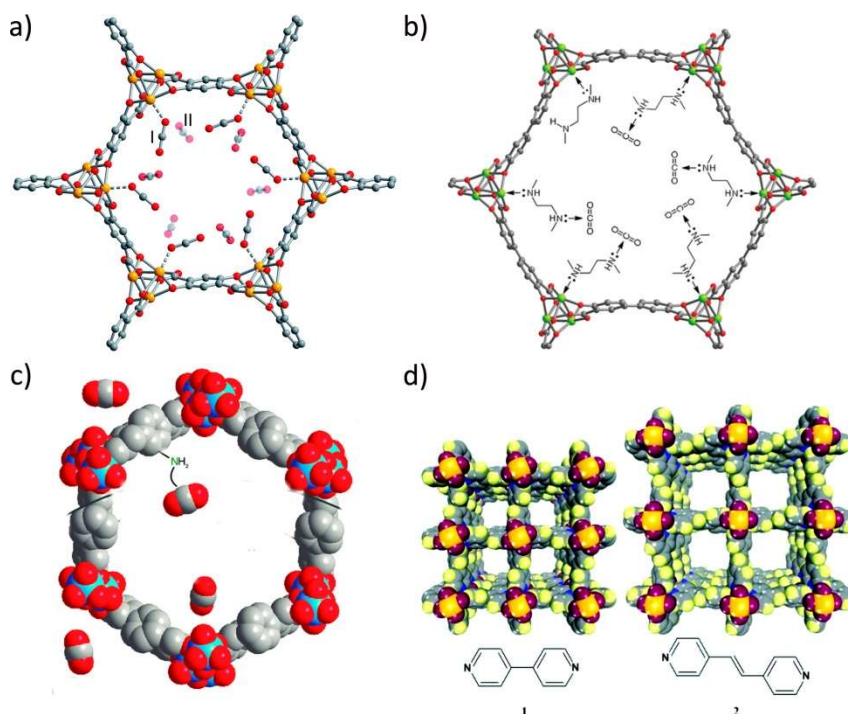


Fig.1.6: (a) Structure of Mg-MOF-74 that interacts with CO_2 molecules.²⁸ (b) Structure of dimethylethylenediamine functionalized $\text{Mg}_2(\text{dobpdc})$.²⁷ (c) Structure of IRMOF-74 showing the interaction of amine functionalized ligands with CO_2 molecules.²⁵ (d) Tetragonal crystal structures of $[\text{Cu}(\text{bpy-1})_2(\text{SiF}_6)]$ (left) and $[\text{Cu}(\text{bpy-2})_2(\text{SiF}_6)]$ (right). The dimensions of these channels are controlled by the bpy-1 and bpy-2 linkers.²⁹

Finally, non-metallic groups inside the framework can also be used to improve the CO_2 adsorption capacity through the strong interactions between CO_2 molecules and non-metallic groups inside the framework. A good example of this approach are MOFs produced from the coordination of fluorinated M-XF_6 pillars ($\text{M} = \text{Co}, \text{Ni}, \text{Cu}, \text{and Zn}$; $\text{X} = \text{Si}, \text{Ti}, \text{and Sn}$) to N-donor type ligands. These MOFs

show high CO₂ uptake and selectivity thanks to the “perfect” size of the channels and the interaction between CO₂ molecules and fluorine atoms. Among this family, SIFSIX-1-Cu (Cu(4,4'-bpy)₂(SiF₆); (4,4'-bpy = 4,4'-bipyridine)) and SIFSIX-2-Cu-i (Cu(dpa)₂(SiF₆); (dpa = 4,4'-dipyridylacetylene)) display CO₂ uptake capacities of 19.1 and 19.2 wt % at ambient pressure, respectively. This is the highest uptake reported for a MOF without coordinative unsaturated metal sites (Fig.1.6d).^{29,30}

1.3.1.2. H₂ adsorption

Because of its abundance, high combustion heat, and formation of non-hazardous combustion products, mostly being water hydrogen, is an excellent replacement for coal and gasoline as an energy source. Although H₂ has ultrahigh energy per mass compared to other fuel sources, its low ambient temperature and density result in a low energy per unit volume that requires new methods for its safe storage, transport, and an increase of its penetration.³¹

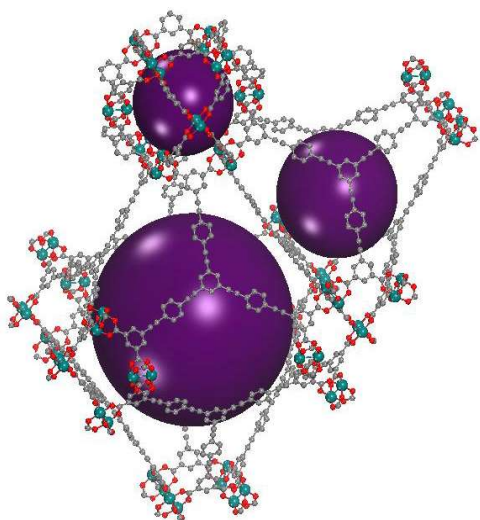


Fig.1.7: Representation of the solved structure of NU-100.²⁰

Since surface area is highly correlated with the amount of gas adsorbed, a first strategy was tuning the pore shape and size. For example, NU-100, a copper paddle wheel based MOF with the formula Cu₃(L)(H₂O)₃ (L = 1,3,5 - tris [(1,3- carboxylic acid – 5 - (4-(ethynyl)phenyl)ethynyl]-benzene) and an S_{BET} of 6143 m² g⁻¹, have shown the highest capacity to store H₂ at 77 K and 56 bar as 99.5 mg g⁻¹ (Fig.1.7).²⁰ In 2016, Zhou *et al.* reported the MOF PCN-6, built up by the assembly of Cu²⁺ and 4,4',4''-s-triazine-2,4,6-triyl-tribenzoic acid. This later MOF showed a capacity to adsorb H₂ as 72 mg g⁻¹ at 77 K and 50 bar.³³

H₂ can be stored as a pressurized gas in cryogenic conditions or with the help of porous materials through physisorption and chemisorption. In this context, the use of absorbent materials provides fast adsorption and desorption kinetics conditions and decreases the need for energy and pressure. In this regard, MOFs, with their highly porous and diverse nature, have been proved to be good candidates.³²

Since surface area is highly correlated with the amount of gas adsorbed, a first strategy was tuning the pore shape and size. For example, NU-100, a copper paddle wheel

As explained in the previous section, introducing open metal sites in the framework can also increase the H₂ adsorption capacity. For example, Long *et al.* reported the synthesis of Mn₂(dsbdc) (dsbdc = 2,5-disulfido-1,4-benzenedicarboxylate) with coordinatively-unsaturated metal centers. The presence of the open metal sites helped to increase the uptake twice through interaction with H₂ molecules (1.6 wt% at 77 K and 1.2 bar).³⁴

1.3.1.3. CH₄ adsorption

Because of its low CO₂ production during combustion, natural gas is considered another environmental friendly energy source that could serve as a replacement for gasoline and coal. In order to extend its usage, safe transportation and storage conditions should be provided. The low energy density of methane presents a challenge when applied for use in transportation. In this point of view, usage of an adsorbent material can provide storage conditions at room temperature and under low pressures, which is not possible with the compressing methods.³⁵

As adsorbent materials, MOFs have already proven to be efficient materials to store high amounts of methane at low pressures compared to compressing it to an empty tank. Among many others, HKUST-1 has been shown as an excellent candidate thanks to its exceptional natural gas adsorption capability with 270 cm³ (STP) cm⁻³ at 65 bar and 298 K. To date, HKUST-1 is the only material capable of fulfilling DOE targets (263 cm³ (STP) cm⁻³ at 65 bar and 298 K). Its high adsorption is related to the interaction of the open metal sites with methane molecules at low pressures and the interaction with the oxygen molecules at high pressures.³⁶ Recently, shaping of HKUST-1 as a monolithic dense structure without decreasing its adsorption capacity has been reported by Fairen-Jimenez *et al.* This is the first literary material that could reach DOE target values of 259 cm³ (STP) cm⁻³ at 65 bar after densification and shaping.³⁷ (Fig.1.8)

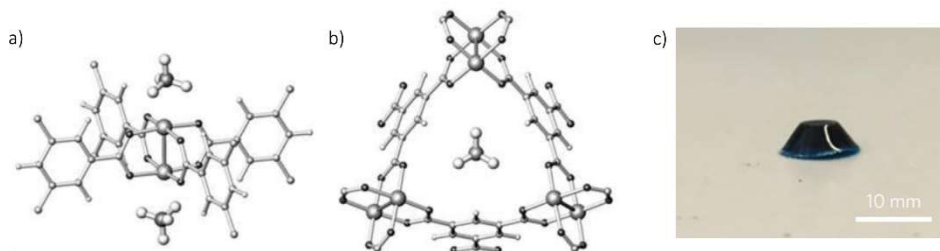


Fig.1.8: Representation of interaction of CH₄ molecules with the unsaturated metal sites (a) and the octahedral cage (b) of the HKUST-1.³⁸ (c) Photograph of monolithic HKUST-1.³⁷

Besides HKUST-1, other MOFs have shown good performances in volumetric storage of methane gas. Some of these MOFs are PCN-14 ($239 \text{ cm}^3 \text{ cm}^{-3}$ at 65 bar),³⁹ Co-MOF-74 ($249 \text{ cm}^3 \text{ cm}^{-3}$ at 65 bar),³⁹ Ni-MOF-74 ($260 \text{ cm}^3 \text{ cm}^{-3}$ at 65 bar),³⁹ and NOTT-100 ($242 \text{ cm}^3 \text{ cm}^{-3}$ at 65 bar).^{40,41}

1.3.2. Water sorption applications

As mentioned before, there are many investigations being conducted to produce MOFs with special designs in order to improve the sorption capacity for gases, such as methane, carbon dioxide and hydrogen. Since the first discovered MOFs (e.g. HKUST-1 and MOF-5) were not stable in moistures conditions, water sorption features was later explored with the advent of water stable MOFs. In these studies, it turned out that MOFs present high water uptake with type V isotherms (Fig.1.9), which is useful for some industrial applications such as adsorption heat transformation (AHT).⁴²

In order to decrease the consumption of electrical power, creating efficient and environmental friendly cooling systems has been attempted so many times.

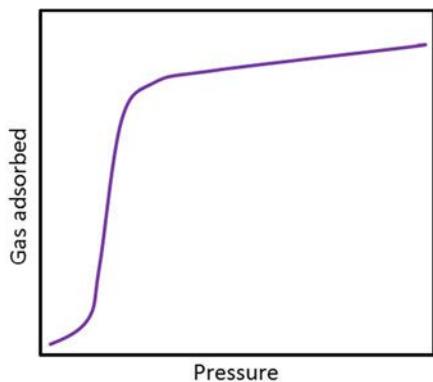


Fig.1.9: Representative S-shape, type V isotherm.

Adsorption and desorption based processes are good candidates to be employed as green refrigerating systems by using low temperature waste heat or solar collectors as energy source instead of electricity and water as a working liquid. Thanks to their stability under humid conditions, MOFs are efficient materials to be used in these applications. They present S-shape adsorption isotherm (Fig.1.9) which provides with high working capacity on very narrow window of relative pressures and low regeneration temperatures.⁴³

The AHT systems depend on use of thermal energy to supply cold and heat. The process occurs as a cycle that starts with the evaporation of the water by using the heat from the surrounding. The adsorbent adsorbs water vapour and heat is released to the surrounding at an intermediate temperature since the adsorption of the water is an exothermic process. As the adsorbent is getting saturated with water, regeneration (desorption of the adsorbed water) is needed so the desorption starts at a relatively high temperature. The desorbed water is subsequently condensed, while releasing heat at an intermediate temperature. This can work as an adsorption cycle

as heat pump to produce heat at the intermediate temperature, using effectively heat of condensation or adsorption or to produce cold at the lower temperature by using heat of evaporation (chiller) (Fig.1.10).⁴⁴

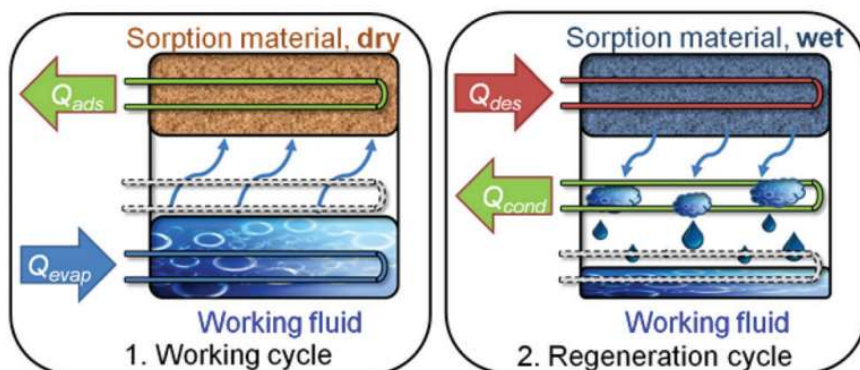


Fig.1.10: Working cycles of a sorption based chiller/heat pump.⁴⁴

To be considered as efficient materials for AHT applications, MOFs have to fulfil some requirements. The sorption should be sharp, presenting a type V isotherm in the pressure range between 5% and 35% relative humidity with a water sorption capacity higher than $0.2 \text{ g}_{\text{water}} \text{ g}^{-1}$ and regeneration temperature lower than $120 \text{ }^\circ\text{C}$. Janiak and Henninger *et al.* reported that CAU-10-H ($\text{Al}(\text{OH})(1,3\text{-BDC})$) can be a good candidate for this application. They could perform 10000 water adsorption/desorption cycles with the sorption peak at 25% relative humidity with a permanent capacity of $0.34 \text{ g}_{\text{water}} \text{ g}^{-1}$.^{45,46} In another study, UiO-66- NH_2 and MIL-125- NH_2 have also shown as good candidates exhibiting high water uptake and high stabilities even after 40 cycles (Fig.1.11).⁴⁴ Recently, Gordeeva *et al.* reported that Zr-fumarate (or MOF-801) can also be an efficient material for air conditioning applications, showing low temperature working range (up to $85 \text{ }^\circ\text{C}$) and uptake up to $0.21 \text{ g}_{\text{water}} \text{ g}^{-1}$.⁴⁷

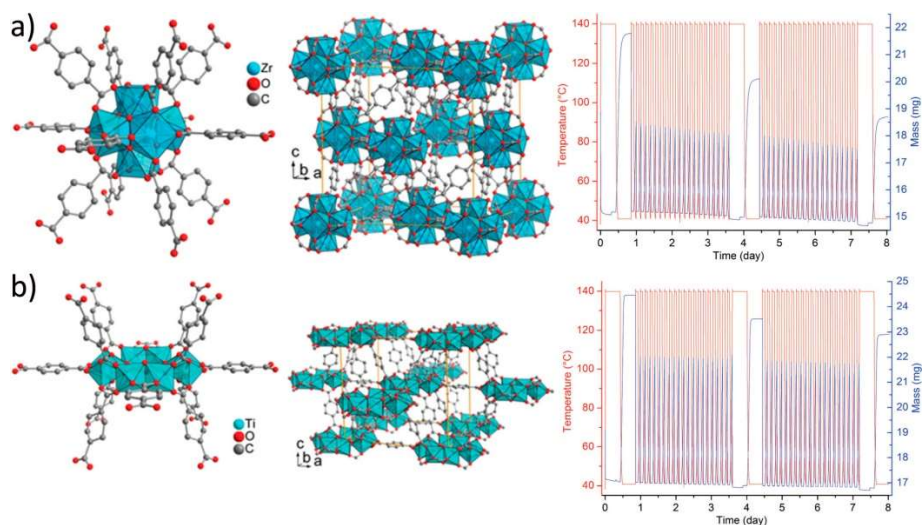


Fig.1.11: (a) Structure of UiO-66-NH₂ an octahedral cluster and related water sorption cycles. (b) Structure of MIL-125 built up from a TiO₆ octahedral cluster and related water sorption cycles of MIL-125 (right).⁴⁴

1.3.3. Catalysis

MOFs, with their adjustable chemical composition (metal and organic moieties) and high surface area, are potential catalysts for homogenous and heterogeneous catalysis processes. In order to design MOFs as efficient catalysts, different strategies have been developed. They include using metal nodes, defective MOFs, functionalized linkers and active species supported by MOFs.^{48,49}

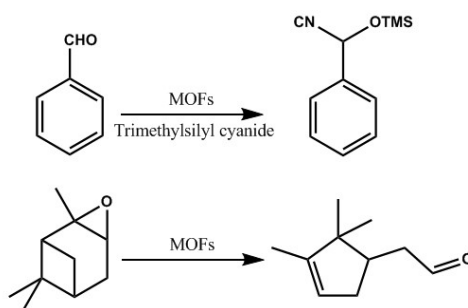


Fig.1.12: Cyanosilylation of benzaldehyde (above) and rearrangement of α -pinene oxide to campholenic aldehyde (below).

The first approach is taking advantage of unsaturated sites of metal nodes, which can act as catalytic centers in certain catalysis reactions. Since these metal sites exhibit Lewis acid character, these materials are preferable catalysts for the reactions that could be catalyzed by Lewis acids. For example, MOFs are useful in cyanosilylation reactions. HKUST-1 is an efficient catalyst for cyanosilylation of aldehydes thanks to its inherent Lewis acidity arisen from unsaturated Cu^{2+} sites.⁵⁰ In addition to cyanosilylation reactions, HKUST-1 was utilized as a catalyst in the isomerization of terpene derivatives, such as the rearrangement of α -pinene oxide to campholenic aldehyde, and the cyclization of citronellal to isopulegol (Fig.1.12).⁵¹ Another way to take advantage of the open metal sites in the framework is generating defects in the structure by controlling the synthesis of MOFs. As an example, a sulfone-functionalized MOF, USTC-253 (University of Science and Technology China), was synthesized by adding trifluoroacetic acid (TFA) during the synthesis of the USTC-253 was material to produce a defect-containing MOF sample (Fig.1.13). The catalytic activity of the defective USTC-253 studied in the CO_2 cycloaddition to propylene oxide at room temperature with 1 bar pressure. USTC-253-TFA afforded 81.3% conversion in the presence of $n\text{Bu}_4\text{NBr}$ (TBAB) as a cocatalyst at room temperature.⁵²

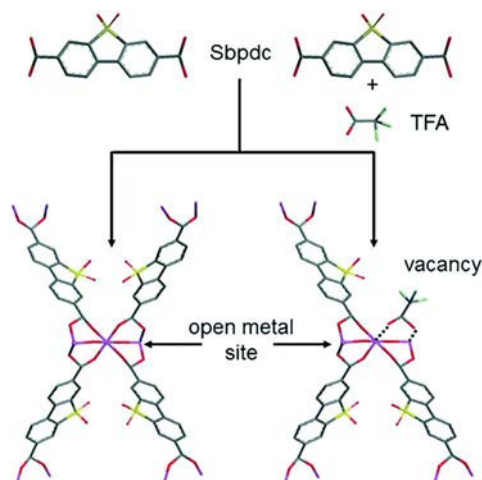


Fig.1.13: Synthesis of USTC-253 and defect- engineering by adding TFA to the synthesis.⁵²

Introducing functional linkers to the framework is the third way to control the catalysis reaction. Presence of functional groups on the aromatic linkers has an important role on the intrinsic catalytic activity of the metal nodes due to inductive effects. Addition of electron withdrawing groups, such as $-\text{NO}_2$ and SO_3H , enhances the Lewis acidity of the metal nodes and correspondingly, the catalytic

activity also increases. This effect was studied on UiO-66 and MIL-101 and which were effectively used as catalyst for different reactions such as epoxide ring opening and oxidative coupling of benzylamines to imines.⁵³

Finally, another approach involves using MOFs as a support to active species including inorganic nanoparticles (iNP). iNPs are highly active materials to be used in catalysis. However, they tend to aggregate and lose or decrease their reactivity. In addition to that, their small size precludes recollection of the catalyst from media and recycling of the material. All these factors make large scale industrial applications very challenging. In this sense, with their high stability and large surface area, MOFs are good candidates to be used as a support in preventing aggregation and ease the collection of iNPs from the reaction media. To date, several MOF based composites have been shown as efficient catalysts for very important reactions that include CO oxidation, alcohol oxidation, hydrogenation and C-C coupling reactions (Sonogoshira, Suzuki-Miyaura and Ullman coupling). In general, ZIF-8, UiO-66, MIL-101(Cr) and HKUST-1 have been shown as good supports for iNPs (Pt, Pd, Au, Cu/Pd, CeO₂, Pt/Pd, Au/CeO₂ and Au/Pd). The resulting composites have been used in those reactions mentioned before with conversion percentage higher than 98% (Fig. 1. 14).^{54,55}

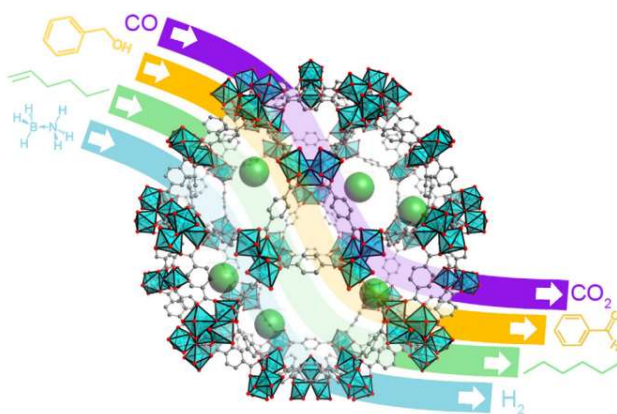


Fig.1.14: Schematic Illustration of some representative reactions catalysed by MOF supported iNPs.⁵⁵

1.4. Synthesis of MOFs at Scale

As seen above, MOFs have emerged as a focus of academic fascination and commercial opportunity due to their unprecedented porous structures that imply a plethora of potential applications. However, translating these new materials into disruptive technologies, it is crucial to manufacture them at the required scale, purity and price. For example, the use of MOFs to store CH₄ as a fuel for vehicles would require megaton scale production of MOFs.⁵⁶ Or for CO₂ capture, since more than 8000 million tons of CO₂ are produced from coal-fired power stations annually many millions of tons of MOFs should be needed to capture it.^{57,58} In the laboratory, MOFs are most commonly produced in milligram scales, with multi-day reaction times and using expensive organic solvents. Their synthesis is often the balance of a number of competing forces, with a range of kinetic and thermodynamic products possible, meaning that a narrow set of reaction conditions are often possible for a successful synthesis. The large gap between laboratory production and that required for commercial application has created a strong imperative to develop efficient and versatile means of producing MOFs at scale.

As scale up production methods are developed, parameters for assessing their viability have become important. Of these, the key parameter is the space-time yield (STY), a measure of forces, with a range of kinetic and thermodynamic products possible, meaning that a narrow set of reaction conditions are often possible for a successful synthesis. The large gap between laboratory production and that required for commercial application has created a strong imperative to develop efficient and versatile means of producing MOFs at scale. As scale up production methods are developed, parameters for assessing their viability have become important. Of these, the key parameter is the space-time yield (STY), a measure of the amount of MOF able to be produced per unit volume of reactor in a 24 h period. In concert with this, we recently proposed that the absolute value (in g h⁻¹) is also important. Many new production techniques are still in the early stages, meaning that the calculated STY may be prone to overextrapolation. Other important factors are measures of product quality (such as surface area and phase purity), particle size control, yield, and the versatility of the technique. There are several challenges common to the bulk of the prospective scale up methods:

(a) Use of organic solvents. At scale, their cost, toxicity and in some cases flammability become significant issues.

(b) Anion build up. Typically, metal salts are employed as precursor molecules. At scale, nitrates present a safety hazard, and anions such as chlorides can prove corrosive. Oxide and hydroxide metal precursors are preferable.

(c) Ligand availability. Many MOFs require bespoke organic ligands. Production methods that could also produce these starting materials are in development.

(d) Particle size control. Applications such as membranes require nanometre sized particles, whereas larger particles are desired to stop unwanted movement of the MOF particles in storage applications. Control of this is an important attribute.

(e) Activation. MOFs require removal of non-volatile solvents and unreacted starting materials from their pores. This is a major consideration at large scale.

(f) Shaping of MOF powders produced is also required for using them in real industrial applications.

All these challenges, which are specific for each MOF family due to their different composition and coordination nature, together with their extreme porosity, make the synthesis of these materials more complex than zeolites; each MOF requires bespoke conditions. In recent years, a number of approaches for addressing these challenges have been considered, including electrochemical, microwave and mechanochemical syntheses as well as spray drying and continuous flow production. Electrochemical synthesis of MOFs was developed by BASF and their initial purpose was to exclude anions by using metal electrodes as metal sources. Microwave-assisted synthesis, flow chemistry and spray-drying synthesis allow for a faster crystallization rate and production of smaller MOF crystals. In mechanochemical synthesis, no external heating or solvent is needed, reducing the washing and activation labour after the synthesis. Given the rapid progress in the development of these techniques, there has been a recent rise in commercial entities that seek to utilise and/or produce MOFs. This section seeks to provide an update on progress of these companies, with direct input from them. BASF pioneered large-scale, bespoke solvothermal techniques primarily for use in vehicular natural gas storage. Following this, spin-out companies have been established, often based upon novel reaction techniques originally developed in a research setting. Some spin-out companies also seek to develop MOF-based products in addition to the broader supply of MOFs to the research community.

1.4.1. Production of MOFs: from laboratory to industrial scale

In 1995, Nalco Chemical Company and Omar Yaghi claimed the use of solvothermal synthesis to obtain MOFs.⁵⁹ Up until now, this synthetic approach is the most common way to obtain grams of MOFs in the laboratory around the world. This method involves mixing solutions of the inorganic salt with the organic linker in a sealed reactor vessel and subsequent heating to promote the growth of insoluble

frameworks that precipitate as fine crystals.^{60,61} This sealed approach allows the reaction mixture be heated up to temperatures and pressures above the solvent's boiling point to solubilize, partially or completely, otherwise insoluble reagents and form extended networks. It has become a benchmark in MOF chemistry, and a large variety of MOF families such as MIL series,^{62,63} MOF-74,^{27,64} UiOs^{65–67} and PCNs^{68,69} have been synthesized following this principle.

However, despite the tremendous academic interest those MOFs have generated in the last two decades, with thousands of new structures and with very promising applications, only very few of them are produced at large scale and used in real world applications.^{49,70–74} The main reasons for this are the lack of stability of most of the structures towards temperature and humidity, the high cost of the raw materials and, above all, the difficulty of scaling up the synthesis and the post-synthetic stages in a cost-effective way whilst maintaining the product quality and reproducibility between batches. In addition, while the solvothermal approach is a well-known industrial method for chemical synthesis, its application for large scale MOF production is not feasible as MOF synthesis relies on the nucleation at a reactor vessel surface. Up-scaling the reactor vessel significantly decreases the surface to volume ratio and consequently, reduces the efficiency of the reaction. Additional problems include: long reaction times (hours or days), large amounts of solvents used, low quality of materials obtained, high complexity and cost in the up-scaling.⁷⁵

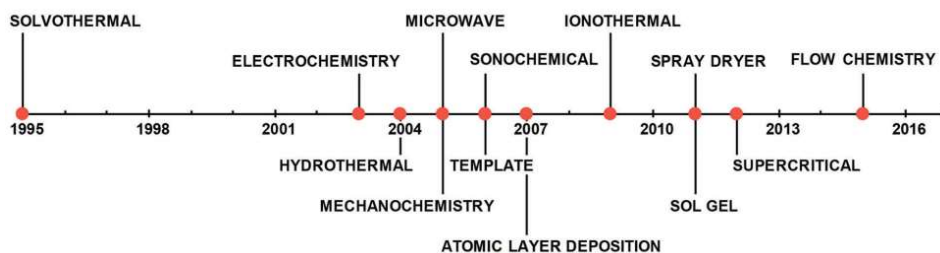


Fig.1.15: Timeline of the most common synthetic approaches patented for the synthesis of MOFs.^{59,76–85}

In order for any production MOF process to be industrially viable a number of key aspects have to be considered: (i) a versatile method is crucial in order to accommodate the maximum number of MOF structures with the same piece of equipment; (ii) the possibility to avoid harsh processing conditions such as high

temperature and pressure will reduce capital and operating costs and alleviate safety concerns; (iii) a switch from batch to continuous processing would be beneficial offering higher output per unit time and a continuous steady-state operation leading to significantly reduced downtimes, labour costs, reactor volumes, as well as constant and consistent production; and (iv) a high space-time-yield (STY) parameter which measures the amount of MOF produced per m³ of reaction mixture per day. All these factors make the scale-up of MOF production challenging and have motivated many researchers and engineers to explore and develop novel and commercially viable routes to produce MOFs in an efficient, reproducible and cost-effective way.^{86,87} Fig.1.15 shows the timeline of the most common synthetic processes developed in the last two decades. In this section, energy-efficient processes with reduced reaction times that facilitate the up-scaling and the continuous operation will be persecuted. These methods/processes includes in electrochemical,⁷⁶ microwave⁷⁹ and mechanochemistry⁸⁸ approaches and the more recent routes, the spray drying⁸³ and flow chemistry.⁸²

1. 4. 1. 1. Electrochemical synthesis

Electrochemistry can be defined as the study of interconversion between chemical and electrical energy. It combines electricity and chemistry and deals with chemical changes caused by an electrical current.

Taking advantage of the potential of electrochemistry to synthesize materials and their large experience in the domain, the company BASF first patented the use of electrosynthesis to produce MOFs in 2005.⁸⁹ The synthesis consisted on immersing a copper plate in a solution containing the organic linker, 1,3,5-benzenetricarboxylic acid (BTC), and an electrolyte. The copper plate, which acts as the electrode, was used as the source of Cu(II) ions. When a certain current or voltage was applied, the Cu(II) ions were released from the copper electrode to the solution and reacted with the dissolved linker. In this patent, a powder of electrochemically produced HKUST-1 that consisted of octahedral crystals (size: 0.5–5 mm) could be fabricated after applying a voltage of 12–19 V and a current of 1.3 A for 150 min. The surface area of this synthesized HKUST-1 was 1820 m² g⁻¹, which is higher than that reported for the solvothermally synthesized HKUST-1 (1550 m² g⁻¹).⁹⁰

Since this first patent, electrochemical synthesis of MOFs (Table 1.1) has attracted great attention because it can offer many advantages. One of them is the possibility to run the synthesis of MOFs in a continuous way. It also allows their synthesis under milder conditions than typical solvothermal or microwave

syntheses, reducing the reaction time. Indeed, while solvothermal synthesis might take hours or days, electrochemical methods can produce the MOF material within minutes or hours. In addition to these, the electrochemistry method provides the ability to control the MOF synthesis directly during the reaction by controlling the passed current or applied voltage (Table 1.1). Furthermore, the electrochemistry method offers the possibility to synthesize homogeneous thin films or coatings.⁹¹

Electrosynthesis of MOFs can be classified in two main methods: (i) the anodic dissolution, which was the first route patented by BASF; and (ii) the cathodic deposition. In the anodic deposition, an applied electric potential induces the release of metal ions from the electrode, which then react with an organic linker present in the solution leading to the formation of a MOF film. In this case, the use of a metallic electrode (instead of metal salts) as the source of metal cations avoids the formation of any corrosive anions (mainly, nitrate and acetate anions) or any by-products. The anodic dissolution is typically carried out in a two-electrode set-up without a reference electrode, and the use of protic solvents is usually needed to ensure the evolution of hydrogen and avoid the reduction of metal ions at the counter electrode. In addition, the use of a sacrificial compound (e.g. acrylonitrile, acrylic or maleic esters) that are preferentially reduced or a counter electrode with a suitable overpotential for hydrogen evolution is recommended.⁹² In the cathodic deposition, a solution containing the organic linker, the metal ions, and a so-called probase is contacted with a cathodic surface. In this approach, the MOF film deposition results from increasing the pH near the cathodic surface, where the electrochemical reduction of the probase occurs. An example of a probase is the nitrite ions coming from the reduction of nitrates, which are able to deprotonate the organic linker and form the MOF.⁹³

Since the electrochemical synthesis of HKUST-1 by BASF using the anodic dissolution was reported, there have been many efforts to understand and optimize this new route (Fig. 1.16 a). Fransaer *et al.* recently proposed a mechanism for the anodic dissolution synthesis of HKUST-1 that consists in four phases: (i) initial nucleation; (ii) growth of HKUST-1 islands; (iii) intergrowth; and (iv) crystal detachment.⁹⁴ When an electric potential is applied, the oxidation of the anode starts and the Cu(II) ions are released into the solution. The nucleation of the HKUST-1 phase starts once the critical ion concentration on the surface of the anode is reached. The nucleation is progressive and the dimensions of the crystals depend on the synthesis time and choice of the solvent. The HKUST-1 layers grow at the MOF–solution interface confirming that Cu(II) ions, which are dissolved at the interface, diffuse through the HKUST-1 crystals before they react with the organic linker. This migration of ions is accompanied by the creation of voids at the

substrate–HKUST-1 interface, resulting in the formation of fragile layers of HKUST-1 crystals that are easily detached from the substrate. Simultaneously, van der Veen and Domke *et al.* described this anodic dissolution mechanism from a more chemical point of view.⁹⁵ These authors identified that chemical species involved in the electrosynthesis of HKUST-1 are initially $\text{Cu(I)}_2\text{O}$, which results from the oxidation of the copper plate in the presence of H_2O or O_2 . Then, $\text{Cu(I)}_2\text{O}$ is further oxidized to Cu(II)O that can react with the organic linker and lead to the formation of HKUST-1 crystals.

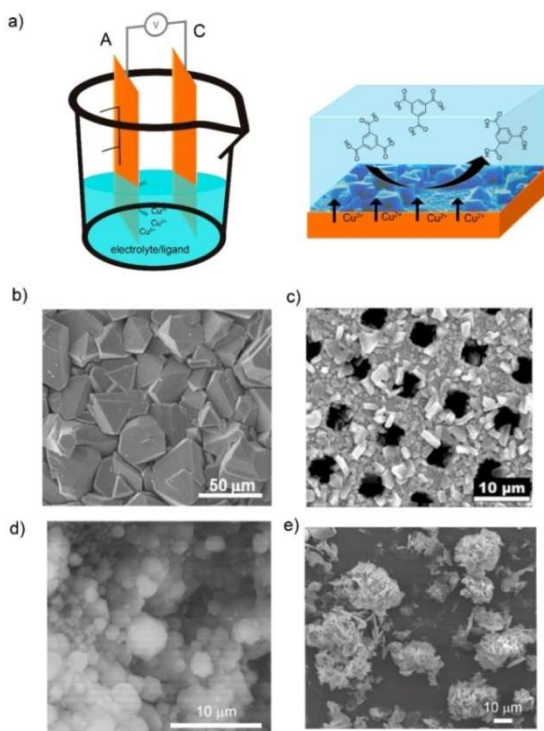


Fig.1.16: Electrosynthesis of MOFs by anodic dissolution. (a) Schematic illustration showing the anodic dissolution cell (left) and the formation of HKUST-1 on the anode electrode (right). (b) SEM image of HKUST-1 on a copper electrode. (c) SEM image of HKUST-1 on a copper mesh. (d) SEM image of ZIF-8 particles on a zinc electrode. (e) SEM images of flower-shaped MOF-5 on a zinc electrode.^{96, 98, 103, 106}

square wave functions were used instead of a continuous mode.⁹⁷ Denayer *et al.* found that the frequency of these square wave functions does not influence the HKUST-1 coating of the copper electrode.⁹⁸

To date, it is known that small variations of the applied electric potential and passed electric current, the nature of the solvent and its conductivity, and nature of the electrolyte have a strong influence on the anodic dissolution synthesis of HKUST-1. For example, the applied electric potential is important due to the direct influence on the generation of Cu(II) ions from the copper electrode. As observed by De Vos *et al.*, higher voltages applied by square wave functions provided higher concentration of Cu(II) cations because of the higher dissolution rate of the copper metal (Fig. 1.16 b). These conditions led to the formation of coatings with smaller crystals of HKUST-1 in agreement with the nucleation theory.⁹⁶ In the same line, Gascon *et al.* observed better results in terms of HKUST-1 coverage of the electrode when

Solvent media is also influencing the electrochemical crystallization of HKUST-1. De Vos *et al.*⁹⁶ and Denayer *et al.*⁹⁸ observed the formation of larger crystals when the amount of water (from 10 to 50% in volume) was increased in the electrolyte water/ethanol solution because it slowed down the reaction by the hydration of the Cu(II) cations. In addition, detachment of HKUST-1 crystals from the electrode was observed for water contents higher than 50%. Under these conditions, Gascon *et al.* detected the formation of a secondary phase consisting of a catena-triaqua- m -(1,3,5-benzenetricarboxylate)-copper(II) compound.⁹⁹ More recently, Deyaner *et al.* investigated the effect of other organic solvents (e.g. methanol, ethanol, 2-propanol, acetonitrile, N,N-dimethylformamide (DMF), and dimethylsulfoxide (DMSO)) in the electrochemical formation of HKUST-1 (Fig. 1.16 c).¹⁰⁰ They observed that the crystal size increases when increasing the water content in methanol and ethanol; less dense and uniform HKUST-1 layers are obtained in 2-propanol; HKUST-1 crystal morphology is different when using acetonitrile instead of methanol or ethanol; octahedral crystals are generated in DMF; and the amount of water does not influence the synthesis of HKUST-1 in DMSO, as it does in methanol or ethanol.

Because of the low conductivity of the reaction media, electrolytes that enhance charge transport in solution are generally used. Tributylmethylammonium methyl sulfate (MTBS) is usually recommended for syntheses carried out in organic media and, indeed, it showed a positive role on the HKUST-1 synthesis. For example, increase of conductivity by increasing the concentration of MTBS in the electrolyte solution reduced the ohmic drop of the solution and increased the production yield of HKUST-1. However, Deyaner *et al.* found some disadvantages related to the use of MTBS in the electrochemical formation of HKUST-1 thin films. They observed structural damages of the copper mesh and the generation of non-adhesive HKUST-1 crystals at the surface of the anode. On the contrary, they could get more control over the synthesis in the absence of MTBS because of lower current density in the system.⁹⁸ Another disadvantage of using MTBS was reported by Hartmann *et al.*, who observed a decrease in the surface area of HKUST-1 that was attributed to the presence of the electrolyte salt in its pores.¹⁰¹

Beyond the archetypical HKUST-1, the syntheses of other MOFs have been envisaged using anodic dissolution. Remarkably, Gascon *et al.* demonstrated the possibility to electrochemically synthesize ZIF-8, MIL-53 and MIL-100(Al).⁹⁷ Since then, De Vos and Fransaeer *et al.* optimized the quality of the synthesized MIL-100(Fe) by performing the electrochemical synthesis under high pressure and high temperature.¹⁰² Also, Attfield and Dryfe *et al.* improved the synthesis of zeolitic imidazolate frameworks (ZIF) (e.g. ZIF-4, ZIF-7, ZIF-8, ZIF-14, and ZIF-67)

coatings (Fig. 1.16 d) by increasing the reaction times (a proxy for higher metal ion concentration), the organic linker concentration and the reaction temperature.¹⁰³ With this anodic dissolution, luminescent rare earth based MOFs were also prepared by Fransaer *et al.* on electrically conductive solid substrates.¹⁰⁴ Here, Tb-BTC and Gd-BTC layers were electrochemically synthesized on terbium and gadolinium metal foils by immersing the foil in a water–ethanol solution containing the organic linker, the electrolyte (MTBS) and applying a constant current of 1 mA cm².

Within this variety of MOFs, the electrochemical synthesis of MOF-5 has also been largely investigated. Cao *et al.* reported the anodic dissolution electrosynthesis of thin films of rod-like MOF-5 crystals.¹⁰⁵ They could generate dense and thick MOF-5 films by using zinc electrodes in an aqueous solution containing H₂BDC and ammonium fluoride as the electrolyte salt and applying voltage (2 V) at 65 °C. Liang *et al.* synthesized MOF-5 in the form of flower shape by using molten salt in the electrolyte solution and 1-butyl-3-methylimidazole (Bmim) bromine as a template (Fig. 1.16 e).^{106,107} This MOF-5 was synthesized using a zinc plate as the anode, a titanium plate as the cathode, and a DMF and BMIM bromide mixture containing H₂BDC and zinc nitrate hexahydrate as the electrolyte solution. The reaction was done in atmospheric conditions and applying a current density of 0.025 A cm² for 2 h.

As stated above, the second main route for the electrochemical synthesis of MOFs is the cathodic deposition. In 2011, Dinca *et al.* first investigated the cathodic deposition of MOFs¹⁰⁸ to resolve two major limitations of the anodic dissolution (Fig. 1.17 a): (i) the deposition surface (anode surface) is used to produce the metal cations and thus, it is eroded in a continuous manner throughout the synthesis; and (ii) the selection of the anode metal is limited since the anode is also used as the metal resource. In this cathodic deposition, the metal salt, which is dissolved in the electrolyte solution together with the organic linker and the probase, is used as the metal precursor. To show the potentiality of this approach, Dinca *et al.* showed the synthesis of HKUST-1 and MOF-5 in only 15 min at room temperature (Fig. 1.17 b). For it, they used fluorine doped tin oxide (FTO) as the working electrodes, Ag/Ag(cryptand) as the reference electrode, and a DMF: water (100 : 1) (v : v) mixture containing the organic linkers and the metal salts as the electrolyte solvent. In these syntheses, it was found that the nature of the metal salt plays a crucial role. This importance is due to the nature of the counter anions, which act as a probase and can inhibit or favor the formation of the desired MOF.¹⁰⁹ For example, as the synthesis of MOF-5 starts with the formation of Zn₅(OH)₈(H₂O)₂(NO₃)₂, the use of chlorine anions can inhibit its formation due to the formation of Zn₅(OH)₈(Cl)₂(H₂O)₂. On the contrary, the use of nitrate anions can help on its

formation since they can act as the probase and participate in the formation of the intermediate specie.

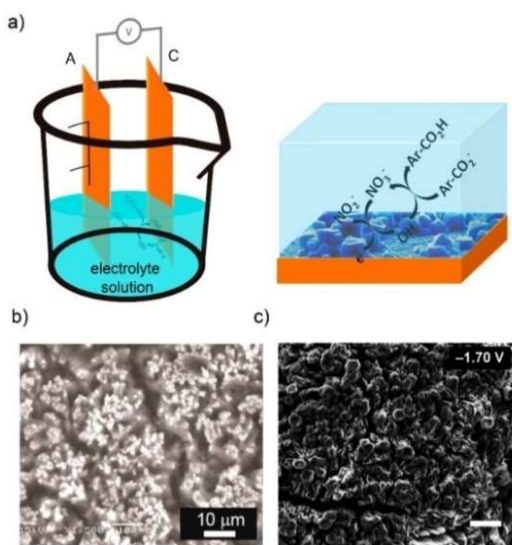


Fig.1.17: MOF synthesis by cathodic deposition. (a) Schematic illustration showing the cathodic dissolution cell (left) and the reaction that takes place on the cathode electrode (right). (b) SEM images of MOF-5 deposited on the cathode surface. (c) SEM images of bilayer structures of MOF-5 and $(\text{Et}_3\text{NH})_2\text{Zn}_3(\text{BDC})_4$.^{109,110}

The aptitude of the cathodic deposition to favor the formation films was also exploited by the same authors to form more complex biphasic MOF thin films at room temperature from single deposition baths using potential bias as the main user input.¹¹⁰ In this case, bilayer structures of MOF-5 and $(\text{Et}_3\text{NH})_2\text{Zn}_3(\text{BDC})_4$ (applied potential: 1.7 V) (Fig. 1.17 c), mixed structures of MOF-5 and $(\text{Et}_3\text{NH})_2\text{Zn}_3(\text{BDC})_4$ (applied potential: 1.1 V), and layers of only $(\text{Et}_3\text{NH})_2\text{Zn}_3(\text{BDC})_4$ (applied potential: 1.5 V) were fabricated tuning the applied potential.

Later innovations on the electrochemical synthesis of MOFs have been centered on the development of new methodologies such as electrophoretic deposition,^{111,112} galvanic displacement,¹¹³ anodic–cathodic deposition¹¹⁴ or bipolar electrochemistry.¹¹⁵ For example, Ameloot *et al.* combined both anodic and cathodic deposition to perform the modulated synthesis of UiO-66 simultaneously on both anode and cathode surfaces.¹¹⁴ For this synthesis, zirconium films were used as electrodes and H_2BDC was dissolved in a mixture of DMF, nitric acid (electrolyte), water and acetic acid (AA). AA was used as a modulator to increase the amount of linker defects and therefore, the BET surface area. However, increase of AA also decreased the crystallinity because of the increase of the competition between BDC and AA. It was found that denser packed films with smoother surfaces were formed on the anode when an AA concentration of 0.5 M or 1 M was used, and that larger octahedral UiO-66 crystals were obtained for AA concentrations higher than 5 M. In this process, when the AA concentration increased, the complexation of released Zr(IV) ions also increased leading to a decrease of the anodic deposition. On the contrary, when the concentration of AA decreased, the concentration of released Zr(IV) ions increased, thereby increasing the deposition on the cathode.

Another interesting example was reported by Bradshaw and Kuhn *et al.* who used bipolar electrochemistry (BE) to produce Janus-type MOF composites inducing the site selective ZIF-8 or HKUST-1 crystallization on a polarized metallic wire under an electric field. In BE, a conducting object is exposed to an electric field established between two electrodes in a solution this induces a positive and negative polarization between the two opposite sides of the object and a redox reactions can occur.¹¹⁵

Table 1: Electrochemical synthesis of MOFs with different routes and conditions.

<i>Anodic Desorption</i>					
MOF	Substrates	Solvent	Electrolyte	S _{BET} (m ² g ⁻¹)	Ref
HKUST-1	Cu electrode	MeOH	-	1820	89
	Cu electrode	EtOH:H ₂ O	MTBS	-	96
	Cu mesh	EtOH:H ₂ O	-	-	98
	Cu electrode	EtOH:H ₂ O	MTBS	1440	97
	Cu electrode	EtOH:H ₂ O, organic solvents	MTBS	-	100
	Cu mesh				101
ZIF-8	Cu electrode	EtOH:H ₂ O, EtOH	MTBS	1309	97
	Zn electrode	AcN:H ₂ O	MTBS	1600	103
	Zn electrode	DMF:H ₂ O	MTBS	1730	103
ZIF-4	Zn electrode	DMF:H ₂ O	MTBS	75	103
ZIF-14	Zn electrode	DMF:H ₂ O	MTBAMS	598	103
ZIF-7	Zn electrode	DMF:H ₂ O	MTBAMS	358	103
ZIF-64	Co electrode	DMF:H ₂ O	MTBAMS	1521	97
MIL-53(Al)	Al electrode	DMF:H ₂ O	NaCl or KCl	1200	97
MIL-100(Al)	Al electrode	EtOH:H ₂ O	-	969	102
MIL-100(Fe)	Fe electrode	EtOH:H ₂ O	MTBS	-	104
Tb-BTC	Tb foil	EtOH:H ₂ O	MTBS	-	104
Gd-BTC	Gd foil	EtOH:H ₂ O	MTBS	-	105
MOF-5	Zn plate	EtOH:H ₂ O	NH ₄ F	-	106,107
	Zn and Ti plate	DMF	BMIM	914	89
<i>Cathodic Deposition</i>					
MOF	Substrates	Method	Ref		
MOF-5	FTO	Cathodic	108		
		Anodic and Cathodic			
UiO-66	Zr-foil	Cathodic	114		
MOF-5 /(Et ₂ NH ₂) ₂ Zn ₃ (BDC) ₄	FTO	Cathodic	109		
<i>Others</i>					
MOF	Substrates	Method	Ref		
ZIF-8	Zn wire	BE	115		
UiO-66	FTO	Electrophoretic deposition	112		
		Electrophoretic deposition	111		
		Galvanic displacement	113		
HKUST-1	Porous stainless steel	Electrophoretic deposition	111		
		BE	115		
MIL-53	FTO	Electrophoretic deposition	112		
NU-1000	FTO	Electrophoretic deposition	112		

Abbreviations: MTBS, methyltributylammonium methyl sulfate; MTBAMS, methyltributylammonium methyl sulphate; BMIM, 1-butyl-3-methylimidazole; FTO, fluorine doped tin oxide; BE, bipolar electrochemistry.

1. 4. 1. 2. Microwave synthesis

Microwave (MW) irradiation is a widely used method in organic chemistry. In recent years it has been used for the synthesis of inorganic nanomaterials, zeolites and MOFs, among others.^{116–119} The method is based on the interaction of electromagnetic waves with any material containing mobile electric charges, such as polar molecules in a solvent or conducting ions in a solid. Contrary to classical solvothermal methods, where thermal energy is transferred from the heat source to the solution through the reaction vessel, in MW synthesis the irradiation interacts directly with the reactants, resulting in more efficient and faster heating. Additionally, in MW synthesis crystallisation occurs at the hot spots that form due to the direct heating of the solvent, in contrast to the wall of the reactor vessel as with conventional heating methods. Consequently, it is much faster and results in a smaller particle size. In this section, we describe some remarkable examples of the preparation of MOFs via microwave irradiation.

The pioneering work on MW synthesis of MOFs by Jhung *et al.* reported the water-based synthesis of the chromium trimesate MIL-100 MOF in the presence of hydrofluoric acid.¹²⁰ The synthesis was performed in a microwave oven at 220 °C for 1, 2 or 4 h with the reaction mixture in a sealed Teflon autoclave. The results showed the presence of unreacted metallic chromium species for reaction times less than 2 h. The crystal yield obtained after 4 h was 44%, which is comparable to the 45% achieved in the conventional synthesis in 4 days. Two years later, the same group reported the synthesis of spherical nanocrystals of chromium terephthalate MIL-101 MOF.¹²¹ In this work, they showed that crystal size increases with increasing irradiation time, ultimately allowing the isolation of particles with a high surface area.

The MW synthesis of IRMOF-1, IRMOF-2, and IRMOF-3 was reported by Ni *et al.* who obtained microcrystals with a relatively uniform size and identical cubic morphology in less than 2 min.¹²² They showed that the crystal size can be varied from micrometer to submicrometer by manipulating the concentration of the starting material. The same synthesis was conducted by Choi *et al.* who investigated how the power level, irradiation time, temperature, solvent concentration and substrate composition affected the crystallinity and morphology of MOF-5.¹²³ The microwave irradiation lead to crystals after only 30 min of reaction time, whereas 24 h were necessary with the conventional method. The optimum microwave conditions lead to uniform cubic crystals with average size of 20–25 nm and with a BET surface area of 3008 m² g⁻¹.

MW irradiation is an attractive method to synthesize MOFs with biomedical applications, such as iron-carboxylate MOFs, because uniform nanocrystals are easily achievable. For instance, in 2009, Lin and co-workers described the MW synthesis of 200 nm nanoparticles of iron-MIL-101 MOF and its amino functionalized version.¹²⁴ The starting materials were dissolved in DMF and then rapidly heated to 150 °C and held at this temperature for 10 min.

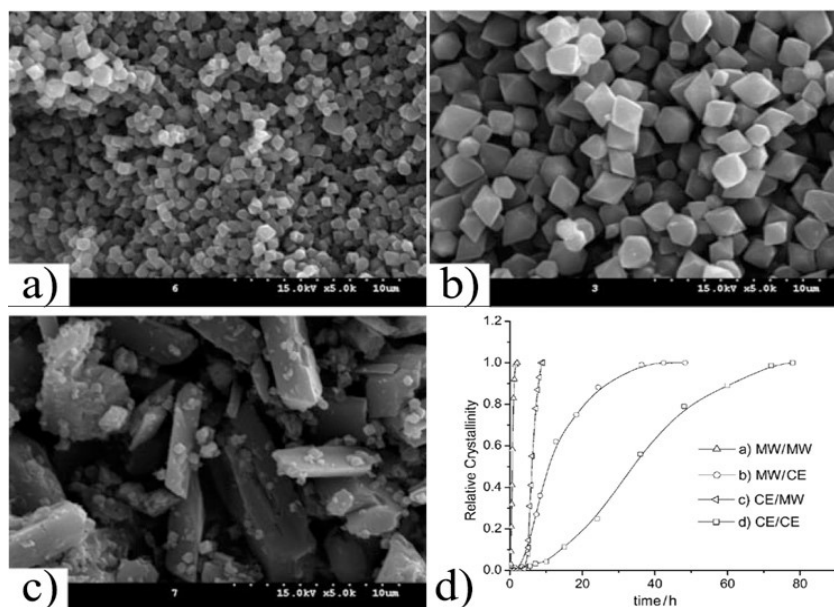


Fig.1.18: SEM images of synthesis of MIL-53(Fe). Synthesis at 70 °C with (a) ultrasounds for 35 min, (b) microwave for 2 h, and (c) conventional electric heating for 3 days (d) comparison crystallization curves for the synthesis of MIL-53(Fe) in two steps by (a) microwave, (b) microwave and conventional electric heating, (c) conventional electric heating and microwave and (d) conventional electric heating.^{118,125}

Several studies have been performed comparing conventional electric (CE) heating, MW and ultrasound (US) methods in order to understand the accelerated US and MW syntheses.^{126–129} For example, in 2009, Haque *et al.* performed a kinetic study on the synthesis of MIL-53-Fe.¹²⁵ They found that the crystallization rate (both nucleation and crystal growth) decreased in the order: US > MW >> CE. These results suggested that physical effects, such as hot spots, are more important than chemical effects in the accelerated syntheses performed under US and MW conditions (Fig. 1.18). A similar study was performed by Chalati *et al.* where the synthesis of iron fumarate MIL-88A nanoparticles was compared with the classical solvothermal, MW and US methods.¹³⁰ With the CE heating a polydisperse sample of 200 nm nanoparticles was obtained, whereas 100 nm monodisperse nanoparticles

but with very low yields were obtained with the US method and <100 nm monodisperse nanoparticle with high yields were obtained with the MW method.

The zeolitic imidazolate framework, ZIF-8, has been synthesized with MW irradiation and CE heating at 140 °C in 4 h and 20 h respectively.¹³¹ In addition to the reduced reaction time, the ZIF-8 obtained by microwave heating had a larger surface area and micropore volume compared with the ZIF-8 synthesized with CE heating.

There are a few reports available showing the effectiveness of MW irradiation for the synthesis of lanthanide–organic frameworks. For example, Silva *et al.* obtained quality single-crystals of the microporous cationic $[\text{Ce}_2(\text{pydc})_2(\text{Hpydc})(\text{H}_2\text{O})_2]\text{Cl}$ (where pydc is 2,5-pyridinedicarboxylic acid) by applying MW heating for 20 min at 200 °C.¹³² In 2014, Vileda *et al.*, synthesized a series of lanthanide (Eu, Gd and Tb) bisphosphonates using conventional hydrothermal synthesis (180 °C, 3 days), MW-assisted heating (40 °C, 5 seconds) and US-assisted synthesis (room temperature, 5 min).¹³³ Under CE heating, microcrystalline materials that did not possess any significant catalytic activity were obtained, whereas the application of MW and US resulted in nanocrystals that exhibited relatively high catalytic activity and excellent selectivity to 2-methoxy-2-phenylethanol (100% yield within 48 h of reaction time). A recent work by Cao and co-workers showed the gram scale production of nine isostructural microporous lanthanide MOFs via a microwave over 5 min.¹³⁴ The same synthesis but under conventional solvothermal reaction required seven days to produce the same materials with a similar yield. Moreover, with the solvothermal method, only 10 milligrams of quality material could be obtained while MW synthesis yielded up to 2 grams.

In 2013, D'Alessandro and co-workers reported the efficient synthesis of MIL-140A, MIL-140B and MIL-140A-NH₂ frameworks using MW irradiation.¹³⁵ They obtained products with purer phase and higher quality in significantly less time than the CE heating method. In recent years, zirconium-based MOFs have attracted great attention due to their exceptionally high thermal and chemical stability. In this context, a process optimization for the UiO-66 MW assisted synthesis was presented by Taddei and co-workers.¹³⁶ The optimized synthesis required 15 min of pre-mixture of the initial solutions and 15 min at 120 °C. The reaction yield was 83% and no significant negative effects on morphology, crystal size, or defects were found from the use of MW assisted heating in comparison with those synthesized by CE heating. One exciting area that it has been explored with MW in the last 2 years is the defect engineering of UiO-66. Babarao and co-workers presented an experimental and theoretical study showing the correlation between

the defect concentration composition in UiO-66 and their carbon dioxide adsorption properties.¹³⁷ They presented a detailed MW-assisted solvothermal synthesis protocol to prepare pure phases of high-quality crystalline UiO-66 frameworks with different defect concentrations. Highly crystalline UiO-66 octahedral shaped crystals were obtained in a short reaction time of 5 min using hydrochloric acid and formic acid as modulators.

1. 4. 1. 3. Mechanochemical synthesis

Mechanosynthesis is a well-known technique in metallurgy and mineral processing but, within the last few decades, it has expanded rapidly into many areas of chemistry such as catalysis, inorganic chemistry and pharmaceutical synthesis.¹³⁸⁻¹⁴¹ The central concept behind this synthesis method is to promote chemical reactions by milling or grinding solids without any or with only minimal amounts of solvents.^{142,143} With this approach, the conventional solvothermal MOF reactors are substituted by a mortar and pestle or in a mechanical process by automated ball mills. In general, the mechanical milling process is higher in energy and ensures the reproducibility between batches. In addition to the solvent free conditions, this approach leads to a faster and more efficient synthesis of MOFs obtaining quantitative yields and allows using MOF precursors with low solubility such as oxides, hydroxides and carbonates. However, the big limitation lies in up-scaling mechanosynthesis, it is essentially a batch processing technique with a relatively low rate of production. Furthermore, it should be noted that despite a ‘solvent-free’ synthesis, purification may still be needed and may require a solvent.¹⁴⁴ Nevertheless this synthesis approach is the most environmentally friendly process to produce MOFs, and hence could reduce significantly the cost of production.^{145,146}

The three different mechanochemical approaches used for MOF production are: Solvent-Free Grinding (SFG), which is the simplest method and avoids the use of solvent; Liquid-Assisted Grinding (LAG), which is more versatile, and quicker, as it uses catalytic amounts of liquid phases which increase the mobility of the reagents; and finally, Ion-and-Liquid Assisted Grinding (ILAG), which uses a catalytic liquid with traces of salt additives to accelerate the MOF formation. Using these techniques, the synthesis for almost all families of MOFs has been demonstrated, and selected studies will be explained in this section.¹⁴⁷

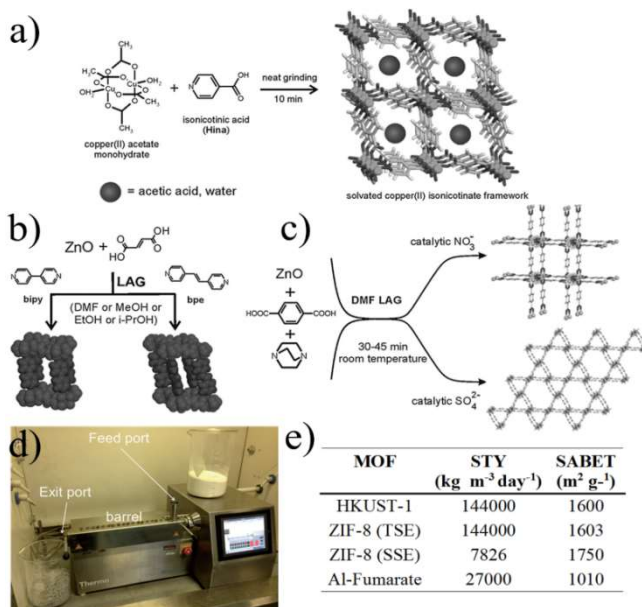


Fig.1.19: Mechanochemical synthesis of MOFs. (a) Neat grinding, (b) liquid-assisted grinding (c) ion- and liquid-assisted grinding, exploiting the catalytic effect of nitrates and sulphates (d) twin screw extruder with key parts highlighted. (e) Table of space time yields (STYs) and BET surface area for the synthesis of MOFs synthesized by extrusion methods.^{144, 156}

A first work by James and co-workers employed the SFG method, milling a dry mixture of copper acetate and isonicotinic acid (HINA) powder for 10 min resulting in the formation of copper(II) isonicotinate MOF with acetic acid and water molecules occluded in the pores (Fig. 1.19 a).¹⁴⁸ Using the same approach, the same group performed a screening study, grinding sixty different combinations of twelve different divalent metal salts, composed of copper, nickel and zinc, together with five different carboxylate organic linkers for 15 min.¹⁴⁹ As a result, several crystalline structures including two microporous HKUST-1 and $\text{Cu}(\text{INA})_2$ MOFs were obtained.

One important advantage of this approach is the possibility to synthesize MOFs with only water as a by-product allowing the complete elimination of the purification stage. This is achieved by using hydroxides or oxides as the metal source which then in combination with the protons generated from the organic ligand forms H_2O .

Following this strategy, Tanaka and co-workers presented the mechanical dry conversion of zinc oxide and an imidazole ligand into ZIF-8.¹⁵⁰ The process was investigated for reaction times of 3 to 240 h, yielding the best BET surface area

(1480 m² g⁻¹) at 96 h. The decrease of the BET surface area after 96 h was due to the formation of amorphous domains during the mechanochemical reaction. The same year, Balema and co-workers reported the preparation of the yttrium based MIL-78 MOF under completely liquid-free conditions and using a metal hydride for the first time as a starting material and forming hydrogen as a by-product.¹⁵¹

Very recently, Xu and co-workers reported the synthesis of MIL-101(Cr) without the addition of solvent and hydrofluoric acid.¹⁵² The chromium salt and the terephthalic acid were ground for 30 min at room temperature and then, transferred into an autoclave at 220 °C for 4 h, yielding a material with a BET surface area of 3517 m² g⁻¹ and with a reduced particle size compared to the batch process.

In 2006, Braga and co-workers demonstrated for the first time how the addition of small amounts of solvent to the powder mixture precursors could effectively improve the crystallization of the compounds and accelerate the synthesis.¹⁵³ They synthesized the one-dimensional coordination polymer CuCl₂(dace) (where dace is the trans-1,4-diaminocyclohexane) by grinding the starting materials for 5–10 min in the presence of water or DMSO, which was then removed by thermal and vacuum treatment. In 2009, Friscic and Fabian demonstrated the ability to selectively and quantitatively build different metal–organic architectures by simply changing the amount and type of solvent using the same starting materials. In this specific work, they presented the formation of four coordination polymers and two porous structures by grinding zinc oxide and fumaric acid in the presence of different types of solvents.¹⁵⁴ In 2010, Klimakow *et al.* synthesized the well-known HKUST-1 and its benzenetribenzoate-based analogue MOF-14 via the LAG approach. The MOFs were obtained by grinding the copper acetate monohydrate salt with the corresponding organic linkers for 25 min. Acetic acid was formed as a by-product, which blocked the micropores and consequently resulted in a smaller BET surface area compared to other synthetic approaches.¹⁵⁵ James and co-workers showed that by adding small amounts of liquid by-products via SFG method, before the mechanical process, the synthesis could be accelerated.¹⁵⁶ By adding small amounts of acetic acid into the precursor mixtures, the formation of Cu(INA)₂ MOF was dramatically accelerated, while for HKUST-1, due to the lower solubility of the trimesic acid, no improvement was reported. In 2010, the same group studied by X-ray diffraction the structural properties of [Zn₂(fma)₂(bipy)] (where fma corresponds to fumaric acid and bipy to 4,40 – bipyridine) prepared by mechanosynthesis (see Fig. 1.19 b).¹⁵⁷ The acetic acid and H₂O by-products occluded in the pores were removed by thermal treatment and the interpenetrated structure was refined using Rietveld methods. Also, Sun and Xia *et al.* reported the synthesis of MOF-505 by using copper acetate and 3,3',5,5'-

biphenyltetracarboxylic acid. They grinded the precursors with 0.4 mL of DMF for 80 min to produce the optimized product with BET surface area of 977 m² g⁻¹.¹⁵⁸

In 2015, Prochowicz *et al.* described the “SMART” (SBU based Mechanochemical Approach for pRecursor Transformation) strategy for the synthesis of IRMOFs.¹⁵⁹ The successful mechanochemical synthesis was performed by mixing pre-assembled oxo-zinc amidate clusters with terephthalic acid in the presence of microlitres of N,N-diethylformamide (DEF) over 60 min. Additionally, the study showed the importance of the acid–base relationship between reagents in this type of approach.

Recent work by Friscic and co-workers presented the synthesis of UiO-66 and UiO-66-NH₂ at gram scale by adding different amounts of N,N-dimethylformamide (DMF) and methanol to the solid mixtures of the reactants as well as exposing the powder mixture to methanol vapours at 45 °C for 3 days and 1 week, respectively.¹⁶⁰ The best BET surface area obtained for UiO-66 was 1020 m² g⁻¹ with 75 min grinding, and 945 m² g⁻¹ for UiO-66-NH₂ after 90 min grinding, both in the presence of methanol, for the materials exposed to methanol vapors. More recently, Farha, Friscic and Uzarevic *et al.* demonstrated the synthesis of highly porous NU-901 and UiO-67 synthesis by using the Zr₁₂-acetate cluster in high yields in the presence of low amount of DMF. Among both MOFs, UiO-67 was synthesized in gram scale to prove the feasibility of the methodology.¹⁶¹

The third mechanochemical methodology, ILAG, was demonstrated to be highly efficient for the synthesis of pillared-layered MOFs. For example, the zinc pillared material based on terephthalic acid and dabco (1,4-diazabicyclooctane) was synthesized after 45 min reaction by adding catalytic amounts of an alkali metal or ammonium nitrate salt into the mixture (Fig. 1.19 c).¹⁶² Using the same starting materials, but replacing the ammonium nitrate with sulphates, yielded the same pillared-layered structure but on a hexagonal grid. A second example was presented, showing the mechanochemical ILAG approach for the room temperature synthesis of ZIF-8, using zinc oxide as the starting material and stoichiometric amounts of ammonium salts.¹⁶³ In this case, the use of salts enabled the synthesis with imidazole, leading to the selective ZIF topology formation by changing the type of ammonium salt and adjusting the reaction times.

Mechanochemistry is a versatile method that allows the synthesis of most of the common MOF structures. Thus far, most examples described a production at less than one gram scale. As an alternative, extrusion techniques have been explored for the up-scaling of MOF production under solvent-free conditions. Extrusion is one of the major continuous manufacturing processes used in industries, such as

food, metallurgy, plastics and pharmaceuticals, and has shown very promising results for the synthesis and shaping of MOFs. In 2015, James and co-workers showed the synthesis of HKUST-1, ZIF-8 and aluminium fumarate MOF with twin-screw extrusion (TSE) at the gram scale. Fig. 1.19 d shows the TSE used for the synthesis of MOFs, which consists of a feed port where the MOF precursors were introduced into a heatable barrel containing the screw and an exit port in which a die can be attached to shape the final material. HKUST-1 was synthesized by extruding copper hydroxide and trimesic acid in the presence of methanol. The extrudate was stirred in ethanol and dried at 150 °C for 2 h yielding a N₂ BET surface area of 1738 m² g⁻¹. In the case of ZIF-8, the synthesis was performed by a single screw extrusion (SSE), where the zinc carbonate and the 2-methylimidazole ligand were extruded at 200 °C without the addition of any solvent. In this case, the activation was carried out by stirring the material in methanol and drying it at 150 °C, yielding a N₂ BET surface area of 1738 m² g⁻¹. A last example was obtained by introducing a mixture of aluminium sulphate, sodium hydroxide and fumaric acid into the twin extruder at 150 °C. In this case, the by-product was removed by washing the extrudates with water, and obtaining a N₂ BET surface area of 1010 m² g⁻¹. Extrusion is an efficient way to produce MOFs under solvent free conditions with high with very promising space-time-yields (STY) (Fig. 1.19 e). In fact, kilogram scale production could be achieved by using a large-scale equipment and paired with a more detailed knowledge and understanding of the MOF synthesis by this methodology.

1. 4. 1. 4. Spray-drying synthesis

Spray-drying (SD) process has been a well-established method in industry for decades. The basic idea behind this method is the production of dispersed powder from a liquid or slurry that is rapidly evaporated with a hot gas. The development of the SD method evolved over a period from 1870s through early 1900s. SD was first patented in 1872 by Samuel Percy,¹⁶⁴ but it was not until the World War II when it gained importance due to transportation needs. SD was used to reduce the weight of food and other species by removing their liquid content (mainly, water). Since then, SD has been widely used for the production of dried pharmaceuticals, bone and tooth amalgams, beverages, flavors, milk and egg products soaps and detergents, and many other products.¹⁶⁵ More recently in history, SD has extended its use to the encapsulation and miniaturization of multiple species,^{166,167,168} with the idea of protecting them, controlling their release, and increasing their solubility and dispersability. It has also been employed for preparing very homogeneous mixtures

of reactants,^{169,170} a crucial step that has facilitated the fabrication of certain materials.

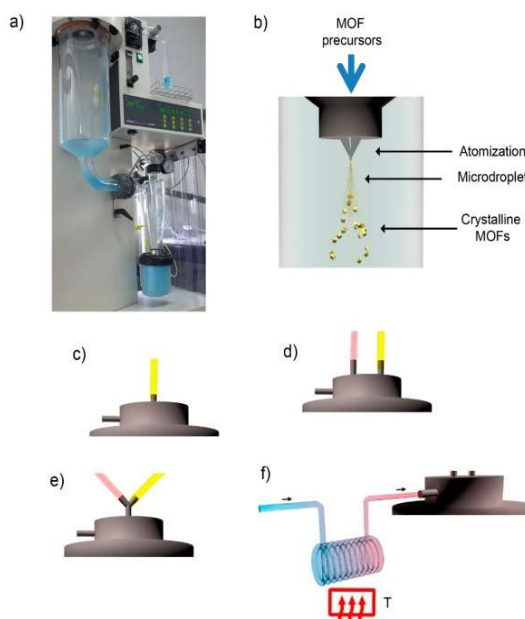


Fig.1. 20: Spray-drying method for the production of MOFs. (a) Photograph of the spray-dryer while it is used to fabricate HKUST-1. (b) Schematic illustration of the spray-drying synthesis of MOFs. The MOF precursor solution can be introduced into the spray drier using a: (c) two-fluid nozzle; (d) three-fluid nozzle; (e) T-junction; and (f) continuous flow reactor coupled to a two-fluid nozzle.^{171,173}

Beyond the use of SD in these applications, the local heating of micro- and submicrometer droplets that occurs during the SD process can also be used to conduct chemical reactions. Thus far, this concept has mainly been utilized for discovering and isolating metastable phases of materials that can be only reached thanks to the fast drying conditions of the SD method.¹⁶⁷

In 2013, Maspoch *et al.* expanded this concept to the synthesis of supramolecular materials and, in particular, MOFs.¹⁷¹ The main principle of the process was based on the fast drying of atomized microdroplets of a solution that contains the MOF precursors (Fig. 1.20 a and b). Thus, the process starts with atomization of a solution of the MOF precursors into a spray of microdroplets. This step is accomplished by

simultaneously injecting one or more solutions, at a certain rate, (hereafter, feed rate) and compressed air or nitrogen gas, at another certain rate (hereafter, flow rate). Thus, each precursor droplet contacts – and is suspended by – a gas stream heated to a certain temperature (hereafter, inlet temperature), causing the solvent to be heated and evaporated and inducing the MOF precursors (e.g. metal ions and organic ligands) to react forming MOF nanoparticles inside each droplet. At this moment, the newly formed MOF nanoparticles accumulate and merge into compact or hollow spherical MOF superstructures/beads while the solvent is fully evaporated. These MOF superstructures/beads are finally collected inside a collector located at the end of the spray drier instrument.

Table 1.2: MOFs synthesized by spray-dryer with different introducing modes and conditions.

<i>Two Fluid Nozzle</i>						
MOF	Metal salt/ligand/solvent	Feed (mL min ⁻¹)	Inlet T (°C)	Yield (%)	S _{BET} (m ² g ⁻¹)	Ref
HKUST-1	Cu(NO ₃) ₂ ·2.5H ₂ O/ BTC/ DMF:EtOH:H ₂ O	4.5	180	70	1260	171
Cu-BDC	Cu(NO ₃) ₂ ·2.5H ₂ O/BDC/ DMF	4.5	180	70	543	171
NOTT-100	Cu(NO ₃) ₂ ·2.5H ₂ O/BPTC/ DMF:H ₂ O	4.5	180	54	1140	171
MOF-14	Cu(NO ₃) ₂ ·2.5H ₂ O/ BTB/ DMF:EtOH:H ₂ O	4.5	180	30	-	171
Zn-MOF-74	Zn(NO ₃) ₂ ·6H ₂ O/ DHBDC/ DMF:H ₂ O	4.5	180	50	-	171
Mg-MOF-74	Mg(NO ₃) ₂ ·6H ₂ O/DHBDC/ DMF:EtOH:H ₂ O	4.5	180	35	-	171
Ni-MOF-74	Ni(NO ₃) ₂ ·6H ₂ O/ DHBDC/ DMF:EtOH:H ₂ O	4.5	180	40	-	171
MIL-88B	FeCl ₃ /NH ₂ -BDC/ DMF:MeOH:H ₂ O	4.5	180	27	-	171
<i>Three Fluid Nozzle</i>						
MOF	Metal salt/ligand/ solvent	Feed (mL min ⁻¹)	Inlet T (°C)	Yield (%)	S _{BET} (m ² g ⁻¹)	Ref
ZIF-8	Zinc acetate/ MiM/ H ₂ O	4.5	180	10	941	171
Cu-PB	Cu(NO ₃) ₂ / K ₃ Co(CN) ₆ / H ₂ O	4.5	180	20	617	171
SIFSIX-3-Co	CoSiF ₆ / Pyrazine/ MeOH	2.4	85	44	-	172
SIFSIX-3-Ni	NiSiF ₆ / Pyrazine/ MeOH	2.4	85	-	-	172
SIFSIX-3-Cu	CuSiF ₆ ·H ₂ O/ Pyrazine/ MeOH	2.4	85	55	-	172
SIFSIX-3-Zn	ZnSiF ₆ ·xH ₂ O/ Pyrazine/ MeOH	2.4	85	57	-	172
SIFSIX-1-Zn	ZnSiF ₆ ·xH ₂ O/4,4'-bipyridine/ MeOH	2.4	85	40	1300	172
TIFSIX-1-Cu	Cu(NO ₃) ₂ ·2.5H ₂ O/ 4,4'-bipyridine/MeOH	2.4	130	79	1650	172
<i>T Junction</i>						
MOF	Metal salt/ligand/ solvent	Feed (mL min ⁻¹)	Inlet T (°C)	Yield (%)	S _{BET} (m ² g ⁻¹)	Ref
MIL-88A	FeCl ₃ /Fumaric acid/ DMF:MeOH:H ₂ O	4.5	180	40	-	171
MOF-5	Zinc acetate/BDC/ DMF	4.5	180	60	1215	171
IRMOF-3	Zinc acetate/NH ₂ -BDC/ DMF	4.5	180	70	-	171
MPM-1-TIFSIX	TiF ₆ ·(NH ₄) ₂ / Cu(NO ₃) ₂ ·2.5H ₂ O/ H ₂ O:MeCN	2.4	150	74	805	172
<i>Continuous Flow</i>						
MOF	Metal salt/ligand/ solvent	Feed (mL min ⁻¹)	T ₁ /Inlet T (°C)	Yield (%)	S _{BET} (m ² g ⁻¹)	Ref
UiO-66	ZrCl ₄ / BDC/ DMF: H ₂ O	2.4	115/180	70	1106	173
UiO-66-NH ₂	ZrCl ₄ /NH ₂ -BDC/DMF:H ₂ O	2.4	115/180	67	752	173
UiO-66-NO ₂	ZrCl ₄ /NO ₂ -BDC/Acetic acid:H ₂ O	2.4	115/180	62	679	173
UiO-66-Br	ZrCl ₄ / 2-bromo-BDC/ DMF: H ₂ O	2.4	115/180	68	527	173
UiO-66-(OH) ₂	ZrCl ₄ / (OH) ₂ -BDC/ DMF:H ₂ O	2.4	115/180	81	401	173
UiO-66-acetamido	ZrCl ₄ /(OH) ₂ -BDC/ DMF: H ₂ O	2.4	115/180	51	586	173
UiO-66-NDC	ZrCl ₄ /1,4-NDC/ DMF: H ₂ O	2.4	115/180	45	431	173
UiO-66-NDC	ZrCl ₄ /2,6-NDC/ DMF:H ₂ O	2.4	115/180	49	557	173
MIL-100	Fe(NO ₃) ₃ ·9H ₂ O/ BTC/ DMF	2.4	135/180	78	1039	173
Ni ₈ (OH) ₄ (H ₂ O) ₂ (L) ₆	Ni(CH ₃ COO) ₂ ·4H ₂ O/ 1H-pyrazole-4-carboxylic acid/ DMF: H ₂ O	2.4	100/180	60	377	173

Abbreviations: BTC, trimesic acid; BDC, 1,4-benzenedicarboxylic acid; BPTC, biphenyl-3,3',5,5'-tetracarboxylic acid; BTB, 1,3,5-tris(4-carboxyphenyl)benzene; DHBDC, 2,5-dihydroxyterephthalic acid; DMF, dimethylformamide; EtOH, ethanol; MeOH, methanol; MiM, 2-methyl imidazole; NDC, naphthalenedicarboxylic acid.

Table 1.2 lists all MOFs together with the optimized conditions and yields that have been synthesized using the SD method so far. Besides the optimization of the synthesis parameters such as type of reagents/solvents, feed/flow rates and inlet temperature, a very important aspect that needs to be carefully selected when one wants to synthesize a specific MOF by SD is how the precursor solution is introduced into the spray drier. To date, there are four major modes for introducing the MOF precursor solution: (i) use of a two-fluid nozzle (Fig. 1.20 c); (ii) use of a three-fluid nozzle (Fig. 1.20 d); (iii) use a T-junction (Fig. 1.20 e); and (iv) use a continuous flow coupled to a reactor (Fig. 1.20 f).

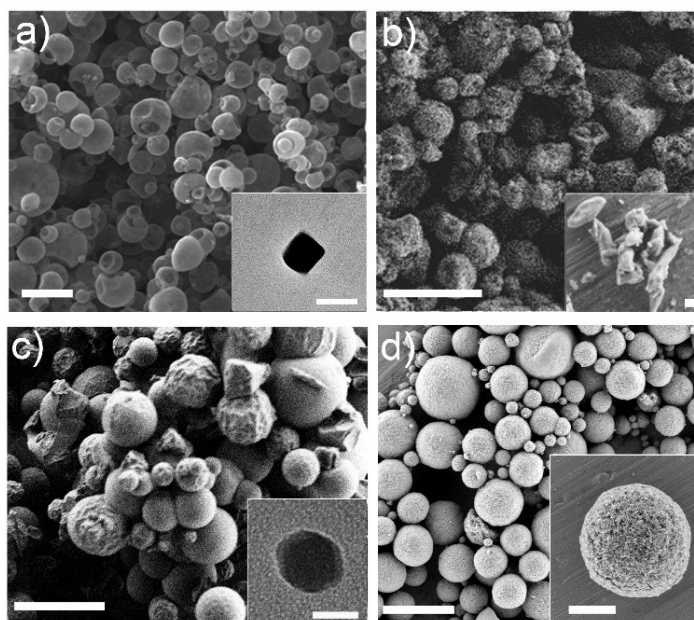


Fig.1. 21: SEM and TEM images of several MOFs synthesized by spray-drying. a) Hollow spherical superstructures of HKUST-1 synthesized using a two-fluid nozzle. Inset shows a TEM image of a single HKUST-1 nanoparticle. b) Spherical superstructures of MIL-88A synthesized using a T-junction. Inset shows a SEM image of MIL-88A particles. c) Superstructures of ZIF-8 synthesized using a three-fluid nozzle. Inset shows a TEM image of a single ZIF-8 nanoparticle. d) Compact superstructures/beads of UiO-66 synthesized using a continuous flow reactor coupled to a two-fluid nozzle. Inset shows a SEM image of a single bead. Scale bars: 10 μm (c), 5 μm (a,d), 2 μm (b, inset d), 200 nm (inset b), and 50 nm (inset a,c).^{174, 175}

The use of two-fluid nozzle is the simplest process. It is based on the preparation of a homogeneous solution or suspension that contains all MOF precursors, which is then injected through a two-fluid nozzle.¹⁷¹ This two-fluid nozzle allows the simultaneous injection of this precursor solution at a certain feed rate and compressed air or nitrogen gas at another certain flow rate. In general, this method is very useful to synthesize MOFs that are built up from mononuclear metal ions or smaller metal clusters or secondary building-units (SBUs). An archetypical

class of MOFs that can be fabricated using this approach is the large family of MOFs constructed from Cu(II) paddlewheel units and polycarboxylate linkers. For example, HKUST-1 (also known as Cu-BTC or Basolitet C300) can be synthesized by spray-drying a solution of $\text{Cu}(\text{NO}_3)_2 \cdot 2.5\text{H}_2\text{O}$ and trimesic acid (H_3BTC) (3 : 2 molar ratio) in DMF, ethanol and water (1 : 1 : 1) with a feed rate of 4.5 mL min^{-1} , a flow rate of 336 mL min^{-1} and an inlet temperature of $180 \text{ }^\circ\text{C}$. They could be obtained as hollow spherical MOF superstructures (size: $2.4 \pm 0.4 \text{ mm}$) or nanoparticles (size: $75 \pm 28 \text{ nm}$) (Fig. 1.21 a).

Second and third routes for introducing the MOF precursors inside the spray drier instrument are very similar.¹⁷¹ They are based on using multi-fluid nozzles, to independently atomize the solutions containing the MOF precursors, or additional channels, to independently inject them. Both approaches enable mixing of the precursor solutions just before they are heated into the atomized droplets. In the first approach, mixing occurs inside the drying chamber, thanks to the coalescence of the atomized droplets, whereas in the second one, mixing is done through a connector inserted before the two-fluid nozzle. Using either variation decreases the probability that unwanted species or micrometre-sized MOFs will form in the precursor solution before it is spray-dried. They also enable the use of reagents (e.g. bases) to accelerate MOF formation, thus increasing yields and purities and enabling the synthesis of new hollow MOF superstructures and related nanocrystals. To date, both approaches have allowed the synthesis of several MOFs, including MIL-88A,¹⁷¹ ZIF-8^{171,174} and Fe-BTC/MIL-100¹⁷⁴(Fig.1.21 b and c).

In the last approach, the MOF precursor solution is passed through a continuous-flow reactor just before the entrance of the spray dryer.¹⁷³ This process begins by injecting the precursor solution into a continuous coil flow reactor encased in a thermostatic oil tank, where it is heated at a certain temperature (T_1) to promote the SBU formation and nucleation. Here, the residence time of the precursor solution in the coil flow reactor is controlled by the rate of the pump (the feed rate). Since the outlet flow of the reactor is connected directly to the nozzle of the spray-dryer, the pre-heated solution is automatically injected into the spray-drier at the same feed rate. The solution is then atomized using a two-fluid nozzle, and is dried at a certain inlet temperature and flow rate, such that the MOF growth is confined to the atomized microdroplets.

In most of the cases, this last continuous process enables the collection of dried MOFs shaped in the form of compact micrometre superstructures/beads instead of the hollow ones usually obtained in the first three strategies. This difference is attributed to the formation, inside the reactor, of a suspension containing a primary nucleus. In a general spray-drying process, the atomized

droplets are exposed to hot air, the solvent evaporates and consequently, the droplet surface shrinks. During this process, hollow superstructures are formed when there is a non-linear change in precursor concentration at the droplet: specifically, it causes the formation of an impermeable shell and the generation of gas at the core. However, in this latter case, uniform precursor concentration and droplet temperature are reached, owing to the presence of the uniformly-distributed nuclei in the droplet. The rate at which the nucleus can be brought to the surface by diffusion is lower than the rate at which the nucleus can grow during the drying–evaporation process. This difference favors a linear change in precursor concentration and temperature at the droplet, and consequently, drives the formation of dense superstructures.

The main advantage of this last SD approach is that it allows the synthesis of MOFs assembled from high-nuclearity SBUs. Indeed, numerous members of the family of UiO-66 (e.g. UiO-66- NH₂, UiO-66-Br, etc.) as well as Fe-BTC/MIL-100 and [Ni₈(OH)₄(H₂O)₂(L)₆]_n (where L = 1H-pyrazole-4-carboxylic acid) series were synthesized using the resulting spray-drying continuous flow-assisted synthesis. For example, UiO-66 was synthesized using ZrCl₄ and BDC as reagents, DMF and H₂O as solvents, an initial concentration of 0.1 M for both reagents, a final molar ratio (Zr/BDC/H₂O/DMF) of 1 : 1 : 30 : 135, a T₁ of 115 °C; an inlet temperature of 180 °C, and a flow rate of 336 mL min⁻¹. Under these optimized conditions, in which the amount of water, the feed rate and the coil temperature were found to be very important, UiO-66 was fabricated with a space-time yield of 19.6 kg m⁻³ day⁻¹ (Fig. 1.21 d).

Lastly, the innovations of using SD in the MOF field have been centered on the use of new chemistries to build and/or modify MOFs;^{175,172} the synthesis of multivariate or multimetallic MOFs;^{176,171} and the mixture of MOFs with other materials to make composites.^{171,177} With this aim, the use of SD has been extended to the synthesis of porous materials that are not based on coordination bonds but on hydrogen bonds.¹⁷² For instance, MPM-1-TIFSIX, a porous material based on the hydrogen-bonded assembly of [Cu₂(ade)₄(TiF₆)₂] (ade = adenine) paddlewheels (Fig. 1.22 a), was synthesized by spray-drying an aqueous solution of Cu(NO₃)₂·2.5(H₂O) and TiF₆(NH₄)₂ along with a solution of adenine in water/acetonitrile mixture using a 2-fluid nozzle and an inlet temperature of 150 °C. Moreover, SD was also very recently found to be a fast method to postsynthetically modify MOFs using conventional covalent chemistry (Fig. 1.22 b).¹⁷⁵ To perform this modification, a suspension of presynthesized MOF crystals is spray-dried together with the desired reagent. With this simple method, two MOFs, the amine terminated UiO-66-NH₂ and the aldehyde-terminated ZIF-90, were rapidly post-

synthetically modified with aldehydes and amines, respectively, using the well-known Schiff-base condensation reaction and achieving conversion efficiencies up to 20% and 42%, respectively. Moreover, it was demonstrated that the aldehyde groups of ZIF-90 could be cross-linked using a diamine molecule with a conversion efficiency of 70%.

Another advantage of SD as a synthetic method in the MOF field is the possibility to synthesize multi-metallic and multivariate MOFs. From an experimental point of view, the synthesis of these multi-component MOFs does not require technological changes. Its main principle is based on mixing different metal ions or organic linkers in the MOF precursor solution that is spray-dried. With this approach, Wang *et al.* showed the synthesis of lanthanide-based MOF nanoparticles in which the ratio of Tb(III)/Eu(III) was controlled (Fig. 1.22 c).¹⁷⁶ They proved that the resulting MOF nanoparticles could be used as promising nanothermometers with high detection sensitivities, spatial resolutions and short acquisition times. Similarly, multi-variate UiO-66s were synthesized by mixing different ratios of two (benzenedicarboxylic acid and 2-bromobenzenedicarboxylic acid) or three (benzenedicarboxylic acid, 2-aminobenzenedicarboxylic acid and 2-bromobenzenedicarboxylic acid) organic linkers in the MOF precursor solution (Fig. 1.22 d).¹⁷³ The resulting UiO-66 materials showed tunable pore surface area. For example, the surface area decreased with increasing equivalents of 2-bromobenzenedicarboxylic acid: 818 m² g⁻¹ for 0.6; 678 m² g⁻¹ for 1.3; and 570 m² g⁻¹ for 2.3.

Finally, SD is also a very simple and fast method to produce MOF-based composites. As above, these MOF-based composites can be created by just mixing other materials – pre-synthesized or their precursors for in situ synthesis – in the MOF precursor solution. With this basic idea, MasPOCH *et al.* demonstrated that different substances such as magnetic inorganic nanoparticles (Fig. 1.22 e),¹⁷¹ inorganic salts (NaCl, CaCl₂ and LiCl) ^{171,178} (Fig. 1.22 f) and fluorescent molecules¹⁷¹ can be combined with MOFs, thereby creating different types of composite materials that combine the intrinsic properties of MOFs and these other materials. Finally, the same authors showed that SD method can be also used to combine MOFs with organic polymers.¹⁷⁷ In this specific case, pre-synthesized HKUST-1 nanocrystals were encapsulated into polystyrene spheres to improve the hydrolytic stability of HKUST-1.

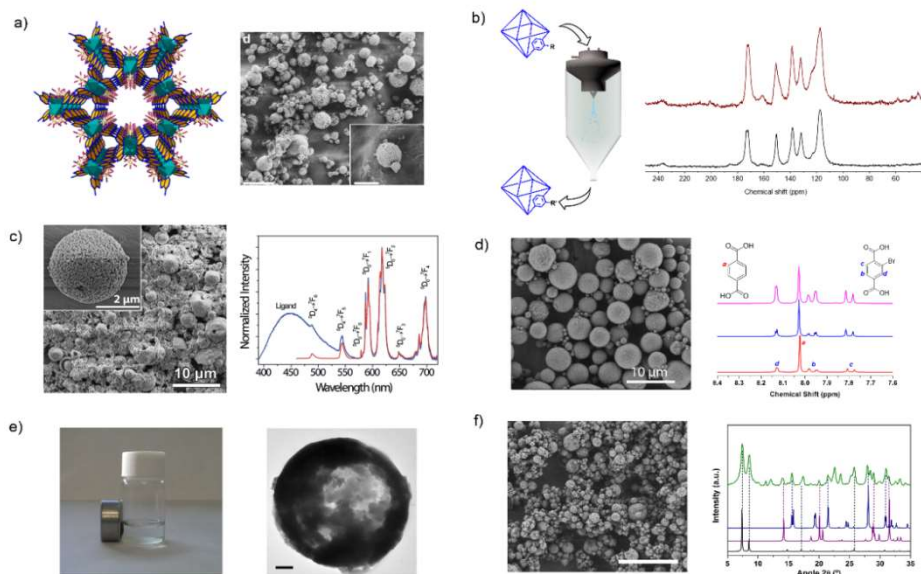


Fig.1. 22: Spray-drying method for building and/or modifying MOFs. a) Crystal structure and SEM image of MPM-1 -TIFSIX. Scale bar: 20 μm and inset: 5 μm . b) Schematic illustration of the post-synthetic modification of MOFs using spray-drying and ^{13}C MAS-NMR spectra that confirms the formation of the CH=N imine group. c) SEM image of a multi-metallic lanthanide-based MOF and excitation spectra of it. Scale bar: 10 μm and inset: 2 μm . d) SEM image of a multi-variate UiO-66 and NMR spectra confirming that both BDC and BDC-Br are forming the UiO-66 structure. Scale bar: 10 μm . e) HKUST-1 coupled with magnetic nanoparticles. Scale bar: 200 nm. f) SEM image of UiO-66 coupled with CaCl_2 and XRD pattern of the composite material showing the presence of both components. Scale bar: 20 μm . ^{174, 175, 172, 176, 177, 179}

1. 4. 1. 5. Flow chemistry

Flow chemistry is a continuous processing technology used in the pharma and agrochemical sectors over the last two decades. Recently, its application to the synthesis of functional nanomaterials, such as inorganic nanoparticles, quantum dots, metal oxides and MOFs, has shown great promise. Contrary to batch reactions, in a flow chemistry setup, the chemical reactions occur in a continuously flowing stream in a tube or pipe rather than in a reaction vessel. This results in several main advantages: (a) the surface area-to-volume ratio for a reaction mixture in a flow reactor is much higher than in a batch-type reactor giving inherent improvements to heat and mass transfer leading to a much rapid syntheses; (b) flow chemistry allows for precise control over the reaction parameters which facilitates the synthesis optimization and the reproducibility between batches; (c) harsh reaction conditions can be safely reached due to excellent transport intensification properties of the reactors; (d) typically less solvent is used and the energy consumption is lower; (e)

downstream processes and quality control methods can be easily integrated in the flow processes; and (f) these type of reactors are readily scaled-up. Flow chemistry is thus a cost-effective method that follows the green principle and satisfies the requirements for industrial production. Not surprisingly, several researchers have started to use flow chemistry to synthesize MOFs (Table 3). In the last year, numerous works have been reported in the literature and, in this section they will be classified such reports into three different categories: (a) microfluidic reactors (MR), which manipulate the reagents in channels that are geometrically constrained at the microscale; (b) plug flow reactors (PFR) where the reagents are pumped through a tube or pipe and consumed as they flow down the length of the reactor; and (c) stirred tank reactors (CSTR) where the MOF precursor are introduced into a tank reactor while products are continuously removed.

Table 1.3: MOFs synthesized by flow chemistry with different approaches and conditions.

<i>Microfluidic Reactor</i>					
MOF	Residence time	T (°C)	STY (kg m ⁻³ day ⁻¹)	S _{BET} (m ² g ⁻¹)	Ref
HKUST-1	-	RT	-	620	179
HKUST-1	1 min	90	5.8	1105	180
MOF-5	3 min	120	-	3185	180
IRMOF-3	3 min	120	-	2428	180
UiO-66	15 min	140	-	1509	180
MIL-88b	4 min	95	-	-	181
ZIF-8	15 s	RT	210000	1770	182
Ce-BDC	30 s	230	-	-	183
UiO-66	0.44-2.2 min	120	-	922-1206	184
<i>Plug Flow Reactor</i>					
MOF	Residence time	T (°C)	STY (kg m ⁻³ day ⁻¹)	S _{BET} (m ² g ⁻¹)	Ref
HKUST-1	1.2 min	85	4533	1805	185
UiO-66	10 min	130	1186	672	185
NOTT-400	15 min	85	1078	741	185
Al-Fum	1 min	65	97159	1054	186
HKUST-1	5 min	60	-	1673	187
MIL-53(Al)	20 min	250	1021	919	188
MIL-53(Al)	20 min	250	1300	1010	188
STA-12(Cd)	5-20 min	70	-	134	189
ZIF-8	<5 s	100	11625	1806	190
ZIF-8	<5 s	100	-	1780	190
CAU-13	20 min	130	3049	401	189
CPO-27	<5 s	300	1501	1030	191
HKUST-1	20 min	250	730	1554	188
HKUST-1	<5 s	300	4399	1950	191
UiO-66	45 min	120	428	1263	189
STA-12	20 min	70	428	134	189
HKUST-1	1 min	360 W	64800	1550	192
MIL-53(Al)	4 min	200 W	3618	1376	192
UiO-66	7 min	200 W	7204	1052	192
MOF-74(Ni)	<1 s	150	2160	840	193
<i>Stirred Tank Reactors</i>					
MOF	Residence time	T (°C)	STY (kg m ⁻³ day ⁻¹)	S _{BET} (m ² g ⁻¹)	Ref
UiO-66	8-40 h	100-120	-	810	194
MOF-5	5 h	140	1000	2302	195

Table 1.3 lists all MOFs together with the optimized conditions and space-time-yields that have been synthesized using the flow chemistry method so far. In 2011, Ameloot and co-workers were first to show that microfluidics could be used for the synthesis of metal–organic materials.¹⁷⁹ They synthesized metal–organic crystals in a microscale reactor, in which the reagent phases were injected into an immiscible carrier fluid, causing the spontaneous formation of droplets where the reaction occurs (Fig. 9b). In this case, the immiscibility of the water and oil phases was exploited as a template for the controlled formation of hollow metal–organic copper trimesate HKUST-1 microcapsules. The authors described the crystallisation process as a dynamic on-going process of nucleation and crystal growth that resulted in the formation of crystalline MOF membranes with a uniform wall thickness.

Two years later, Faustini *et al.* reported the solvothermal and hydrothermal synthesis of MOFs and MOF-composite superstructures using oil microdroplets as reactors.¹⁸⁰ Four representative MOF structures, copper trimesate HKUST-1, zinc terephthalate MOF-5, zinc aminoterephthalate IRMOF-3 and zirconium terephthalate UiO-66, were synthesized, yielding substantially faster kinetics in comparison to the conventional batch processes (Fig.1.23). In addition, they reported the possibility of creating MOF heterostructures using imidazolate frameworks (ZIFs) in a two-step process. Firstly, the iron oxide precursor solution and the oil phase were injected and reacted in a microreactor at 80 °C for 2 min. Then, the resulting iron oxide particles were transported downstream to a second microreactor, where they merged and reacted with a mixture of ZIF-8 precursor (zinc nitrate and 2-methylimidazolate in methanol, and polystyrenesulphonate). This led to the creation of core–shell Fe₃O₄@ZIF-8 composite superstructures.

The same year, Coronas and co-workers demonstrated the feasibility of the droplet-based microfluidic approach for the crystallization of the iron fumarate MIL-88B MOF. In this study, they confirmed that the size of the resulting crystals was dependent of the temperature and residence time. They observed a continuous increase in particle size with average sizes increasing from 90 to 900 nm with higher residence times and/or higher temperatures. In addition, D'Arras and co-workers demonstrated the possibility of synthesizing new structures using microsystems.¹⁸³ They reported the structure of a new cerium(III)–terephthalate MOF which was synthesized flow-type reactor at high temperature and pressure with a very short residence time.

Then, Polyzoidis *et al.* and Tai *et al.* reported the synthesis of ZIF-8 and UiO-66 nanoparticles respectively in a PFA (perfluoroalkoxy) microreactor showing that by varying the residence time and the molar ratio of the reactants. They were able to

modify the size and shape of the final crystals from a few nanometres to several micrometres.^{182,184}

Recently, defect control in UiO-66 synthesis by adjusting the residence time in microfluidic reactor was reported by Zhao and Thomas *et al.* They showed that the pore structure in these MOFs comprises intrinsic micropores and mesopores ranging from 2 to 13.5 nm when low residence time were used. However, these missing metal nodes could be sequentially repaired by increase these residence times.¹⁹⁶ Furthermore, they reported the preparation of thin layers of ZrBTB (where BTB is 1,3,5-tris(4-carboxyphenyl) benzene acid) nanosheets by using microfluidic flow reactor synthesis with higher adsorption capacity compared with the ZrBTB synthesized by solvothermal methods.¹⁹⁷ These two last examples demonstrate that microfluidic systems are ideal for reaction optimization and screening experiments within the laboratory. However, in order to synthesize large quantities of MOFs, it is better to use reactors with larger channel dimensions, as these are more suitable for large volumetric throughput.

Moving to the PFR reactors, the first work was reported in 2012 by Gimeno-Fabre *et al.* who showed the synthesis of HKUST-1 and Ni-CPO-27 in a counter current mixing reactor, where the MOF precursors were mixed with a preheated supercritical water stream at high pressures.¹⁴⁵ The high temperatures were used in order to increase the rate of crystal growth, with a limitation in that heating beyond 300 °C could lead to the formation of metal oxides as a waste-product. Three years later, the same reactor was used to demonstrate the large scale production of ZIF-8 and the control of the size and shape of the crystals by adding ammonium hydroxide or trimethylamine in the reaction mixture.¹⁹⁰ The STY obtained in this process was 11625 kg m⁻³ day⁻¹ and with a surface area of 1800 m² g⁻¹. Retaining the use of supercritical water and an ethanol stream, Bayliss *et al.* developed a system to produce MIL-53(Al) and HKUST-1 under continuous flow conditions obtaining a STY of 1300 kg m⁻³ day⁻¹ and 730 kg m⁻³ day⁻¹, respectively.¹⁸⁸ These last two methods produced high quality materials with high STY. However, high temperatures and pressures were still required, which increase the overall cost of the process and could limit the practicality of the technique at industrial scale.

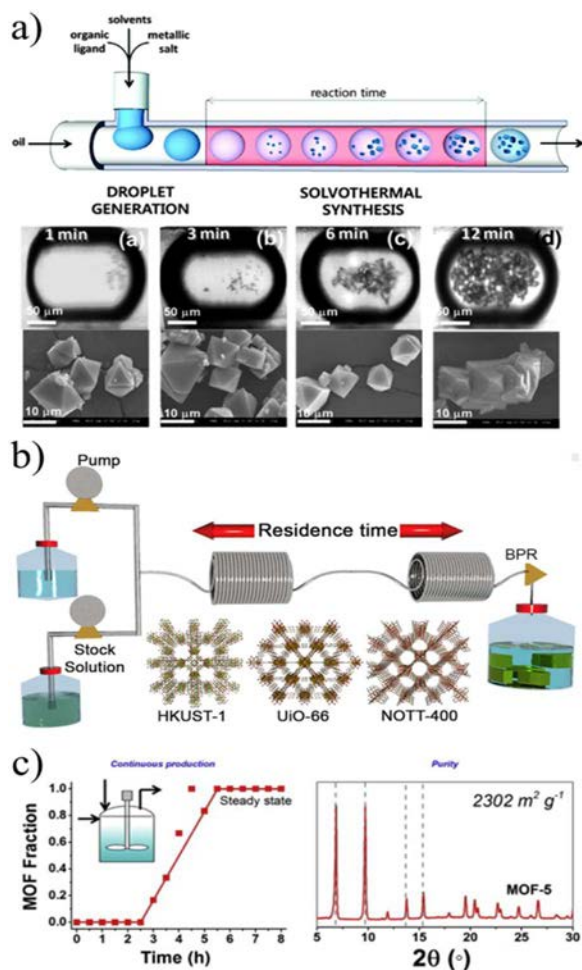


Fig.1. 23: Flow chemistry methods for the production of MOFs. a) Schematic representation of a continuous flow microfluidic device for producing MOF crystals (top). Optical and SEM images of HKUST-1 crystals obtained via the microfluidic approach at different residence time. b) Schematic representation showing the continuous flow synthesis of HKUST-1, UiO-66 and NOTT-400 of MOFs. c) Reaction profile of the solvothermal synthesis of MOF-5 crystals with its corresponding x-ray pattern diffraction and BET surface area value.^{183, 186, 198}

In 2013, Chang *et al.* reported the proof-of-concept mesoscale flow production of HKUST-1 with a surface area of 1673 m² g⁻¹ using 5 min as a residence time.¹⁸⁷ The particle size of the MOF could be adjusted by changing the relative ratios of the solvents and reaction temperatures from 150 nm to 4 μm. To demonstrate the versatility and efficacy of flow reactors to produce MOFs, Rubio-Martinez and co-workers used a PFR reactor to synthesize the copper trimesate HKUST-1, the zirconium terephthalate UiO-66 and the scandium biphenyl-

tetracarboxylate NOTT-400, all with different reaction requirements (Fig.1.23).¹⁸⁵ The materials were obtained in 5, 10 and 15 min, respectively, without loss in yield or product quality. It was demonstrated that the results could be up-scaled 30-fold using a bench-top reactor, allowing a production rate greater than a kilogram per day and a STY of $4533 \text{ kg m}^{-3} \text{ day}^{-1}$ using a bench-top reactor. The successful up-scaling of this process was demonstrated in a second publication, where the production of the aluminum fumarate MOF was proved in four different stainless-steel tubular flow reactors: a 10 mL coil tubing at laboratory scale, two intermediate stages with 107 mL and 374 mL reactor volume, and a pilot-scale 1.394 L reactor, delivering unprecedented production rates and STYs ($97159 \text{ kg m}^{-3} \text{ day}^{-1}$) while maintaining the product quality.¹⁸⁶ To our best knowledge, this is the highest reported value of STY for a MOF produced by continuous methods. Additionally, the reactor design used in this work demonstrated the possibility to readily translate reaction parameters from the laboratory scale to pilot scale without any re-optimization of the reaction conditions, while maintaining the STY values within the same range. The last work using PFR comes from Stock and co-workers, who presented the synthesis of UiO-66, CAU-13 and STA-12 - a new cadmium phosphonate network-using a 16 mL PTFE reactor yielding a STY of $428 \text{ kg m}^{-3} \text{ day}^{-1}$ and $3049 \text{ kg m}^{-3} \text{ day}^{-1}$ for UiO-66 and CAU-13, respectively.¹⁸⁹ One year later, the same was group reported the water-based synthesis the zirconium fumarate and UiO-66-NH₂ starting from a slurry of the starting solutions.

In a slightly different reactor design, two recent works reported the combination of microwave assisted heating with a PFR system. The first study from 2015 by Albuquerque *et al.* reported on a system where the microwave reactor was attached to the flow reactor in order to accelerate the nucleation of the MOFs and to improve the reproducibility of the synthesis.¹⁹³ The MOF precursors of MOF-74(Ni) were introduced first into the nucleation zone that consisted of a microwave reactor and consequently, the material was introduced into a PFA coil for 8 min to grow the final crystals. As a result, they obtained a better crystallinity in a shorter reaction time and achieved a STY of $2160 \text{ kg m}^{-3} \text{ day}^{-1}$. The second work by Taddei *et al.* presented the synthesis of UiO-66, HKUST-1 and MIL-53(Al) in 6.2 and 53 mL PTFE flow reactors heated by microwave.¹⁹² The materials were obtained in 7, 1 and 4 min of residence time, while maintaining the product quality and resulting in high STY of $7204 \text{ kg m}^{-3} \text{ day}^{-1}$, $64800 \text{ kg m}^{-3} \text{ day}^{-1}$ and $3618 \text{ kg m}^{-3} \text{ day}^{-1}$ for UiO-66, HKUST-1 and MIL-53(Al), respectively. Then, Stock *et al.* reported synthesis of Zr-based MOFs in water and acetic acid by using a PFR reactor at 85°C. They produced highly porous Zr-fum and UiO-66-NH₂ with STY of $2733 \text{ kg m}^{-3} \text{ day}^{-1}$ and $4346 \text{ kg m}^{-3} \text{ day}^{-1}$, respectively.⁸⁶

The use of stirred CSTR was showcased by two groups, synthesizing UiO-66-NH₂ and MOF-5. The first work by Schoenecker and co-workers showed the synthesis of the amine functionalized UiO-66 in DMF by convention heating.¹⁹⁴ In this system, the MOF precursors were pumped into a pre-mixing tank over 15 min and then, introduced into a 2 liter flow crystallization reactor over 8 to 40 h during which time small aliquots of the intermediate product were collected at different times to bulk reaction kinetics. The product obtained had good crystallinity but the BET surface area and the yield were below the values reported in batch. A later study by McKinstry *et al.* presented the synthesis of MOF-5 in a CSTR at atmospheric pressure, obtaining the desired quality and with a STY of 1000 kg m⁻³ day⁻¹ (see Fig. 9c).¹⁹⁵

1.5. Downstream Processes

After any MOF synthesis, careful processing is required to obtain the final functional material. Directly after the synthesis, the product slurry needs to be washed with the reaction solvent to remove any unreacted and by-products, e.g. using a centrifuge or a Buchner filter. Subsequently, an activation process is required to remove guest molecules, trapped within the framework, to obtain the expected surface area of the structure. Depending on the MOF structure, these two stages can be the most time limiting stages of the process and become hugely significant in the large-scale production. The last stages of the process consist in drying and shaping the MOFs as well as a heat activation step before testing. Fig. 1.24 shows a diagram of the typical downstream processes for the synthesis of a MOF.

Despite promising advances in MOF synthesis, there are still challenges remaining related to the downstream processing. On the laboratory scale, these processes are well established and sufficient to obtain milligram amounts of quality materials. However, these conventional downstream methods are not well-suited to high production rates. The first stage, the washing and separation of the small crystals from the mother liquid still is a major obstacle for the large scale production MOFs. There are many well established types of equipment for solid-liquid separation such as centrifuges, cyclones, settling chambers, classifiers or filters, in addition to the direct evaporation of the mother liquor. However, the small size of the MOF particles, their low concentration in the solvent, as well as their density approaching that of the solvent (due to the high porosity), makes separation via most conventional methods inefficient or expensive at an industrial scale.¹⁹⁸

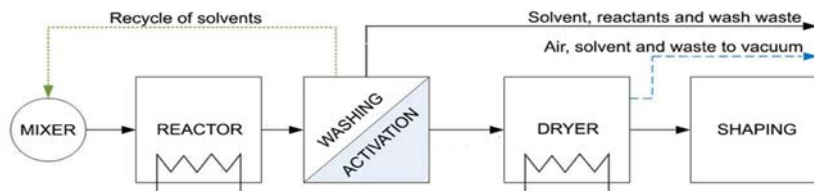


Fig.1. 24: Continuous MOF process. Schematic representation of the different stages of the continuous process for MOFs production: synthesis, washing, activation, drying and shaping.

Once the MOF slurry has been cleaned of the excess linkers and by-products, the activation stage is the next step of the process in order to obtain the highest porosity and BET surface area of the framework. Several strategies exist to remove the unreacted and solvent molecules trapped in the pores of the MOFs without collapsing the framework.¹⁹⁹ The most common procedure is a simple heating of the MOF to certain temperature under vacuum. Each MOF has its optimal protocol in order to obtain the highest surface area but generally the temperature should be between the boiling point of the solvent and the decomposition temperature of the structure. However, in most cases, this strategy leads to a lower surface area, or to a collapse of the structure due to the high surface tension and capillary forces imposed on the structure by the liquid-gas phase transition of the trapped solvent molecules. An alternative strategy is to exchange the solvent used for the synthesis with one that has a lower boiling point such as methanol, chloroform or acetone prior to heating the sample under vacuum. This strategy is laborious as generally most MOFs require soaking for a long period of time to ensure that the new solvent infiltrates. For example, in the case of MOF-74 and UiO-66 both MOFs require a soaking in daily refreshed methanol for 3 and 7 days respectively to ensure the complete removal of DMF (solvent used for the synthesis and washing stage) from the pores.^{67,200} Some frameworks, such as ZIF-8 and MIL-53(Al) require a solvent exchange process with methanol with an additional thermal treatment, 300 °C for 2 h and 330 °C for 72 h, respectively, to obtain the BET surface areas of 1630 m² g⁻¹ and 1590 m² g⁻¹, respectively.^{63,201}

An attractive substitute for the solvent exchange method is the use of supercritical CO₂. This relatively new strategy consists of exchanging the synthetic solvent for a one that is miscible with liquid CO₂ such as ethanol or methanol and then, subsequently exchanging this second one for liquid CO₂ at high pressure and temperature for several hours. The difference here is that the CO₂ supercritical phase eliminates surface tension and capillary forces making this activation method much milder than the conventional and solvent exchange methods. There are several MOFs that have been effectively activated with this strategy. For example, MOF-200 and MOF-210, where a simple solvent exchange followed by pore

evacuation under vacuum was not effective, were successfully activated, without losing the porosity, by a full solvent exchange with liquid CO₂.²⁰² The surface areas obtained were 4530 and 6240 m² g⁻¹, respectively. Another example is the supercritical CO₂ activation of bio-MOF-100, where the DMF solvated samples were soaked in ethanol for 48 h, and an exchange/activation with CO₂ liquid over a period of 8 h yielded a BET surface area of 4300 m² g⁻¹.²⁰³ In a variant of this method, the sample is placed in a column and the supercritical CO₂ flows through the sample instead of using static CO₂ exchange. This method was presented by Koh and co-workers, who activated UMCM-9 microporous coordination polymers via supercritical CO₂ flow activation yielding a surface area BET of 4970 m² g⁻¹.²⁰⁴

Later novelties on the activation have been based on freeze drying activation techniques, which uses thermal cycling and the vacuum sublimation of solvents (benzene and cyclohexane) at low temperatures to avoid the impact of capillary forces on porous structures in order to control the stability of frameworks and improve its porosity.²⁰⁵ Recently, Rubio-Martinez *et al.* presented for the first time the use of megasonics as an alternative strategy for the simultaneous separation and activation of MOF crystals.²⁰⁶ Its operating principle is based on the application of high frequency ultrasound to the MOF solution, leading to the separation of the solid MOF particles from the solvent. Additionally, the megasonic treatment leads to activation by the simultaneous removal of occluded reagents from the MOF crystals. This one-step process showed an improvement of up to 47% the surface area of the final product compared to conventional methods. The method removes one stage from the downstream processing and is readily scalable and thus capable of producing commercially usable product at a large scale.

Shaping of MOF powders produced in any of the fabrication methods explained above is also mandatory for using them in real industrial applications. For instance, extruded or compact MOFs in the form of beads, pellets and monolithic bodies are required if MOFs want to be used for gas separation and storage applications. In methane storage (e.g. Adsorbed Natural Gas or ANG), for example, it is of utmost importance to fill the storage tanks with the largest amount of adsorbent; a condition that can only be achieved if MOF powders are densely packed. Furthermore, powdered MOFs are usually more difficult to be handled and can potentially contaminate pipes during charge/ discharge cycles. For other applications such as functional textiles,²⁰⁷ alternative shaping and/or integration methods that process MOFs into paper sheets,²⁰⁸ fibers,²⁰⁹ membranes,^{210,211} foams²¹² or coatings²¹³ are also needed (Fig. 1.25). Considering the potential adsorption-related applications of MOFs, most of the efforts done in shaping MOFs have been dedicated to their densification. The objective of densification is to pack the

maximum amount of an active MOF on a certain volume without losing its integrity and adsorption capacity. Dailly *et al.* calculated that doubling the density of HKUST-1 powder would result in an adsorbent with performances comparable of those of the state-of-the-art carbons at intermediate pressures (30–100 bars).²¹⁴ However, despite the high industrial importance of shaping MOF powders, the interest of academic research groups to face this problematic is quite recent. In fact, the structuration of MOFs into shaped bodies was initiated by some companies (mainly, BASF), which tend to keep these shaping processes as in-house know-how or are only disseminated in patents. In this context, BASF published the first patent application concerning “shaped bodies containing metal–organic frameworks” in 2002. This patent was centered in the fabrication of MOF-2 and MOF-5 pellets using an eccentric press. In this process, both MOFs were mixed with graphite that acts as a binder improving their mechanical strength.²¹⁵

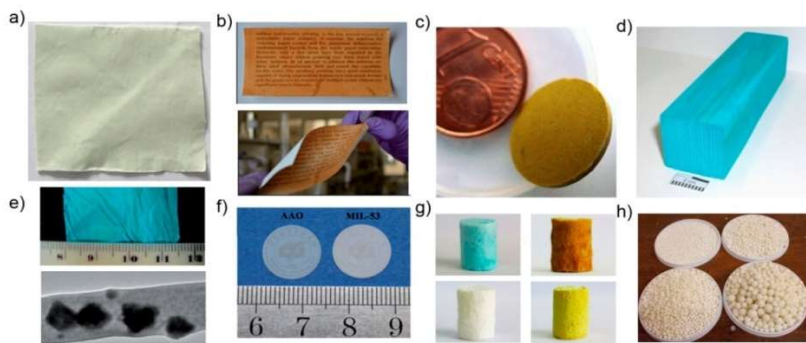


Fig.1. 25: Functional textiles; b) Paper sheets; c) Pellets; d) Extruded monolith; e) Fibers; f) Membrane; g) Foams; and h) Granules. ^{208, 209, 210, 212,216,217}

Pelletization under pressure is probably the most common method used for densifying MOFs. In this process, a fine powder is pressed at a certain pressure to give pellets that can be crushed or fractionized by sieving. In some cases, before MOF powder is pressed, it can be blended with a binder to improve the cohesion between crystals and their mechanical strength. There are however two factors of this method that tend to affect the final adsorption properties of the pellet shaped MOFs. From one side, the pressure applied can crush the structure of the MOF due to its low mechanical stability. From the other side, the use of binders can dilute the porous powder and/or cause pore blockage, resulting in a reduced performance per unit mass (or volume) of the adsorbent.

As shown in Table 1.4, the influence of the pressure applied during pelletization of MOF powders was studied in some representative MOFs. However, systematic studies that correlate the pelletization conditions with the resulting

adsorption properties of MOFs are very limited, and some discrepancies can be found. A general tendency when compressed pellets are processed is a decrease of the BET surface area and porosity of MOFs. This is specially the case for HKUST-1 that is mechanically fragile. For HKUST-1, it has been described that a significant loss of its BET surface area occurs at moderate pressures. Ahn *et al.* reported a loss of 50% of its BET surface area when the applied pressure was around 10 MPa,²¹⁸ whereas Bazer-Bachi *et al.*²¹⁹ and Peterson *et al.*²²⁰ found a similar decrease when pressures of 80 MPa and 70 MPa were applied, respectively. Other MOFs have shown better mechanical resistance. For example, UiO-66 and analogues, which are known for their high mechanical and thermal stability owing to their 12-fold connected clusters in the three spatial directions, were shown better stability during the compression process. Here, Peterson *et al.* observed a loss lower than 10% of the BET surface area of UiO-66 when it was pelletized under a pressure of 70 MPa.²²⁰ Dietzel *et al.* also reported the total conservation of the BET surface area of CPO-27 after tableting it at 100 MPa, whereas its porous character totally disappears at 1 GPa.²²¹ In the case of ZIF-8, the BET surface area was well preserved until a pressure of 700 MPa. Above this pressure, different reports revealed some discrepancies. While BazerBachi *et al.* observed a loss lower than 20% of its BET surface area,²¹⁹ Chapman *et al.* observed a loss of 50% at pressures above 1 GPa.²²² This difference can be attributed to non-reported parameters, such as the pressure increase rate and the dwell time, which can dramatically influence the integrity of the final pellet.

Binders are sometimes utilized during this pelletization process. As state above, they basically serve to improve the cohesion between MOF crystals and their mechanical stability. Some tested binders include graphite,²²³ polyvinyl alcohol (PVA)²²⁴ and cellulose ester.²¹⁹ To our knowledge, however, there is no a systematic, rational study on the influence of the nature and concentration of these binders on the BET surface area and general properties of MOFs during their pelletization.

The presence of binders is also necessary in other shaping processes, including foaming, extrusion, granulation and cake crushing. In all these procedures, MOF powders are initially dispersed in a solvent/binder mixture. The choice of the binder gives a certain texture and property to the mixture, which is then manipulated in different ways to obtain the desired MOF shapes. For example, in the extrusion process, the MOF solvent/binder mixture forms a paste that can then be extruded to induce shaping of the MOF into different morphologies (Table 1.4). Following this latter method, Kaskel *et al.* mixed HKUST-1 crystals with a silicone resin and a plasticizer to form a paste that was subsequently extruded into

monolithic HKUST-1 strings in a ram extruder. In this case, the decrease of the BET surface area was significant (70% of its initial BET surface area) due to the presence of binders and heating conditions, but the performance of the extruded monolith was higher than the monolith obtained by in situ synthesis of HKUST-1 in cordierite honeycombs.²²⁵ The extrusion method was also used by Ren *et al.* to prepare UiO-66 spherical pellets (with a BET surface area of 674 m² g⁻¹ that corresponds to 50% of its initial value) from a paste made of UiO-66 and 10 wt% sucrose/H₂O mixture using a granulator.²²⁶

Table 1.4: Examples of shaped MOFs using pelletization, foaming and extrusion methods.

<i>Pellet</i>				
MOF	Pressure	Binder	Property	Ref
HKUST-1	-	Alox C and grahite	Very high adsorption capacity for CO ₂	223
	70 and 700 MPa	Without binder	50% decrease of the BET surface area (after 700 MPa)	220
	0.24 – 40 MPa	Cellulose ester, K15M	Maintained ammonia removal capacity	219
	3-35 MPa	Without binder	76% decrease of the BET surface area (after 40 Mpa)	218
MIL-53(Al)	1-8 bar	Polyvinyl alcohol	50% decrease of the BET surface area (after 10 MPa)	218
			Below 5 bar, constant selectivity Above 5 bar, selectivity decreased. 22% decrease of the BET surface area	224 227
UiO-66	-	Graphite	Suitable material for o-xylene over p- and m-xylene separation at low concentrations	
	70 and 700 MPa	Without binder	Maintained BET surface area 16% decrease in octane loadings (after 700 MPa)	220
ZIF-8	398-1432 Mpa	Cellulose ester, K15M	10% decrease of the BET surface area (after 1432 MPa)	219
SIM-1	40-398 Mpa	Cellulose ester, K15M	No change in catalytic reactivity	219
CPO-27-Ni	0.1-1 GPa	Without binder	28% decrease of the BET surface area (after 398 Mpa)	221
<i>Foam</i>				
MOF		Binder	Property	Ref
MIL-101 (Cr)		Ni foam	Decrease in hydrogen storage capacities (19%)	216
UiO-66		Polyurethane	Maintaining more than 70% of the adsorption capacity for benzene and n-hexane	228
UiO-66-NH ₄ , Mg-MOF-74, HKUST-1, ZIF-8		Carboxymethylcellulose	-	229
HKUST-1 @Fe ₃ O ₄		Carboxymethylcellulose	High catalytic activity in C-H oxidation	229
<i>Extrusion</i>				
MOF		Binder	Property	Ref
HKUST-1		Silres MSE 100 Culmial MHPC 20000 P	70% decrease of the S _{BET}	225
Zr-MOF		Sucrose and water	50% decrease of the S _{BET}	226

Starting from the binder-solvent–MOF mixture, monolithic MOF foams can also be formed (Table 1.4). In this case, the nature of the binder tends to form macroporous foam-type solids in which the MOF can be entrapped. Similar MOF foams can also be produced by synthesizing the MOF in the presence of pre-formed foam. Using both approaches, foams with MIL-101,²¹⁶ HKUST-1²³⁰ and UiO-66²²⁸ were prepared. For example, Wang *et al.* synthesized a foam monolith composed of HKUST-1@Fe₃O₄-MF (MF means magnetic fluid) by dispersing HKUST-1@Fe₃O₄-MF particles in an aqueous carboxymethylcellulose solution. The treatment with acetonitrile and finally drying led to the formation of monolithic foams with high catalytic activity for C–H oxidation.²²⁹

Other shaping processes require the formation of a dried MOF cake that is crushed. Here, the MOF powder is mixed with a certain amount of a binder (typically, polyvinyl alcohol (PVA)) and the resulting mixture is dissolved in a solvent forming a paste. This paste is then dried, crushed and sieved into the wanted particle size fraction. Denayer *et al.* used this method to prepare MIL-53(Al) pellets using PVA as the binder. As revealed by N₂ adsorption isotherms, the MIL-53(Al) pellets showed a loss of BET surface area of 32% but maintained good CH₄/CO₂ selectivity capacities.²²⁴ Finally, other methodologies have also started to be explored to incorporate MOFs into fibers²¹⁷ and papers, and shape them into alginate-based spherical beads²³¹ or ceramic beads.²³²

These few examples indicate that the shaping of MOFs for specific applications is still in an embryonic stage and strong efforts have still to be dedicated to the rational study of this process if we want to be able to access to the real commercial applications. It is also clear that, in adsorption-related applications, this shaping process must respect the relatively low thermal, chemical and mechanical stability of MOFs, so that their adsorption capacities are mostly preserved. For other applications, however, this latter condition is not so important. In catalysis, for example, Bazer-Bachi *et al.* observed that, even though pelletization of ZIF-8 decreased its adsorption properties, it did not change its catalytic activity.²¹⁹

1.6. Perspectives and Commercial Developments

Since the first patent filed in 1995 and assigned to the Nalco Chemical Company, commercialisation of MOFs progressed gradually until the first MOF-based products released in 2016 by MOF Technologies and Numat Technologies (Fig. 1.26).^{233,234} MOF production at scale is now underway, which will help secure customer confidence and open the door for other MOF-based products. However, the growing market will push the MOF suppliers for further cost-efficiency,

reproducibility and environmental sustainability to remain competitive. Here is a brief summary of companies working with MOFs in production, technology development and retail to date.

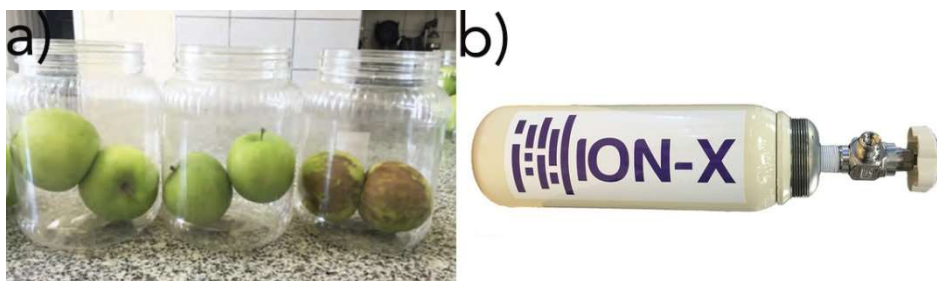


Fig.1. 26: Commercially available MOF-based products released in 2016. a) NT-7815 micro-adsorbent for extending the storage life and quality of many fruits and vegetables by Decco Post-Harvest and MOF Technologies and b) ION-X gas storage tank for storing speciality gases used in the electronics manufacturing industry by Numat Technologies.²³⁵

MOF Technologies was founded in 2012 based on patented mechanochemical manufacturing technology invented at the Queen's University of Belfast.⁸⁸ This innovative process allows the production of MOFs using little or no solvents. Solvent-free synthesis has advantages in both waste and energy management. Solvent waste is a major issue in the chemical industry. The energy required to initiate reaction can sometimes be reduced using mechanical energy rather than thermal energy. Recently this method has been configured for continuous production through extrusion which is scalable.

It is unknown how many MOFs can be manufactured using mechanochemical synthesis. However, MOF Technologies offer a wide catalogue for direct purchase. At the end of 2016, they sold around 100 kg of MOFs from their catalogue: magnesium formate, Cu-BTC (HKUST-1), ZIF-8, Al(OH) fumarate, ZIF-67, Mg-MOF-74 and Zn-SIFSIX-pyrazine. See Table 1.5 for a summary of MOFs for sale from each manufacturer.

MOF Technologies were the first to announce a MOF-based commercial product available through fruit and vegetable supplier Decco Worldwide Post-Harvest Holdings. The product has been registered with the U.S. Environmental Protection Agency under the proprietary name NT-7815 (EPA reference: 2792-79). NT-7815 is described as a micro-adsorbent delivering 0.7 wt% of 1-MCP, which is a gas that blocks postharvest ethylene responses, extending the storage life and quality of many fruits and vegetables. MOF Technologies has not released any details regarding the MOF incorporated within the product. With the announcement of the new product, MOF Technologies have expanded their production facility

capable of producing 15 kg h⁻¹ in preparation for full scale between 5 and 10 tons per year from 2018 depending on which MOF.²³⁶

Table 1.5: Sales catalogue of MOFs available by each manufacturer.

MOF	Manufacturer
Al(OH) fumarate	MOF Apps
	MOF Technologies
CAU-10	ProfMOF
Cu-BTC	BASF
	MOF Apps
	MOF Technologies
Fe-BTC	BASF
Mg formate	BASF
	MOF Technologies
Mg-MOF-74	MOF Technologies
MIL-100	KRICT
	MOF Apps
MIL-101-NH ₂	MOF Apps
MIL-53	BASF
MIL-68	MOF Apps
MOF-177	BASF
PCN-250(Fe)	Framergy
UiO-66 series	Inven2
	MOF Apps
	ProfMOF
ZIF-67	MOF Apps
	MOF Technologies
ZIF-8	BASF
	MOF Apps
	MOF Technologies
	STREM Chemicals Inc.
Zn-SIFSIX-pyrazine	MOF Technologies

NuMat Technologies established in 2013, have also released a MOF-based product called ION-X based on a proprietary set of MOFs for storing gases such as arsine, phosphine and boron trifluoride for the electronics industry.²³⁵ The company is setting up a facility in Asia that will receive MOF-filled tanks from the United States. NuMat has a partnership with one of the top gas companies in Asia who will fill the tanks with gas, which will then be distributed to customers. Since Asia which contains most of the major manufacturers of electronics in the world, this position will likely offer direct access to this market which is 70% of the total demand. NuMat will lead the initial production of the proprietary set of MOFs for ION-X and have explored multiple manufacturing methods including flow, mechanochemical, solvothermal and others.

MOF Apps, founded in 2013, are the exclusive licensee for UiO-66 and the zirconium-based family of MOFs. With a focus on MOF Application Services, the company aims to bring research and industry together to identify and develop commercially viable application opportunities in the areas of gas storage, industrial cooling, toxic gas protection and healthcare. MOF Apps develops and offers

integrated solutions using MOFs, which are costcompetitive and which outperform state-of-the art systems. MOF Apps have sold the most amount of MOF to a leading vehicle manufacturer in August 2015 to test as adsorbed natural gas fuel platform.²³⁷

ProDia was a Horizon 2020 project funded through the European commission. It is a consortium of over 15 parties focused on the development of reliable production methods of nanoporous materials and their applications. Pilot-scale production of up to 100 kg were led by Johnson Matthey for water-based synthesis, MOF Technologies for mechanosynthesis and Axel One for spray-drying synthesis.²³⁸

ProfMOF founded in 2015 by a group of scientists at the University of Oslo, Inven2 and Kongsberg, focused on the commercialization of the MOF-material. ProfMOF prefer waterbased and continuous flow production of MOFs. Prof Norbert Stock, inventor of CAU series and advisor for ProfMOF, has developed the water-based synthesis method for some of the zirconium MOFs and CAUs series.^{86,239,240} The ProfMOF catalogue includes: CAU-10, UiO-66, UiO-66-ADC, UiO-66-FA, UiO-66-BDC, UiO-66-BDC-NH₂, UiO-66-BDC-COOH and UiO-66-BPDC/UiO-67.²⁴¹

STREM Chemicals Inc. has become a distributor of MOFs manufactured in agreement with various MOF companies including KRICT, Inven2 and Framergy. Their catalogue includes: (CuI)₄(DABCO)₂, (CuI)₄(C₆H₁₄N₂)₂, C₆H₁₂N₄(CuCN)₅, PCN-250(Fe) CONEKTICt F250 by Framergy, MIL-100(Fe) KRICT F100 by KRICT, ZIF-8 and UiO-66 by Inven2.²⁴²

Sigma-Aldrich is a distributor of MOFs supplied by BASF under the product names Basolites and Basosivt. Fig.1.27 shows the total number of academic publications that reference these products. The actual number of sales or quantities is unavailable and therefore, these numbers represent the minimum. According to this data, Sigma-Aldrich has made at least a total of 1198 sales for research purposes. Their catalogue includes: Cu-BTC Basolites C300 by BASF, MIL-53 Basolites A100 by BASF, Fe-BTC Basolites F300 by BASF, ZIF-8 Basolites Z1200 by BASF, MOF-177 Basolites Z377 by BASF, Mg-Formate Basosivt M050 by BASF and Al-fumarate Basolites A520 by BASF (no longer available).²⁴³

Pseudo-startup MOFWORX from CSIRO Australia is commercializing MOFs based on patented flowchem manufacturing technology together with a diverse material and applicationbased portfolio. The group has built a reactor called Mindi (the aboriginal name for a mythological serpent that spits out white powder) that is capable of 10 kg h⁻¹ production. The company aims to become a product

development house for MOF-based technologies supported by their own manufacturing capability.²⁴⁴

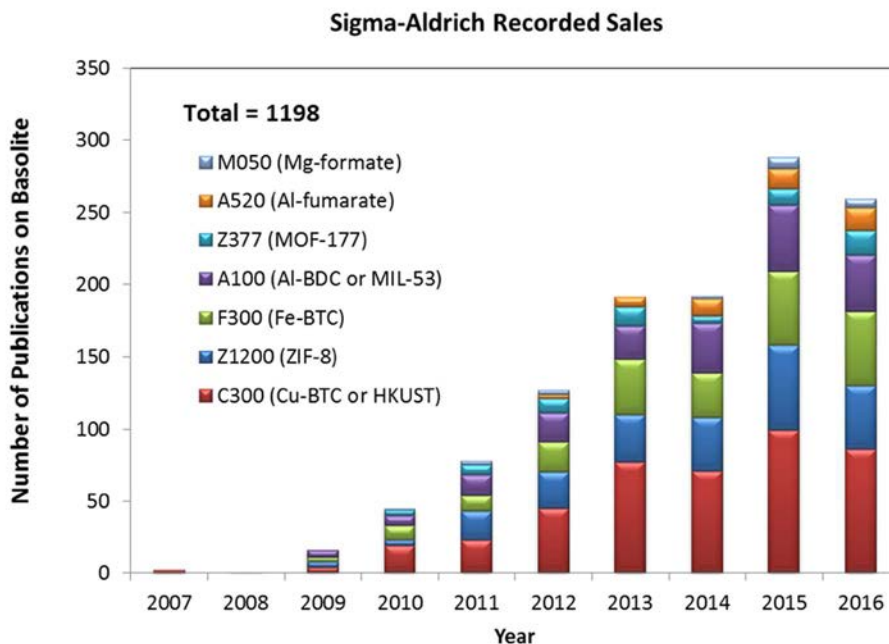


Fig.1. 27: Number of publications referring to the Basolite® and Basosiv™ products supplied by Sigma-Aldrich.

Other companies are working towards the commercialization of MOFs such as MOFGen, Framergy, ACSYNAM and Promethean particles.²⁴⁵⁻²⁴⁸ MOFGen are developing nanoporous materials for materials for a number of applications including medical devices, wound-healing and consumer healthcare. Framergy own the license for PCN-250 which can be used for natural gas capture and storage, and currently sold through STREM Chemical Inc. Promethean particles have commissioned a continuous flow reactor based on super critical water capable of producing 1000 tons per year. The companies have focused on nanoparticle production for inks electronics industry but are capable of shifting to MOF production if the market becomes more attractive.

1.7. References

1. J. Zhang, J. Wang and J. Ma, *J. Zhejiang Univ. Sci.*, 2005, 6A (10), 1095–1099.
2. B. Jha and D. N. Singh, *Fly Ash Zeolites*, Springer, 2016.
3. C. J. Rhodes, *Annu. Rep. Prog. Chem., Sect. C: Phys. Chem.*, 2007, 103, 287.
4. M. E. Davis, C. Saldarriaga, C. Montes, J. Garces and C. Crowdert, *Nature*, 1988, 331, 698–699.
5. K. Cheetham, G. Férey and T. Loiseau, *Angew. Chem.*, 1999, 38, 3268–3292.
6. R. P. Townsend and E. N. Coker, *Introduction to Zeolite Science and Practice*, Elsevier, 2001.
7. J. Vermesse, D. Vidal and P. Malbrunot, *Langmuir*, 1996, 12, 4190–4196.
8. B. M. Weckhuysen and J. Yu, *Chem. Soc. Rev.*, 2015, 44, 7022–7024.
9. G. Slater and A. I. Cooper, *Science*, 2015, 348, aaa8075-1.
10. H. C. Zhou, J. R. Long and O. M. Yaghi, *Chem. Rev.*, 2012, 112, 673–674.
11. B. F. Hoskins and R. Robson, *J. Am. Chem. Soc.*, 1990, 112, 1546–1554.
12. O. M. Yaghi and L. Guangming, *Angew. Chem.*, 1995, 34, 207–209.
13. O. M. Yaghi, M. O’Keeffe, N. W. Ockwig, H. K. Chae, M. Eddaoudi and J. Kim, *Nature*, 2003, 423, 705.
14. S. S.Y. Chui, S. M.F. Lo, J. P. H. Charmant, A. G. Orpen and I. D. Williams, *Science*, 1999, 283, 1148.
15. H. K. Kim, W. S. Yun, M.-B. Kim, J. Y. Kim, Y.-S. Bae, J. Lee and N. C. Jeong, *J. Am. Chem. Soc.*, 2015, 137, 10009–10015.
16. H. Li, M. Eddaoudi, M. O’Keeffe and O. M. Yaghi, *Nature*, 1999, 402, 276.
17. B. Rungtaweeworantit, C. S. Diercks, M. J. Kalmutzki and O. M. Yaghi, *Faraday Discuss.*, 2017, 201, 9–45.
18. H. Furukawa, K. E. Cordova, M. O’Keeffe and O. M. Yaghi, *Science*, 2013 341, 974.
19. G. Slater and A. I. Cooper, *Science*, 2015, 348, aaa8075-1.
20. O. K. Farha, A. Ö. Yazaydin, I. Eryazici, C. D. Malliakas, B. G. Hauser, M. G. Kanatzidis, S. T. Nguyen, R. Q. Snurr and J. T. Hupp, *Nat. Chem.*, 2010, 2, 944–948.
21. J. Lee, O. K. Farha, J. Roberts, K. A. Scheidt, S. T. Nguyen and J. T. Hupp, *Chem. Soc. Rev.*, 2009, 38, 1450–1459.
22. V. I. Isaeva and L. M. Kustov, *Pet. Chem.*, 2010, 50, 167–180.
23. S. Achmann, G. Hagen, J. Kita, I. M. Malkowsky, C. Kiener and R. Moos, *Sensors*, 2009, 9, 1574–1589.
24. M. X. Wu and Y.-W. Yang, *Adv. Mater.*, 2017, 29, 1606134.

25. C. A. Trickett, A. Helal, B. A. Al-Maythalony, Z. H. Yamani, K. E. Cordova and O. M. Yaghi, *Nat. Rev. Mater.*, 2017, 2 (17045), 1-16.
26. Z. Bao, L. Yu, Q. Ren, X. Lu and S. Deng, *J. Colloid Interface Sci.*, 2011, 353, 549–556.
27. T. M. McDonald, W. R. Lee, J. A. Mason, B. M. Wiers, C. S. Hong and J. R. Long, *J. Am. Chem. Soc.*, 2012, 134, 7056–7065.
28. W. L. Queen, M. R. Hudson, E. D. Bloch, J. A. Mason, M. I. Gonzalez, J. S. Lee, D. Gygi, J. D. Howe, K. Lee, T. A. Darwish, M. James, V. K. Peterson, S. J. Teat, B. Smit, J. B. Neaton, J. R. Long and C. M. Brown, *Chem. Sci.*, 2014, 5, 4569–4581.
29. S. D. Burd, S. Ma, J. A. Perman, B. J. Sikora, R. Q. Snurr, P. K. Thallapally, J. Tian, L. Wojtas and M. J. Zaworotko, *J. Am. Chem. Soc.*, 2012, 134, 3663–3666.
30. P. Nugent, Y. Belmabkhout, S. D. Burd, A. J. Cairns, R. Luebke, K. Forrest, T. Pham, S. Ma, B. Space, L. Wojtas, M. Eddaoudi and M. J. Zaworotko, *Nature*, 2013, 495, 80.
31. M. P. Suh, H. J. Park, T. K. Prasad and D.W. Lim, *Chem. Rev.*, 2012, 112, 782–835.
32. H. Li, K. Wang, Y. Sun, C. T. Lollar, J. Li and H.-C. Zhou, *Mater. Today*, 2018, 21, 108–121.
33. S. Ma, J. Eckert, P. M. Forster, J. W. Yoon, Y. K. Hwang, J. S. Chang, C. D. Collier, J. B. Parise and H.C. Zhou, *J. Am. Chem. Soc.*, 2008, 130, 15896–15902.
34. T. Runčevski, M. T. Kapelewski, R. M. Torres-Gavosto, J. D. Tarver, C. M. Brown and J. R. Long, *Chem. Commun.*, 2016, 52, 8251–8254.
35. Y. He, W. Zhou, G. Qian and B. Chen, *Chem. Soc. Rev.*, 2014, 43, 5657–5678.
36. Y. Peng, V. Krungleviciute, I. Eryazici, J. T. Hupp, O. K. Farha and T. Yildirim, *J. Am. Chem. Soc.*, 2013, 135, 11887–11894.
37. T. Tian, Z. Zeng, D. Vulpe, M. E. Casco, G. Divitini, P. A. Midgley, J. Silvestre-Albero, J.-C. Tan, P. Z. Moghadam and D. Fairen-Jimenez, *Nat. Mater.*, 2017, 17, 174-180.
38. Y. He, W. Zhou, T. Yildirim and B. Chen, *Energy Environ. Sci.*, 2013, 6, 2735–2744.
39. J. A. Mason, M. Veenstra and J. R. Long, *Chem. Sci.*, 2014, 5, 32–51.
40. X. Duan, Y. He, Y. Cui, Y. Yang, R. Krishna, B. Chen and G. Qian, *RSC Adv.*, 2014, 4, 23058–23063.
41. Y. He, Z. Zhang, S. Xiang, F. R. Fronczek, R. Krishna and B. Chen, *Chem. - Eur. J.*, 2012, 18, 613–619.

42. J. Canivet, A. Fateeva, Y. Guo, B. Coasne and D. Farrusseng, *Chem. Soc. Rev.*, 2014, 43, 5594–5617.
43. M. F. de Lange, K. J. F. M. Verouden, T. J. H. Vlugt, J. Gascon and F. Kapteijn, *Chem. Rev.*, 2015, 115, 12205–12250.
44. F. Jeremias, V. Lozan, S. K. Henninger and C. Janiak, *Dalt. Trans.*, 2013, 42, 15967–15973.
45. D. Fröhlich, S. K. Henninger and C. Janiak, *Dalton Trans.*, 2014, 43, 15300–15304.
46. D. Fröhlich, E. Pantatosaki, P. D. Kolokathis, K. Markey, H. Reinsch, M. Baumgartner, M. A. Van Der Veen, D. E. De Vos, N. Stock, G. K. Papadopoulos, S. K. Henninger and C. Janiak, *J. Mater. Chem. A*, 2016, 4, 11859–11869.
47. M. V Solovyeva, L. G. Gordeeva, T. A. Krieger and Y. I. Aristov, *Energy Convers. Manage.* 2018, 174, 356–363.
48. A. Dhakshinamoorthy, Z. Li and H. Garcia, *Chem. Soc. Rev.*, 2018, 47, 8134–8172.
49. D. Farrusseng, S. Aguado and C. Pinel, *Angew. Chem.*, 2009, 48, 7502–7513.
50. K. Schlichte, T. Kratzke and S. Kaskel, *Microporous Mesoporous Mater.*, 2004, 73, 81–88.
51. L. Alaerts, E. Séguin, H. Poelman, F. Thibault-Starzyk, P. A. Jacobs and D. E. De Vos, *Chem. – Eur. J.*, 2006, 12, 7353–7363.
52. Z. R. Jiang, H. Wang, Y. Hu, J. Lu and H. L. Jiang, *ChemSusChem*, 2015, 8, 878–885.
53. G. Akiyama, R. Matsuda, H. Sato and S. Kitagawa, *Chem Asian J.*, 2014, 9, 2772–2777.
54. A. Santiago-Portillo, J. F. Blandez, S. Navalón, M. Álvaro and H. García, *Catal. Sci. Technol.*, 2017, 7, 1351–1362.
55. P. Falcaro, R. Ricco, A. Yazdi, I. Imaz, S. Furukawa, D. Maspoch, R. Ameloot, J. D. Evans and C. J. Doonan, *Coord. Chem. Rev.*, 2016, 307, 237–254.
56. K. Konstas, T. Osl, Y. Yang, M. Batten, N. Burke, A. J. Hill and M. R. Hill, *J. Mater. Chem.* 2012, 22, 16698–16708.
57. S. Anderson and R. Newell, *Annu. Rev. Environ. Resour.*, 2004, 29, 109–142.
58. M. E. Boot-Handford, J. C. Abanades, E. J. Anthony, M. J. Blunt, S. Brandani, N. Mac Dowell, J. R. Fernández, M.-C. Ferrari, R. Gross, J. P. Hallett, R. S. Haszeldine, P. Heptonstall, A. Lyngfelt, Z. Makuch, E. Mangano, R. T. J. Porter, M. Pourkashanian, G. T. Rochelle, N. Shah, J. G. Yao and P. S. Fennell, *Energy Environ. Sci.* 2013, 7, 130–189.

59. EP0790253 (A2), 1997.
60. A. Rabenau, *Angew. Chem.*, 1985, 24, 1026–1040.
61. A. T. Çolak, G. Pamuk, O. Z. Yeşilel and F. Yüksel, *Solid State Sci.*, 2011, 13, 2100–2104.
62. C. Serre, F. Millange, C. Thouvenot, M. Noguès, G. Marsolier, D. Louër and G. Férey, *J. Am. Chem. Soc.*, 2002, 124, 13519–13526.
63. T. Loiseau, C. Serre, C. Huguenard, G. Fink, F. Taulelle, M. Henry, T. Bataille and G. Férey, *Chem. - Eur. J.*, 2004, 10, 1373–1382.
64. H. Deng, S. Grunder, K. E. Cordova, C. Valente, H. Furukawa, M. Hmadeh, F. Gándara, A. C. Whalley, Z. Liu, S. Asahina, H. Kazumori, M. O’Keeffe, O. Terasaki, J. F. Stoddart and O. M. Yaghi, *Science*, 2012, 336, 1018–1023.
65. J. H. Cavka, S. Jakobsen, U. Olsbye, N. Guillou, C. Lamberti, S. Bordiga and K. P. Lillerud, *J. Am. Chem. Soc.*, 2008, 130, 13850–13851.
66. L. Valenzano, B. Civalieri, S. Chavan, S. Bordiga, M. H. Nilsen, S. Jakobsen, K. P. Lillerud and C. Lamberti, *Chem. Mater.*, 2011, 23, 1700–1718.
67. M. J. Katz, Z. J. Brown, Y. J. Colón, P. W. Siu, K. A. Scheidt, R. Q. Snurr, J. T. Hupp and O. K. Farha, *Chem. Comm.*, 2013, 49, 9449–9451.
68. D. Feng, Z.-Y. Gu, J.-R. Li, H.-L. Jiang, Z. Wei and H.-C. Zhou, *Angew. Chem.*, 2012, 51, 10307–10310.
69. D. Feng, K. Wang, Z. Wei, Y.-P. Chen, C. M. Simon, R. K. Arvapally, R. L. Martin, M. Bosch, T.-F. Liu, S. Fordham, D. Yuan, M. A. Omary, M. Haranczyk, B. Smit and H.-C. Zhou, *Nat. Commun.*, 2014, 5 (5723), 1-8.
70. J. R. Li, J. Sculley and H. C. Zhou, *Chem. Rev.*, 2012, 112, 869–932.
71. P. Horcajada, R. Gref, T. Baati, P. K. Allan, G. Maurin, P. Couvreur, G. Férey, R. E. Morris and C. Serre, *Chem. Rev.*, 2012, 112, 1232–1268.
72. K. Sumida, D. L. Rogow, J. A. Mason, T. M. McDonald, E. D. Bloch, Z. R. Herm, T. H. Bae and J. R. Long, *Chem. Rev.*, 2012, 112, 724–781.
73. M. Gaab, N. Trukhan, S. Maurer, R. Gummaraju and U. Müller, *Microporous Mesoporous Mater.*, 2012, 157, 131–136.
74. M. D. Allendorf, C. A. Bauer, R. K. Bhakta and R. J. T. Houk, *Chem. Soc. Rev.*, 2009, 38, 1330-1352.
75. N. Stock and S. Biswas, *Chem. Rev.*, 2012, 112, 933–969.
76. WO2005049484 (A1), 2006.
77. US2005154222 (A1), 2006.
78. WO2007023295 (A2), 2007.
79. KR20060122576 (A), 2006.
80. US2010181212 (A1), 2010.
81. US8065904 (B1), 2011.
82. US2016346757 (A1), 2016.
83. US9352489 (B2), 2016.

84. EP2716360 (A2), 2014.
85. WO2014013274 (A2), 2014.
86. H. Reinsch, S. Waitschat, S. M. Chavan, K. P. Lillerud and N. Stock, *Eur. J. Inorg. Chem.*, 2016, 2016, 4490–4498.
87. Y. Sun and H. C. Zhou, *Sci. Technol. Adv. Mater.*, 2015, 16, 54202.
88. US8466285 (B2), 2006.
89. U. Mueller, M. Schubert, F. Teich, H. Puetter, K. Schierle-Arndt and J. Pastré, *J. Mater. Chem.*, 2006, 16, 626–636.
90. M. Taddei, D. A. Steitz, J. A. Van Bokhoven and M. Ranocchiari, *Chem. Eur. J.*, 2016, 22, 3245–3249.
91. W. J. Li, M. Tu, R. Cao and R. A. Fischer, *J. Mater. Chem. A*, 2016, 4, 12356–12369.
92. H. Al-Kutubi, J. Gascon, E. J. R. Sudhölter and L. Rassaei, *ChemElectroChem*, 2015, 2, 462–474.
93. US 8764887 B2, 2012.
94. N. Campagnol, T. R. C. Van Assche, M. Li, L. Stappers, M. Dincă, J. F. M. Denayer, K. Binnemans, D. E. De Vos and J. Fransaer, *J. Mater. Chem. A*, 2016, 4, 3914–3925.
95. P. Schäfer, M. A. Van Der Veen and K. F. Domke, *Chem. Commun.*, 2016, 52, 4722–4725.
96. R. Ameloot, L. Stappers, J. Fransaer, L. Alaerts, B. F. Sels and D. E. De Vos, *Chem. Mater.*, 2009, 21, 2580–2582.
97. A. Martinez Joaristi, J. Juan-Alcañiz, P. Serra-Crespo, F. Kapteijn and J. Gascon, *Cryst. Growth Des.*, 2012, 12, 3489–3498.
98. T. R. C. Van Assche, G. Desmet, R. Ameloot, D. E. De Vos, H. Terry and J. F. M. Denayer, *Microporous Mesoporous Mater.*, 2012, 158, 209–213.
99. J. Gascon, S. Aguado and F. Kapteijn, *Microporous Mesoporous Mater.*, 2008, 113, 132–138.
100. T. R. C. Van Assche, N. Campagnol, T. Muselle, H. Terry, J. Fransaer and J. F. M. Denayer, *Microporous Mesoporous Mater.*, 2016, 224, 302–310.
101. M. Hartmann, S. Kunz, D. Himsl, O. Tangermann, S. Ernst and A. Wagener, *Langmuir*, 2008, 24, 8634–8642.
102. N. Campagnol, T. Van Assche, T. Boudewijns, J. Denayer, K. Binnemans, D. De Vos and J. Fransaer, *J. Mater. Chem. A*, 2013, 1, 5827–5830.
103. S. D. Worrall, H. Mann, A. Rogers, M. A. Bissett, M. P. Atfield and R. A. W. Dryfe, *Electrochim. Acta*, 2016, 197, 228–240.
104. N. Campagnol, E. Rezende Souza, D. E. De Vos, K. Binnemans and J. Fransaer, *Chem. Commun.*, 2014, 50, 12680–12683.
105. W. J. Li, J. Lü, S. Y. Gao, Q. H. Li and R. Cao, *J. Mater. Chem. A*, 2014, 2, 19473–19478.

106. H. M. Yang, X. L. Song, T. L. Yang, Z. H. Liang, C. M. Fan and X. G. Hao, *RSC Adv.*, 2014, 4, 15720–15726.
107. H. Yang, X. Liu, X. Song, T. Yang, Z. Liang and C. Fan, *Trans. Nonferrous Met. Soc. China*, 2015, 25, 3987–3994.
108. M. Li and M. Dincă, *J. Am. Chem. Soc.*, 2011, 133, 12926–12929.
109. M. Li and M. Dincă, *Chem. Mater.*, 2015, 27, 3203–3206.
110. M. Li and M. Dincă, *Chem. Sci.*, 2014, 5, 107–111.
111. H. Zhu, H. Liu, I. Zhitomirsky and S. Zhu, *Mater. Lett.*, 2015, 142, 19–22.
112. I. Hod, W. Bury, D. M. Karlin, P. Deria, C. W. Kung, M. J. Katz, M. So, B. Klahr, D. Jin, Y. W. Chung, T. W. Odom, O. K. Farha and J. T. Hupp, *Adv. Mater.*, 2014, 26, 6295–6300.
113. R. Ameloot, L. Pandey, M. Van der Auweraer, L. Alaerts, B. F. Sels and D. E. De Vos, *Chem. Commun.*, 2010, 46, 3735.
114. I. Stassen, M. Styles, T. Van Assche, N. Campagnol, J. Fransaer, J. Denayer, J. C. Tan, P. Falcaro, D. De Vos and R. Ameloot, *Chem. Mater.*, 2015, 27, 1801–1807.
115. S. Yadnum, J. Roche, E. Lebraud, P. Négrier, P. Garrigue, D. Bradshaw, C. Warakulwit, J. Limtrakul and A. Kuhn, *Angew. Chem.*, 2014, 126, 4082–4086.
116. I. Bilecka and M. Niederberger, *Nanoscale*, 2010, 2, 1358–1374.
117. M. Gharibeh, G. A. Tompsett, K. S. Yngvesson and W. C. Conner, *J. Phys. Chem. B*, 2009, 113, 8930–8940.
118. N. A. Khan and S. H. Jung, *Coord. Chem. Rev.*, 2015, 285, 11–23.
119. A. de la Hoz, Á. Díaz-Ortiz and A. Moreno, *Chem. Soc. Rev.*, 2005, 34, 164–178.
120. S. H. Jung, J. H. Lee and J. S. Chang, *Bull. Korean Chem. Soc.*, 2005, 26, 880–881.
121. S. H. Jung, J. H. Lee, J. W. Yoon, C. Serre, G. Férey and J. S. Chang, *Adv. Mater.*, 2007, 19, 121–124.
122. Z. Ni and R. I. Masel, *J. Am. Chem. Soc.*, 2006, 128, 12394–12395.
123. J. S. Choi, W. J. Son, J. Kim and W. S. Ahn, *Microporous Mesoporous Mater.*, 2008, 116, 727–731.
124. K. M. L. Taylor-Pashow, J. Della Rocca, Z. Xie, S. Tran and W. Lin, *J. Am. Chem. Soc.*, 2009, 131, 14261–14263.
125. E. Haque, N. A. Khan, J. H. Park and S. H. Jung, *Chem. Eur. J.*, 2010, 16, 1046–1052.
126. N. A. Khan and S.-H. Jung, *Bull. Korean Chem. Soc.*, 2009, 30, 2921–2926.
127. D. W. Jung, D.-A. Yang, J. Kim, J. Kim and W.-S. Ahn, 2010, 39, 2883–2887.

128. N. A. Khan, I. J. Kang, H. Y. Seok and S. H. Jung, *Chem. Eng. J.*, 2011, 166, 1152–1157.
129. E. Haque and S. H. Jung, *Chem. Eng. J.*, 2011, 173, 866–872.
130. T. Chalati, P. Horcajada, R. Gref, P. Couvreur and C. Serre, *J. Mater. Chem.*, 2011, 21, 2220–2227.
131. J. H. Park, S.-H. Park and S.-H. Jung, *J. Korean Chem. Soc.*, 2009, 53, 553–559.
132. P. Silva, A. A. Valente, J. Rocha and F. A. Almeida Paz, *Cryst. Growth Des.*, 2010, 10, 2025–2028.
133. S. M. F. Vilela, D. Ananias, J. A. Fernandes, P. Silva, A. C. Gomes, N. J. O. Silva, M. O. Rodrigues, J. P. C. Tomé, A. A. Valente, P. Ribeiro-Claro, L. D. Carlos, J. Rocha and F. A. A. Paz, *J. Mater. Chem. C*, 2014, 2, 3311–3327.
134. P. P. Bag, X. S. Wang and R. Cao, *Dalton Trans.*, 2015, 44, 11954–11962.
135. W. Liang and D. M. D’Alessandro, *Chem Commun.*, 2013, 49, 3706–3708.
136. M. Taddei, P. V. Dau, S. M. Cohen, M. Ranocchiari, J. A. van Bokhoven, F. Costantino, S. Sabatini and R. Vivani, *Dalton Trans.*, 2015, 44, 14019–14026.
137. W. Liang, C. J. Coghlan, F. Ragon, M. Rubio-Martinez, D. M. D’Alessandro and R. Babarao, *Dalton Trans.*, 2016, 45, 4496–4500.
138. A. L. Garay, A. Pichon and S. L. James, *Chem. Soc. Rev.*, 2007, 36, 846–855.
139. G. Kaupp, *CrystEngComm*, 2003, 5, 117–133.
140. T. Friščić, *Chem. Soc. Rev.*, 2012, 41, 3493–3510.
141. P. Balaz, *Mechanochemistry in Nanoscience and Minerals Engineering*, Springer, 2008.
142. V. V. Boldyrev, *Solid State Ionics*, 1993, 63, 537–543.
143. A. Stolle, T. Szuppa, S. E. S. Leonhardt and B. Ondruschka, *Chem. Soc. Rev.*, 2011, 40, 2317–2329.
144. D. E. Crawford and J. Casaban, *Adv. Mater.*, 2016, 28, 5747–5754.
145. S. L. James, C. J. Adams, C. Bolm, D. Braga, P. Collier, T. Friščić, F. Grepioni, K. D. M. Harris, G. Hyett, W. Jones, A. Krebs, J. Mack, L. Maini, A. Guy Orpen, I. P. Parkin, W. C. Shearouse, J. W. Steed and D. C. Waddell, *Chem. Soc. Rev.*, 2012, 41, 413–447.
146. D. Braga and F. Grepioni, *Chem Commun.*, 2005, 3635–3645.
147. T. Friščić, *J. Mater. Chem.*, 2010, 20, 7599–7605.
148. A. Pichon, A. Lazuen-Garay and S. L. James, *CrystEngComm*, 2006, 8, 211–214.
149. A. Pichon and S. L. James, *CrystEngComm*, 2008, 10, 1839–1847.
150. S. Tanaka, K. Kida, T. Nagaoka, T. Ota and Y. Miyake, *Chem Commun.*, 2013, 49, 7884–7886.

151. N. K. Singh, M. Hardi and V. P. Balema, *Chem Commun.*, 2013, 49, 972–974.
152. K. Leng, Y. Sun, X. Li, S. Sun and W. Xu, *Cryst. Growth Des.*, 2016, 16, 1168–1171.
153. D. Braga, M. Curzi, A. Johansson, M. Polito, K. Rubini and F. Grepioni, *Angew. Chem.*, 2006, 45, 142–146.
154. T. Friščić and L. Fábán, *CrystEngComm*, 2009, 11, 743–745.
155. M. Klimakow, P. Klobes, A. F. Thünemann, K. Rademann and F. Emmerling, *Chem. Mater.*, 2010, 22, 5216–5221.
156. W. Yuan, A. L. Garay, A. Pichon, R. Clowes, C. D. Wood, A. I. Cooper and S. L. James, *CrystEngComm*, 2010, 12, 4063–4065.
157. 159 K. Fujii, A. L. Garay, J. Hill, E. Sbircea, Z. Pan, M. Xu, D. C. Apperley, S. L. James and K. D. M. Harris, *Chem. Commun.*, 2010, 46, 7572–7574.
158. Y. Chen, H. Wu, Z. Liu, X. Sun, Q. Xia and Z. Li, *Ind. Eng. Chem. Res.*, 2018, 57, 703–709.
159. A. M. Fidelli, B. Karadeniz, A. J. Howarth, I. Huskić, L. S. Germann, I. Halasz, M. Etter, S.-Y. Moon, R. E. Dinnebier, V. Stilinović, O. K. Farha, T. Friščić and K. Užarević, *Chem. Commun.*, 2018, 54, 6999–7002.
160. D. Prochowicz, K. Sokołowski, I. Justyniak, A. Kornowicz, D. Fairen-Jimenez, T. Friščić and J. Lewiński, *Chem. Commun.*, 2015, 51, 4032–4035.
161. K. Užarević, T. C. Wang, S. Y. Moon, A. M. Fidelli, J. T. Hupp, O. K. Farha and T. Friščić, *Chem. Commun.*, 2016, 52, 2133–2136.
162. T. Friščić, D. G. Reid, I. Halasz, R. S. Stein, R. E. Dinnebier and M. J. Duer, *Angew. Chem.*, 2010, 49, 712–715.
163. P. J. Beldon, L. Fábán, R. S. Stein, A. Thirumurugan, A. K. Cheetham and T. Friščić, *Angew. Chem.*, 2010, 49, 9640–9643.
164. US125406, 1872.
165. R. P. Patel, M. P. Patel and A. M. Suthar, *Indian J. Sci. Technol.*, 2009, 2, 44–47.
166. D. Charalampopoulos and R. A. Rastall, *Prebiotics and Probiotics Science and Technology*, Springer, 2009.
167. K. Okuyama, M. Abdullah, I. Wuled Lenggoro and F. Iskandar, *Adv. Powder Technol.*, 2006, 17, 587–611.
168. J. Thiele, M. Windbergs, A. R. Abate, M. Trebbin, H. C. Shum, S. Förster and D. A. Weitz, *Lab Chip*, 2011, 11, 2362–2368.
169. B. Rivas-Murias, J. F. Fagnard, P. Vanderbemden, M. Traianidis, C. Henrist, R. Cloots and B. Vertruyen, *J. Phys. Chem. Solids*, 2011, 72, 158–163.
170. R. Sun, Y. Lu and K. Chen, *Mater. Sci. Eng. C*, 2009, 29, 1088–1092.

171. A. Carné-Sánchez, I. Imaz, M. Cano-Sarabia and D. Maspoch, *Nat. Chem.*, 2013, 5, 203–211.
172. V. Guillerm, L. Garzón-Tovar, A. Yazdi, I. Imaz, J. Juanhuix and D. Maspoch, *Chem. Eur. J.*, 2017, 23, 6829–6835.
173. L. Garzón-Tovar, M. Cano-Sarabia, A. Carné-Sánchez, C. Carbonell, I. Imaz and D. Maspoch, *React. Chem. Eng.*, 2016, 1, 533–539.
174. A. Garcia Marquez, P. Horcajada, D. Grosso, G. Ferey, C. Serre, C. Sanchez and C. Boissiere, *Chem. Commun.*, 2013, 49 (3848), 1–11.
175. L. Garzón-Tovar, S. Rodríguez-Hermida, I. Imaz and D. Maspoch, *J. Am. Chem. Soc.*, 2017, 139, 897–903.
176. Z. Wang, D. Ananias, A. Carné-Sánchez, C. D. S. Brites, I. Imaz, D. Maspoch, J. Rocha and L. D. Carlos, *Adv. Funct. Mater.*, 2015, 25, 2824–2830.
177. A. Carné-Sánchez, K. C. Stylianou, C. Carbonell, M. Naderi, I. Imaz and D. Maspoch, *Adv. Mater.*, 2015, 27, 869–873.
178. L. Garzón-Tovar, J. Pérez-Carvajal, I. Imaz and D. Maspoch, *Adv. Funct. Mater.*, 2017, 27, 1–10.
179. R. Ameloot, F. Vermoortele, W. Vanhove, M. B. J. Roefsaers, B. F. Sels and D. E. De Vos, *Nat. Chem.*, 2011, 3, 382–387.
180. M. Faustini, J. Kim, G. Y. Jeong, J. Y. Kim, H. R. Moon, W. S. Ahn and D. P. Kim, *J. Am. Chem. Soc.*, 2013, 14619–14626.
181. L. Paseta, B. Seoane, D. Julve, V. Sebastian, C. Tellez and J. Coronas, *ACS Appl. Mater. Interfaces*, 2013, 130913131427004.
182. A. Polyzoidis, T. Altenburg, M. Schwarzer, S. Loebbecke and S. Kaskel, *Chem. Eng. J.*, 2016, 283, 971–977.
183. L. D'Arras, C. Sassoie, L. Rozes, C. Sanchez, J. Marrot, S. Marre and C. Aymonier, *New J. Chem.*, 2014, 38, 1477–1483.
184. S. Tai, W. Zhang, J. Zhang, G. Luo, Y. Jia, M. Deng and Y. Ling, *Microporous Mesoporous Mater.*, 2016, 220, 148–154.
185. M. Rubio-Martinez, M. P. Batten, A. Polyzos, K.-C. Carey, J. I. Mardel, K.-S. Lim and M. R. Hill, *Sci. Rep.*, 2014, 4, 5443.
186. M. Rubio-Martinez, T. D. Hadley, M. P. Batten, K. Constanti-Carey, T. Barton, D. Marley, A. Mönch, K.-S. Lim and M. R. Hill, *ChemSusChem*, 2016, 9, 938–941.
187. K. J. Kim, Y. J. Li, P. B. Kreider, C.-H. Chang, N. Wannemacher, P. K. Thallapally and H. G. Ahn, *Chem. Commun.*, 2013, 49, 11518.
188. P. A. Bayliss, I. A. Ibarra, E. Pérez, S. Yang, C. C. Tang, M. Poliakoff and M. Schröder, *Green Chem.*, 2014, 16, 3796.
189. S. Waitschat, M. T. Wharmby and N. Stock, *Dalton Trans.*, 2015, 44, 11235–11240.

190. A. S. Munn, P. W. Dunne, S. V. Y. Tang and E. H. Lester, *Chem. Commun.*, 2015, 51, 12811–12814.
191. M. Gimeno-Fabra, A. S. Munn, L. A. Stevens, T. C. Drage, D. M. Grant, R. J. Kashtiban, J. Sloan, E. Lester and R. I. Walton, *Chem. Commun.*, 2012, 48, 10642–10644.
192. M. Taddei, D. A. Steitz, J. A. van Bokhoven and M. Ranocchiari, *Chem. – Eur. J.*, 2016, 22, 3245–3249.
193. G. H. Albuquerque, R. C. Fitzmorris, M. Ahmadi, N. Wannemacher, P. K. Thallapally, B. P. McGrail and G. S. Herman, *Chem. Commun.*, 2015, 17, 5502–5510.
194. P. M. Schoenecker, G. A. Belancik, B. E. Grabicka and K. S. Walton, *AIChE J.*, 2013, 59, 1255–1262.
195. C. McKinstry, R. J. Cathcart, E. J. Cussen, A. J. Fletcher, S. V. Patwardhan and J. Sefcik, *Chem. Eng. J.*, 2016, 285, 718–725.
196. Y. Wang, L. Li, P. Dai, L. Yan, L. Cao, X. Gu and X. Zhao, *J. Mater. Chem. A*, 2017, 5, 22372–22379.
197. 199 Y. Wang, L. Li, L. Yan, X. Gu, P. Dai, D. Liu, J. G. Bell, G. Zhao, X. Zhao and K. M. Thomas, *Chem. Mater.*, 2018, 30, 3048–3059.
198. G. D. Ulrich, *Chemical engineering process design and economics: a practical guide*, Process Pub, 2004.
199. J. E. Mondloch, O. Karagiari, O. K. Farha and J. T. Hupp, *CrystEngComm*, 2013, 15, 9258–9264.
200. L. J. Wang, H. Deng, H. Furukawa, F. Gándara, K. E. Cordova, D. Peri and O. M. Yaghi, *Inorg. Chem.*, 2014, 53, 5881–5883.
201. K. S. Park, Z. Ni, A. P. Côté, J. Y. Choi, R. Huang, F. J. Uribe-Romo, H. K. Chae, M. O’Keeffe and O. M. Yaghi, *Proc. Natl. Acad. Sci.*, 2006, 103, 10186–10191.
202. H. Furukawa, N. Ko, Y. B. Go, N. Aratani, S. B. Choi, E. Choi, A. Ö. Yazaydin, R. Q. Snurr, M. O’Keeffe, J. Kim and O. M. Yaghi, *Science*, 2010, 329, 424–428.
203. J. An, O. K. Farha, J. T. Hupp, E. Pohl, J. I. Yeh and N. L. Rosi, *Nat. Commun.*, 2012, 3, 604.
204. K. Koh, J. D. Van Oosterhout, S. Roy, A. G. Wong-Foy and A. J. Matzger, *Chem. Sci.*, 2012, 3, 2429–2432.
205. Y. P. He, Y.-X. Tan and J. Zhang, *Inorg. Chem.*, 2012, 51, 11232–11234.
206. M. Rubio-Martinez, T. Leong, P. Juliano, T. D. Hadley, M. P. Batten, A. Polyzos, K.-S. Lim and M. R. Hill, *RSC Adv.*, 2016, 6, 5523–5527.
207. M. Yu, W. Li, Z. Wang, B. Zhang, H. Ma, L. Li and J. Li, *Sci. Rep.*, 2016, 6, 22796.
208. B. Garai, A. Mallick and R. Banerjee, *Chem. Sci.*, 2016, 7, 2195–2200.

209. Y. N. Wu, F. Li, H. Liu, W. Zhu, M. Teng, Y. Jiang, W. Li, D. Xu, D. He, P. Hannam and G. Li, *J. Mater. Chem.*, 2012, 22, 16971–16978.
210. S. Qiu, M. Xue and G. Zhu, *Chem. Soc. Rev.*, 2014, 43, 6116–6140.
211. Y. Zhang, Q. Gao, Z. Lin, T. Zhang, J. Xu, Y. Tan, W. Tian and L. Jiang, *Sci. Rep.*, 2014, 4, 4947.
212. J. Ren, H. W. Langmi, B. C. North and M. Mathe, *Int. J. Energy Res.*, 2015, 39, 607–620.
213. Z. Wang, J. Liu, S. Grosjean, D. Wagner, W. Guo, Z. Gu, L. Heinke, H. Gliemann, S. Bräse and C. Wöll, *ChemNanoMat*, 2015, 1, 338–345.
214. M. Beckner and A. Dailly, *Appl. Energy*, 2015, 149, 69–74.
215. US 6893564 B2, 2011.
216. J. Ren, T. Segakweng, H. W. Langmi, B. C. North and M. Mathe, *J. Alloys Compd.*, 2015, 645, S170–S173.
217. J. Zhao, M. D. Losego, P. C. Lemaire, P. S. Williams, B. Gong, S. E. Atanasov, T. M. Blevins, C. J. Oldham, H. J. Walls, S. D. Shepherd, M. A. Browe, G. W. Peterson and G. N. Parsons, *Adv. Mater. Interfaces*, 2014, 1, 1400040.
218. J. Kim, S.-H. Kim, S.-T. Yang and W. S. Ahn, *Microporous Mesoporous Mater.*, 2012, 161, 48–55.
219. D. Bazer-Bachi, L. Assié, V. Lecocq, B. Harbuzaru and V. Falk, *Powder Technol.*, 2014, 255, 52–59.
220. G. W. Peterson, J. B. DeCoste, T. G. Glover, Y. Huang, H. Jasuja and K. S. Walton, *Microporous Mesoporous Mater.*, 2013, 179, 48–53.
221. M. Tagliabue, C. Rizzo, R. Millini, P. D. C. Dietzel, R. Blom and S. Zanardi, *J. Porous Mater.*, 2011, 18, 289–296.
222. K. W. Chapman, G. J. Halder and P. J. Chupas, *J. Am. Chem. Soc.*, 2009, 131, 17546–17547.
223. S. Cavenati, C. A. Grande, A. E. Rodrigues, C. Kiener and U. Müller, *Ind. Eng. Chem. Res.*, 2008, 47, 6333–6335.
224. V. Finsy, L. Ma, L. Alaerts, D. E. De Vos, G. V. Baron and J. F. M. Denayer, *Microporous Mesoporous Mater.*, 2009, 120, 221–227.
225. P. Küsgens, A. Zgaverdea, H. G. Fritz, S. Siegle and S. Kaskel, *J. Am. Ceram. Soc.*, 2010, 93, 2476–2479.
226. J. Ren, N. M. Musyoka, H. W. Langmi, A. Swartbooi, B. C. North and M. Mathe, *Int. J. Hydrogen Energy*, 2015, 40, 4617–4622.
227. M. A. Moreira, J. C. Santos, A. F. P. Ferreira, J. M. Loureiro, F. Ragon, P. Horcajada, K. E. Shim, Y. K. Hwang, U. H. Lee, J. S. Chang, C. Serre and A. E. Rodrigues, *Langmuir*, 2012, 28, 5715–5723.
228. M. L. Pinto, S. Dias and J. Pires, *ACS Appl. Mater. Interfaces*, 2013, 5, 2360–2363.

- 229.** Y. Chen, X. Huang, S. Zhang, S. Li, S. Cao, X. Pei, J. Zhou, X. Feng and B. Wang, *J. Am. Chem. Soc.*, 2016, 138, 10810–10813.
- 230.** U. Betke, S. Proemmel, J. G. Eggebrecht, S. Rannabauer, A. Lieb, M. Scheffler and F. Scheffler, *Chem. Ing. Tech.*, 2016, 88, 264–273.
- 231.** A. I. Spjelkavik, Aarti, S. Divekar, T. Didriksen and R. Blom, *Chem. Eur. J.*, 2014, 20, 8973–8978.
- 232.** S. Aguado, J. Canivet and D. Farrusseng, *Chem. Commun.*, 2010, 46, 7999–8001.
- 233.** MOF Technologies Announces World’s First Commercial Application of Metal Organic Framework Technology by Decco Worldwide at MOF 2016, 2016.
- 234.** R. T. O. 2016, MOFs offer safer toxic gas storage. Chemistry World available at: <http://https://www.chemistryworld.com/news/mofs-offer-safer-toxic-gas-storage-/1017610.article>, accessed: 8th February 2017.
- 235.** Frameworks for commercial success, *Nat. Chem.*, 2016, 8, 987–987.
- 236.** Fundamentals and Applications of Advanced Porous Materials - CSIRO available at: <http://https://events.csiro.au/Events/2016/June/23/Advanced-Porous-Materials>.
- 237.** MOFapps – News, available at: <http://mofapps.com/news.html>, accessed: 8th February 2017.
- 238.** ProDIA, available at: <http://prodia-mof.eu/>, accessed: 27th March 2017.
- 239.** A. C. Dreischarf, M. Lammert, N. Stock and H. Reinsch, *Inorg. Chem.*, 2017, 56, 2270-2277.
- 240.** S. Waitschat, H. Reinsch and N. Stock, *Chem. Commun.*, 2016, 52, 12698–12701.
- 241.** Discover our MOF products | ProfMOF available at: <http://profmof.com/discover-our-mof-products/>, accessed: 8th February 2017.
- 242.** MOF, available at: <http://https://secure.strem.com/catalog/family/MOF/>, accessed: 8th February 2017.
- 243.** Metal Organic Frameworks, available at: <http://www.sigmaaldrich.com/technical-documents/articles/materials-science/metal-organic-frameworks.html>, accessed: 8th February 2017.
- 244.** Home, available at: <http://https://www.mofworx.com/>, accessed: 8th February 2017.
- 245.** The MOF company, <http://themofcompany.com>.
- 246.** Framergy, available at: <http://www.framergy.com/>, accessed: 8th February 2017.
- 247.** ACSYNAM, available at: <http://https://acsynam.com/>, accessed: 8th February 2017.

- 248.** Promethean to Showcase Manufacturing Capability with MOF production, 2016, available at: <http://www.prometheanparticles.co.uk/promethean-to-showcase-manufacturing-capability-with-mof-production/>, accessed: 8th February 2017.

CHAPTER 2

Objectives

As seen in the previous chapter, MOFs are an emerging class of porous materials with industrial relevance in many fields, including gas storage and separation, catalysis, adsorption heat transformations (AHTs), and contaminant sequestration. However, industry and academic experts widely agree that the effective exploitation and commercialisation of MOFs depend on the development of scalable, sustainable and cost-effective fabrication processes. Ideally, such green processes should enable continuous manufacturing of MOFs from non-toxic reagents in an energy-efficient way. In this context, there are many factors of the current fabrication methods – including both production and downstream steps - that should be taken into account, revised and further optimized. For example, the use of organic solvents in the processes can be an issue at scale production because of their cost, toxicity or flammability. Choice of metal salt can also be critical for large scale fabrication since nitrates present a safety hazard, and anions such as chlorides can be corrosive to metal reactors. Also, efficient activation and shaping of the produced MOF powders needs to be better understood and optimized to use them in real life applications.

In the above context, the main objective of this Thesis focuses on developing basic knowledge on the aqueous synthesis of MOFs and their shaping with the aim of approaching the production of MOFs at scale. More specifically, the three major objectives of this Thesis are:

- Avoid the use of common chloride or nitrate salt of metals, which show potential corrosion or hazard problems at scale production of MOFs, to synthesize MOFs in water. To this end, the family of industrially relevant metal acetylacetonates will be tested.
- Demonstrate the continuous flow spray drying synthesis of MOFs in water. The main objective herein will be to demonstrate for the first time that water can be used as the solvent for the MOF synthesis via spray drying. For this, the different synthetic parameters involved in the production of two archetypical Zr-MOFs will need to be optimized.
- Study the effect of densification on the textural and mechanical properties for different archetypical MOFs (UiO-66, UiO-66-NH₂, UiO-67, and HKUST-1) and test the stability of the shaped tablets under humid conditions.

CHAPTER 3

Metal Acetylacetonates as a Source
of Metals for Aqueous Synthesis of
Metal–Organic Frameworks

This chapter is based on the following article:

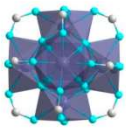
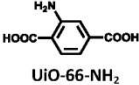
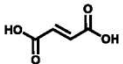
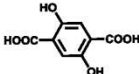
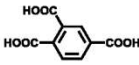
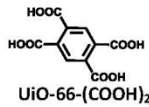
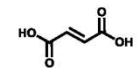
Ceren Avcı-Camur, Javier Perez-Carvajal, Inhar Imaz, Daniel Maspoch. (2018). ACS Sustainable Chem. Eng. 6, 11, 14554-14560.

3.1. Introduction

Metal acetylacetonate (acac) complexes that are formed of highly labile acetylacetonate linkers have found widespread use in industry,¹ including in vulcanization of plastics for rubber;^{2,3} curing processes for coatings (e.g., epoxy resins);⁴⁻⁷ as oxidative reagents for degradation of organic pollutants⁸ and also shelf-stable nonwoven fabrics and films used in dippers, wipes, towels and bathmats;⁹ as polyvinyl chloride (PVC) stabilizers;¹⁰ and as catalysts in many polymerizations.¹¹⁻¹³ For example, $Zr(acac)_4$ is used to initiate lactide polymerization and copolymerization for the production of bioresorbable materials; in drug-releasing processes; and to form scaffolds for tissue cultures and in biodegradable implants for surgical use.¹⁴ In most of these processes, metal acetylacetonate complexes are considered green reagents due to their low toxicity and ease of handling in air.¹⁵

MOFs are among the most attractive porous materials known today, owing to their myriad potential industrial applications as mentioned in **Chapter 1**. However, their practical use has been limited by the paucity of environmentally friendly methods suitable for large-scale production.¹⁶⁻¹⁹ The production process of MOFs generally needs high temperatures and the use of expensive, toxic, flammable and/or teratogenic organic solvents (such as DMF). Therefore, it is crucial to be able to fabricate MOFs in aqueous conditions, as water is safer and cheaper than using organic solvents. To date, some advances have been made in producing MOFs in water by mixing the organic linker, the metal salt (mainly nitrates, chlorides and oxochlorides) and acetic acid at high temperatures (Table 3.1). However, such salts can be problematic, as they present serious oxidative reactivity and toxicity hazards, and some of them are corrosive to metal-based reactors.^{18,20} To overcome these drawbacks, De Vos *et al.* and Stock *et al.* replaced the above-mentioned metal salts with metal sulfates in the aqueous synthesis of diverse MOFs (UiO-type and CAU-10) at high temperatures.^{21,22} Indeed, the sulfate ion is less corrosive, safer and greener than the corresponding anions of the aforementioned salts, and its use obviates the use of acetic acid. However, large concentrations of metal sulfates can compromise the framework rigidity and porosity of the resulting MOFs, due to interactions between the sulfate anions and the metal cations.^{23,24}

Table 3.1: Summary of the aqueous syntheses of the selected MOFs reported in the literature.

Cluster	Ligand / MOF	Metal source	Solvent	T (°C)	BET (m ² g ⁻¹)	Ref.
	 UiO-66-NH ₂	Zr(NO ₃) ₄	H ₂ O/AA	Reflux	833	27
		ZrOCl ₂	H ₂ O/AA	90 °C	1150	24
		ZrOCl ₂	H ₂ O/AA	150 °C	1261	28
		Zr(SO ₄) ₂	H ₂ O	Reflux	420	21
		Zr(acac) ₄	H ₂ O/AA	RT	1106	This work
	 Zr-fumarate	ZrOCl ₂	H ₂ O/AA	90 °C	1200	24
		ZrOCl ₂	H ₂ O/AA	150 °C	664	28
		Zr(acac) ₄	H ₂ O/AA	RT	1249	This work
	 UiO-66-(OH) ₂	Zr(NO ₃) ₄	H ₂ O/AA	Reflux	705	27
		ZrOCl ₂	H ₂ O/AA	95 °C	940	24
		Zr(acac) ₄	H ₂ O/AA	RT	733	This work
	 UiO-66-COOH	ZrCl ₄	H ₂ O	100 °C	661	29
		Zr(acac) ₄	H ₂ O/AA	90 °C	452	This work
		Zr(NO ₃) ₄	H ₂ O/AA	Reflux	494	27
		Zr(SO ₄) ₂	H ₂ O	Reflux	250	21
ZrCl ₄		H ₂ O	100 °C	516	29	
 UiO-66-(COOH) ₂	Zr(acac) ₄	H ₂ O/AA	90 °C	538	This work	
	Al ₂ (SO ₄) ₃ and NaAlO ₂	H ₂ O/EtOH	130 °C	-	22	
	Al(acac) ₃	H ₂ O	90 °C	520	This work	
 MIL-88A	FeCl ₃	H ₂ O	85 °C	-	30	
	Fe(acac) ₃	H ₂ O	RT	-	This work	

As part of our ongoing research to devise new methods for production of MOFs in water, we have sought alternatives to the metal sources cited above. In this chapter, it is shown that metal acetylacetonate complexes can serve as metal sources for aqueous synthesis of MOFs in good yields. As proof of concept, we used Zr(acac)₄ to prepare five members of the UiO-type family of MOFs, including UiO-66-NH₂, Zr-fumarate (also known as MOF-801), UiO-66-(OH)₂, UiO-66-COOH and UiO-66-(COOH)₂ (Table 3.1). We also extended our study

to other metal acetylacetonates such as $\text{Al}(\text{acac})_3$ (to produce CAU-10) and $\text{Fe}(\text{acac})_3$ (to produce MIL-88A). Encouragingly, we found that many of these reactions proceed in high yields at room temperature (RT), which is a remarkable finding given that aqueous synthesis of MOFs without heating has scarcely been reported.^{25,26}

3.2. Experimental section

3.2.1. Materials and methods

Zirconium acetylacetonate, iron(III) acetylacetonate, aluminum acetylacetonate, 2-aminoterephthalic acid, fumaric acid, 2-carboxyterephthalic acid, 2,5-dicarboxyterephthalic acid, isophthalic acid and acetic acid were purchased from Sigma-Aldrich. All reagents were used without further purification. All reactions were performed using deionized water, obtained from a Milli-Q system (18.2 $\text{M}\Omega\cdot\text{cm}$).

X-ray powder diffraction (XRPD) patterns were collected on an X'Pert PRO MPDP analytical diffractometer (Panalytical) at 45 kV and 40 mA using $\text{Cu K}\alpha$ radiation ($\lambda = 1.5419 \text{ \AA}$). Nitrogen and carbon dioxide adsorption and desorption measurements were performed at 77 K and room temperature respectively using an Autosorb-IQ-AG analyzer (Quantachrome Instruments). Specific surface area (S_{BET}) was determined by applying the BET equation to the adequate region of the nitrogen isotherms: the range was taken between 0.025 and 0.06 P/P_0 for UiO-66-NH_2 and COOH , and between 0.05 and 0.1 P/P_0 for the others.³¹ Prior to the measurements, samples were degassed inside the cell under primary vacuum at 200 °C for 6 h (UiO-66-NH_2) or at 150 °C for 10 h (Zr-fumarate) or at 100 °C for 3 h (UiO-66-(OH)_2) or at 70 °C for 12 h (UiO-66-COOH and UiO-66-(COOH)_2) or at 150 °C for 16 h (CAU-10). Gravimetric water vapor-sorption isotherms were measured using a DVS vacuum instrument (Surface Measurement Systems Ltd.). The weight of the dried powder ($\approx 20 \text{ mg}$) was constantly monitored with a high-resolution microbalance ($\pm 0.1 \text{ }\mu\text{g}$) and recorded at 25 °C ($\pm 0.2 \text{ }^\circ\text{C}$) under pure water vapor pressures. ^1H NMR spectra were collected on a Bruker AVANCE III 400 MHz spectrometer. Ten mg of each sample were digested in 0.5 mL of 1.2 wt % of HF solution prepared in DMSO-d_6 . From each spectrum, the amount of acetic acid per cluster was calculated. Field-emission scanning electron microscopy (FESEM) images were collected on a FEI Magellan 400 L scanning electron microscope at an acceleration voltage of 2.0 kV.

3.2.2. Synthesis of MOFs

Synthesis of UiO-66-NH₂ at room temperature

Zr(acac)₄ (1169 mg, 2.4 mmol) and 2-aminoterephthalic acid (435 mg, 2.4 mmol) were mixed under stirring in 6 mL of a 50% (v/v) solution of acetic acid in water for 72 h at room temperature. The resulting yellow dispersion was washed once with water and three times with ethanol at room temperature. The solid was dried for 12 h at 65 °C in a conventional oven to afford the final product (yield: 90%).

Synthesis of Zr-fumarate at room temperature

Zr(acac)₄ (1169 mg, 2.4 mmol) and fumaric acid (278 mg, 2.4 mmol) were mixed under stirring in 6 mL of a 33% (v/v) or 50% (v/v) solution of acetic acid in water for 72 h at room temperature. The resulting white dispersion was washed once with water and three times with ethanol at room temperature. The solid was dried for 12 h at 65 °C in a conventional oven to afford the final product (yield: 83% to 88%).

Synthesis of UiO-66-(OH)₂ at room temperature

Zr(acac)₄ (1169 mg, 2.4 mmol) and 2,5-dihydroxyterephthalic acid (476 mg, 2.4 mmol) were mixed under stirring in 6 mL of a 66% (v/v) solution of acetic acid in water for 72 h at room temperature. The resulting yellow dispersion was washed once with water and three times with ethanol at room temperature. The solid was dried for 12 h at 65 °C in a conventional oven to afford the final product (yield: 90%).

Synthesis of UiO-66-(COOH)₂ at 90 °C

Zr(acac)₄ (2194 mg, 4.5 mmol) and 2,5-dicarboxyterephthalic acid (1144 mg, 4.5 mmol) were mixed under stirring in 6 mL of a 33%, 50% or 66% (v/v) solution of acetic acid in water for 24 h at 90 °C. The resulting white dispersion was washed three times with water at room temperature. The solid was dried under vacuum to afford the final product (yield: 89% to 91%).

Synthesis of UiO-66-COOH at 90 °C

Zr(acac)₄ (2194 mg, 4.5 mmol) and 2-carboxyterephthalic acid (947 mg, 4.5 mmol) were mixed under stirring in 6 mL of a 66% (v/v) solution of acetic acid in water for 24 h at 90 °C. The resulting white dispersion was washed three

times with water at room temperature. The solid was dried under vacuum to afford the final product (yield: 90%).

Synthesis of MIL-88A at room temperature

Fe(acac)₃ (706 mg, 2.0 mmol) and fumaric acid (232 mg, 2.0 mmol) were mixed under stirring in 5 mL water for 72 h at room temperature. The resulting orange dispersion was washed once with water and three times with ethanol at room temperature. The solid was dried under vacuum to afford the final product (yield: 25%). In a subsequent synthesis, the yield was increased to 60% by running the reaction at 90 °C for 24 h.

Synthesis of CAU-10 at 90 °C

Al(acac)₃ (700 mg, 2.2 mmol) and isophthalic acid (300 mg, 1.8 mmol) were mixed in 6 mL of water for 72 h at 90 °C under stirring. The resulting white dispersion was washed twice with water and several times with ethanol at room temperature. The solid was dried under vacuum to afford the final product (yield: 85%).

3.3. Results and Discussion

UiO-type MOFs are known for their large surface areas, chemical versatility and high hydrothermal, chemical and thermal stability, all of which make them good candidates for industrial applications such as catalysis, gas and pollutant capture, adsorption heat transformation (AHT) and separation processes.^{32–34} Among the different UiO-type MOFs, we started with a room-temperature aqueous batch synthesis of UiO-66-NH₂ from Zr(acac)₄. To this end, 0.4 M of Zr(acac)₄ and 0.4 M of 2-aminoterephthalic acid were added in 6 mL of a 50% (v/v) aqueous solution of acetic acid, and the resulting mixture (pH = 2.3) was stirred for 72 h at room temperature. Note that 0.4 M is the maximum useable concentration for Zr(acac)₄, which, at higher concentrations, becomes highly viscous and paste-like. For the synthesis of UiO-66-NH₂, the optimal concentration of acetic acid was 50% (v/v) (Table 3.2).

Table 3.2. Summary of the yield and S_{BET} values obtained for different samples in the optimization of acetic acid concentration in the synthesis of UiO-66-NH₂ (V_{tot} : 6 ml, reagent concentration: 0.4 M).

Acetic Acid (v/v %)	Yield (%)	S_{BET} (m ² g ⁻¹)
8%	-	-
17%	55	772
25%	60	1008
33%	65	1069
50%	70	1106
66%	60	1064

Note that the concentration of acetic acid was crucial in this synthesis: the reaction only worked in the concentration range of 17% to 66% acetic acid (pH = 3.2 to 2.1). At lower concentrations, there was no reaction, whereas at higher concentrations, an amorphous solid was formed. After 72 h, the resulting yellow dispersion was washed once with water and three times with ethanol.

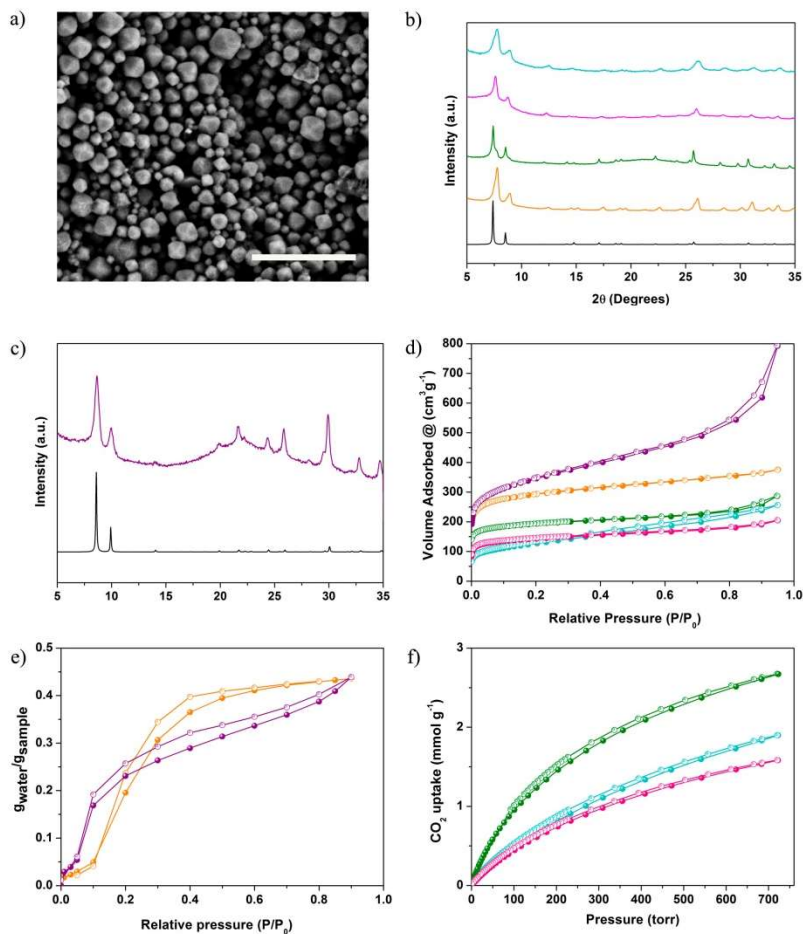


Fig.3.1: (a) Representative FESEM image of UiO-66-NH₂. (b) XRPD patterns for simulated UiO-66 (black) and synthesized UiO-66-NH₂ (orange), UiO-66-(OH)₂ (green), UiO-66-(COOH)₂ (pink) and UiO-66-COOH (blue). (c) XRPD patterns for simulated (black) and synthesized Zr-fumarate (purple). (d) N₂ adsorption (filled dots) and desorption (empty dots) isotherms at 77 K for UiO-66-NH₂ (orange), Zr-fumarate (purple), UiO-66-(OH)₂ (green), UiO-66-(COOH)₂ (pink) and UiO-66-COOH (blue). (e) Water sorption (filled dots) and desorption (empty dots) isotherms at room temperature for UiO-66-NH₂ (orange) and Zr-fumarate (purple) (f) CO₂ sorption (filled dots) and desorption (empty dots) isotherms at room temperature of UiO-66-(OH)₂ (green), UiO-66-(COOH)₂ (pink) and UiO-66-COOH (blue).

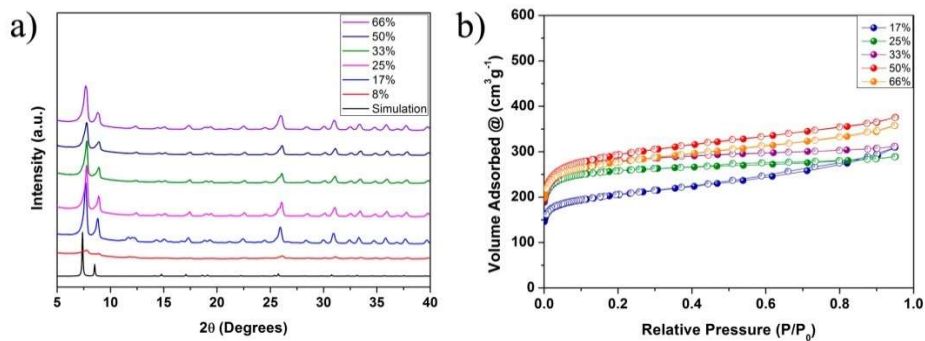


Fig.3.2: (a) XRPD patterns of the UiO-66-NH₂ samples and (b) N₂ adsorption (filled dots), desorption (empty dots) isotherms at 77K of UiO-66-NH₂ samples synthesized by using different concentrations of acetic acid in water (v/v %).

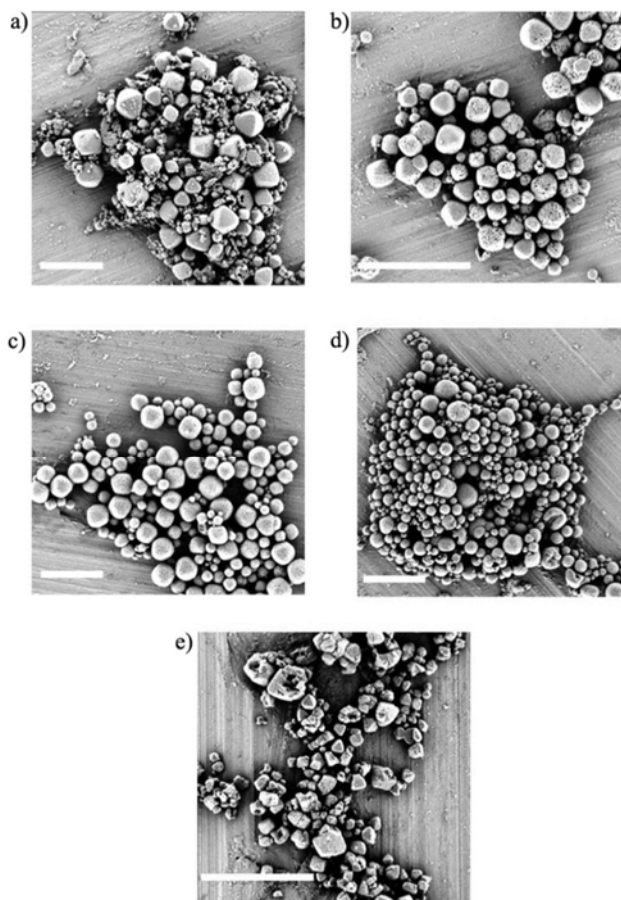


Fig.3.3: FESEM images of the UiO-66-NH₂ samples synthesized by using different concentrations of acetic acid in water (v/v %): 17% (a), 25% (b), 33% (c), 50% (d) and 66% of acetic acid (e) Scale bars: 3 μm.

Finally, the collected solid was dried for 12 h at 65 °C in a conventional oven to afford octahedral UiO-66-NH₂ submicrometer crystals (size: ~0.3–1 μm) as a pure phase (yield: 90%) (Fig.3.1a), as confirmed by X-ray powder diffraction (XRPD) and N₂ sorption measurements ($S_{\text{BET}} = 1106 \text{ m}^2 \text{ g}^{-1}$; Fig.3.1b, d; Fig.3.2 and 3.3). This S_{BET} value is consistent with the literature values for UiO-66-NH₂ synthesized from other metal sources in water (Table 3.1).^{24,28} Moreover, the quality of the synthesized UiO-66-NH₂ was also assessed by analysing its water sorption capacity. The water sorption isotherm showed the expected S-type trend centered at 0.2 P/P₀, with a total water uptake of 0.44 g_{water} g⁻¹ (Fig.3.1e).³⁵ In this sample, the number of missing linkers per [Zr₆(OH)₄L₆] was found to be 0.9 (Fig.3.4), which is in agreement with reported values.³⁶

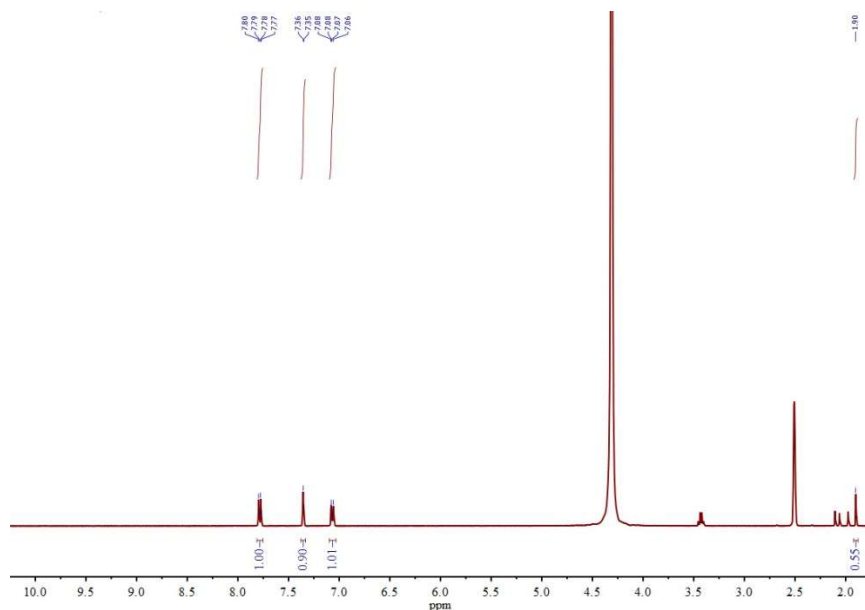


Fig.3.4: ¹H-NMR spectrum of the digested UiO-66-NH₂ (synthesized by using 50 % acetic acid) in HF/DMSOd⁶.

The scalability of the room temperature aqueous synthesis of UiO-66-NH₂ submicrometer crystals using Zr(acac)₄ was demonstrated on the multigram-scale (Fig.3.5). For this, we stirred the precursors (0.4 M) in 500 mL of a mixture of water and acetic acid (50% (v/v)) for 72 h at room temperature. After washing and drying, the resulting UiO-66-NH₂ powder (~53 g; yield: 95%) showed a S_{BET} value of 1000 m² g⁻¹.

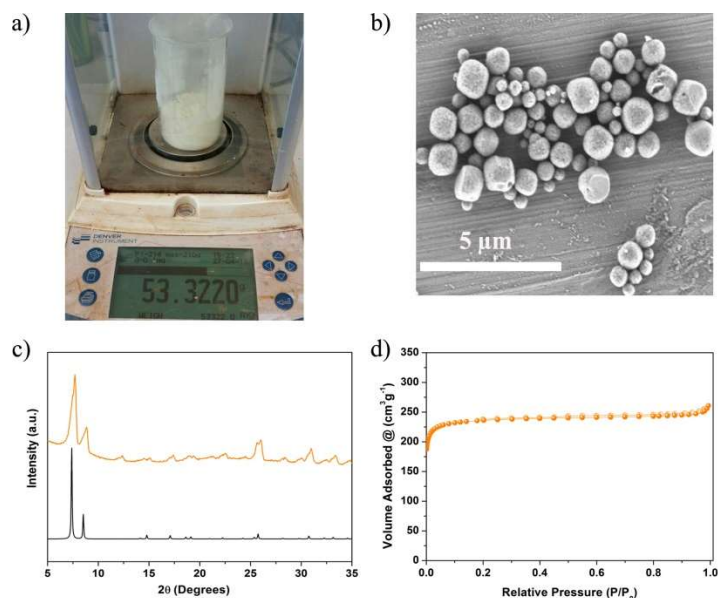


Fig.3.5: Photograph (a), FESEM image (b), XRPD patterns of simulated (black) and synthesized UiO-66-NH₂ (orange) (c) and N₂ adsorption (filled dots) and desorption (empty dots) isotherms at 77 K of the UiO-66-NH₂ (53 g) powder.

We then extended this aqueous synthetic approach to two other UiO-66-type MOFs: Zr-fumarate and UiO-66-(OH)₂. For these syntheses, an aqueous mixture of acetic acid containing 0.4 M of Zr(acac)₄ and 0.4 M of either fumaric acid (for Zr-fumarate) or 2,5-dihydroxyterephthalic acid (for UiO-66-(OH)₂) was stirred for 72 h at room temperature. For Zr-fumarate, the optimal concentration of acetic acid was in the range of 33% to 50% (v/v); and for UiO-66-(OH)₂, it was 66% (v/v) (Table 3.3).

Table 3.3: Summary of the yield and S_{BET} values obtained for different samples in the optimisation of acetic acid concentration for the synthesis of Zr-fumarate and UiO-66-(OH)₂ (V_{tot}: 6 mL; reagent concentration: 0.4 M).

Acetic Acid (v/v %)	Yield (%)		S _{BET} (m ² g ⁻¹)	
	Zr-Fum	UiO-66-(OH) ₂	Zr-Fum	UiO-66-(OH) ₂
8%	-	-	-	-
17%	70	-	750	-
25%	88	90	797	200
33%	88	93	1249	200
50%	83	94	1220	330
66%	87	94	917	733

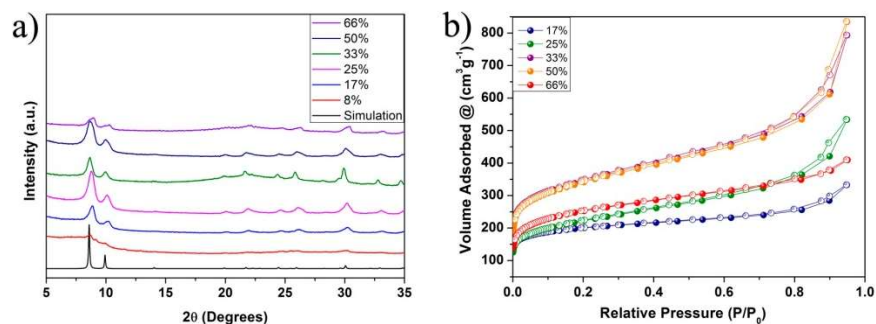


Fig.3.6: XRPD patterns (a), N₂ adsorption (filled dots) and desorption (empty dots) isotherms at 77 K (b) for the Zr-fumarate samples synthesised by using different concentrations of acetic acid in water (v/v).

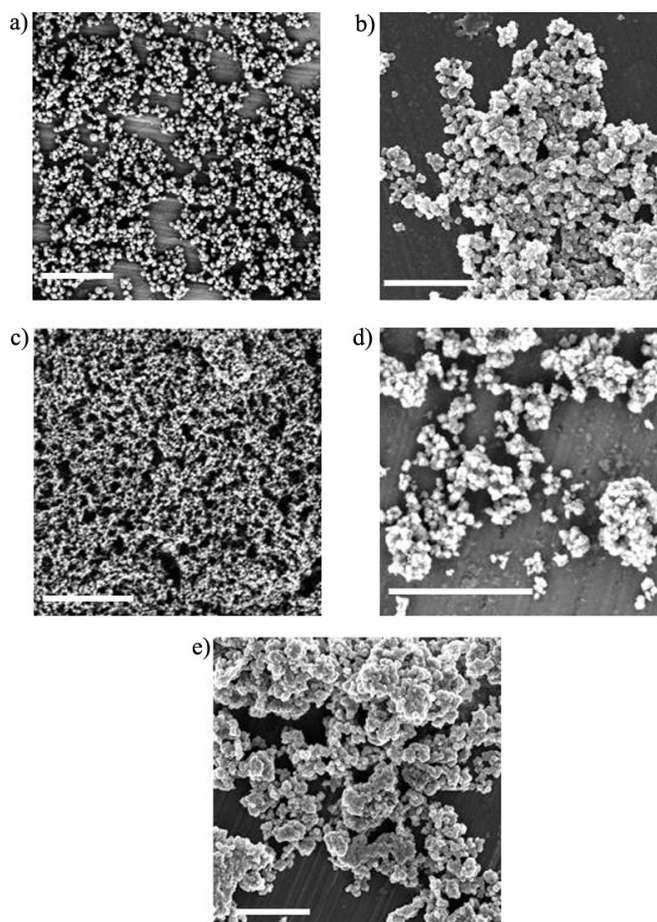


Fig.3.7: FESEM images of the Zr-fumarate samples synthesized by using different concentrations of acetic acid in water (v/v %): 17% (a), 25% (b), 33% (c), 50% (d) and 66% of acetic acid (e) Scale bars: 1 μm.

Under these conditions, aggregates of nanocrystals (size: <50 nm) of Zr-fumarate were synthesized in high yields (83% to 88%) and with an S_{BET} value of 1220–1249 $\text{m}^2 \text{g}^{-1}$. Note that these values are higher than most literature values (Fig.3.1c, d; Fig.3.6 and 7).^{24,37–39} In Zr-fumarate, the number of missing linkers per $[\text{Zr}_6(\text{OH})_4\text{L}_6]$ was calculated as 1.4 (Fig.3.8).³⁹ Given the promise of Zr-fumarate for water-related applications (e.g., delivery of drinking water from ambient air, storage of heat and/or refrigeration),^{24,37–41} we confirmed that synthesized Zr-fumarate retains the typical S-shaped isotherm, centered at 0.08 P/P0, and high water uptake (0.43 $\text{g}_{\text{water}} \text{g}^{-1}$) (Fig.3.1e).

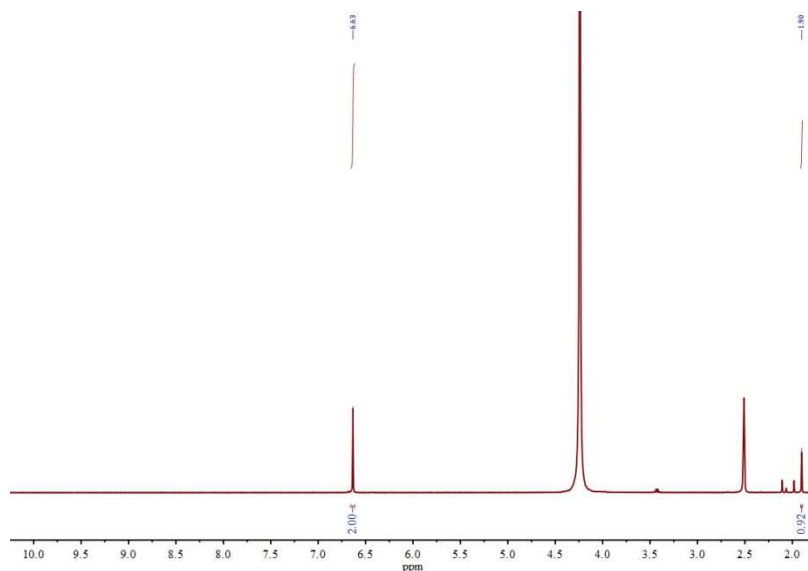


Fig.3.8: ^1H -NMR spectrum of the digested Zr-fumarate (synthesized by using 30 % acetic acid) in $\text{HF}/\text{DMSO-d}^6$.

The $\text{UiO-66}(\text{OH})_2$ was obtained (as aggregates of nanocrystals; size: <100 nm) in high yield (94%), with a number of missing linkers per $[\text{Zr}_6(\text{OH})_4\text{L}_6]$ of 1.3, and with an S_{BET} value of 733 $\text{m}^2 \text{g}^{-1}$. These results are consistent with the previously reported values for $\text{UiO-66}(\text{OH})_2$ synthesized in water (Fig.3.1b,d and Fig.3.9-11).²⁷ Given the interest in $\text{UiO-66}(\text{OH})_2$ for CO_2 -sorption application,^{42,43} the quality of the prepared material was studied by measuring its CO_2 uptake capacity. Total CO_2 uptake was 2.6 mmol g^{-1} at 700 Torr, which is consistent with the previously reported values (Fig.3.1f).^{24,37–40}

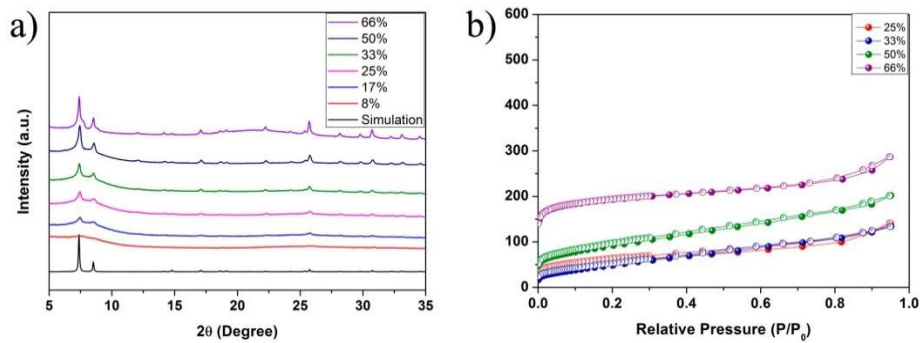


Fig.3.9: XRPD patterns (a), N₂ adsorption (filled dots) and desorption (empty dots) isotherms at 77 K (b) for the UiO-66-(OH)₂ samples synthesized by using different concentrations of acetic acid in water (v/v).

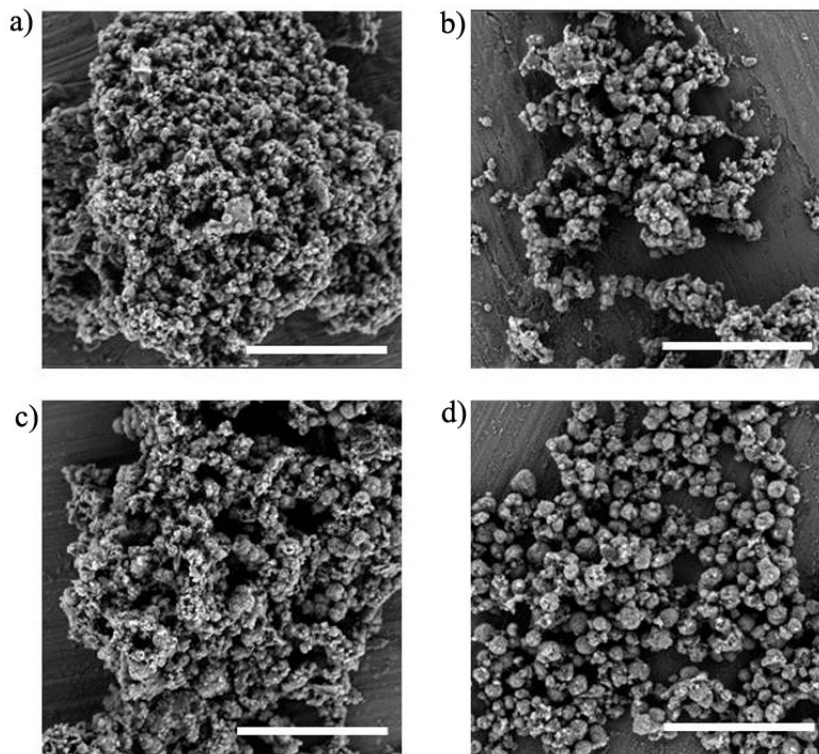


Fig.3.10: FESEM images of the UiO-66-(OH)₂ samples synthesized by using different concentrations of acetic acid in water (v/v %): 25% (a), 33% (b), 50% (c) and 66% of acetic acid (d) Scale bars: 3 μm.

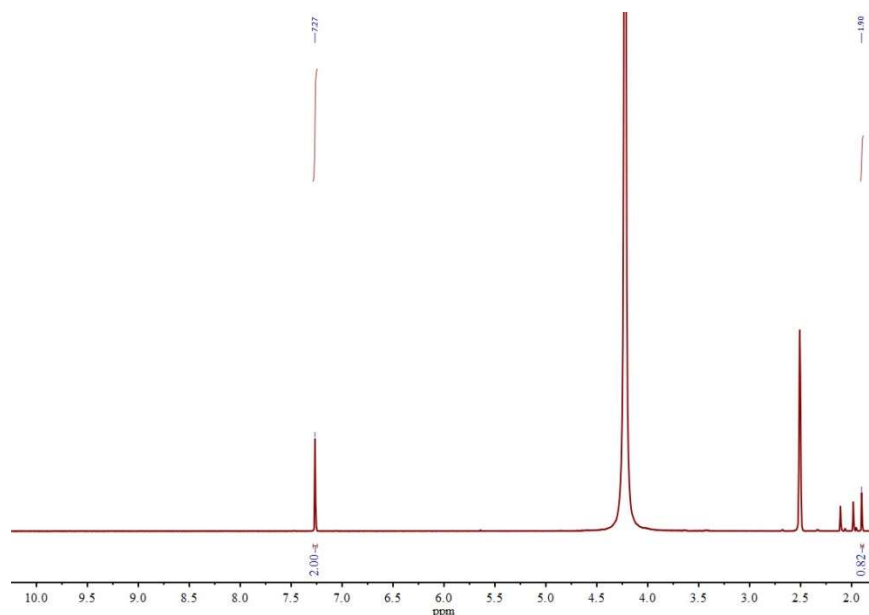


Fig.3.11: $^1\text{H-NMR}$ spectrum of the digested UiO-66-(OH)_2 (synthesized by using 66 % acetic acid) in HF/DMSO-d^6 .

Table 3.4: Summary of the yield and S_{BET} values obtained for different samples in the optimisation of acetic acid concentration for the synthesis of UiO-66-COOH and UiO-66-(COOH)_2 (V_{tot} : 6 mL; reagent concentration: 0.75 M).

Acetic Acid (v/v %)	Yield (%)		S_{BET} ($\text{m}^2 \text{g}^{-1}$)	
	UiO-66-(COOH)_2	UiO-66-COOH	UiO-66-(COOH)_2	UiO-66-COOH
17%	88	-	415	-
33%	90	88	538	268
50%	89	91	518	452
66%	91	90	542	538

Next, the aqueous syntheses of UiO-66-(COOH)_2 and UiO-66-COOH were performed from Zr(acac)_4 . Neither reaction worked at room temperature; they both required a temperature of 90 °C. To this end, an aqueous mixture of acetic acid containing 0.75 M of Zr(acac)_4 and 0.75 M of either 2,5-dicarboxyterephthalic acid (for UiO-66-(COOH)_2) or 2-carboxyterephthalic acid (for UiO-66-COOH) was stirred for 24 h at 90 °C. An acetic acid concentration of 33% to 66% (v/v) gave submicrometer crystals (size: $\sim 0.2\text{--}0.5 \mu\text{m}$) of UiO-66-(COOH)_2 in high yield (89 to 91%) and with a good value S_{BET} of $538 \text{ m}^2 \text{g}^{-1}$ (Figure 3.1 b,d; Table 3.4 and Fig.3.12 and 13).²⁹

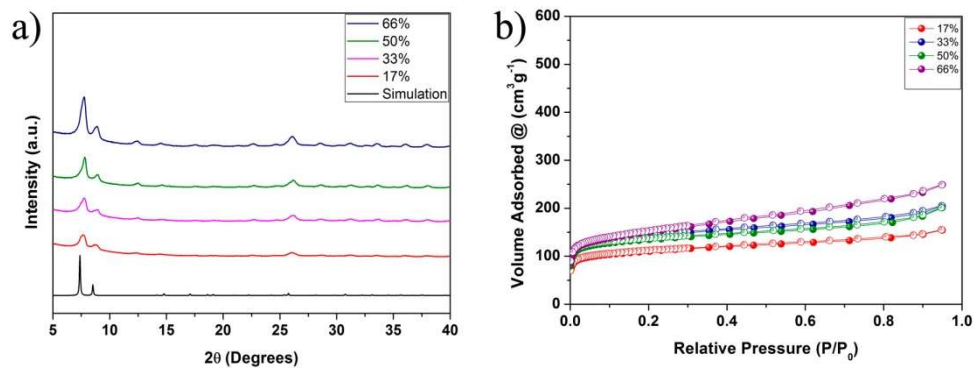


Fig.3.12: XRPD patterns (a), N_2 adsorption (filled dots) and desorption (empty dots) isotherms at 77 K (b) for the UiO-66-(COOH)₂ samples synthesized by using different concentrations of acetic acid in water (v/v).

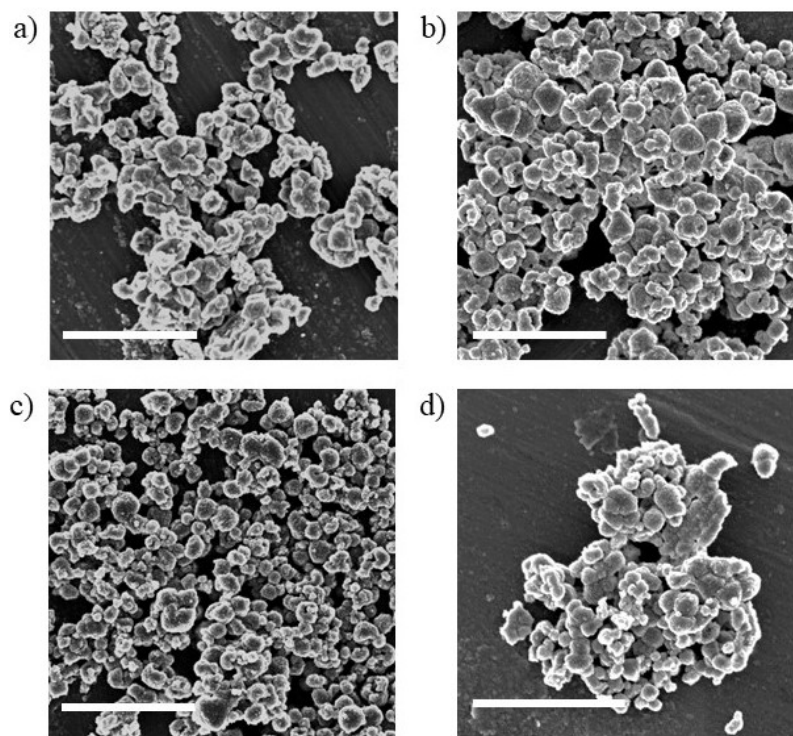


Fig.3.13: FESEM images of the UiO-66-(COOH)₂ samples synthesized by using different concentrations of acetic acid in water (v/v %): 17% (a), 33% (b), 50% (c) and 66% of acetic acid (d) Scale bars: 2 μm .

Similarly, an acid acetic concentration of 66% (v/v) afforded crystals of UiO-66-COOH (as aggregates of crystals; size: < 200 nm) in high yield (90%)

and with a S_{BET} value of $452 \text{ m}^2 \text{ g}^{-1}$ (Fig.3.1b,d; Table 3.4 and Fig.3.14 and 15). The total CO_2 uptake at 700 Torr was 1.6 mmol g^{-1} for UiO-66-(COOH)_2 and 1.9 mmol g^{-1} for UiO-66-COOH (Fig.3.1f).^{29,44}

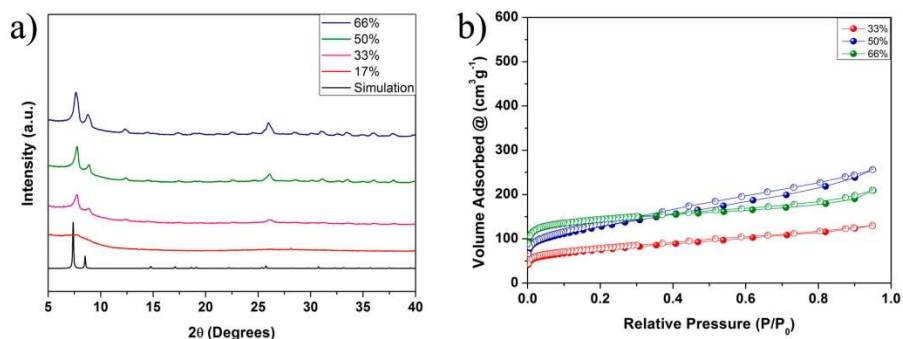


Fig.3.14: XRPD patterns (a), N_2 adsorption (filled dots) and desorption (empty dots) isotherms at 77 K (b) for the UiO-66-COOH samples synthesized by using different concentrations of acetic acid in water (v/v).

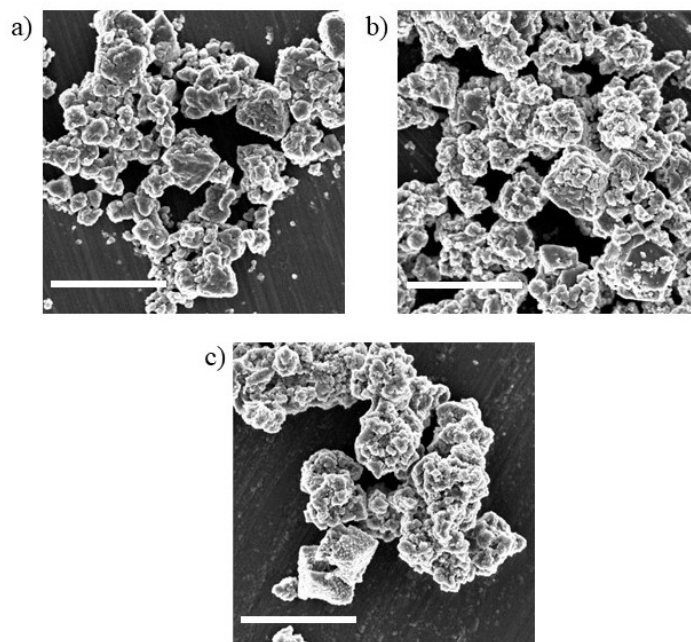


Fig.3.15: FESEM images of the UiO-66-COOH samples synthesized by using different concentrations of acetic acid in water (v/v %): 33% (a), 50% (b) and 66% (c) of acetic acid. Scale bars: 2 μm .

Here, the number of missing linkers per $[\text{Zr}_6(\text{OH})_4\text{L}_6]$ was 1.3 for UiO-66-(COOH)_2 and 1.8 for UiO-66-COOH (Fig.3.16).³⁹ Note here that the slightly

lower surface area observed in UiO-66-COOH²⁹ can be attributed to the presence of high amounts of defects.

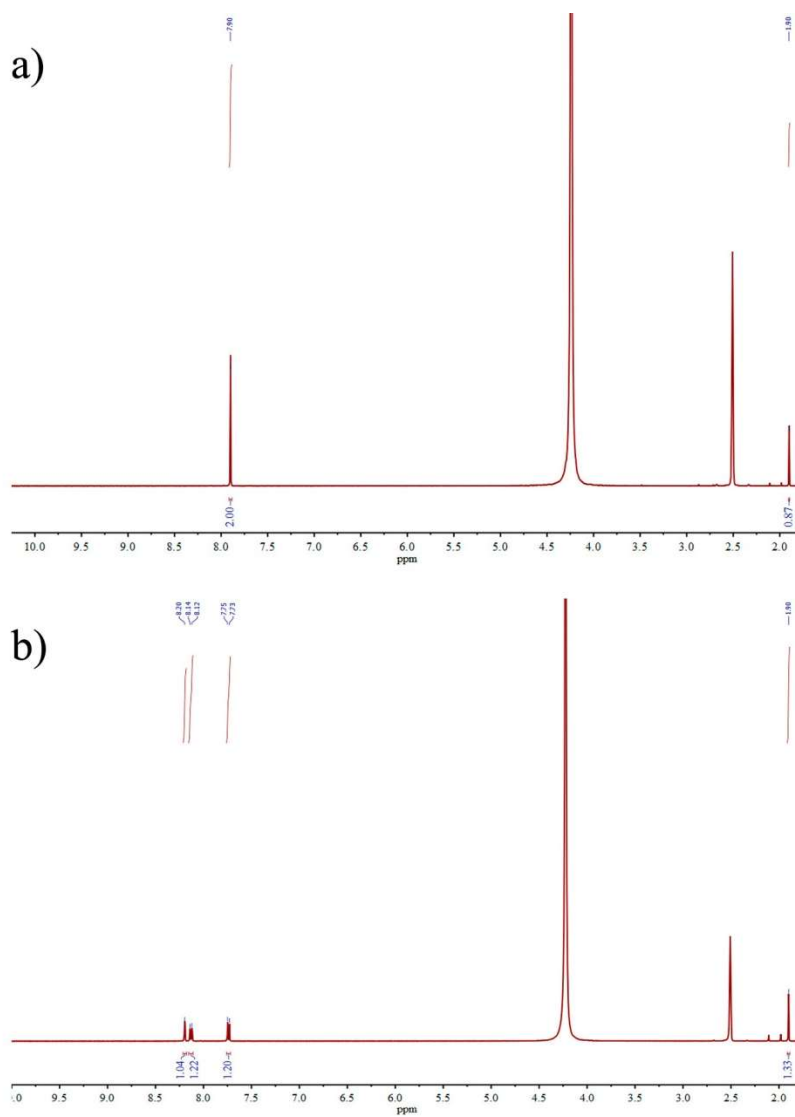


Fig.3.16: ¹H-NMR spectrum of the digested UiO-66-(COOH)₂ (a) and UiO-66-COOH (b) (synthesized by using 33% and 66 % acetic acid, respectively) in HF/DMSO-d₆.

Once demonstrated that UiO-type MOFs could be synthesized in water using Zr(acac)₄, we then sought to prove the generality of our strategy by preparing MOFs based on other metal ions such as iron and aluminum. To this

end, the Fe(III)-based MOF MIL-88A⁴⁴ was synthesized in water by stirring an aqueous mixture of 0.4 M of Fe(acac)₃ and 0.4 M of fumaric acid at room temperature for 72 h. After this period, the resulting orange dispersion was washed once with water and three times with ethanol. The collected solid was dried under vacuum to afford MIL-88A in the form of hexagonal rod-like crystals (yield: 25%; size: ~0.7–1.5 μm; Fig.3.18a).³⁰ Interestingly, the yield could be increased up to 60% by simply heating the aqueous mixture at 90 °C. Because this MOF is well-known for its structural breathing properties, this functionality was confirmed in the synthesized material by comparing the XRPD of the dry powder (closed form) to that of the material after it had been soaked in water for 20 min (open form) (Fig.3.17a).

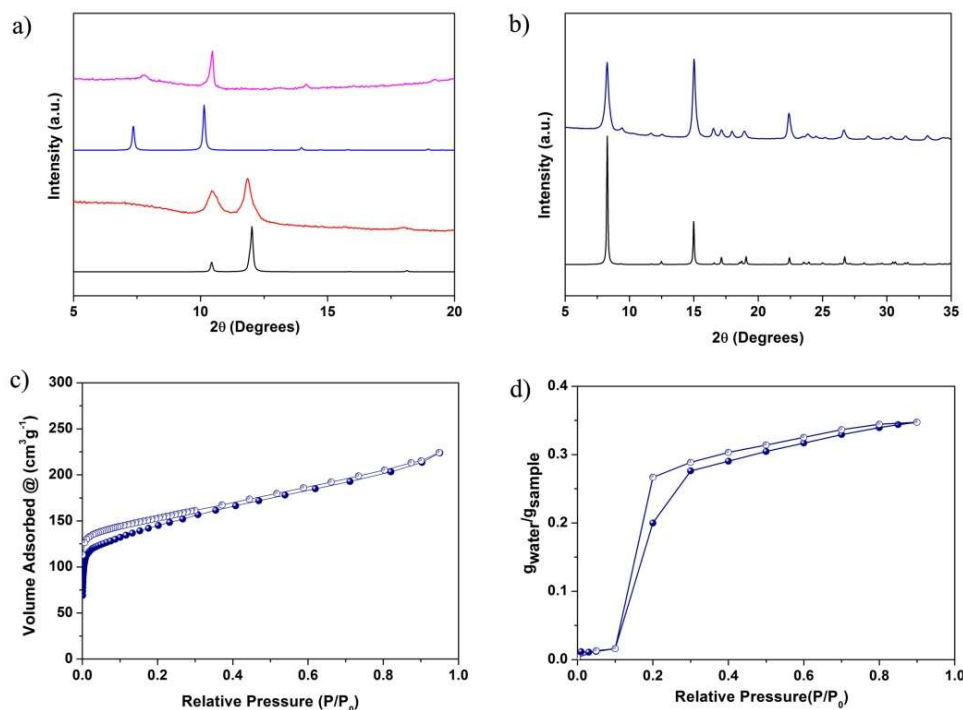


Fig.3.17: (a) XRPD patterns for the open (pink) and closed (red) forms of the synthesized MIL-88A, in comparison to the simulated patterns for the open (blue) and closed (blue) form. (b) XRPD patterns for simulated (black) and synthesized CAU-10 (blue). (c) N₂ adsorption (filled dots) and desorption (empty dots) isotherms at 77 K for CAU-10. (d) Water sorption (filled dots) and desorption (empty dots) isotherms at room temperature for CAU-10.

For an Al(III)-based MOF, we chose CAU-10, as it shows promise for many water sorption applications such as adsorption-driven heat pumps and chillers.⁴⁵ This MOF was synthesized by heating an aqueous mixture of 0.36 M

of $\text{Al}(\text{acac})_3$ and 0.30 M of isophthalic acid at 90 °C under continuous stirring for 72 h. The resulting white dispersion was then washed twice with water and four times with ethanol, and the collected solid dried under vacuum to afford submicrometer crystals of CAU-10 (size: $\sim 0.2\text{--}0.5\ \mu\text{m}$) in good yield (85%; Fig.3.17b; Fig.3.18b). N_2 and water sorption experiments revealed an S_{BET} value of $520\ \text{m}^2\ \text{g}^{-1}$ and total water uptake of $0.34\ \text{g}_{\text{water}}\ \text{g}^{-1}$, with the expected S-type trend centered at $0.2\ \text{P}/\text{P}_0$ (Fig.3.17c, d). These values are all in agreement with the reported values.²²

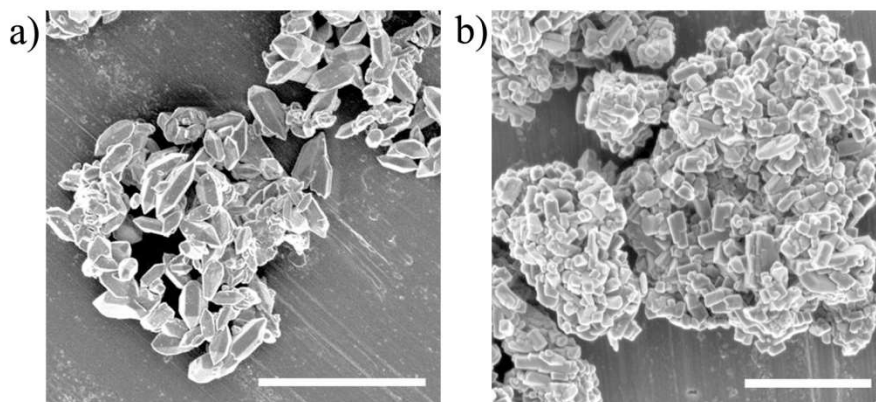


Fig.3.18: Representative FESEM image of the hexagonal rod-like crystals of MIL-88A (Scale bar: 3 μm) (a) and the submicrometre crystals of CAU-10 (Scale bar: 1 μm) (b).

3.4. Conclusions

This work shows that metal acetylacetonate complexes can be used as an alternative source of metals to synthesize MOFs in water. These metal acetylacetonates were used to synthesize various MOFs at either RT (UiO-66- NH_2 , Zr-fumarate, UiO-66-(OH)₂ and MIL-88A) or 90 °C (UiO-66-(COOH)₂, UiO-66- COOH and CAU-10). The yields were all good, ranging from 60% for MIL-88A to >85% for all the others. Because metal acetylacetonate complexes are considered green reagents for numerous industrial processes, this new strategy should enable the development of a simple, environmentally sound process for production of MOFs in water and, consequently, accelerate their commercialization.

3. 3. References

1. R. K. Sodhi, S. Paul, *Catal. Surv. Asia*, 2018, 22, 31–62.
2. H. M. Nor, J. R. Ebdon, *Prog. Polym. Sci.* 1998, 23, 143–177.
3. M. Przybyszewska, M. Zaborski, B. Jakubowski, J. Zawadiak, *eXPRESS Polym. Lett.* 2009, 3, 256–266.
4. K. Yamada, T. Y. Chow, T. Horihata, M. Nagata, *J. Non-Cryst. Solids* 1988, 100, 316–320.
5. T. Ibe, R. B. Frings, A. Lachowicz, S. Kyo, H. Nishide, *Chem. Commun.* 2010, 46, 3475–3477.
6. D. A. Shimp, US Patent US4 847 233, July 27, 1987.
7. J. D. B. Smith, *J. Appl. Polym. Sci.* 1981, 26, 979–986.
8. F. Sannino, P. Pernice, C. Imparato, A. Aronne, G. D’Errico, L. Minieri, M. Perfetti, D. Pirozzi, *RSC Adv.* 2015, 5, 93831–93839.
9. R. L. Hudson, US Patent US5 393 831, June 5, 1993.
10. CN Patent CN103 086 857, June 5, 2013.
11. J. L. Gorczynski, J. Chen, C. L. Fraser, *J. Am. Chem. Soc.* 2005, 127, 14956–14957.
12. Z. Czech, M. Wojciechowicz, *Eur. Polym. J.* 2006, 42, 2153–2160.
13. J. Wu, X. Jiang, L. Zhang, Z. Cheng, X. Zhu, *Polymers*, 2016, 8, 29.
14. P. Dobrzynski, *Polymer*, 2007, 48, 2263–2279.
15. R. J. Levis, *Sax’s Dangerous Properties of Industrial Materials*, 8th ed.; Van Nostrand Reinhold: New York, 1992.
16. P. A. Julien, C. Mottillo, T. Friscic, *Green Chem.*, 2017, 19, 2729–2747.
17. (a) M. Rubio-Martinez, C. Avei-Camur, A. W. Thornton, I. Imaz, D. MasPOCH, M. R. Hill, *Chem. Soc. Rev.* 2017, 46, 3453–3480. (b) J. Zhang, G. B. White, M. D. Ryan, A. J. Hunt, M. J. Katz, *ACS Sustainable Chem. Eng.* 2016, 4, 7186–7192. (c) L. Paseta, G. Potier, S. Sorribas, J. Coronas, *ACS Sustainable Chem. Eng.* 2016, 4, 3780–3785. (d) H. V. Doan, Y. Fang,; B. Yao, Z. Dong, T. J. White, A. Sartbaeva, U. Hintermair, V. P. Ting, *ACS Sustainable Chem. Eng.* 2017, 5, 7887–7893.
18. H. Reinsch, *Eur. J. Inorg. Chem.* 2016, 2016, 4290–4299.
19. H. Reinsch, N. Stock, *Dalton Trans.* 2017, 46, 8339–8349.
20. M. Gaab, N. Trukhan, S. Maurer, R. Gummaraju, U. Müller, *Microporous Mesoporous Mater.* 2012, 157, 131–136.
21. H. Reinsch, B. Bueken, F. Vermoortele, I. Stassen, A. Lieb, K. P. Lillerud, D. De Vos, *CrystEngComm*, 2015, 17, 4070–4074.

22. D. Lenzen, P. Bendix, H. Reinsch, D. Fröhlich, H. Kummer, M. Möllers, P. P. C. Hügenell, R. Glaser, S. Henninger, N. Stock, *Adv. Mater.*, 2018, 30, 1705869-1705869.
23. H. Reinsch, I. Stassen, B. Bueken, A. Lieb, R. Ameloot, D. De Vos, *CrystEngComm*, 2015, 17, 331–337.
24. H. Reinsch, S. Waitschat, S. M. Chavan, K. P. Lillerud, N. Stock, *Eur. J. Inorg. Chem.* 2016, 2016, 4490–4498.
25. M. Sanchez-Sanchez, N. Getachew, K. Diaz, M. Diaz-Garcia, Y. Chebude, I. Diaz, *Green Chem.* 2015, 17, 1500–1509.
26. L. Garzon-Tovar, A. Carne-Sanchez, C. Carbonell, I. Imaz, D. MasPOCH, *J. Mater. Chem. A* 2015, 3, 20819–20826.
27. Z. Hu, Y. Peng, Z. Kang, Y. Qian,; D. Zhao, *Inorg. Chem.* 2015, 54, 4862–4868.
28. C. Avci-Camur, J. Troyano, J. Perez-Carvajal, A. Legrand, D. Farrusseng, I. Imaz, D. MasPOCH, *Green Chem.* 2018, 20, 873–878.
29. F. Ragon, B. Campo, Q. Yang, C. Martineau, A. D. Wiersum, A. Lago, V. Guillerm, C. Hemsley, J. F Eubank, M. Vishnuvarthan, F. Taulelle, P. Horcajada, A. Vimont, P. L. Llewellyn, M. Daturi, S. Devautour-Vinot, G. Maurin, C. Serre, T. Devic, G. Clet, *J. Mater. Chem. A* 2015, 3, 3294–3309.
30. J. Wang, J. Wan, Y. Ma, Y. Wang, M. Pu, Z. Guan, *RSC Adv.* 2016, 6, 112502–112511.
31. **(a)** P. Llewellyn, G. Maurin, J. Rouquerol, *Adsorption by Powders and Porous Solids*, 2nd ed.; Academic Press: Poland, 2012. **(b)** D. A. Gomez-Gualdron, P. Z. Moghadam, J. T. Hupp,; O. K. Farha, K. Q. Snurr, *J. Am. Chem. Soc.* 2016, 138, 215–224.
32. **(a)** J. H. Cavka, S. Jakobsen, U. Olsbye, N. Guillou, C. Lamberti, S. Bordiga, K. P. A Lillerud, *J. Am. Chem. Soc.* 2008, 130, 13850–13851. **(b)** Y. Bai, Y. Dou, L. H. Xie, W. Rutledge, J. R. Li, H. C. Zhou, *Chem. Soc. Rev.* 2016, 45, 2327–2367. **(c)** Y. Han, J.-R. Li, Y. Xie, G. Guo, *Chem. Soc. Rev.* 2014, 43, 5952–5981.
33. X. Liu, N. K. Demir, Z. Wu, K. Li, *J. Am. Chem. Soc.* 2015, 137, 6999–7002.
34. **(a)** H. Kim, S. Yang, S. R. Rao, S. Narayanan, E. A. Kapustin, H. Furukawa, A. S. Umans, O. M. Yaghi, E. N. Wang, *Science*, 2017, 356, 430–434. **(b)** L. Garzon-Tovar, J. Perez-Carvajal, I. Imaz, D. MasPOCH, *Adv. Funct. Mater.*, 2017, 27, 1606424.

35. F. Jeremias,; V. Lozan,; S. K. Henninger,; C. Janiak, Dalton Trans., 2013, 42, 15967–15973.
36. M. R. DeStefano, T. Islamoglu, S. J. Garibay, J. T. Hupp, O. K. Farha, Chem. Mater. 2017, 29, 1357–1361.
37. H. Furukawa, F. Gandara, Y.-B. Zhang, J. Jiang, W. L. Queen, M. R. Hudson, O. M. Yaghi, J. Am. Chem. Soc. 2014, 136, 4369–4381.
38. J. Canivet, J. Bonnefoy, C. Daniel, A. Legrand, B. Coasne, D. Farrusseng, New J. Chem. 2014, 38, 3102–3111.
39. Z. Hu, I. Castano, S. Wang, Y. Wang, Y. Peng, Y. Qian, C. Chi, X. Wang, D. Zhao, Cryst. Growth Des., 2016, 16, 2295–2301.

CHAPTER 4

Aqueous Production of Spherical Zr-MOF Beads via Continuous-Flow Spray-Drying

This chapter is based on the following article:

*Ceren Avci-Camur, Javier Troyano, Javier Pérez-Carvajal, Alexandre Legrand, David Farrusseng, Inhar Imaz, Daniel Maspoch. (2018).
Green Chem. 20, 873-878.*

4.1. Introduction

As mentioned in **Chapters 1 and 3**, green methods for MOF synthesis should be aqueous, as water is safer and cheaper than using organic solvents. However, this is not trivial, as most organic linkers are poorly soluble in water and most MOFs are not stable in water.¹⁻³ This drawback is even more pronounced for continuous-fabrication methods, whereby the reaction time between organic linkers and metal ions is significantly lower compared to that in batch methods. However, to date, major advances have been made in the aqueous synthesis of MOFs using continuous-flow chemistry. In these methods, water-solubility issues have been mitigated mainly by using sodium salts of the organic linkers and by increasing the length of the tubing systems to increase the reaction time. For example, Schröder and Poliakoff *et al.* reported a continuous-flow aqueous synthesis of MIL-53-Al ($S_{\text{BET}} = 1010 \text{ m}^2 \text{ g}^{-1}$) based on the reaction of $\text{Al}(\text{NO}_3)_3 \cdot 9\text{H}_2\text{O}$ with sodium terephthalate for 10 min at 250 °C.⁴ Similarly, Blom *et al.* showed that CPO-27-Ni ($S_{\text{BET}} = 1085 \text{ m}^2 \text{ g}^{-1}$) could be synthesised in water by reacting $\text{Ni}(\text{OAc})_2 \cdot 2\text{H}_2\text{O}$ with sodium 2,5-dihydroxyterephthalate for 20 min at 90 °C.⁵ Also, Stock *et al.* produced UiO-66-NH₂ ($S_{\text{BET}} = 1150 \text{ m}^2 \text{ g}^{-1}$) by reacting $\text{ZrOCl}_2 \cdot 8\text{H}_2\text{O}$ and 2-aminoterephthalic acid and Zr-fumarate ($S_{\text{BET}} = 1200 \text{ m}^2 \text{ g}^{-1}$) and by reacting $\text{ZrOCl}_2 \cdot 8\text{H}_2\text{O}$ with fumaric acid for 22 min at 85 °C in the presence of acetic acid.⁶ Interestingly, Lester *et al.* recently demonstrated the large-scale aqueous fabrication of ZIF-8 (810 g h^{-1}) by reacting $\text{Zn}(\text{OAc})_2 \cdot 2\text{H}_2\text{O}$ and 2-methylimidazole with a base for 5 min in a pilot-scale, continuous counter-current reactor.⁷

Another approach to the continuous fabrication of MOFs is spray-drying, as introduced in **Chapter 1**,⁸⁻¹¹ a mature technology that has been widely deployed in many industrial sectors. Existing lab-scale spray-drying processes can easily be scaled-up to the pilot scale, including for tonne-scale production. Briefly, this technique entails the transformation of a liquid stream (solution, suspension or emulsion) into a dried powder upon rapid evaporation of the solvent using a hot gas. In 2013, our group demonstrated that, when the liquid stream contains metal ions and organic linkers, spray-drying can also be used to simultaneously synthesise and shape MOFs in the form of hollow or compact microscale spheres or beads.^{9,10,12} More recently, we showed that high-nuclearity MOF (e.g. UiO-type family) beads can also be produced by employing a continuous-flow process at the entrance to the spray-drier.²⁹ However, to date, all spray-drying syntheses of MOFs have involved organic solvents such as N,N'-dimethylformamide (DMF).¹³⁻¹⁶

Zr-Type MOFs are characterised by their large surface areas, chemical versatility and remarkably high hydrothermal, chemical and thermal stabilities, making them promising for catalysis, gas and pollutant capture and adsorption, heat transformation and separation processes.^{12,17-19} Synthesis of this MOF family can be improved through the use of acids. Moreover, acetic acid can also be incorporated into UiO-type structures, leading to networks that contain missing-linker defects and that usually exhibit higher uptake capacities.²⁰

In this chapter, we demonstrate the utility of continuous-flow spray-drying for aqueous fabrication and shaping of spherical Zr-MOF microbeads. This rapid technique uses reaction times of only 60 to 90 seconds. The ability to synthesise and shape MOFs in a single step is important for industrial applications, most of which demand specific shapes (e.g. tablets, extrudates, granulates or monoliths).²¹⁻²⁴ As a proof of concept, we prepared two water-stable members of the UiO-type family: UiO-66-NH₂ and Zr-fumarate (also known as MOF-801), were prepared. Then, the BET surface areas (S_{BET}) from N₂ sorption and the water sorption properties of these beads were evaluated.

4.2. Experimental Section

4.2.1. Materials and methods

Zirconium oxychloride octahydrate, 2-aminoterephthalic acid, fumaric acid and acetic acid were purchased from Sigma-Aldrich. All reagents were used without further purification. All reactions were performed using deionised water, obtained from a Milli-Q system (18.2 M Ω cm).

X-ray powder diffraction patterns were collected on an X'Pert PRO MPDP analytical diffractometer (Panalytical) at 40 kV and 40 mA using CuK α radiation ($\lambda = 1.5419 \text{ \AA}$). Nitrogen adsorption and desorption measurements were performed at 77 K using an Autosorb-IQ-AG analyser (Quantachrome Instruments). The specific surface area (S_{BET}) was determined by applying the BET equation to the adequate region of the nitrogen isotherms. The pore volume was determined from the adsorbed volume at P/P₀ 0.3 of each isotherm. Prior to the measurements, the samples were degassed inside the cell under primary vacuum at 200 °C for 6 h (UiO-66-NH₂) or at 150 °C for 12 h (Zr-fumarate). Gravimetric water vapour-sorption isotherms were measured using a DVS vacuum instrument (Surface Measurement Systems Ltd). The weight of

the dried powder (≈ 20 mg) was constantly monitored with a high-resolution microbalance (± 0.1 μg) and recorded at 25 $^{\circ}\text{C}$ (± 0.2 $^{\circ}\text{C}$) under pure water vapour pressures. Field-emission scanning electron microscopy (FESEM) images were collected on an FEI Magellan 400 L scanning electron microscope at an acceleration voltage of 2.0 kV, and on an FEI Quanta 650F scanning electron microscope at an acceleration voltage of 20.0 kV, using aluminium as a support. The degree of insertion of acetate inside the UiO-66-NH₂ and Zr-fumarate frameworks was analysed by first digesting the samples, and then studying the resulting solutions by ¹H-NMR. For UiO-66-NH₂, the acetate/BDC-NH₂ molar ratio was calculated by comparison of the integration of a doublet at 7.75 ppm corresponding to NH₂-BDC and a singlet at 1.9 ppm corresponding to acetate. In the case of Zr-fumarate, the acetate/fumarate molar ratio was calculated by comparison of the integration of a singlet at 6.64 ppm corresponding to fumarate and a singlet at 1.9 ppm corresponding to acetate. ¹H-NMR spectra were collected on a Bruker AVANCE III 400 MHz spectrometer. Thermogravimetric analyses were performed on a PerkinElmer TGA 8000 thermogravimetric analyser. A heating rate of 10 $^{\circ}\text{C min}^{-1}$ was used from room temperature up to 700 $^{\circ}\text{C}$.

4.2.2. Optimised aqueous synthesis of UiO-66-NH₂ by continuous-flow spray-drying

ZrOCl₂·8H₂O (773 mg, 2.4 mmol) and 2-aminoterephthalic acid (435 mg, 2.4 mmol) were mixed under stirring in 12 mL of a 30% (v/v) solution of acetic acid in water. The resulting mixture was injected, with agitation maintained, into a coil-flow reactor (Pyrex; 3 mm, inner diameter) at a feed rate (Q_{f}) of 2.4 mL min^{-1} and a bath temperature (T_{c}) of 90 $^{\circ}\text{C}$. The pre-heated yellow slurry was then spray-dried at a flow rate (Q_{d}) of 336 mL min^{-1} (spray-cap hole diameter: 0.5 mm) and an inlet temperature (T_{in}) of 150 $^{\circ}\text{C}$, using a B-290 Mini Spray Dryer (BUCHI Labortechnik). The resulting yellow powder was collected, dispersed in ethanol at room temperature, precipitated by centrifugation three times, left to stand in ethanol overnight, and washed twice with acetone. The solid was dried for 12 h at 75 $^{\circ}\text{C}$ in a conventional oven to afford the final product (yield: 64%).

4.2.3. Optimised aqueous synthesis of Zr-fumarate by continuous-flow spray-drying

ZrOCl₂·8H₂O (644 mg, 2.0 mmol) and fumaric acid (232 mg, 2.0 mmol) were mixed under stirring in 10 mL of a 30% (v/v) solution of acetic acid in

water. The resulting mixture was injected into a coil-flow reactor (Pyrex; 3 mm, inner diameter), with agitation maintained, at a feed rate of 2.4 mL min^{-1} and bath temperature (T_c) of $90 \text{ }^\circ\text{C}$. The resulting white slurry was spray-dried at a flow rate Q_{dg} of 336 mL min^{-1} and an inlet temperature (T_{in}) of $140 \text{ }^\circ\text{C}$. The resulting white powder was collected, dispersed in water at room temperature, left to stand overnight, and precipitated by centrifugation twice. This process was then repeated with ethanol instead of water. The solid was dried for 12 h at $75 \text{ }^\circ\text{C}$ in a conventional oven to afford the final product (yield: 58%).

4.3. Results and Discussion

4.3.1. Aqueous synthesis of UiO-66-NH₂ beads

A schematic illustration of the aqueous continuous-flow spray-drying set-up is shown in Fig.4.1. In a typical synthesis, an equimolar mixture of $\text{ZrOCl}_2 \cdot 8\text{H}_2\text{O}$ and 2-aminoterephthalic acid (BDC-NH₂) in a mixture of water and acetic acid was injected into a coil-flow reactor (i.d: 3 mm), which was placed into a silicone bath. The reaction was run using a specific coil-flow reactor temperature (T_c ; in $^\circ\text{C}$) and a liquid-feed rate (Q_{lf} ; in mL min^{-1}). The resulting yellow slurry was then spray-dried at a specific inlet temperature (T_{in} ; in $^\circ\text{C}$) and a drying-gas (N_2) flow rate (Q_{dg} ; in mL min^{-1}) using a B-290 Mini Spray Dryer (BUCHI Labortechnik). The beads were collected, washed with ethanol and acetone, and then dried at $75 \text{ }^\circ\text{C}$ in air.

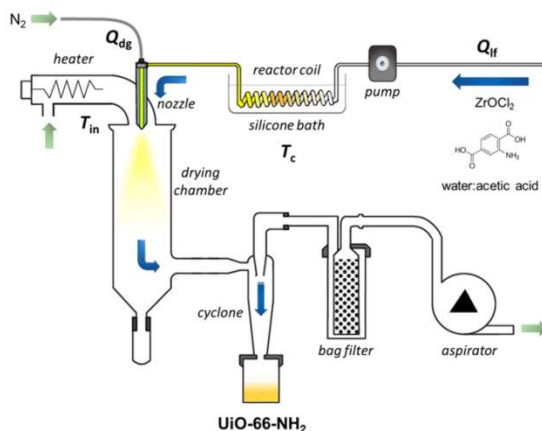


Fig.4.1: Schematic illustration of the set-up for the aqueous continuous-flow spray-drying synthesis of UiO-66-NH₂.

In addition to the optimisation of standard synthetic parameters (e.g. stoichiometry), the continuous-flow spray-drying method also demands the evaluation of T_c , T_{in} , Q_{lf} and Q_{dg} . Using this method, we initially produced UiO-66-NH₂ beads using a 0.05 M solution of ZrOCl₂·8H₂O and a 1: stoichiometric ratio of ZrOCl₂·8H₂O and BDC-NH₂. The total molar ratio of Zr/BDC-NH₂/acetic acid was defined as 1:1:50, which corresponds to an acetic acid concentration of 14% (v/v) in water. The optimal T_c was found to be 90 °C, as using lower values led to UiO-66-NH₂ with smaller S_{BET} values (Table 4.1).

Table 4.1: Summary of the yield and S_{BET} values obtained for different samples in the optimisation of bath temperature (T_c) for the synthesis of UiO-66-NH₂.

Bath temperature, T_c (°C)	Yield (%)	S_{BET} (m ² g ⁻¹)
90	70	840
85	61	531
80	86	468
75	76	236

T_{in} = 150 °C; Q_{lf} = 2.4 mL min⁻¹; Q_{dg} = 336 mL min⁻¹; [Zr] = 0.05 M; 14% (v/v %) acetic acid in water; V_{TOT} = 6 mL.

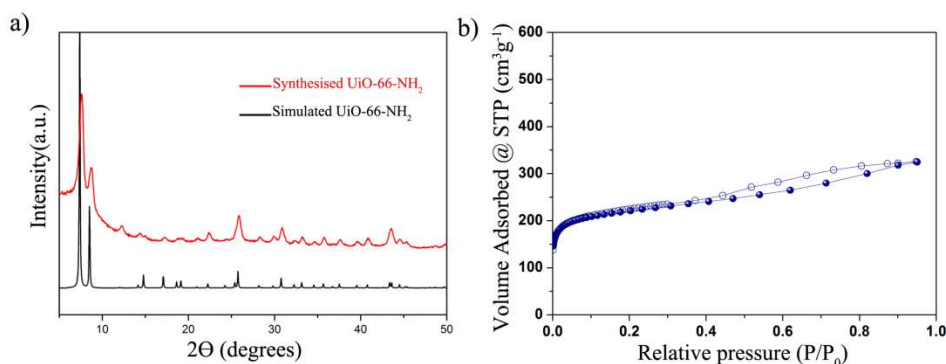


Fig.4.2: Characterization of UiO-66-NH₂ produced by aqueous continuous-flow spray-drying under the initial synthetic conditions ([Zr]= 0.05 M; 860 μL of 14 %, v/v % acetic acid in water; Q_{lf} = 2.4 mL min⁻¹; T_c = 90 °C). (a) XRPD diffractogram compared to the simulated powder pattern for UiO-66. (b) N₂ adsorption/desorption isotherm at 77 K.

The optimal Q_{if} was defined as 2.4 mL min^{-1} , as higher values led to incomplete drying of the droplets. The residence time inside the coil-flow reactor was 63 s. As an additional green measure, we sought to minimise T_{in} , as this would translate to lower energy use and cost. Thus, T_{in} was set to $150 \text{ }^{\circ}\text{C}$, which was the lowest temperature at which the solvent fully evaporated inside the spray-dryer. Finally, a Q_{dg} of 336 mL min^{-1} was used, based on earlier findings that it enables optimal nebulisation for MOF synthesis.^{9,10} The resulting yellow powder (yield: 70%) was characterised by XRPD, which confirmed the formation of crystalline UiO-66-NH₂ (Fig.4.2a). The microporosity of this sample was analysed by N₂ adsorption measurements at 77 K (Fig.4.2b), giving an estimated S_{BET} of $840 \text{ m}^2 \text{ g}^{-1}$. This S_{BET} value is within the range reported for UiO-66-NH₂ synthesised in DMF.^{10,25,26}

To explore the synergic effects of coupling spray-drying to continuous-flow, we synthesised UiO-66-NH₂ using each of these techniques separately. Spray-drying alone provided a non-porous amorphous product, whereas continuous-flow synthesis alone afforded UiO-66-NH₂ as a crystalline solid but in a much lower yield (6%) than that obtained with the coupled method.

Table 4.2. Summary of the yield and S_{BET} values obtained for different samples in the optimisation of reagent concentration for the synthesis of UiO-66-NH₂.

[Zr] (M)	% (v/v %) acetic acid in water	Yield (%)	S_{BET} ($\text{m}^2 \text{ g}^{-1}$)
0.05	14	70	840
0.1	28	68	717
0.2	56	72	1036

$T_c = 90 \text{ }^{\circ}\text{C}$; $T_{\text{in}} = 150 \text{ }^{\circ}\text{C}$; $Q_{\text{if}} = 2.4 \text{ mL min}^{-1}$; $Q_{\text{dg}} = 336 \text{ mL min}^{-1}$; $V_{\text{TOT}} = 6 \text{ mL}$

Having successfully produced UiO-66-NH₂ by continuous-flow spray-drying, we then sought to increase the yield by optimising the reagent concentrations. There are two main factors that limit the usable amounts of reagents in this reaction: the solubility of the organic ligand in water; and the blockage of the reaction coil during synthesis, due to the accumulation of precipitates. The maximum useable concentration of $\text{ZrOCl}_2 \cdot 8\text{H}_2\text{O}$ and BDC-NH₂ that we identified was 0.2 M for each reagent (Table 4.2). Since the total molar ratio of Zr/BDC-NH₂/acetic acid was kept at 1 : 1 : 50, the concentration

of acetic acid in water was 56% (v/v). These conditions afforded compact spherical UiO-66-NH₂ beads (size: 2–12 μm) in high yield (72%) and with a larger SBET (1036 m² g⁻¹) than that obtained previously (Fig.4.3). Thermogravimetric analysis (TGA) revealed that these UiO-66-NH₂ beads are stable up to near 400 °C, as depicted in Fig.4.4.

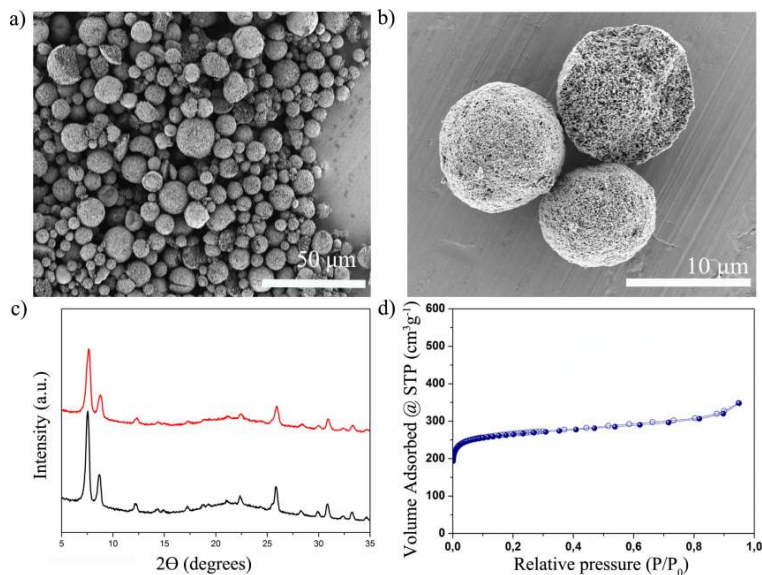


Fig.4.3: Characterisation of UiO-66-NH₂ produced under optimised synthetic conditions ([Zr] = 0.2 M; 3.2 mL of acetic acid (56% v/v in water); Q_{if} = 2.4 mL min⁻¹; T_c = 90 °C). (a, b) Representative FESEM images showing the compact microspherical beads of UiO-66-NH₂. (c) XRPD diffractogram (red) compared to the simulated powder pattern for UiO-66 (black). (d) N₂ adsorption (filled dots) desorption (empty dots) isotherm at 77 K.

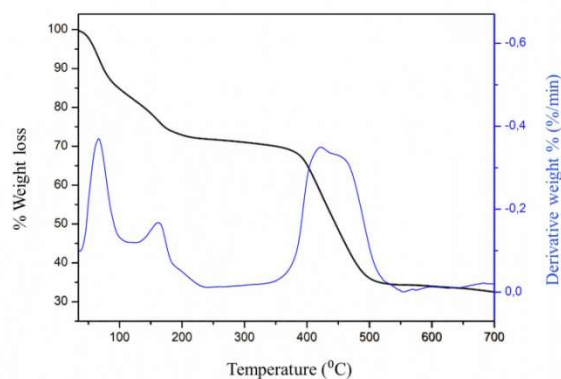


Fig.4.4: TGA profile of UiO-66-NH₂ beads produced under optimised synthetic conditions ([Zr] = 0.2 M; 3.2 mL of 56 % (v/v) acetic acid in water; Q_{if} = 2.4 mL min⁻¹; T_c = 90 °C).

4.3.2. Modulator effects on the synthesis of UiO-66-NH₂ beads

The gain in the S_{BET} value in the synthesised UiO-66-NH₂ beads was attributed to the increased concentration of acetic acid. Given that the addition

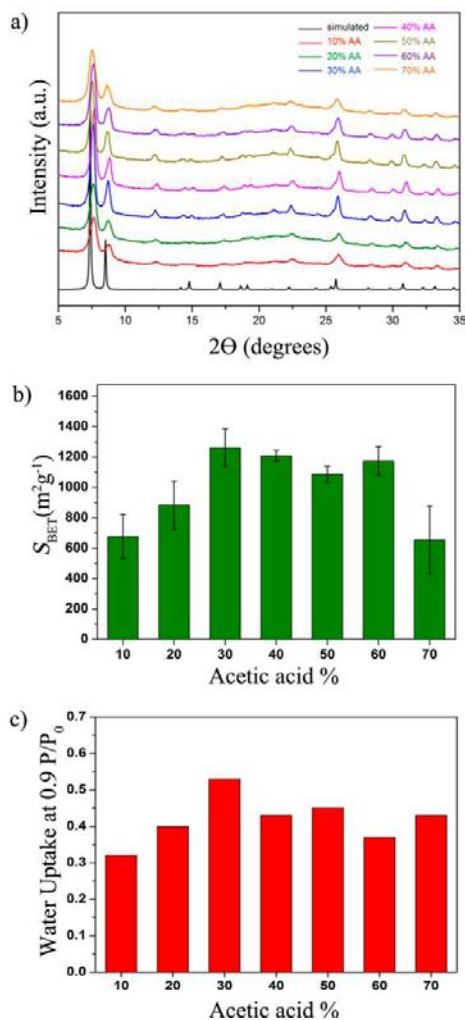


Fig.4.5: (a) XRPD diffractograms of UiO-66-NH₂ synthesised using different concentrations of acetic acid (v/v, in water) compared to the simulated powder pattern for UiO-66 (black). (b, c) S_{BET} values (b) and maximum water uptake values (c) for UiO-66-NH₂ samples prepared using different concentrations of acetic acid.

of acids (e.g. hydrochloric or acetic acid) can improve the formation and the crystallinity of UiO-type materials²⁷⁻²⁹ and that they can be incorporated into the structures leading usually to higher uptake capacities,²⁴ we reasoned that this effect could depend on the concentration. Thus, we studied the influence of the modulator in the continuous-flow spray-drying synthesis of UiO-66-NH₂ beads by systematically increasing the concentration of acetic acid from 10% to 70% (v/v) under the optimised synthetic conditions (vide supra). To assess the reproducibility of the chemistry, each concentration was tested in triplicate. The resulting powders were characterised by XRPD and all these powders were crystalline UiO-66-NH₂ (Fig.4.5a). However, UiO-66-NH₂ beads synthesised using acetic acid at concentrations from 30% to 60% exhibited better crystallinity, as evidenced by the calculated full width at half maximum (FWHM) values and average crystallite sizes (Table 4.3) by using Scherrer equation shown as follows:

$$D = \frac{K\lambda}{(\beta \cos \theta)}$$

where D is particle size (in nm), K is a dimensionless shape factor that is 0.9, λ is the X-ray wavelength (in nm) which is 0.15405 nm, β is the corrected FWHM (in radians) and θ is the Bragg angle (in degrees).

Table 4. 3: Full width at half maximum (FWHM) values of UiO-66-NH₂ samples and particle domain sizes determined by Scherrer equation.

AA% used in the synthesis	FWHM	Particle size (nm) calculated by Scherrer Eqn.
10%	0.57	18
20%	0.50	21
30%	0.36	33
40%	0.38	31
50%	0.38	31
60%	0.46	24
70%	0.52	20

FESEM confirmed that the formation of microscale structures ranging in shape from donut-like (at acetic acid concentrations [v/v] of 10% and 20%) to a more spherical shape (at concentrations $\geq 30\%$; Fig.4.6).

Remarkably, a similar trend had already been reported in the modulated hydrothermal batch synthesis of Zr-MOFs,^{30,31} whereby crystallinity was optimised by increasing the modulator up to a certain point, above which was observed a loss in crystallinity. For these more crystalline samples, the molar ratio of acetate/BDC-NH₂ in the structure determined by ¹H-NMR ranged from 0.03 to 0.13, the values that agree with those reported in the literature for samples of UiO-66 synthesised in the presence of acids at high temperatures (Fig. 3.7 and 3.8).³²

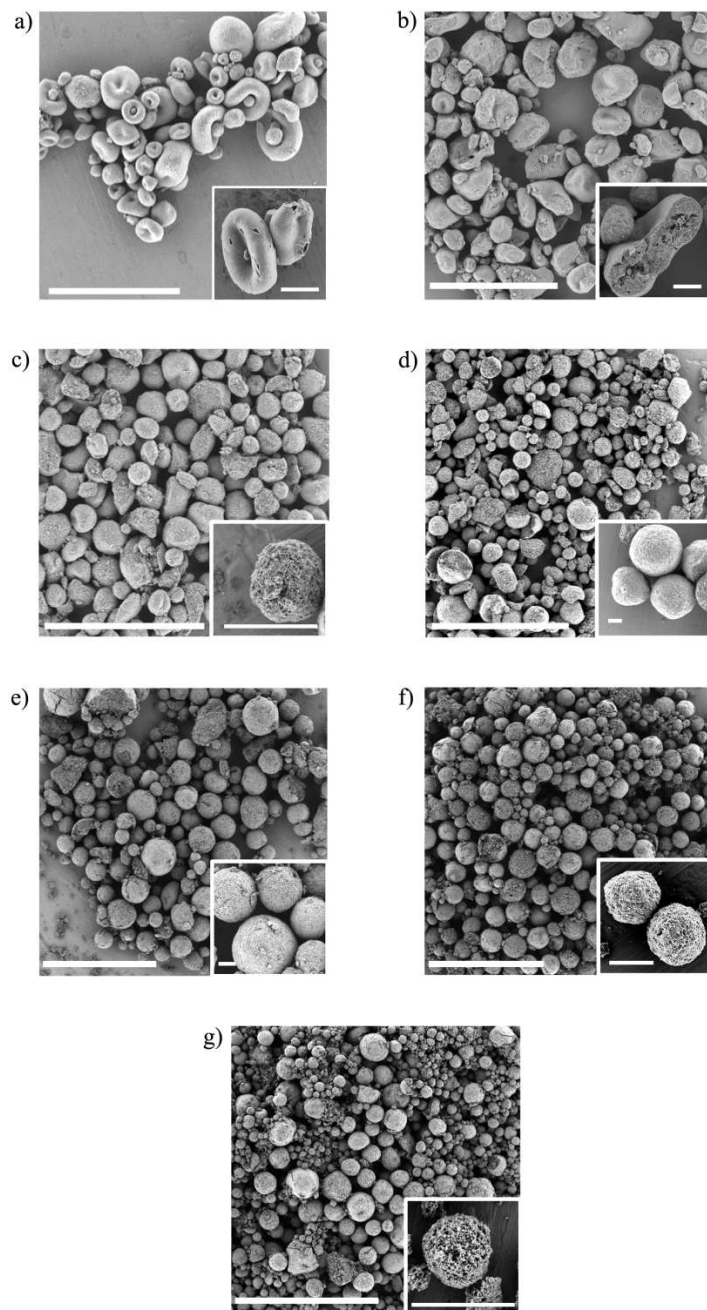


Fig.4.6: FESEM images of UiO-66-NH₂ beads synthesised using different concentrations of acetic acid in water (v/v %): a) 10 %, b) 20 %, c) 30 %, d) 40 %, e) 50 %, f) 60 % and g) 70 %. Scale bars: 30 μ m (a), 50 μ m (b-g) and 5 μ m (insets).

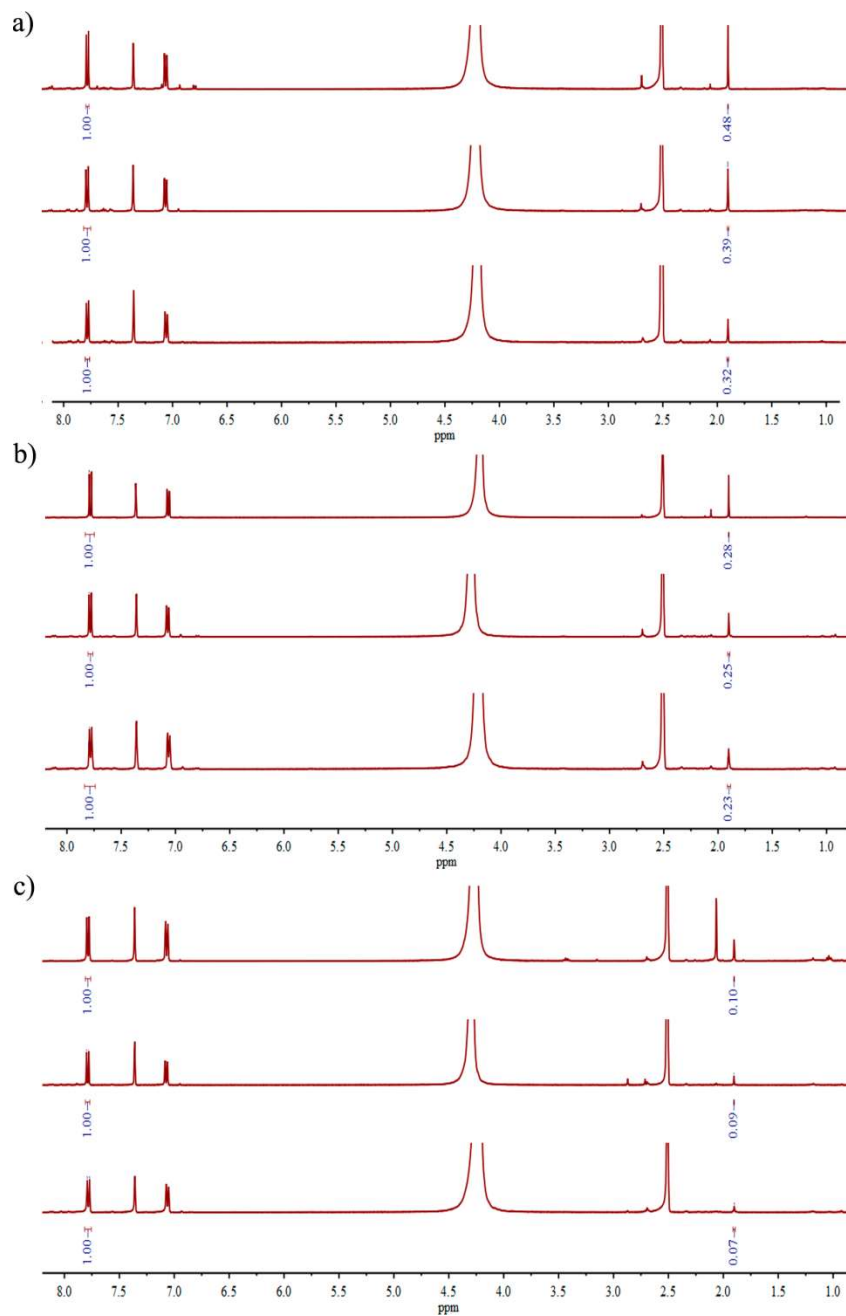


Fig.4.7: $^1\text{H-NMR}$ spectra of UiO-66-NH_2 synthesised using different concentrations of acetic acid in water (v/v %), after digestion with HF in DMSO-d_6 solution: (a) 10 %, (b) 20 % and (c) 30 %.

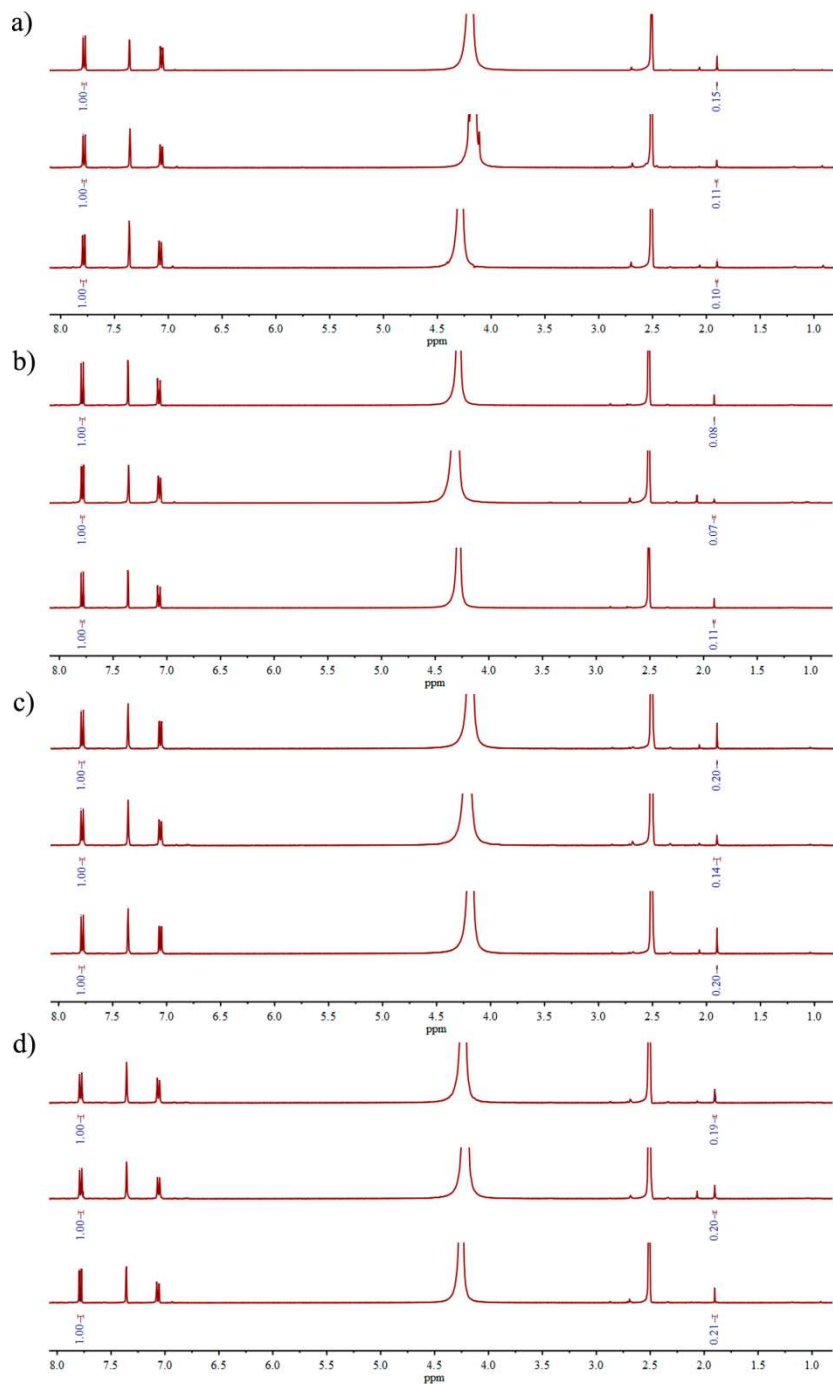


Fig.4.8: $^1\text{H-NMR}$ spectra of UiO-66-NH₂ synthesised using different concentrations of acetic acid in water (v/v %), after digestion with HF in DMSO-d₆ solution: (a) 40 %, (b) 50 %, (c) 60 % and (d) 70 %.

We measured the N₂ adsorption isotherms on all synthesised UiO-66-NH₂ (Fig.4.9). We found that, when using acetic acid at concentrations from 30% to 60%, the synthesised UiO-66-NH₂ beads exhibited the greatest mean values for S_{BET} (Fig.4.5b), consistent with their greater crystallinity. In this range, the maximum mean SBET was 1261 m² g⁻¹ at an acetic acid concentration of 30%, which is within the range reported for UiO-66-NH₂ samples synthesised in DMF or water using acids such as HCl.^{6,33}

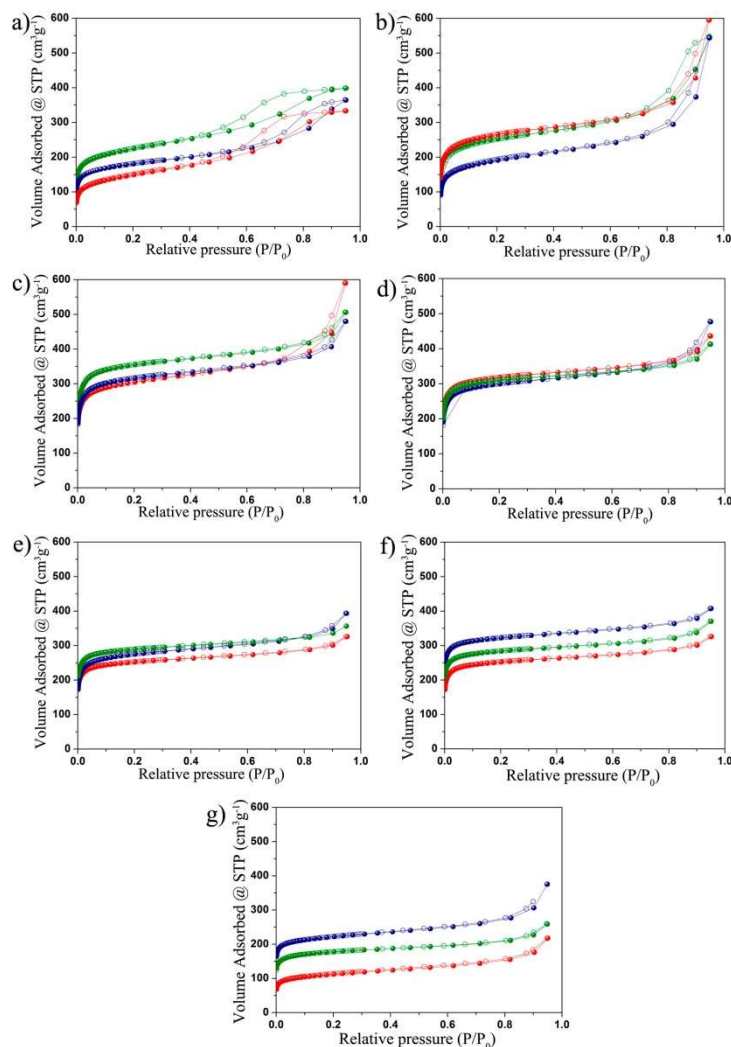


Fig.4.9: N₂ adsorption isotherms at 77 K for three different batches of UiO-66-NH₂ synthesised using concentrations of acetic acid in water (v/v %) (a) 10 % (mean: 678 m² g⁻¹), (b) 20 % (mean: 885 m² g⁻¹), (c) 30 % (mean: 1261 m² g⁻¹), (d) 40 % (mean: 1209 m² g⁻¹), (e) 50 % (mean: 1087 m² g⁻¹), (f) 60 % (mean: 1173 m² g⁻¹) and (g) 70 % (mean: 655 m² g⁻¹).

Likewise, the water sorption isotherms revealed that this range of acetic acid concentrations provided the greatest water uptake, with the highest value ($0.57 \text{ g}_{\text{water}} \text{ g}^{-1}$) seen also at an acetic acid concentration of 30%, as well as the expected S-type trend, centred at $0.2 P/P_0$ (Fig.4.5c, Fig.4.10).³⁴

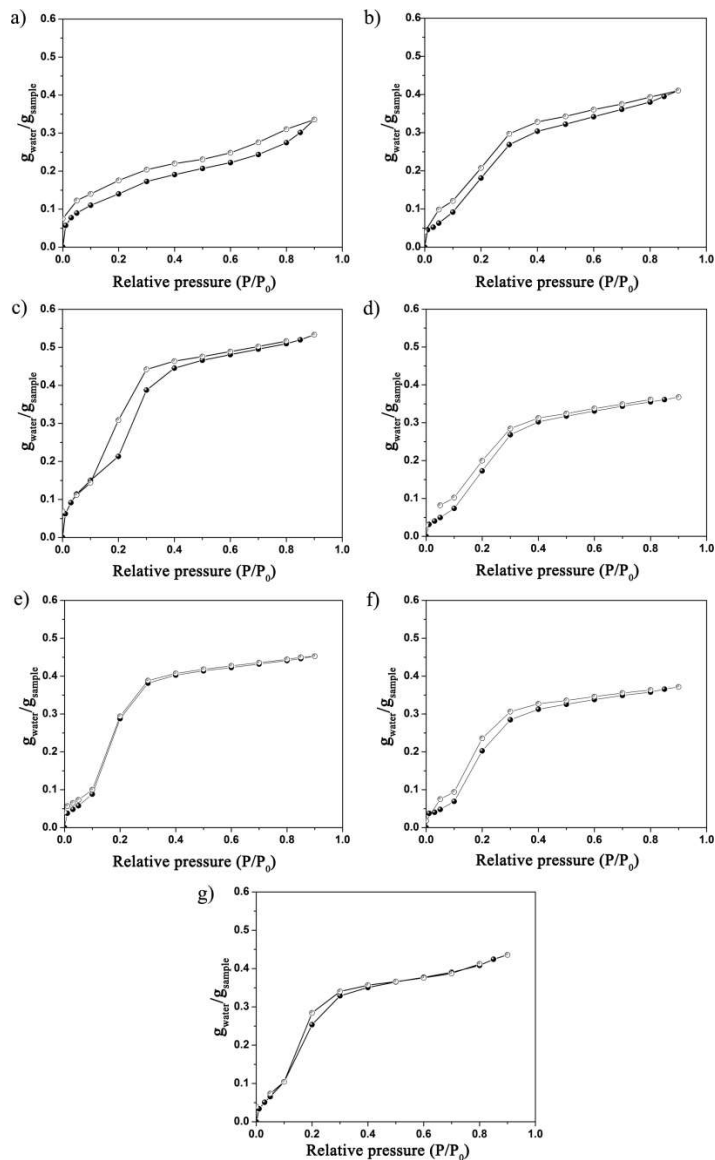


Fig.4.10: Water sorption and desorption isotherms at 25 °C for UiO-66-NH₂ synthesised at different concentrations of acetic acid in water (v/v): (a) 10 %, (b) 20 %, (c) 30 %, (d) 40 %, (e) 50 %, (f) 60 % and (g) 70 %.

4.3.3. Modulated aqueous synthesis of Zr-fumarate beads

Encouraged by these results, the aqueous continuous-flow spray-drying method to the synthesis of Zr-fumarate beads.^{19,35} We followed a synthetic protocol analogous to that which we had earlier used for UiO-66-NH₂, and studied the influence of the concentration of acetic acid on the production of Zr-fumarate beads. In this case, acetic acid concentration values of 10% and 60% both led to quasi-amorphous materials (Fig.4.11a). However, concentrations from 20% to 50% provided Zr-fumarate, as evidenced by XRPD (Fig.4.11 a). Here, FESEM revealed the formation of micron-sized spherical beads comprising nanoparticles of Zr-fumarate (Fig.4.11 b and Fig.4.12).

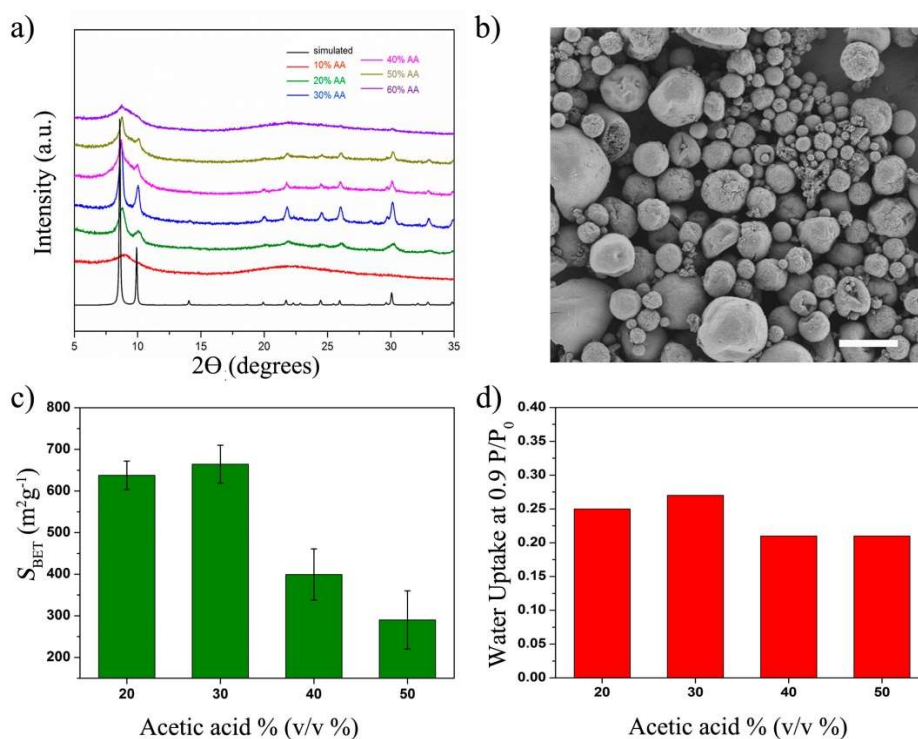


Fig.4.11: (a) XRPD diffractograms of Zr-fumarate synthesised using different amounts of acetic acid compared to the simulated powder pattern for Zr-fumarate (black). (b) Representative FESEM images of Zr-fumarate beads synthesised using a 30% of acetic acid. (c, d) S_{BET} values (c) and maximum water uptakes (d) of Zr-fumarate samples prepared using different amounts of acetic acid.

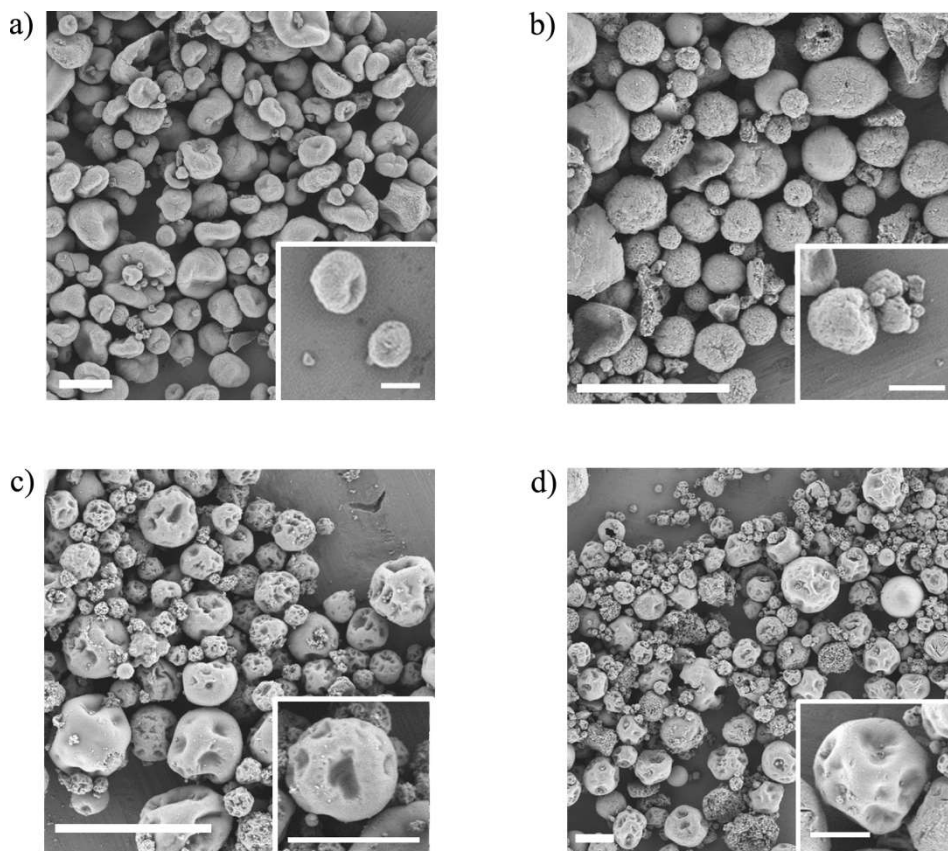


Fig.4.12: FESEM images of Zr-fumarate synthesised using different concentrations of acetic acid in water (v/v %): a) 20 %, b) 30 %, c) 40 % and d) 50 %. Scale bars: 10 μm , 5 μm (insets).

In this range, an acetic acid concentration of 30% provided optimal crystallinity (Table 4.4). All synthesised samples contained an acetate/fumarate molar ratio between 0.2–0.3, which perfectly agrees with those previously reported for this MOF (Fig.4.13).³¹

Table 4. 4: Full width at half maximum (FWHM) values of Zr-fumarate samples and particle domain sizes determined analogous to UiO-66-NH₂.

AA% used in the synthesis	FWHM	Particle size (nm) calculated by Scherrer Eqn.
20%	0.49	30
30%	0.33	72
40%	0.58	22
50%	0.60	21

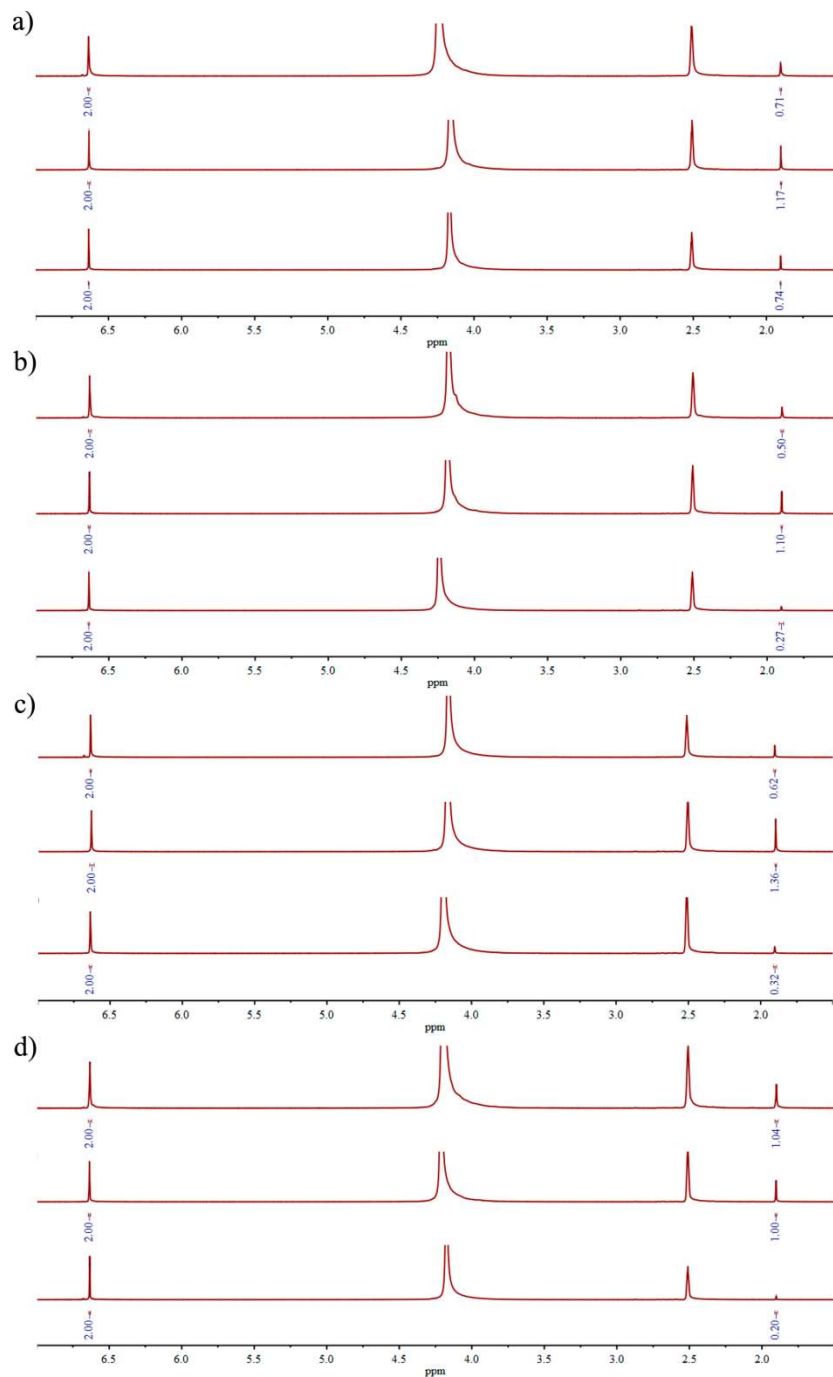


Fig.4.13: $^1\text{H-NMR}$ spectra of Zr-fumarate synthesised using different concentrations of acetic acid in water (v/v %), after digestion with HF in DMSO-d_6 solution: a) 20 %, b) 30 %, c) 40 % and d) 50 %.

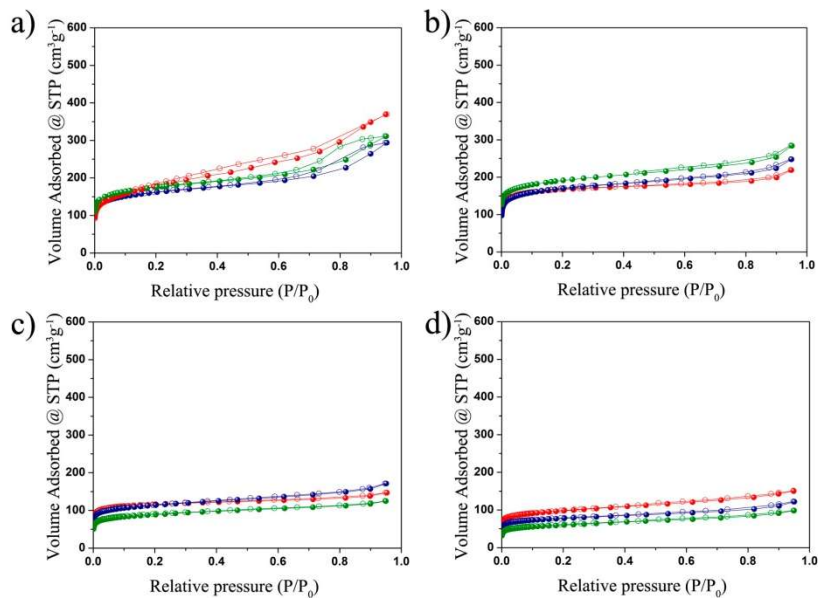


Fig.4.14: N_2 adsorption isotherms at 77 K for three different batches of Zr-fumarate synthesised using concentrations of acetic acid in water (v/v %) a) 20 % (mean: $637 \text{ m}^2 \text{ g}^{-1}$), b) 30 % (mean: $664 \text{ m}^2 \text{ g}^{-1}$), c) 40 % (mean: $399 \text{ m}^2 \text{ g}^{-1}$) and d) 50 % (mean: $290 \text{ m}^2 \text{ g}^{-1}$).

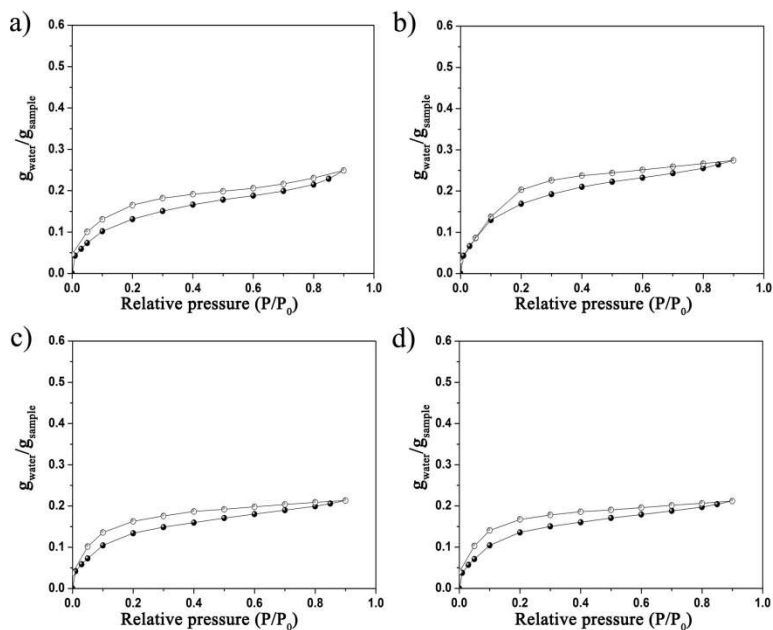


Fig.4.15: Water sorption and desorption isotherms at 25 °C for Zr-fumarate synthesised at different concentrations (v/v) of acetic acid in water: a) 20 %, b) 30 %, c) 40 % and d) 50 %.

The N₂ and water sorption isotherms showed that the quality of the synthesised Zr-fumarate beads correlated to their crystallinity (Fig.4.14). In fact, the maximum mean S_{BET} value (664 m² g⁻¹) was obtained at an acetic acid concentration of 30% (Fig.4.11c). This value was comparable to that previously reported for a water-batch synthesis,³¹ but lower than that reported for an aqueous continuous-flow synthesis (ca. 1000 m² g⁻¹).²⁹ Water-sorption studies revealed similar behaviour, with a maximum water uptake of 0.27 g_{water} g⁻¹ at an acetic acid concentration of 30% (Fig.4.11d). This value is slightly lower than that achieved for Zr-fumarate synthesised under hydrothermal conditions and a reaction time of 16 h (0.36 g_{water} g⁻¹).³⁶

4.3.4. Multi-gram synthesis of UiO-66-NH₂ beads

We next demonstrated the scalability of this aqueous synthesis by fabricating UiO-66-NH₂ beads on the multigram-scale (40 g; Fig.4.16 a). To this end, we employed the optimised conditions described above.

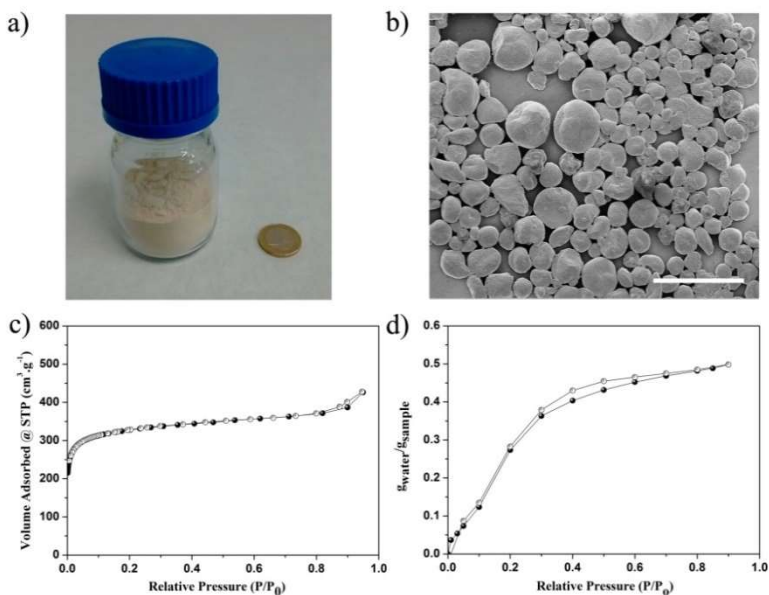


Fig.4.16: (a) Photograph of UiO-66-NH₂ (40 g) synthesized in optimized conditions. (b) FESEM images showing the UiO-66-NH₂ microbeads synthesized at the gram scale. The scale bar is 30 μm. (c) N₂ adsorption (filled dots) and desorption (empty dots) isotherms at 77 K for UiO-66-NH₂ microbeads. (d) Water adsorption (filled dots) and desorption (empty dots) isotherms for UiO-66-NH₂ beads.

Thus, 792 mL of a 0.2 M equimolar mixture of ZrOCl₂·8H₂O and BDC-NH₂ in acetic acid in water (30% v/v) were injected into the coil-flow reactor

(T_c : 90 °C) at a liquid-feed rate (Q_{lf}) of 2.4 mL min⁻¹, and then spray-dried at a flow rate (Q_{dg}) of 336 mL min⁻¹ and an inlet temperature (T_{in}) of 150 °C for 5.5 h. After washing and drying, the resulting UiO-66-NH₂ beads (40 g; yield: 85%; Fig.4.16b) showed an S_{BET} value of 1270 m² g⁻¹ and a total water uptake of 0.49 g_{water} g⁻¹ (Fig.4.16c and d). These values are similar to those obtained in the milligram-scale synthesis. Additionally, we confirmed the long-term stability of the fabricated beads by comparing the XRPD patterns and S_{BET} values of a freshly prepared sample and a 1-year-old sample. We did not observe any significant differences between the two samples (Fig.4.17).

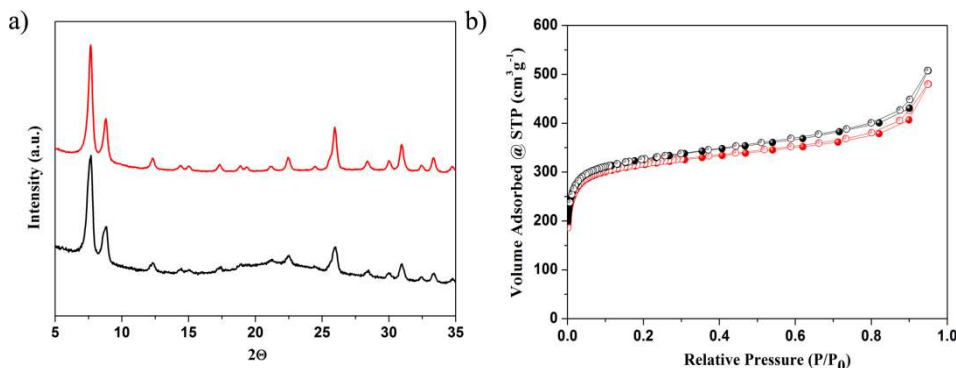


Fig.4.17: XRPD patterns (a) and N₂ adsorption isotherms (b) for freshly prepared (black) and one-year aged (red) UiO-66-NH₂ beads.

4.4. Conclusions

This work developed a continuous-flow spray-drying method for aqueous production of two representative Zr-MOFs: UiO-66-NH₂ and Zr-fumarate. For both Zr-MOFs, a modulator (acetic acid) concentration of 30% (v/v in water) was found to be optimum, as it yielded microbeads whose S_{BET} and water-uptake values were comparable to the literature values obtained using other methods. In addition, this method obviates post-synthetic shaping methods, which usually reduce the porosity of MOFs. Lastly, as a proof-of-concept on the scalability of our spray-drying approach it was used to fabricate several grams of UiO-66-NH₂ beads. Thus, this work opens the possibility of using spray-drying, a mature process already integrated in many industrial sectors, as a green method for the continuous one-step fabrication of shaped MOF microbeads.

4.5. References

1. N. C. Burtch, H. Jasuja and K. S. Walton, *Chem. Rev.*, 2014, 114, 10575–10612.
2. B. S. Gelfand and G. K. H. Shimizu, *Dalton Trans.*, 2016, 45, 3668–3678.
3. Y.-H. Shih, Y.-C. Kuo, S. Lirio, K.-Y. Wang, C.-H. Lin and H.-Y. Huang, *Chem. Eur. J.*, 2017, 23, 42–46.
4. P. A. Bayliss, I. A. Ibarra, E. Perez, S. Yang, C. C. Tang, M. Poliakoff and M. Schröder, *Green Chem.*, 2014, 16, 3796–3802.
5. T. Didriksen, A. I. Spjelkavik and R. Blom, *J. Flow Chem.*, 2017, 7, 13–17.
6. H. Reinsch, S. Waitschat, S. M. Chavan, K. P. Lillerud and N. Stock, *Eur. J. Inorg. Chem.*, 2016, 27, 4490–4498.
7. A. S. Munn, P. W. Dunne, S. V. Y. Tang and E. H. Lester, *Chem. Commun.*, 2015, 51, 12811–12814.
8. A. Garcia Marquez, P. Horcajada, D. Grosso, G. Ferey, C. Serre, C. Sanchez and C. Boissiere, *Chem. Commun.*, 2013, 49, 3848–3850.
9. A. Carné-Sánchez, I. Imaz, M. Cano-Sarabia and D. MasPOCH, *Nat. Chem.*, 2013, 5, 203–211.
10. L. Garzon-Tovar, M. Cano-Sarabia, A. Carne-Sanchez, C. Carbonell, I. Imaz and D. MasPOCH, *React. Chem. Eng.*, 2016, 1, 533–539.
11. V. Guillerm, L. Garzon-Tóvar, A. Yazdi, I. Imaz, J. Juanhuix and D. MasPOCH, *Chem. – Eur. J.*, 2017, 23, 6829–6835.
12. L. Garzón-Tovar, J. Pérez-Carvajal, I. Imaz and D. MasPOCH, *Adv. Funct. Mater.*, 2017, 27, 1606424.
13. T. H. Kim and S. G. Kim, *Saf. Health Work*, 2011, 2, 97–104.
14. K.-W. Kim and Y. H. Chung, *Toxicol. Res.*, 2013, 29, 187–193.
15. K. C. A. Bromley-Challenor, N. Caggiano and J. S. Knapp, *J. Ind. Microbiol. Biotechnol.*, 2000, 25, 8–16.
16. C. A. Redlich, W. S. Beckett, J. Sparer, et al., *Ann. Intern. Med.*, 1988, 108, 680–686.
17. J. H. Cavka, S. Jakobsen, U. Olsbye, N. Guillou, C. Lamberti, S. Bordiga and K. P. Lillerud, *J. Am. Chem. Soc.*, 2008, 130, 13850–13851.
18. X. Liu, N. K. Demir, Z. Wu and K. Li, *J. Am. Chem. Soc.*, 2015, 137, 6999–7002.
19. H. Kim, S. Yang, S. R. Rao, S. Narayanan, E. A. Kapustin, H. Furukawa, A. S. Umans, O. M. Yaghi and E. N. Wang, *Science*, 2017, 356, 430–434.

20. G. C. Shearer, S. Chavan, S. Bordiga, S. Svelle, U. Olsbye and K. P. Lillerud, *Chem. Mater.*, 2016, 28, 3749–3761.
21. T. Tian, J. Velazquez-Garcia, T. D. Bennett and D. Fairen-Jimenez, *J. Mater. Chem. A*, 2015, 3, 2999–3005.
22. J. Dhainaut, C. Avci-Camur, J. Troyano, A. Legrand, J. Canivet, I. Imaz, D. Maspoch, H. Reinsch and D. Farrusseng, *CrystEngComm*, 2017, 19, 4211–4218.
23. D. Crawford, J. Casaban, R. Haydon, N. Giri, T. McNally and S. L. James, *Chem. Sci.*, 2015, 6, 1645–1649.
24. I. Stassen, M. Styles, T. Van Assche, N. Campagnol, J. Fransaer, J. Denayer, J.-C. Tan, P. Falcaro, D. De Vos and R. Ameloot, *Chem. Mater.*, 2015, 27, 1801–1807.
25. P. M. Schoenecker, G. A. Belancik, B. E. Grabicka and K. S. Walton, *AIChE J.*, 2013, 59, 1255–1262.
26. O. G. Nik, X. Y. Chen and S. Kaliaguine, *J. Membr. Sci.*, 2012, 413, 48–61.
27. S. Diring, S. Furukawa, Y. Takashima, T. Tsuruoka and S. Kitagawa, *Chem. Mater.*, 2010, 22, 4531–4538.
28. T. Tsuruoka, S. Furukawa, Y. Takashima, K. Yoshida, S. Isoda and S. Kitagawa, *Angew. Chem., Int. Ed.*, 2009, 121, 4833–4837.
29. H. Reinsch, S. Waitschat, S. M. Chavan, K. P. Lillerud and N. Stock, *Eur. J. Inorg. Chem.*, 2016, 27, 4490–4498.
30. S. Waitschat, H. Reinsch and N. Stock, *Chem. Commun.*, 2016, 52, 12698–12701.
31. Z. Hu, I. Castano, S. Wang, Y. Wang, Y. Peng, Y. Qian, C. Chi, X. Wang and D. Zhao, *Cryst. Growth Des.*, 2016, 16, 2295–2301.
32. M. R. DeStefano, T. Islamoglu, S. J. Garibay, J. T. Hupp and O. K. Farha, *Chem. Mater.*, 2017, 29, 1357–1361.
33. F. Jeremias, V. Lozan, S. K. Henninger and C. Janiak, *Dalton Trans.*, 2013, 42, 15967–15973.
34. J. Canivet, J. Bonnefoy, C. Daniel, A. Legrand, B. Coasne and D. Farrusseng, *New J. Chem.*, 2014, 38, 3102–3111.
35. J. Ren, N. M. Musyoka, H. W. Langmi, B. C. North, M. Mathe, X. Kang and S. Liao, *Int. J. Hydrogen Energy*, 2015, 40, 10542–10546.
36. Y. J. Bae, E. S. Cho, F. Qiu, D. T. Sun, T. E. Williams, J. J. Urban and W. L. Queen, *ACS Appl. Mater. Interfaces*, 2016, 8, 10098–10103.

CHAPTER 5

Systematic Study of the Impact of
MOF Densification into Tablets on
Textural and Mechanical Properties

This chapter is based on the following article:

Jeremy Dhainaut, Ceren Avci-Camur, Javier Troyano, Alexandre Legrand, Jerome Canivet, Inhar Imaz, Daniel Maspoch, Helge Reinsch and David Farrusseng. (2017) CrystEngComm. 19, 4211-4218.

5.1. Introduction

Typically, synthesis processes such as batch processes under hydrothermal conditions,¹ or continuous flow processes using water as solvent,² and even solvent-free continuous processes³ lead to the production of MOFs as loose powders. However, and except in very rare cases, their applications require bodies with a specific shape such as tablets, extrudates, granulates, monoliths or coatings to cite only the most common forms. For example, in catalysis, one of the usual forms is tablets which are obtained by pressing powders. Such bodies shall present mechanical resistance to attrition and hydrostatic pressure, while preserving as much as possible the original pore structure. Bazer-Bachi *et al.* reported the catalytic conversion of vegetable oil using ZIF-8 tablets which were as active as loose ZIF-8 powders, paving the way for further application of shaped MOFs in catalysis.⁴ On the other hand, for gas storage, it is of utmost importance to fill the storage tanks with the largest amount of adsorbents. The void fraction within the adsorbent bed is a critical factor to control in the design of an adsorbent independently of its composition or structure.^{5,6} Therefore, MOFs should be pressed into solids of high density such as tablets in order to maximize their volumetric uptake.

Despite important efforts for the development of shaping processes suitable for MOFs, challenges linked to their intrinsic fragility remain.⁷ Limitations can be listed into three categories: (i) relatively low thermal stability with respect to oxides, impeding the use of classical shaping processes which are based on firing a binder-containing formulation after pelletization;⁸ (ii) relatively low chemical stability in the presence of solvents, including water, making extrusion processes not generalisable;⁹ and (iii) relatively low mechanical stability owing to their very high porosity and flexibility, leading to structural collapse when the applied pressure exceeds a given threshold.¹⁰

When taking these limitations into account, mild pelletization by compression appears to be a practical solution for MOFs as it overcomes firing issues and the use of solvent while limiting the structural collapse. Two review articles dealing with MOF densification have made a quite exhaustive inventory in the field, which will not be discussed here.¹¹ Nevertheless, it was concluded that tablets could be obtained by compressing binderless, pure MOF powders.¹² The use of binders such as alumina, silica, graphite, or polyvinyl alcohol was also reported to reduce the structure degradation observed when even moderate

strength is applied, but they also decrease the tablets' overall porosity proportionally.

The optimisation of MOF densification consists of finding a compromise between a gain in mechanical stability of their body and a loss of their initial properties. Ideally, the structural and textural properties of the MOF crystals should be preserved while the tablet density should be as high as possible. For example, Nandasiri *et al.* proposed an optimal tablet density of about 0.5 g cm^{-3} for MOF-5 and MIL-101(Cr) while maintaining their initial porosity.¹³ Similar binderless densification of other MOFs among the most studied, namely ZIF-8,⁴ UiO-66,⁹ UiO-66-NH₂,^{10,14} and HKUST-1,^{4,14} has already been reported. However, the tablet density increase comes with lower textural properties. This is especially the case of HKUST-1, which already collapses at modest applied pressure.

While those works pave the way for the further development of MOFs, parameters related to the shaping itself, such as the compression ramp speed and dwell time are rarely reported, although they can have tremendous importance for the final tablet properties. More surprisingly, very few mechanical tests were made although the tablets were usually reported as robust. As a result, the lack of standardization in densification studies prevents comparing mechanical stability and textural properties from one MOF to another. In addition, we may wonder whether conclusions of MOF structural stability drawn from densification data can be given when an all-or-nothing compression type is applied.

In this chapter, a systematic study based on quantitative descriptors for the densification of UiO-66, UiO-67, UiO-66-NH₂ and HKUST-1 using a R&D tableting machine was performed. To this end, the impact of the compression step on the textural properties (namely the specific surface area and the micropore volume), the bulk density and the mechanical resistance of the resulting tablets were measured. In contrast to the general statement claiming that HKUST-1 can hardly be densified, we show here that robust tablets of HKUST-1 can be obtained without significant degradation of its microporous structure. In addition, we have investigated the use of a low content of expanded natural graphite (ENG) as a dried binder. Finally, we investigated the stability of our tablets after four months in the presence of moisture.

5.2. Experimental Section

5.2.1. Synthesis of MOFs

Synthesis of UiO-66

UiO-66 was prepared based on a protocol proposed by Kim *et al.*¹⁶ A DMF solution with a molar composition of zirconium chloride : terephthalic acid : hydrochloric acid = 1:1:1 was heated at 120 °C for 24 h under stirring. The solid product was recovered by filtration and washed twice with DMF. The remaining solvent entrapped inside the powder was exchanged first with ethanol and then with acetone, using Soxhlet extraction. Finally, UiO-66 was activated under vacuum at 150 °C for 12 h.

Synthesis of UiO-67

UiO-67 was prepared based on a protocol proposed by Shearer *et al.*¹⁸ A DMF solution with a molar composition of zirconium chloride : 4,4'-biphenyldicarboxylic acid : water : benzoic acid = 1:1:1.3:5 was heated at 120 °C for 24 h under stirring. The solid product was recovered by centrifugation and washed three times with DMF, three times with ethanol, and three times with acetone. Finally, UiO-67 was activated under vacuum at 60 °C for 12 h.

Synthesis of UiO-66-NH₂

UiO-66-NH₂ was synthesized using a spray-drying continuous flow method.¹⁸ A precursor suspension of 0.22 M ZrOCl₂·8H₂O and 0.20 M 2-aminoterephthalic acid in a 24 mL mixture of water and acetic acid (1 : 1) was injected into a coil flow reactor at a feed rate of 2.4 mL min⁻¹ and at a temperature of 90 °C. The residence time inside the coil flow reactor was 63 s. The resulting pre-heated solution was then spray-dried in a Mini Spray Dryer B-290 (Büchi Labortechnik) at a flow rate of 336 ml min⁻¹ and an inlet air temperature of 150 °C, using a spray cap with a 0.5 mm-diameter hole, affording a yellow powder. This powder was then redispersed in ethanol and collected by centrifugation. The two-step washing process was repeated with acetone. The final product was dried for 12 h at 60 °C in air. This dried powder was finally activated under vacuum at 200 °C for 6 h (temperature slope of 4 °C min⁻¹).

Synthesis of HKUST-1

HKUST-1 was prepared using the spray-drying technology.¹⁹ A solution of 0.90 M Cu(NO₃)₂·2.5H₂O and 0.60 M 1,3,5-benzenetricarboxylic acid in 135 mL of a mixture of DMF, ethanol and water (1 : 1: 1) was spray-dried in a Mini

Spray Dryer B-290 (Büchi Labortechnik) at a feed rate of 4.5 mL min⁻¹, a flow rate of 336 ml min⁻¹ and an inlet air temperature of 180 °C, using a spray cap with a 0.5 mm-diameter hole, affording a blue powder. This powder was then redispersed in ethanol and precipitated by centrifugation. The two-step washing process was repeated with acetone. The final product was dried for 12 h at 60 °C in air. This dried powder was finally activated under vacuum at 150 °C for 12 h (temperature slope of 4 °C min⁻¹).

5.2.2. Densification method and body characterization

A Medel'Pharm STYL'ONE Evolution tableting instrument was used for the shaping purpose. Prior to compression, the powders were deagglomerated by grinding. The die was then filled at constant volume with 150 mg (UiO-67), 200 mg (UiO-66) or 300 mg (HKUST-1, UiO-66-NH₂) of the MOF powder. A punch diameter of 1.128 cm was used, allowing a tableting surface of 1.00 cm². Asymmetric compression, where the penetration of the upper punch was fixed at 2 mm, was used. From the moment the punches reached the powder filling height (h_0), a compression time of about 4 s was applied to reach a specified thickness following a constant displacement rate. This displacement rate is thickness-dependent. Then the compression was held for 400 ms, before the punches went back to h_0 within 4 s. To avoid any residue on the internal die surface, some cellulose was pressed between two MOF tablets.

After shaping, physical parameters of MOF tablets were measured using a Pharmatron SmartTest 50. These parameters include the weight, thickness, and diameter, allowing calculating the tablet bulk density. The same apparatus was also used to evaluate the tensile strength, by pressing the side of the tablets at a constant 1 mm s⁻¹ displacement rate until a first load drop was detected. Such pressed tablets were usually split into two halves. The degree of densification is reported here as a percentage of the crystal density, which is in theory the highest density that can be achieved for a crystal. Similarly, the specific surface area (S_{BET}) of the tablet was expressed as a percentage of the initial powder. The SSA is a relevant quantitative indicator, as a loss of S_{BET} after compression indicates a partial collapse of the porous structure. Alternatively, the micropore volume can be used equally as a quantitative descriptor of the degradation of the porous networks (Table 5.1).

The main advantage in using these indicators is that they are non-dimensional, bounded between 0 and 100% and hence, can be used to compare MOFs regardless of their intrinsic properties. It is also provided a novel

descriptor called volumetric capacity (V_{cap}), which shall be relevant especially for gas storage applications. The positive effect of the shaping method is characterized by a higher volumetric capacity as compared to that of the initial powder. Moreover, the higher this descriptor is, the better the tablets shall perform for gas storage applications, until an optimum value is reached.

Table 5. 1: Textural properties and resulting volumetric surface of all MOF tablets.

MOF	Pressure (MPa)	Tensile strength (MPa)	S_{BET} (m^2/g)	V_{micro} (cm^3g^{-1})	Bulk density (g/cm^3)	Density (%crystal)	V_{surf} (m^2cm^{-3})	V_{cap} (cm^3cm^{-3})
UiO-66	As-made powder		1426	0.54	0.17	14.0%	242	0.09
	9	0.24	1382	0.47	0.38	31.3%	525	0.18
	18	0.40	1459	0.54	0.43	35.4%	627	0.23
HKUST-1	As-made powder		1288	0.49	0.48	40.0%	618	0.24
	14	0.15	1191	0.43	0.67	55.8%	798	0.29
	24	0.24	1145	0.42	0.70	58.3%	802	0.29
	62	0.78	1133	0.42	0.79	65.8%	895	0.33
	121	1.78	1091	0.40	0.90	75.0%	982	0.36
HKUST-1 + 1wt% ENG	As-made powder		1246	0.46	0.48	40.0%	598	0.22
	14	0.13	1206	0.45	0.68	56.7%	820	0.31
	65	0.91	1137	0.42	0.80	66.7%	910	0.34
	120	1.74	1086	0.40	0.90	75.0%	977	0.36
HKUST-1 + 2wt% ENG	As-made powder		1105	0.42	0.48	40.0%	530	0.20
	23	0.37	1049	0.40	0.71	59.2%	745	0.28
	57	0.99	1006	0.38	0.81	67.5%	815	0.31
	112	1.80	949	0.35	0.93	77.5%	883	0.33
UiO-67	As-made powder		2034	0.90	0.25	35.3%	509	0.23
	17	0.56	1904	0.80	0.39	55.1%	743	0.31
	41	1.28	1832	0.76	0.51	72.0%	934	0.39
	63	2.22	1549	0.70	0.62	87.6%	960	0.43
	82	-	397	0.22	0.70	98.9%	278	0.15
UiO-66-NH₂	As-made powder		842	0.34	0.41	32.4%	345	0.14
	14	0.24	816	0.33	0.50	39.6%	408	0.17
	26	0.46	796	0.32	0.49	38.8%	390	0.16
	57	1.48	697	0.29	0.72	57.0%	502	0.21
	164	4.18	625	0.25	0.93	73.6%	581	0.23

5.2.3. Structure and porosity characterization

PXRD patterns were recorded on a Bruker D8 advance diffractometer using a $\text{CuK}\alpha$ radiation source and a Lynx-Eye detector. Nitrogen adsorption isotherms were measured at 77 K on a BELSORP-mini device from BEL Japan. The samples were outgassed at 150 °C overnight prior to measurement. S_{BET} were determined using the BET method. The micropore volume (V_{micro}) was evaluated from the adsorbed volume of N_2 at $P/P_0 = 0.3$. In order to calculate the bulk density of the tablets, dry masses were estimated from thermogravimetric (TG) analyses measured on a Mettler Toledo TGA-DSC1 using reconstituted air (Fig.5.1 and Table 5.2). Linker defects were also evaluated from TGA, assuming that the remaining weight at 800 °C corresponds to the metal oxide, namely ZrO_2 (UiO-) or CuO (HKUST-1). This allows to determine directly the theoretical weight of a dehydroxylated MOF structure $\text{Zr}_6\text{O}_6(\text{linker})_6$ and Cu_3BTC_2 , which is compared to the experimental remaining weight after solvent loss and dehydroxylation (taking metal oxidation into account). The weight difference is thus attributed to linker defects. This method doesn't take possible cluster defects into account. Powder bulk density, also called tap density, was determined by adding a known mass of deagglomerated MOF powder into a vial with a high height/diameter ratio. Then, the vial was repetitively hit on a hard surface until no more volume change could be observed – generally a few hundred times-, thus allowing measuring the packed bed dimensions. Scanning electron microscopy (SEM) was performed on a Hitachi S-4800.

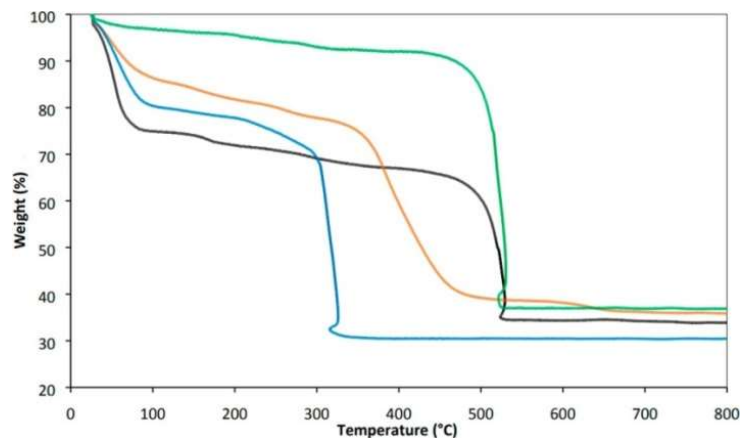


Fig.5.1: Thermogravimetric analyses of as-made MOF powders: UiO-66 (black), UiO-66-NH₂ (orange), UiO-67 (green) and HKUST-1 (blue).

Table 5. 2: Weight losses from TGA and corresponding linker defects of as-made MOF powders.

MOF	Solvent and dehydroxylation	Linker	Remaining metal oxide	Linker defects
UiO-66	33%	33%	34%	17%
UiO-66-NH ₂	23%	38%	39%	25%
UiO-67	8%	55%	37%	17%
HKUST-1	28%	28%	30%	10%

5.3. Results and Discussion

5.3.1. Influence of compression on MOF tablet properties

The impact of the densification step on the final tablet properties including density, S_{BET} and tensile strength is presented in Fig.5.2 First, we can see that the tap densities of MOF powders are very low with respect to their corresponding crystal density: it is only 14% for UiO-66, and the highest value is obtained for HKUST-1 with a relative density of 40%. It can be also noted that while being isostructural to UiO-66, the UiO-66-NH₂ tap density reaches 32% of its crystal density. Here, the difference between these two isostructural MOFs is partly due to the synthesis protocol.

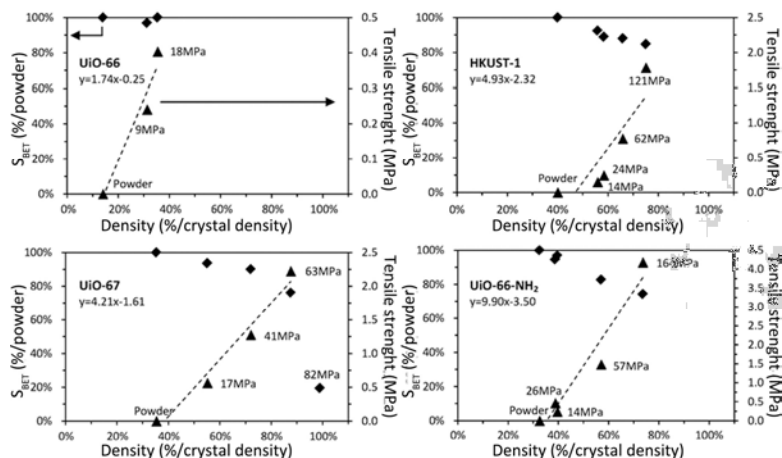


Fig.5.2: Impact of the degree of compression on the textural properties (rhombus) and mechanical strength (triangle) for tablets of UiO-66, HKUST-1, UiO-67 and UiO-66-NH₂. Applied pressures are indicated for each tablet, and the linear relationship tensile strength = f(relative density) is reported. For UiO-67, the tensile strength was not measured above 63 MPa as the structure collapsed.

All MOF tablets were characterized by SEM. Small and rounded crystals of HKUST-1 (Fig.5.3) and UiO-66-NH₂ (Fig.5.4) were observed.

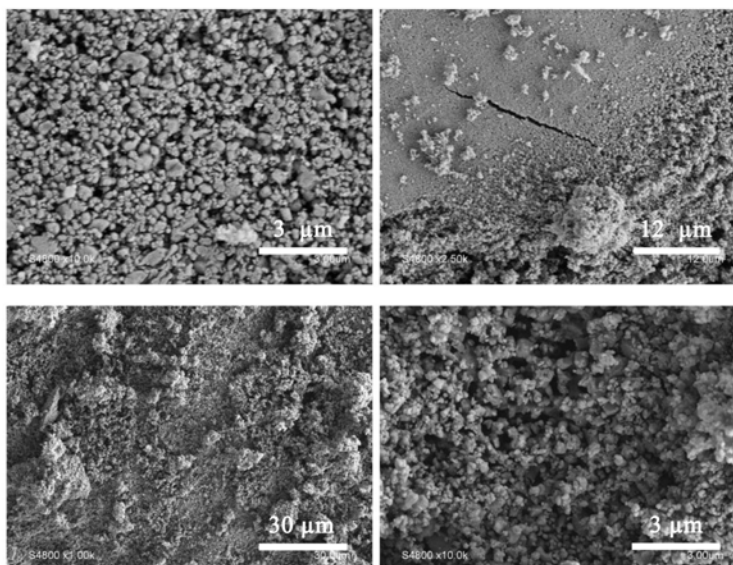


Fig.5.3: SEM images of HKUST-1 optimized tablet on its flat surface (top left), at the fracture (top right), and on its fractured section (bottom).

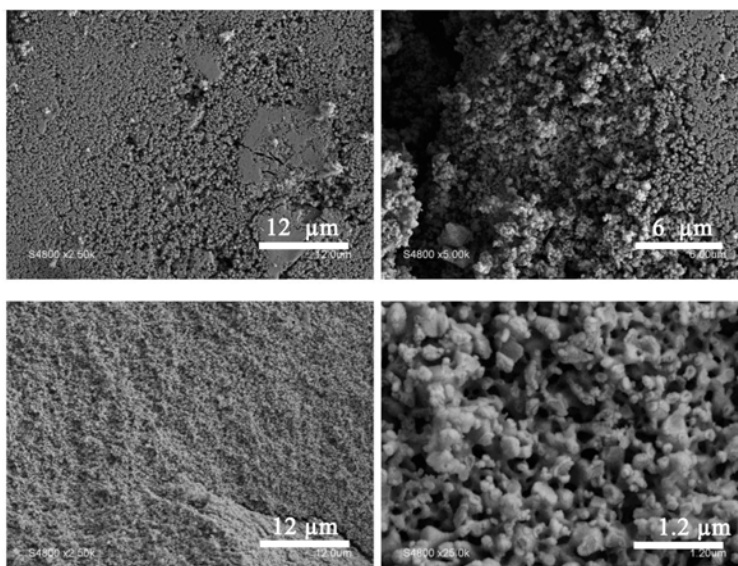


Fig.5.4: SEM images of UiO-66-NH₂ optimized tablet on its flat surface (top left), at the fracture (top right), and on its fractured section (bottom).

No large agglomerate usually produced by spray-drying can be seen,^{18,19} meaning that grinding was successful at deagglomerating. UiO-67 prepared by a solvothermal method leads to micrometric crystals with a bipyramidal shape (Fig.5.5). The latter is typical of the isostructural Zr-based series. While also being a part of this series, UiO-66 crystals are small and rounded (Fig.5.6). This is however in accordance with previous results.¹⁶ Moreover, the SEM images reveal that densification occurs more notably at the surface in contact with the punches.

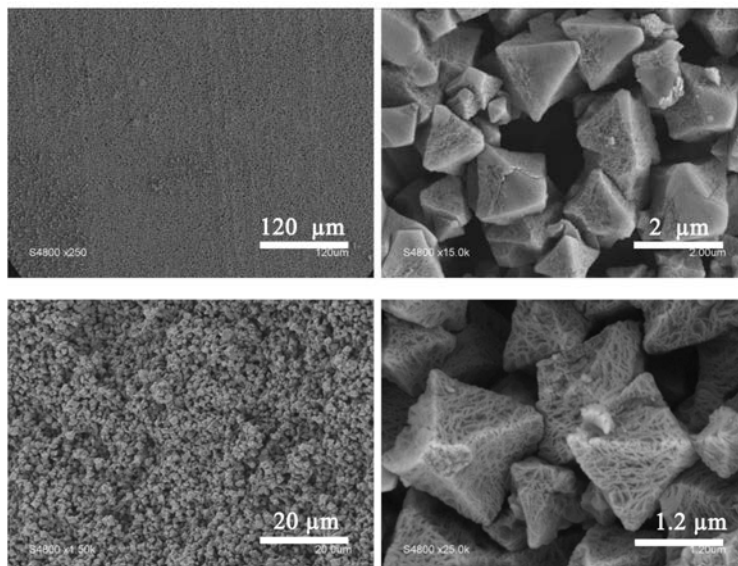


Fig.5.5: SEM images of UiO-67 optimized tablet on its flat surface (top), and on its fractured section (bottom).

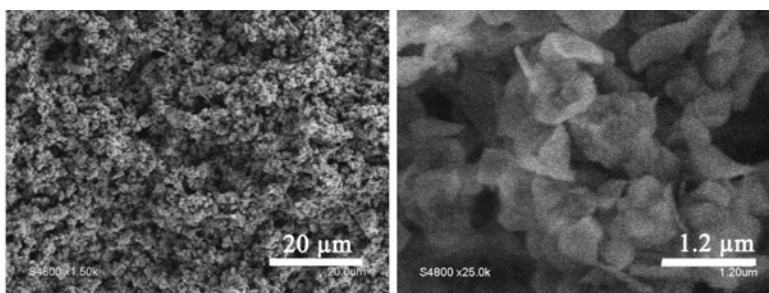


Fig.5.6: SEM images of UiO-66 optimized tablet on its fractured section.

For all studied MOFs, compression can yield tablets with twice higher density than their corresponding powders, while preserving more than 70% of

their initial S_{BET} . For instance, HKUST-1, which has a reputation of being fragile, was densified to 75% of its crystal density while preserving 80% of its initial textural properties when pressed at 121 MPa. One may note that the densest random packing of spheres is about 64 to 74% of their three-dimensional volume.²⁰ Surprisingly, we achieved here comparable values while limiting the loss of textural properties.

As expected, the higher the applied pressure, the higher the achieved densification. More interestingly, we observe a linear relationship between densification and tensile strength for all four studied MOFs below 80% relative density, with a slope being MOF-dependent. To the best of our knowledge, it is the first time that this behaviour is reported.

Obviously, the densification level or the tensile strength cannot be enhanced by an ever increasing applied pressure without leading to porous structure collapse. When the highest density is sought, the loss of microporosity should be as reduced as possible; otherwise, it will affect the tablets' ultimate performances. For UiO-66, no loss of S_{BET} has been observed until 40% relative density, which is the highest level we have investigated as the aim was to reach a mechanical resistance high enough for further production of grains. This does not imply that a higher level of densification cannot be obtained without damaging the porous structure. For other studied MOFs, a modest but somehow linear decrease can be observed with increasing densification. Again, the decreasing rate is MOF-dependent.

Zr-based MOFs are known for their high mechanical and thermal stabilities owing to their 12-fold connected clusters in the three spatial directions.^{21,22} These stabilities can be compromised by the number of missing linkers per node – usually about 2;^{23,24} however, the addition of monocarboxylic acids during the synthesis of UiO-66 proved to enhance its stability.²⁵ UiO-66 and UiO-67 powders prepared by solvothermal synthesis present 17% missing linkers per node (2 out of 12), which is comparable to the literature data.^{24,26} Although UiO-67 possesses the same topology as UiO-66 and the same degree of defects, its mechanical stability under compression is relatively modest as the porous structure collapses between 63 and 82 MPa (S_{BET} loss of about 80%). This is in line with prior studies.^{24,27} Here, we can safely assume that the reason for this collapsing is due to the very high densification degree already reached, beyond 90%, coupled with the very low flexibility of the framework.²⁸

In summary, when MOF powders are pressed into tablets, up to a two-fold bulk density can be achieved at the expense of slightly reduced textural properties. For the production of MOF solids for catalysis, one may press a tablet only to reach an industrially-relevant tensile strength above 0.1 MPa,²⁹ thus limiting the impact of shaping on the gravimetric uptake.

In the case of gas storage and without precluding neither a specific gas nor application conditions, we can foresee that the densification level which would offer the greatest micropore volume per unit of volume should perform better assuming that the interaction is mainly van der Waals. We have calculated the volumetric capacity descriptor by multiplying the tablet microporous volume by their bulk density. This descriptor V_{cap} , presented in Table 5.3, is expressed in cubic centimetre of pore volume per cubic centimetre of tablet (cm^3/cm^3). It can be pointed out that the micropore volume is correlated to the specific surface area and as a consequence, either one or the other can be used as descriptors (Fig.5.7).

Table 5. 3: Textural properties and resulting volumetric capacity of optimized MOF tablets.

MOF	Form	Applied pressure (MPa)	S_{BET} (m^2/g)	V_{micro} (cm^3/g)	Crystal density (g/cm^3)	Bulk density (g/cm^3)	Tensile strength (MPa)	V_{cap} (cm^3/cm^3)
UiO-66	Powder	-	1426	0.54	1.21	0.17	-	0.09
	Tablet	18	1459	0.54		0.43	0.40	0.23
UiO-66-NH ₂	Powder	-	839	0.34	1.26	0.41	-	0.14
	Tablet	164	625	0.25		0.93	4.18	0.23
UiO-67	Powder	-	2034	0.90	0.71	0.25	-	0.23
	Tablet	63	1549	0.70		0.62	2.22	0.43
HKUST-1	Powder	-	1288	0.49	1.20	0.48	-	0.24
	Tablet	121	1091	0.40		0.90	1.78	0.36

Detailed inputs for all tablets can be found in Table 5.3. One may note that in most cases (HKUST-1, UiO-66, UiO-66-NH₂), the “optimized” tablet is the one compressed at the highest pressure; meaning that the optimal pressure might not have been reached here and the volumetric capacity could still be increased. This is especially the case of UiO-66, which is likely to resist compression pressures up to 2.500 MPa with 50% of the initial S_{BET} maintained.⁹ Nevertheless, a remarkable increase of tablet volumetric capacity

can already be observed as compared to their powder counterparts, from 1.5 to 2.6-fold. For example, the volumetric capacity of HKUST-1 can be increased from 0.24 to 0.36 cm^3/cm^3 . According to calculations made by Dailly *et al.*,⁶ such densified HKUST-1 tablets could result in an outperforming adsorbed natural gas (ANG) adsorbent.

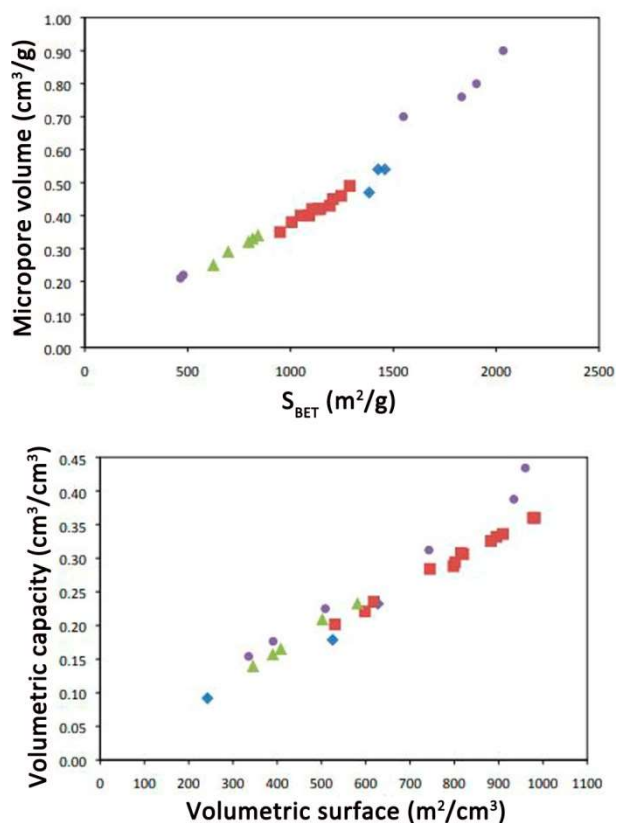


Fig.5.7: Correlations between the micropore volume and the S_{BET} area (up); and between the volumetric capacity and the volumetric surface (down) for UiO-66 (blue rhombus), UiO-66-NH₂ (green triangle), UiO-67 (violet round) and HKUST-1 (red square).

5.3.2. Comparison with literature data

Our results were further compared to the state-of-the-art literature in Fig.5.8. For UiO-66 and UiO-66-NH₂, the loss of S_{BET} as a function of the applied pressure is well in line with the literature data.^{11,12}

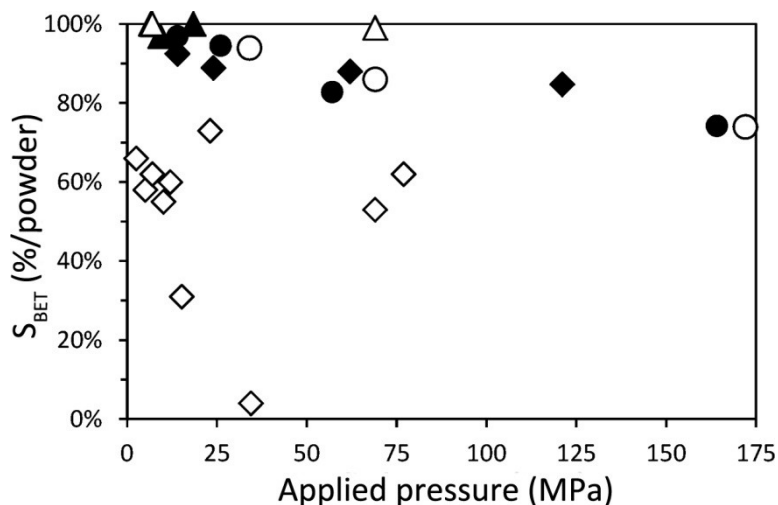


Fig.5.8: S_{BET} loss during compression observed in this work (black) and reported in the literature (white), using UiO-66 (triangle), UiO-66-NH₂ (round) and HKUST-1 (rhombus) powders.^{9,14,15}

However, important discrepancies are observed in the case of HKUST-1. Herein, up to 85% of the original S_{BET} of the powder was preserved at a moderate pressure of 120 MPa, while about 50% S_{BET} loss was reported at lower pressures of 10 and 70 MPa elsewhere.¹⁵ This could arise from several factors: (i) we used a relatively slow rate of pressure increase, which could allow HKUST-1 crystals to rearrange during compression; (ii) as shown in Fig.5.9, the solvent presence within the framework during compression allows maintaining its integrity, while in the literature, HKUST-1 powders are typically activated prior to compression; and (iii) the presence of defects within the MOF structure is likely to lower its resistance during compression. Here, assuming that there is no cluster defect, the HKUST-1 powder used only presents 10% linker defects as shown in Table 5.2. The latter assumption can hardly be verified as it would require shaping exactly the same powders that were used elsewhere. One may note that in the literature, the mechanical resilience of zeolitic MOF single crystals was greatly improved using common solvents, namely ethanol and butanol.³⁰

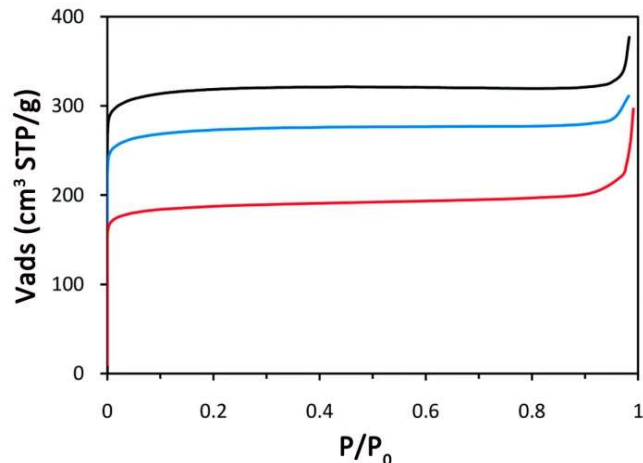


Fig.5.9: Nitrogen adsorption isotherms of the as-made HKUST-1 powder (black/top) and HKUST-1 tablets pressed at 62 MPa with the as-made powder (blue/middle) or with powder fully activated prior to compression (red/bottom).

5.3.3. Addition of expanded natural graphite as the binder for HKUST-1 powder

Graphite is generally used as an additive for improving materials' thermal conductivity.³¹ Graphite was also applied as a mineral binder with UiO-66.³² Herein, up to 2 wt% expanded natural graphite was mixed with the HKUST-1 powder prior to compression, and its impact on both the textural properties and the tensile strength of the resulting tablet was investigated and presented in Fig.5.10.

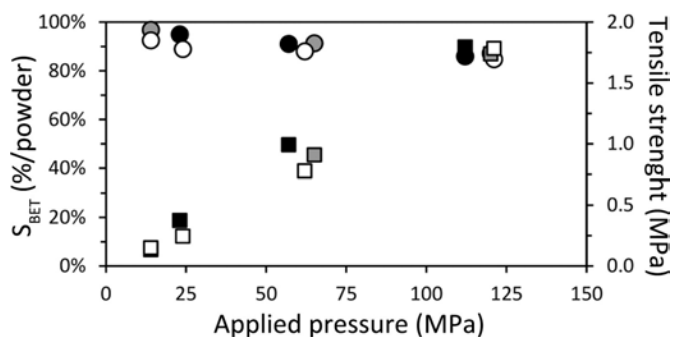


Fig.5.10: Impact of compression on S_{BET} (according to initial powder) and tensile strength of pure HKUST-1 tablets (white) or HKUST-1 mixed with 1 wt% graphite (grey) and 2 wt% graphite (black). Circles represent the S_{BET} (according to initial powder), and squares represent the tensile strength.

No measurable impact on the S_{BET} could be observed at any of the applied pressure, while a minor enhancement of the tensile strength can be noted for 2 wt% ENG, almost independent of the applied pressure. This latter observation is particularly interesting for shaping MOFs at low pressure, thus maximizing the textural properties while reaching robustness high enough for applications.

5.3.4. Overtime ageing of tablets in polyethylene bags

After characterization, each tablet was sealed in a small polyethylene (PE) bag and left on a shelf under room conditions. It should be pointed out that PE bags are not impermeable. Indeed, their permeability to water vapor is $8.6 \times 10^{-4} \text{ cm}^3(\text{STP}) \text{ cm}^{-1} \text{ cmHg}^{-1}$ per day.³³ The packaging in PE bags thus limits but does not prevent the water vapor exchange. The tablets with optimised volumetric capacity were then characterized again 4 months later in order to check their stability in the presence of moisture. The nitrogen adsorption isotherms of the different tablets are shown in Fig.5.11 and their textural properties are summarized in Table 5.4. In the case of UiO-66 and UiO-66-NH₂, only a slight decrease of SSA and micropore volume was observed (−9 to −11%), while the PXRD was unchanged, as shown in Fig.5.12.

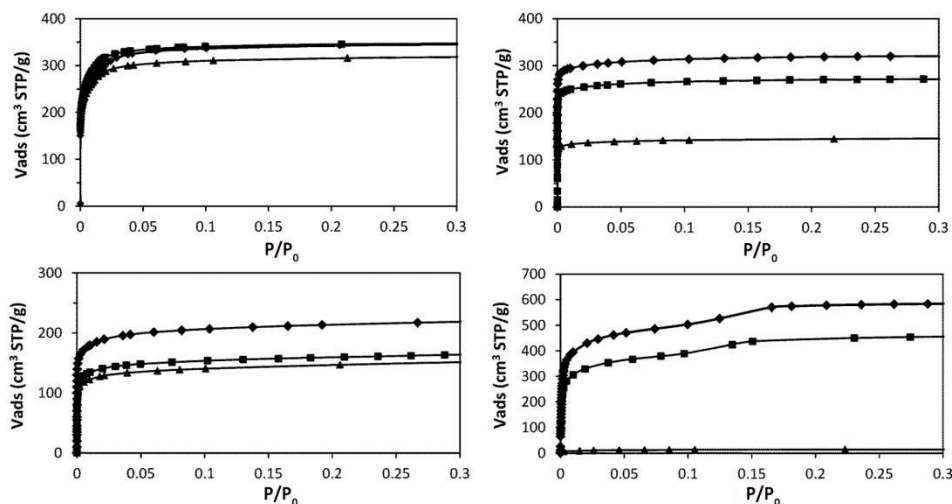
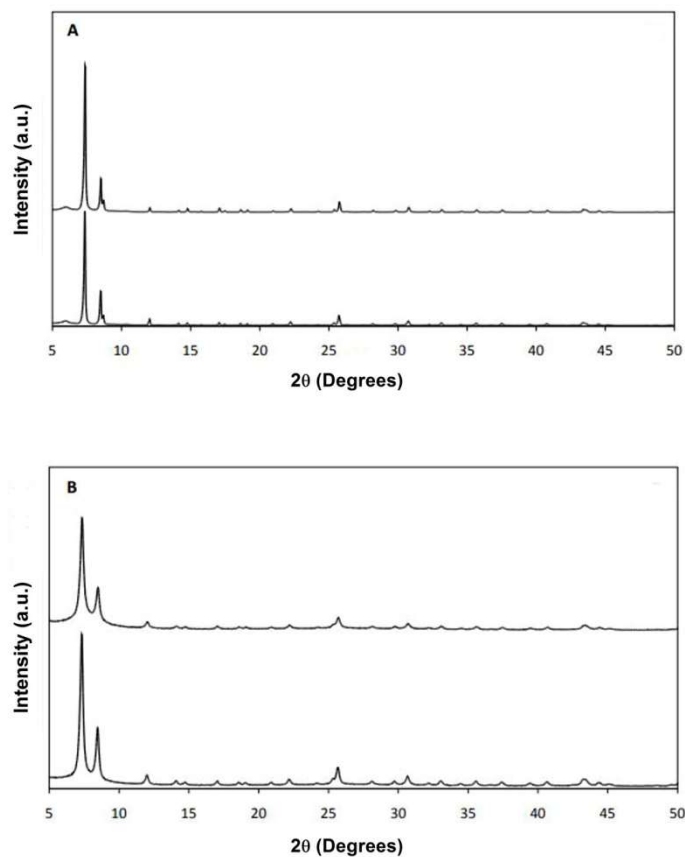


Fig.5.11: Nitrogen adsorption isotherms measured for UiO-66 (top-left), UiO-66-NH₂ (bottom-left), HKUST-1 (top-right) and UiO-67 (bottom-right): activated powders (rhombus), as-made tablets (square) and tablets aged for 4 months under standard room conditions (triangle).

Table 5. 4: Textural properties and resulting volumetric capacity of optimized MOF tablets after ageing for four months in the presence of moisture.

MOF	S_{BET} (m^2/g)	V_{micro} (cm^3/g)
UiO-66	1295	0.49
UiO-66-NH ₂	570	0.24
UiO-67	55	0.02
HKUST-1	580	0.23

**Fig.5.12: Powder XRD patterns of UiO-66 (A) and UiO-66-NH₂ (B) tablets as-made (bottom) and after ageing (top).**

In contrast, for UiO-67 tablets, 96% of their initial S_{BET} was lost after 4 months. Notably, the PXRD patterns shown in Fig.5.13 confirm a drastic loss of

crystallinity. It was shown that UiO-67 is poorly stable under humid conditions.³⁴ However, unlike what was published by DeCoste *et al.*,³⁴ no monoclinic zirconia diffraction peak could be observed; the degraded product can still be identified as pure UiO-67. This result confirms that UiO-67 cannot be used in processes where even traces of water are present.

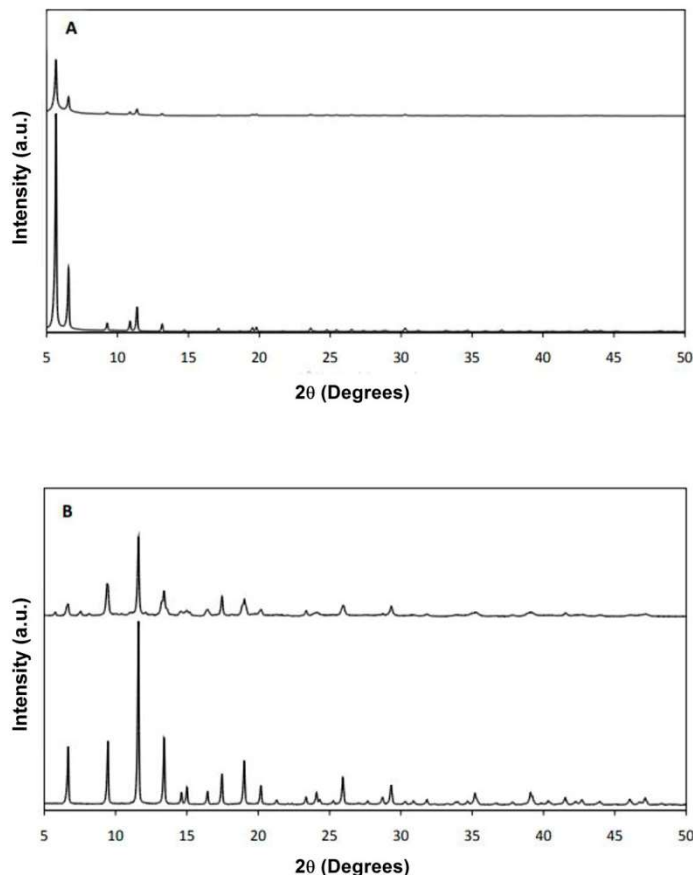


Fig.5.13: XRPD patterns of UiO-67 (A) and HKUST-1 (B) tablets as-made (bottom) and after ageing (top).

The HKUST-1 stability over time was extensively studied as it is one of the best candidates for gas storage and chromatography stationary phase.³⁶ Todaro *et al.* investigated the HKUST-1 decomposition process with air moisture.³⁶ They concluded that Cu–O bond hydrolysis is driven by the accumulation of water molecules during exposure. This phenomenon is reversible for short exposure times, up to 20 days, following a simple vacuum treatment. For longer exposure times, irreversible hydrolysis occurs, but up to

60% of the initial S_{BET} is still preserved after 6 months.³⁶ Interestingly, HKUST-1 tablets aged similarly, with 53% of their initial S_{BET} retained after 4 months. We can deduce that irreversible hydrolysis also occurred after tableting. Therefore, shaping MOF powders into dense tablets does not improve significantly their resistance toward air moisture. One can suppose that the formation of a dense crust of MOFs during tableting slows down the diffusion of moisture within the tablets at first, but does not prevent the degradation.

5.4. Conclusions

In this chapter, a general methodology for comparing the impact of MOF powder compression on the textural and mechanical properties using non dimensional indicators is presented. By compression, the tablet bulk density can be increased by 1.8 to 3.4-fold while the specific surface area decreased between 0 and 30% for all MOFs studied here. For the first time, it is shown that the mechanical stability, deduced from tensile strength tests, is proportional to the bulk density. Both are MOF-dependent.

In contrast to all past densification studies carried out on HKUST-1, it is also demonstrated that robust tablets presenting only limited textural degradation can be obtained. We believe that it arises at least partly from our compression protocol, in which the compression rate and dwell time are thoroughly controlled. As a consequence, densification results obtained in an uncontrolled or poorly-controlled manner such as when using a manual press should be interpreted with care. Moreover, as reported in the case of zeolitic MOF single crystals, the presence of solvent traces within the pores of HKUST-1 seems beneficial during compression. We underline here that depending on the final application, namely catalysis or gas storage, a different strategy can be used. For catalysis, a mild pressure, usually around 20 MPa, seems enough to produce tough and highly porous tablets that can then be grinded and sieved. The use of graphite up to 2 wt% can also be beneficial as it lowers the pressure required to reach certain robustness, thus maximizing the retained textural properties. For gas storage, the maximum volumetric capacity was obtained at the highest applied pressure, except for UiO-67 which collapses at 82 MPa. However, only UiO-66 and UiO-66-NH₂ proved to be stable overtime in the presence of moisture making them highly attractive for further production and applications.

5.5. References

1. A. S. Munn, P. W. Dunne, S. V. Y. Tang and E. H. Lester, *Chem. Commun.*, 2015, 51, 12811-12814.
2. M. Rubio-Martinez, T. D. Hadley, M. P. Batten, K.-C. Carey, T. Barton, D. Marley, A. Mönch, K.-S. Lim and M. R. Hill, *ChemSusChem*, 2016, 9, 938-941; H. Reinsch, S. Waitschat, S. M. Chavan, K. P. Lilerud and N. Stock, *Eur. J. Inorg. Chem.*, 2016, 27, 4490-4498.
3. D. Crawford, J. Casaban, R. Haydon, N. Giri, T. McNally and S. L. James, *Chem. Sci.*, 2015, 6, 1645-1649.
4. D. Bazer-Bachi, L. Assié, V. Lecocq, B. Harbuzaru and V. Falk, *Powder Technol.*, 2014, 255, 52-59.
5. H. C. Foley and A. Qajar, *Ind. Eng. Chem. Res.*, 2014, 53, 19649-1952.
6. M. Beckner and A. Dailly, *Appl. Energy*, 2016, 162, 506-514.
7. A. I. Spjelkavik, A. Sevilime, S. Divekar, T. Didriksen and R. Blom, *Chem. – Eur. J.*, 2014, 20, 8973-8978; B. Böhringer, R. Fischer, M. R. Lohe, M. Rose, S. Kaskel and P. Küsgens, *MOF Shaping and Immobilization*, in *Metal-Organic Frameworks: Applications from Catalysis to Gas Storage*, ed. D. Farrusseng, Wiley-VCH Verlag GmbH & Co. KGaA, Weinheim, Germany, 2011.
8. S. Mitchell, N.-L. Michels and J. Pérez-Ramírez, *Chem. Soc. Rev.*, 2013, 42, 6094-6112; G. T. Whiting, A. D. Chowdhury, R. Oord, P. Paalanen and B. M. Weckhuysen, *Faraday Discuss.*, 2016, 188, 369-386.
9. P. S. Bárcia, D. Guimarães, P. A. P. Mendes, J. A. C. Silva, V. Guillermin, H. Chevreau, C. Serre and A. E. Rodrigues, *Microporous Mesoporous Mater.*, 2011, 139, 67-73; G. W. Peterson, J. B. DeCoste, T. G. Glover, Y. Huang, H. Jasujaand K. S. Walton, *Microporous Mesoporous Mater.*, 2013, 179, 48-53.
10. P. G. Yot, K. Yang, F. Ragon, V. Dmitriev, T. Devic, P. Horcajada, C. Serre and G. Maurin, *Dalton Trans.*, 2016, 45, 4283-4288.
11. F. Akhtar, L. Andersson, S. Ogunwumi, N. Hedin and L. Bergström, *J. Eur. Ceram. Soc.*, 2014, 34, 1643-1666; S. C. McKellar and S. A. Moggach, *Acta Crystallogr., Sect. B: Struct. Sci., Cryst. Eng. Mater.*, 2015, B71, 587-607.
12. K. W. Chapman, G. J. Halder and P. J. Chupas, *J. Am. Chem. Soc.*, 2009, 131, 17546-17547; M. A. Moreira, J. C. Santos, A. F. P. Ferreira, J. M. Loureiro, F. Ragon, P. Horcajada, K.-E. Shim, Y.-K. Hwang, U.-H. Lee, J.-S. Chang, C. Serre and A. E. Rodrigues, *Langmuir*, 2012, 28, 5715-

- 5723; D. Peralta, G. Chaplais, A. Simon-Masseron, K. Barthelet and G. D. Pirngruber, *Ind. Eng. Chem. Res.*, 2012, 51, 4692-4702; R. Zacharia, D. Cossement, L. Lafi and R. Chahine, *J. Mater. Chem.*, 2010, 20, 2145-2151.
13. M. I. Nandasiri, S. R. Jambovane, B. P. McGrail, H. T. Schaefer and S. K. Nune, *Coord. Chem. Rev.*, 2016, 311, 38-52.
 14. G. W. Peterson, J. B. DeCoste, F. Fatollahi-Fard and D. K. Britt, *Ind. Eng. Chem. Res.*, 2014, 53, 701-707.
 15. J. Kim, S.-H. Kim, S.-T. Yang and W.-S. Ahn, *Microporous Mesoporous Mater.*, 2012, 161, 48-55; J. Liu, P. K. Thallapally and D. Strachan, *Langmuir*, 2012, 28, 11584-11589.
 16. S.-N. Kim, Y.-R. Lee, S.-H. Hong, M.-S. Jang and W.-S. Ahn, *Catal. Today*, 2015, 245, 54-60.
 17. G. C. Shearer, S. Forselv, S. Chavan, S. Bordiga, K. Mathisen, M. Bjørgen, S. Svelle and K.-P. Lillerud, *Top. Catal.*, 2013, 56, 770-782.
 18. L. Garzón-Tovar, M. Cano-Sarabia, A. Carné-Sánchez, C. Carbonell, I. Imaz and D. MasPOCH, *React. Chem. Eng.*, 2016, 1, 533-539.
 19. A. Carné-Sánchez, I. Imaz, M. Cano-Sarabia and D. MasPOCH, *Nat. Chem.*, 2013, 5, 203-211.
 20. J. R. Parrish, *Nature*, 1961, 190, 800-.
 21. L. Valenzano, B. Civalieri, S. Chavan, S. Bordiga, M. H. Nilsen, S. Jakobsen, K. P. Lillerud and C. Lamberti, *Chem. Mater.*, 2011, 23, 1700-1718.
 22. M. Kandiah, M. H. Nilsen, S. Usseglio, S. Jakobsen, U. Olsbye, M. Tilset, C. Larabi, E. A. Quadrelli, F. Bonino and K.-P. Lillerud, *Chem. Mater.*, 2010, 22, 6632-6640; Y. Bai, Y. Dou, L.-H. Xie, W. Rutledge, J.-R. Li and H.-C. Zhou, *Chem. Soc. Rev.*, 2016, 45, 2327-2367.
 23. G. C. Shearer, S. Chavan, J. Ethiraj, J. G. Vitillo, S. Svelle, U. Olsbye, C. Lamberti, S. Bordiga and K. P. Lillerud, *Chem. Mater.*, 2014, 26, 4068-4071.
 24. S. M. J. Rogge, J. Wieme, L. Vanduyfhuys, S. Vandenbrande, G. Maurin, T. Verstraelen, M. Waroquier and V. Speybroeck, *Chem. Mater.*, 2016, 28, 5721-5732.
 25. B. Van de Voorde, I. Stassen, B. Bueken, F. Vermoortele, D. De Vos, R. Ameloot, J.-C. Tan and T. D. Bennett, *J. Mater. Chem. A*, 2015, 3, 1737-1742.
 26. M. J. Katz, Z. J. Brown, Y. J. Colón, P. W. Siu, K. A. Scheidt, R. Q. Snurr, J. Hupp and O. Farha, *Chem. Commun.*, 2013, 49, 9449-9451.

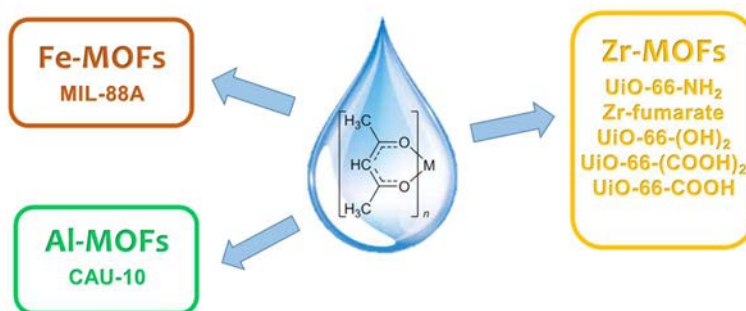
27. H. Wu, T. Yildirim and W. Zhou, *J. Phys. Chem. Lett.*, 2013, 4, 925-930.
28. C. L. Hobday, R. J. Marshall, C. F. Murphie, J. Sotelo, T. Richards, D. R. Allan, T. Düren, F.-X. Coudert, R. S. Forgan, C. A. Morrison and S. A. Moggach, *Angew. Chem., Int. Ed.*, 2016, 55, 2401-2405.
29. S. Yamadaya, M. Oba, T. Hasegawa, K. Ogawa and Y. Kotera, *J. Catal.*, 1970, 19, 264-270.
30. T. D. Bennett, J. Sotelo, J.-C. Tan and S. A. Moggach, *CrystEngComm*, 2015, 17, 286-289.
31. D. Liu, J. J. Purewal, J. Yang, A. Sudik, S. Maurer, U. Mueller, J. Ni and D. J. Siegel, *Int. J. Hydrogen Energy*, 2012, 37, 6109-6117.
32. M. A. Moreira, J. C. Santos, A. F. P. Ferreira, J. M. Loureiro, F. Ragon, P. Horcajda, K.-E. Shim, Y.-K. Hwang, U.-H. Lee, J.-S. Chang, C. Serre and A. E. Rodrigues, *Langmuir*, 2012, 28, 5715-5723.
33. R. L. Hamilton, *Bell Labs Tech. J.*, 1967, 46, 391-415.
34. J. B. DeCoste, G. W. Peterson, H. Jasuja, T. G. Glover, Y.-G. Huang and K. S. Walton, *J. Mater. Chem. A*, 2013, 1, 5642-5650.
35. M. S. Singh, N. R. Dhumal, H. J. Kim, J. Kiefer and J. A. Anderson, *J. Phys. Chem. C*, 2016, 120, 17323-17333.
36. M. Todaro, G. Buscarino, L. Sciortino, A. Alessi, F. Messina, M. Taddei, M. Ranocchiari, M. Cannas and F. M. Gelardi, *J. Phys. Chem. C*, 2016, 120, 12879-12889.

Conclusions

General Conclusions

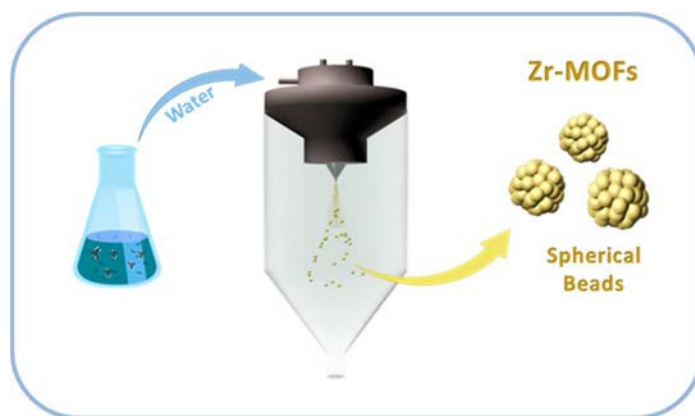
The efforts in this Thesis have been focused on developing basic knowledge on the aqueous synthesis of MOFs and their shaping with the aim of approaching the production of MOFs at scale and accelerating their industrialization.

Firstly, we have shown that metal acetylacetonate complexes can be used as an alternative source of metals into batch synthesis of MOFs in water. To this end, different metal acetylacetonates have been used to synthesize various MOFs at room temperature (UiO-66-NH₂, Zr-fumarate, UiO-66-(OH)₂ and MIL-88A) or 90 °C (UiO-66-(COOH)₂, UiO-66-COOH and CAU-10). The aqueous syntheses of all these MOFs using metal acetylacetonates have been optimized to achieve yields ranging from 60% for MIL-88A to > 85% for all the others. Overall, we have confirmed that metal acetylacetonates can be used as a safer metal source compared to nitrate, chloride and oxychloride salts. In addition to that, for many industrial processes, metal acetylacetonate complexes are utilized as green reagents so our methodology should enable the development of a simple, environmental friendly process to fabricate MOFs in water.

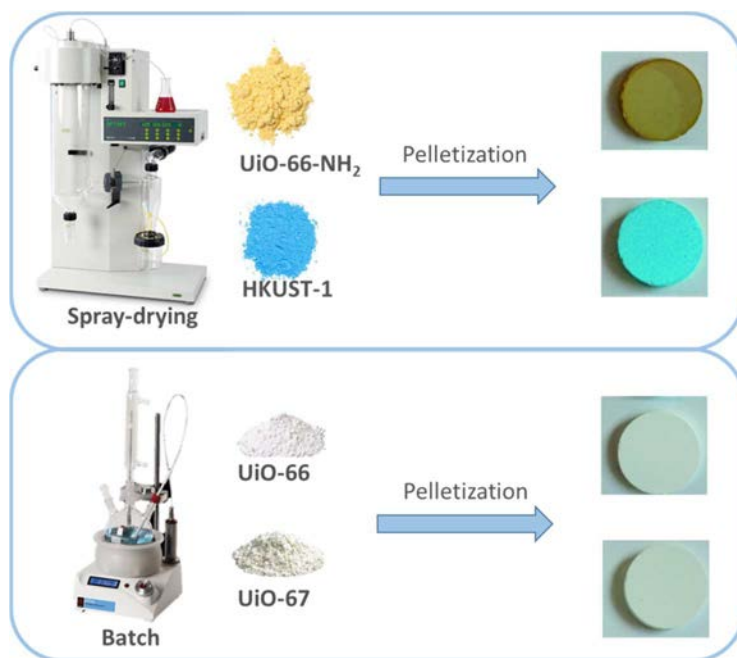


Then, as a second general conclusion, we have shown that the continuous flow spray-drying technique can be used as a continuous and scalable methodology to synthesize MOFs using water as the solvent. In this context, we have demonstrated the aqueous spray-drying synthesis of two archetypical Zr-MOFs in the form of spherical micrometer beads. By using water as the solvent and acetic acid as the modulator, the two Zr-MOFs UiO-66-NH₂ and Zr-

fumarate have been synthesized in yields up to 64% and 58%, respectively. Both synthesized Zr-MOFs have shown comparable porosity characteristics than those synthesized with most traditional methods. In their synthesis, 30% of acetic acid (v/v% in water) was found to be optimum. In order to show the scalability of this water-based spray-drying synthesis, UiO-66-NH₂ was chosen to be produced at the gram scale with 85% yield and good quality in terms of the porosity.



Finally, the powders of UiO-66-NH₂ and HKUST-1 synthesized via spray-drying and UiO-66 and UiO-67 made via batch synthesis have been shaped into tablets to see the impact of densification into tables on their textural and mechanical properties. These tablets have been prepared by mild pelletization using a R&D tableting machine. From this study, we have found a linear relationship between densification and tensile strength for all four studied MOFs, with the slope being MOF-dependent. By the applied pressure, the tablet bulk density has been increased by 1.8 to 3.4-fold, whereas the specific surface area has decreased between 0 and 30% for the MOFs studied. It has been demonstrated that robust UiO-66, UiO-66-NH₂ and HKUST-1 tablets presenting only limited textural degradation can be generated, whereas UiO-67 tablets are produced with higher textural damage. From the stability test under moisture environment, only shaped UiO-66 and UiO-66-NH₂ have been proved to be stable overtime, which proves the feasibility of scaling up the production and shaping methodology for the industrialization of those MOFs.



ANNEX

List of Publications

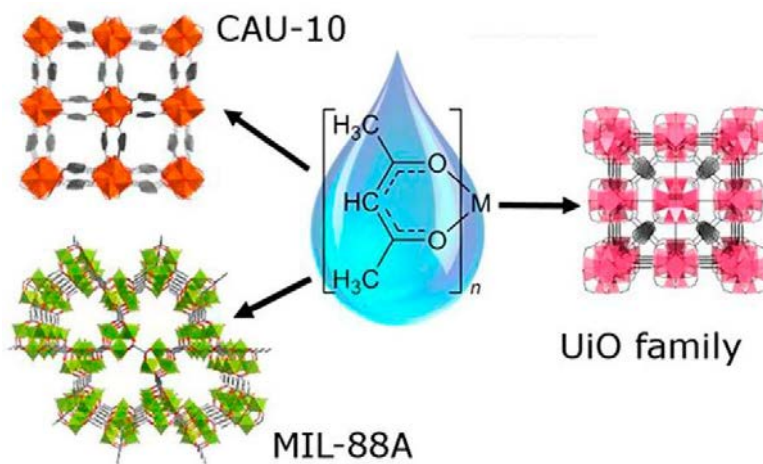
The publications related to the main objectives of this thesis are listed below:

- **Ceren Avci-Camur**, Javier Perez-Carvajal, Inhar Imaz, Daniel Maspoch. (2018). Metal Acetylacetonates as a Source of Metals for Aqueous Synthesis of Metal–Organic Frameworks. *ACS Sustainable Chemistry & Engineering*. 6, 11, 14554-14560.
- **Ceren Avci-Camur**, Javier Troyano, Javier Pérez-Carvajal, Alexandre Legrand, David Farrusseng, Inhar Imaz, Daniel Maspoch. (2018). Aqueous production of spherical Zr-MOF beads via continuous-flow spray-drying. *Green Chemistry*. 20, 873-878.
- Jeremy Dhainaut, **Ceren Avci-Camur**, Javier Troyano, Alexandre Legrand, Jerome Canivet, Inhar Imaz, Daniel Maspoch, Helge Reinsch and David Farrusseng. (2017) Systematic study of the impact of MOF densification into tablets on textural and mechanical properties. *CrystEngComm*. 19, 4211-4218.

The author of this thesis also contributed in the following publication which is not included in the present manuscript:

- Luis Garzón-Tovar, **Ceren Avci-Camur**, David Rodríguez-San-Miguel, Inhar Imaz, Félix Zamora, Daniel Maspoch. (2017) Spray drying for making covalent chemistry II: synthesis of covalent–organic framework superstructures and related composites. *Chemical Communications* 53 (82), 11372-11375.

Metal Acetylacetonates as a Source of Metals for Aqueous Synthesis of Metal–Organic Frameworks



Metal Acetylacetonates as a Source of Metals for Aqueous Synthesis of Metal–Organic Frameworks

Ceren Avci-Camur,[†] Javier Perez-Carvajal,[†] Inhar Imaz,^{*,†,‡} and Daniel Maspoch^{*,†,‡,§}[†]Catalan Institute of Nanoscience and Nanotechnology (ICN2), CSIC and The Barcelona Institute of Science and Technology, Campus UAB, Bellaterra, 08193 Barcelona, Spain[‡]ICREA, Pg. Lluís Companys 23, 08010 Barcelona, Spain

Supporting Information

ABSTRACT: Demand continues for environmentally sound, high-yielding processes for the large-scale production of metal–organic frameworks (MOFs). Here we describe the use of metal acetylacetonate complexes as an alternative source of metals for the aqueous synthesis of MOFs. We have synthesized several carboxylate-based Zr(IV)-(UiO-66-NH₂, Zr-fumarate, UiO-66-(OH)₂, UiO-66-COOH and UiO-66-(COOH)₂), Fe(III)-(MIL-88A) and Al(III)-(CAU-10) porous MOFs from their corresponding metal acetylacetonates in good yields (typically >85%) and, in some cases, at room temperature.

KEYWORDS: Metal–organic frameworks, Green synthesis, Water



INTRODUCTION

Metal acetylacetonate (acac) complexes that are formed of highly labile acetylacetonate linkers have found widespread use in industry,¹ including in vulcanization of plastics for rubber;^{2,3} curing processes for coatings (e.g., epoxy resins);^{4–7} as oxidative reagents for degradation of organic pollutants⁸ and also shelf-stable nonwoven fabrics and films used in dippers, wipes, towels and bathmats;⁹ as polyvinyl chloride (PVC) stabilizers,¹⁰ and as catalysts in many polymerizations.^{11–13} For example, Zr(acac)₄ is used to initiate lactide polymerization and copolymerization for the production of bioresorbable materials; in drug-releasing processes; and to form scaffolds for tissue cultures and in biodegradable implants for surgical use.¹⁴ In most of these processes, metal acetylacetonate complexes are considered green reagents due to their low toxicity and ease of handling in air.¹⁵

Metal–organic frameworks (MOFs) are among the most attractive porous materials known today, owing to their myriad potential industrial applications. However, their practical use has been limited by the paucity of environmentally friendly methods suitable for large-scale production.^{16–19} The production process of MOFs generally needs high temperatures and the use of expensive, toxic, flammable and/or teratogenic organic solvents (such as DMF). Therefore, it is crucial to be able to fabricate MOFs in aqueous conditions, as water is safer and cheaper than using organic solvents. To date, some advances have been made in producing MOFs in water by mixing the organic linker, the metal salt (mainly nitrates, chlorides and oxochlorides) and acetic acid at high temperatures (Table 1). However, such salts can be problematic, as they present serious oxidative reactivity and toxicity hazards, and some of them are corrosive to metal-based reactors.^{18,20} To overcome these drawbacks, De Vos et al. and Stock et al.

replaced the above-mentioned metal salts with metal sulfates in the aqueous synthesis of diverse MOFs (UiO-type and CAU-10) at high temperatures.^{21,22} Indeed, the sulfate ion is less corrosive, safer and greener than the corresponding anions of the aforementioned salts, and its use obviates the use of acetic acid. However, large concentrations of metal sulfates can compromise the framework rigidity and porosity of the resulting MOFs, due to interactions between the sulfate anions and the metal cations.^{23,24}

As part of our ongoing research to devise new methods for production of MOFs in water, we have sought alternatives to the metal sources cited above. Here we show that metal acetylacetonate complexes can serve as metal sources for aqueous synthesis of MOFs in good yields. As proof of concept, we used Zr(acac)₄ to prepare five members of the UiO-type family of MOFs, including UiO-66-NH₂, Zr-fumarate (also known as MOF-801), UiO-66-(OH)₂, UiO-66-COOH and UiO-66-(COOH)₂ (Table 1). We also extended our study to other metal acetylacetonates such as Al(acac)₃ (to produce CAU-10) and Fe(acac)₃ (to produce MIL-88A). Encouragingly, we found that many of these reactions proceed in high yields at room temperature (RT), which is a remarkable finding given that aqueous synthesis of MOFs without heating has scarcely been reported.^{25,26}

EXPERIMENTAL SECTION

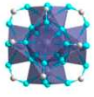
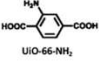
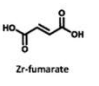
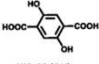
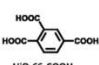
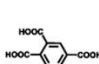
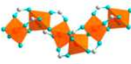
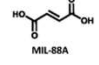
General Procedures, Materials and Instrumentation. Zirconium acetylacetonate, iron(III) acetylacetonate, aluminum acetylacetonate, 2-aminoterephthalic acid, fumaric acid, 2-carboxyterephthalic acid, 2,5-dicarboxyterephthalic acid, isophthalic acid and acetic acid

Received: July 5, 2018

Revised: August 21, 2018

Published: September 10, 2018

Table 1. Summary of the Aqueous Syntheses of the Selected MOFs Reported in the Literature

Cluster	Ligand / MOF	Metal source	Solvent	T (°C)	BET (m ² g ⁻¹)	Ref.
	UiO-66-NH ₂ 	Zr(NO ₃) ₄	H ₂ O/AA	Reflux	833	27
		ZrOCl ₂	H ₂ O/AA	90 °C	1150	24
		ZrOCl ₂	H ₂ O/AA	150 °C	1261	28
		Zr(SO ₄) ₂	H ₂ O	Reflux	420	21
	Zr-fumarate 	Zr(acac) ₄	H ₂ O/AA	RT	1106	This work
		ZrOCl ₂	H ₂ O/AA	90 °C	1200	24
		ZrOCl ₂	H ₂ O/AA	150 °C	664	28
		Zr(acac) ₄	H ₂ O/AA	RT	1249	This work
	UiO-66-(OH) ₂ 	Zr(NO ₃) ₄	H ₂ O/AA	Reflux	705	27
		ZrOCl ₂	H ₂ O/AA	95 °C	940	24
		Zr(acac) ₄	H ₂ O/AA	RT	733	This work
		ZrCl ₄	H ₂ O	100 °C	661	29
	UiO-66-COOH 	Zr(acac) ₄	H ₂ O/AA	90 °C	452	This work
		Zr(NO ₃) ₄	H ₂ O/AA	Reflux	494	27
Zr(SO ₄) ₂		H ₂ O	Reflux	250	21	
ZrCl ₄		H ₂ O	100 °C	516	29	
UiO-66-(COOH) ₂ 	Zr(acac) ₄	H ₂ O/AA	90 °C	538	This work	
	Al ₂ (SO ₄) ₃ and NaAlO ₂	H ₂ O/EtOH	130 °C	-	22	
	Al(acac) ₃	H ₂ O	90 °C	520	This work	
	FeCl ₃	H ₂ O	85 °C	-	30	
CAU-10 	MIL-5BA 	Fe(acac) ₃	H ₂ O	RT	-	This work

were purchased from Sigma-Aldrich. All reagents were used without further purification. All reactions were performed using deionized water, obtained from a Milli-Q system (18.2 MΩ·cm).

X-ray powder diffraction (XRPD) patterns were collected on an X'Pert PRO MPDP analytical diffractometer (Panalytical) at 45 kV and 40 mA using Cu K α radiation ($\lambda = 1.5418 \text{ \AA}$). Nitrogen and carbon dioxide adsorption and desorption measurements were performed at 77 K and room temperature respectively using an Autosorb-IQ-AG analyzer (Quantachrome Instruments). Specific surface area (S_{BET}) was determined by applying the BET equation to the adequate region of the nitrogen isotherms: the range was taken between 0.025 and 0.06 P/P_0 for UiO-66-NH₂ and COOH, and between 0.05 and 0.1 P/P_0 for the others.³¹ Prior to the measurements, samples were degassed inside the cell under primary vacuum at 200 °C for 6 h (UiO-66-NH₂) or at 150 °C for 10 h (Zr-fumarate) or at 100 °C for 3 h (UiO-66-(OH)₂) or at 70 °C for 12 h (UiO-66-COOH and UiO-66-(COOH)₂) or at 150 °C for 16 h (CAU-10). Gravimetric water vapor sorption isotherms were measured using a DVS vacuum instrument (Surface Measurement Systems Ltd.). The weight of the dried powder ($\approx 20 \text{ mg}$) was constantly monitored with a high-resolution microbalance ($\pm 0.1 \mu\text{g}$) and recorded at 25 °C ($\pm 0.2 \text{ }^\circ\text{C}$) under pure water vapor pressures. ¹H NMR spectra were collected on a Bruker AVANCE III 400 MHz spectrometer. Ten mg of each sample were digested in 0.5 mL of 1.2 wt % of HF solution prepared in DMSO-*d*₆. From each spectrum, the

amount of acetic acid per cluster was calculated. Field-emission scanning electron microscopy (FESEM) images were collected on a FEI Magellan 400 L scanning electron microscope at an acceleration voltage of 2.0 kV.

Synthesis of MOFs. Synthesis of UiO-66-NH₂ at Room Temperature. Zr(acac)₄ (1169 mg, 2.4 mmol) and 2-amino-terephthalic acid (435 mg, 2.4 mmol) were mixed under stirring in 6 mL of a 50% (v/v) solution of acetic acid in water for 72 h at room temperature. The resulting yellow dispersion was washed once with water and three times with ethanol at room temperature. The solid was dried for 12 h at 65 °C in a conventional oven to afford the final product (yield: 90%).

Synthesis of Zr-Fumarate at Room Temperature. Zr(acac)₄ (1169 mg, 2.4 mmol) and fumaric acid (278 mg, 2.4 mmol) were mixed under stirring in 6 mL of a 33% (v/v) or 50% (v/v) solution of acetic acid in water for 72 h at room temperature. The resulting white dispersion was washed once with water and three times with ethanol at room temperature. The solid was dried for 12 h at 65 °C in a conventional oven to afford the final product (yield: 83% to 88%).

Synthesis of UiO-66-(OH)₂ at Room Temperature. Zr(acac)₄ (1169 mg, 2.4 mmol) and 2,5-dihydroxyterephthalic acid (476 mg, 2.4 mmol) were mixed under stirring in 6 mL of a 66% (v/v) solution of acetic acid in water for 72 h at room temperature. The resulting yellow dispersion was washed once with water and three times with

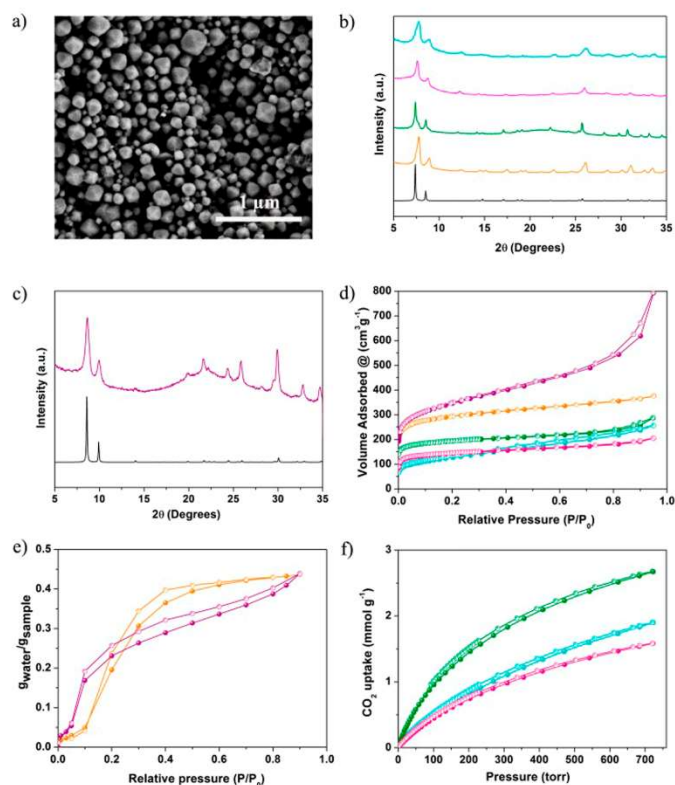


Figure 1. (a) Representative FESEM image of UiO-66-NH₂. (b) XRPD patterns for simulated UiO-66 (black) and synthesized UiO-66-NH₂ (orange), UiO-66-(OH)₂ (green), UiO-66-(COOH)₂ (pink) and UiO-66-COOH (blue). (c) XRPD patterns for simulated UiO-66 (black) and synthesized Zr-fumarate (purple), UiO-66-(OH)₂ (green), UiO-66-(COOH)₂ (pink) and UiO-66-COOH (blue). (d) N₂ adsorption (filled dots) and desorption (empty dots) isotherms at 77 K for UiO-66-NH₂ (orange), Zr-fumarate (purple), UiO-66-(OH)₂ (green), UiO-66-(COOH)₂ (pink) and UiO-66-COOH (blue). (e) Water sorption (filled dots) and desorption (empty dots) isotherms at room temperature for UiO-66-NH₂ (orange) and Zr-fumarate (purple). (f) CO₂ sorption (filled dots) and desorption (empty dots) isotherms at room temperature of UiO-66-(OH)₂ (green), UiO-66-(COOH)₂ (pink) and UiO-66-COOH (blue).

ethanol at room temperature. The solid was dried for 12 h at 65 °C in a conventional oven to afford the final product (yield: 90%).

Synthesis of UiO-66-(COOH)₂ at 90 °C. Zr(acac)₄ (2194 mg, 4.5 mmol) and 2,5-dicarboxyterephthalic acid (1144 mg, 4.5 mmol) were mixed under stirring in 6 mL of a 33%, 50% or 66% (v/v) solution of acetic acid in water for 24 h at 90 °C. The resulting white dispersion was washed three times with water at room temperature. The solid was dried under vacuum to afford the final product (yield: 89% to 91%).

Synthesis of UiO-66-COOH at 90 °C. Zr(acac)₄ (2194 mg, 4.5 mmol) and 2-carboxyterephthalic acid (947 mg, 4.5 mmol) were mixed under stirring in 6 mL of a 66% (v/v) solution of acetic acid in water for 24 h at 90 °C. The resulting white dispersion was washed three times with water at room temperature. The solid was dried under vacuum to afford the final product (yield: 90%).

Synthesis of MIL-88A at Room Temperature. Fe(acac)₃ (706 mg, 2.0 mmol) and fumaric acid (232 mg, 2.0 mmol) were mixed under stirring in 5 mL water for 72 h at room temperature. The resulting orange dispersion was washed once with water and three times with

ethanol at room temperature. The solid was dried under vacuum to afford the final product (yield: 25%). In a subsequent synthesis, the yield was increased to 60% by running the reaction at 90 °C for 24 h.

Synthesis of CAU-10 at 90 °C. Al(acac)₃ (700 mg, 5.4 mmol) and isophthalic acid (947 mg, 4.5 mmol) were mixed in 6 mL of water for 72 h at 90 °C under stirring. The resulting white dispersion was washed twice with water and several times with ethanol at room temperature. The solid was dried under vacuum to afford the final product (yield: 85%).

RESULTS AND DISCUSSION

UiO-type MOFs are known for their large surface areas, chemical versatility and high hydrothermal, chemical and thermal stability, all of which make them good candidates for industrial applications such as catalysis, gas and pollutant capture, adsorption heat transformation (AHT) and separation processes.^{32–34} Among the different UiO-type MOFs, we started with a room-temperature aqueous batch synthesis of

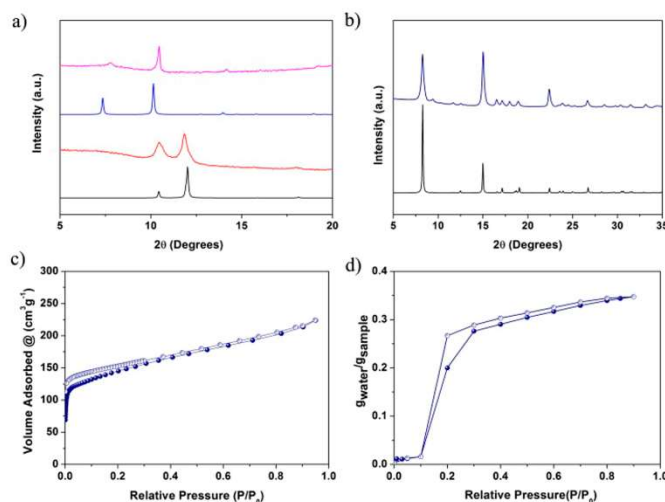


Figure 2. (a) XRPD patterns for the open (pink) and closed (red) forms of the synthesized MIL-88A, in comparison to the simulated patterns for the open (blue) and closed (black) form. (b) XRPD patterns for simulated (black) and synthesized CAU-10 (blue). (c) N_2 adsorption (filled dots) and desorption (empty dots) isotherms at 77 K for CAU-10. (d) Water sorption (filled dots) and desorption (empty dots) isotherms at room temperature for CAU-10.

UiO-66-NH₂ from Zr(acac)₄. To this end, 0.4 M of Zr(acac)₄ and 0.4 M of 2-aminoterephthalic acid were added in 6 mL of a 50% (v/v) aqueous solution of acetic acid, and the resulting mixture (pH = 2.3) was stirred for 72 h at room temperature. Note that 0.4 M is the maximum useable concentration for Zr(acac)₄, which, at higher concentrations, becomes highly viscous and paste-like. For the synthesis of UiO-66-NH₂, the optimal concentration of acetic acid was 50% (v/v) (Table S1). Note that the concentration of acetic acid was crucial in this synthesis: the reaction only worked in the concentration range of 17% to 66% acetic acid (pH = 3.2 to 2.1). At lower concentrations, there was no reaction, whereas at higher concentrations, an amorphous solid was formed. After 72 h, the resulting yellow dispersion was washed once with water and three times with ethanol. Finally, the collected solid was dried for 12 h at 65 °C in a conventional oven to afford octahedral UiO-66-NH₂ submicrometer crystals (size: ~0.3–1 μm) as a pure phase (yield: 90%) (Figure 1a), as confirmed by X-ray powder diffraction (XRPD) and N_2 sorption measurements (S_{BET} = 1106 m² g⁻¹; Figure 1b and 1d; Figures S1–S3). This S_{BET} value is consistent with the literature values for UiO-66-NH₂ synthesized from other metal sources in water (Table 1).^{24,28} Moreover, the quality of the synthesized UiO-66-NH₂ was also assessed by analyzing its water sorption capacity. The water sorption isotherm showed the expected S-type trend centered at 0.2 P/P₀ with a total water uptake of 0.44 g_{water} g⁻¹ (Figure 1e).³⁵ In this sample, the number of missing linkers per [Zr₆(OH)₄L₆] was found to be 0.9 (Figure S4), which is in agreement with reported values.³⁶

The scalability of the room temperature aqueous synthesis of UiO-66-NH₂ submicrometer crystals using Zr(acac)₄ was demonstrated on the multigram-scale (Figure S5). For this, we stirred the precursors (0.4 M) in 500 mL of a mixture of

water and acetic acid (50% (v/v)) for 72 h at room temperature. After washing and drying, the resulting UiO-66-NH₂ powder (~53 g; yield: 95%) showed a S_{BET} value of 1000 m² g⁻¹.

We then extended our aqueous synthetic approach to two other UiO-66-type MOFs: Zr-fumarate and UiO-66-(OH)₂. For these syntheses, an aqueous mixture of acetic acid containing 0.4 M of Zr(acac)₄ and 0.4 M of either fumaric acid (for Zr-fumarate) or 2,5-dihydroxyterephthalic acid (for UiO-66-(OH)₂) was stirred for 72 h at room temperature. For Zr-fumarate, the optimal concentration of acetic acid was in the range of 33% to 50% (v/v); and for UiO-66-(OH)₂, it was 66% (v/v) (Table S2 and S3). Under these conditions, aggregates of nanocrystals (size: <50 nm) of Zr-fumarate were synthesized in high yields (83% to 88%) and with an S_{BET} value of 1220–1249 m² g⁻¹. Note that these values are higher than most literature values (Figure 1c,d; Figures S6–S8).^{23,37–39} In Zr-fumarate, the number of missing linkers per [Zr₆(OH)₄L₆] was calculated as 1.4 (Figure S9).³⁸ Given the promise of Zr-fumarate for water-related applications (e.g., delivery of drinking water from ambient air, storage of heat and/or refrigeration),^{24,37–41} we confirmed that synthesized Zr-fumarate retains the typical S-shaped isotherm, centered at 0.08 P/P₀, and high water uptake (0.43 g_{water} g⁻¹) (Figure 1e). The UiO-66-(OH)₂ was obtained (as aggregates of nanocrystals; size: <100 nm) in high yield (94%), with a number of missing linkers per [Zr₆(OH)₄L₆] of 1.3, and with an S_{BET} value of 733 m² g⁻¹. These results are consistent with the previously reported values for UiO-66-(OH)₂ synthesized in water (Figure 1b,d; Figures S10–S13).²⁷ Given the interest in UiO-66-(OH)₂ for CO₂-sorption application,^{42,43} the quality of the prepared material was studied by measuring its CO₂ uptake capacity. Total CO₂ uptake was 2.6 mmol g⁻¹ at 700

Torr, which is consistent with the previously reported values (Figure 1f).^{24,37–40}

Next, we performed aqueous syntheses of UiO-66-(COOH)₂ and UiO-66-COOH from Zr(acac)₄. Neither reaction worked at room temperature; they both required a temperature of 90 °C. To this end, an aqueous mixture of acetic acid containing 0.75 M of Zr(acac)₄ and 0.75 M of either 2,5-dicarboxyterephthalic acid (for UiO-66-(COOH)₂) or 2-carboxyterephthalic acid (for UiO-66-COOH) was stirred for 24 h at 90 °C. An acetic acid concentration of 33% to 66% (v/v) gave submicrometer crystals (size: ~0.2–0.5 μm) of UiO-66-(COOH)₂ in high yield (89 to 91%) and with a good value S_{BET} of 538 m² g⁻¹ (Figure 1b,d; Table S4 and Figures S14–S16).²⁹ Similarly, an acetic acid concentration of 66% (v/v) afforded crystals of UiO-66-COOH (as aggregates of crystals; size: < 200 nm) in high yield (90%) and with a S_{BET} value of 452 m² g⁻¹ (Figure 1b,d; Table S4 and Figures S18–S20). The total CO₂ uptake at 700 Torr was 1.6 mmol g⁻¹ for UiO-66-(COOH)₂ and 1.9 mmol g⁻¹ for UiO-66-COOH (Figure 1f).^{29,44} Here, the number of missing linkers per [Zr₆(OH)₄L₆] was 1.3 for UiO-66-(COOH)₂ and 1.8 for UiO-66-COOH (Figures S17 and S21).³⁹ Note here that the slightly lower surface area observed in UiO-66-COOH³⁹ can be attributed to the presence of high amounts of defects.

Once we demonstrated that UiO-type MOFs could be synthesized in water using Zr(acac)₄, we then sought to prove the generality of our strategy by preparing MOFs based on other metal ions such as iron and aluminum. To this end, the Fe(III)-based MOF MIL-88A⁴⁴ was synthesized in water by stirring an aqueous mixture of 0.4 M of Fe(acac)₃ and 0.4 M of fumaric acid at room temperature for 72 h. After this period, the resulting orange dispersion was washed once with water and three times with ethanol. The collected solid was dried under vacuum to afford MIL-88A in the form of hexagonal rod-like crystals (yield: 25%; size: ~0.7–1.5 μm; Figure S22).³⁰ Interestingly, the yield could be increased up to 60% by simply heating the aqueous mixture at 90 °C. Because this MOF is well-known for its structural breathing properties, this functionality was confirmed in the synthesized material by comparing the XRPD of the dry powder (closed form) to that of the material after it had been soaked in water for 20 min (open form) (Figure 2a).

For an Al(III)-based MOF, we chose CAU-10, as it shows promise for many water sorption applications such as adsorption-driven heat pumps and chillers.⁴⁵ This MOF was synthesized by heating an aqueous mixture of 0.36 M of Al(acac)₃ and 0.30 M of isophthalic acid at 90 °C under continuous stirring for 72 h. The resulting white dispersion was then washed twice with water and four times with ethanol, and the collected solid dried under vacuum to afford submicrometer crystals of CAU-10 (size: ~0.2–0.5 μm) in good yield (85%; Figure 2b; Figure S23). N₂ and water sorption experiments revealed an S_{BET} value of 520 m² g⁻¹ and total water uptake of 0.34 g_{water} g⁻¹, with the expected S-type trend centered at 0.2 P/P₀ (Figure 2c, 2d). These values are all in agreement with the reported values.²²

CONCLUSION

We have shown that metal acetylacetonate complexes can be used as an alternative source of metals to synthesize MOFs in water. We used metal acetylacetonates to synthesize various MOFs at either RT (UiO-66-NH₂, Zr-fumarate, UiO-66-OH₂ and MIL-88A) or 90 °C (UiO-66-(COOH)₂, UiO-66-COOH

and CAU-10). The yields were all good, ranging from 60% for MIL-88A to >85% for all the others. Because metal acetylacetonate complexes are considered green reagents for numerous industrial processes, our strategy should enable the development of a simple, environmentally sound process for production of MOFs in water and, consequently, accelerate their commercialization.

ASSOCIATED CONTENT

Supporting Information

The Supporting Information is available free of charge on the ACS Publications website at DOI: 10.1021/acssuschemeng.8b03180.

Additional synthetic details, XRPD patterns, surface area measurements, FESEM images (PDF)

AUTHOR INFORMATION

Corresponding Authors

*I. Imaz. E-mail: inhar.imaz@icn2.cat.

*D. MasPOCH. E-mail: daniel.masPOCH@icn2.cat.

ORCID

Inhar Imaz: 0000-0002-0278-1141

Daniel MasPOCH: 0000-0003-1325-9161

Notes

The authors declare no competing financial interest.

ACKNOWLEDGMENTS

This work was supported by the Spanish MINECO (project PN MAT2015-65354-C2-1-R); the Catalan AGAUR (project 2014 SGR 80); the ERC, under EU-FP7 (ERC-Co 615954); and the EU Horizon 2020 research and innovation programme PRODIGIA (grant agreement #685727). It was also funded by the CERCA Programme/Generalitat de Catalunya. ICN2 acknowledges the support of the Spanish MINECO through the Severo Ochoa Centres of Excellence Programme, under grant SEV-2013-0295.

REFERENCES

- (1) Sodhi, R. K.; Paul, S. An Overview of Metal Acetylacetonates: Developing Areas/Routes to New Materials and Applications in Organic Syntheses. *Catal. Surv. Asia* 2018, 22, 31–62.
- (2) Nor, H. M.; Ebdon, J. R. Telechelic Liquid Natural Rubber: A Review. *Prog. Polym. Sci.* 1998, 23, 143–177.
- (3) Przybyszewska, M.; Zaborski, M.; Jakubowski, B.; Zawadiak, J. Zinc Chelates as New Activators for Sulphur Vulcanization of Acrylonitrile-Butadiene Elastomer. *EXPRESS Polym. Lett.* 2009, 3, 256–266.
- (4) Yamada, K.; Chow, T. Y.; Horihata, T.; Nagata, M. A Low Temperature Synthesis of Zirconium Oxide Coating using Chelating Agents. *J. Non-Cryst. Solids* 1988, 100, 316–320.
- (5) Ibe, T.; Frings, R. B.; Lachowicz, A.; Kyo, S.; Nishide, H. Nitroxide Polymer Networks Formed by Michael Addition: on Site-Cured Electrode-Active Organic Coating. *Chem. Commun.* 2010, 46, 3475–3477.
- (6) Shimp, D. A. Metal Acetylacetonate/Alkylphenol Curing Catalyst for Polycyanate Esters of Polyhydric Phenols. US Patent US4 847 233, July 27, 1987.
- (7) Smith, J. D. B. Metal Acetylacetonates as Latent Accelerators for Anhydride/epoxy Cured Epoxy Resins. *J. Appl. Polym. Sci.* 1981, 26, 979–986.
- (8) Sannino, F.; Pernice, P.; Imparato, C.; Aronne, A.; D'Errico, G.; Minieri, L.; Perfetti, M.; Pirozzi, D. Hybrid TiO₂-Acetylacetonate Amorphous Gel-Derived Material with Stably Adsorbed Superoxide

- Radical Active in Oxidative Degradation of Organic Pollutants. *RSC Adv.* **2015**, *5*, 93831–93839.
- (9) Hudson, R. L. Shelf Stable Nonwoven Fabrics and Films. US Patent US5 393 831, June 5, 1993.
- (10) Preparation Method for High-Brightness Calcium Acetylacetonate for PVC (Polyvinyl Chloride) Heat Stabilizer. CN Patent CN103 086 857, June 5, 2013.
- (11) Gorczynski, J. L.; Chen, J.; Fraser, C. L. Iron Tris-(dibenzoylmethane)-Centered Polylactide Stars: Multiple Roles for the Metal Complex in Lactide Ring-Opening Polymerization. *J. Am. Chem. Soc.* **2005**, *127*, 14956–14957.
- (12) Czech, Z.; Wojciechowicz, M. The Crosslinking Reaction of Acrylic PSA Using Chelate Metal Acetylacetonates. *Eur. Polym. J.* **2006**, *42*, 2153–2160.
- (13) Wu, J.; Jiang, X.; Zhang, L.; Cheng, Z.; Zhu, X. Iron-Mediated Homogeneous ICAR ATRP of Methyl Methacrylate under ppm Level Organometallic Catalyst Iron(III) Acetylacetonate. *Polymers* **2016**, *8*, 29.
- (14) Dobrzynski, P. Mechanism of ϵ -Caprolactone Polymerization and ϵ -Caprolactone/Trimethylene Carbonate Copolymerization Carried out with Zr(Acac)₃. *Polymer* **2007**, *48*, 2263–2279.
- (15) Levis, R. J. *Sax's Dangerous Properties of Industrial Materials*, 8th ed.; Van Nostrand Reinhold: New York, 1992.
- (16) (a) Julien, P. A.; Mottillo, C.; Friscic, T. Metal-Organic Frameworks Meet Scalable and Sustainable Synthesis. *Green Chem.* **2017**, *19*, 2729–2747.
- (17) (a) Rubio-Martinez, M.; Avci-Camur, C.; Thornton, A. W.; Imaz, I.; Maspocho, D.; Hill, M. R. New Synthetic Routes Towards MOF Production at Scale. *Chem. Soc. Rev.* **2017**, *46* (11), 3453–3480. (b) Zhang, J.; White, G. B.; Ryan, M. D.; Hunt, A. J.; Katz, M. J. Dihydroxylevoglucosone (Cyrene) As a Green Alternative to N,N-Dimethylformamide (DMF) in MOF Synthesis. *ACS Sustainable Chem. Eng.* **2016**, *4* (12), 7186–7192. (c) Paseta, L.; Potier, G.; Sorribas, S.; Coronas, J. Solventless Synthesis of MOFs at High Pressure. *ACS Sustainable Chem. Eng.* **2016**, *4* (7), 3780–3785. (d) Doan, H. V.; Fang, Y.; Yao, B.; Dong, Z.; White, T. J.; Sartbaeva, A.; Hintermaier, U.; Ting, V. P. Controlled Formation of Hierarchical Metal–Organic Frameworks Using CO₂-Expanded Solvent Systems. *ACS Sustainable Chem. Eng.* **2017**, *5* (9), 7887–7893.
- (18) Reinsch, H. Green⁺ Synthesis of Metal-Organic Frameworks. *Eur. J. Inorg. Chem.* **2016**, *2016*, 4290–4299.
- (19) Reinsch, H.; Stock, N. Synthesis of MOFs: a Personal View on Rationalisation, Application and Exploration. *Dalton Trans.* **2017**, *46*, 8339–8349.
- (20) Gaab, M.; Trukhan, N.; Maurer, S.; Gummaraju, R.; Müller, U. The Progression of Al-Based Metal-Organic Frameworks – From Academic Research to Industrial Production and Applications. *Microporous Mesoporous Mater.* **2012**, *157*, 131–136.
- (21) Reinsch, H.; Bueken, B.; Vermoortele, F.; Stassen, I.; Lieb, A.; Lillerud, K. P.; De Vos, D. Green Synthesis of Zirconium-MOFs. *CrystEngComm* **2015**, *17*, 4070–4074.
- (22) Lenzen, D.; Bendix, P.; Reinsch, H.; Fröhlich, D.; Kummer, H.; Möllers, M.; Hügenell, P. P. C.; Gläser, R.; Henninger, S.; Stock, N. Scalable Green Synthesis and Full-Scale Test of the Metal–Organic Framework CAU-10-H for Use in Adsorption-Driven Chillers. *Adv. Mater.* **2018**, *30*, 1705869.
- (23) Reinsch, H.; Stassen, I.; Bueken, B.; Lieb, A.; Ameloot, R.; De Vos, D. First Examples of Aliphatic Zirconium MOFs and the Influence of Inorganic Anions on their Crystal Structures. *CrystEngComm* **2015**, *17*, 331–337.
- (24) Reinsch, H.; Waitschat, S.; Chavan, S. M.; Lillerud, K. P.; Stock, N. A Facile “Green” Route for Scalable Batch Production and Continuous Synthesis of Zirconium MOFs. *Eur. J. Inorg. Chem.* **2016**, *2016*, 4490–4498.
- (25) Sanchez-Sanchez, M.; Getachew, N.; Diaz, K.; Diaz-Garcia, M.; Chebude, Y.; Diaz, I. Synthesis of Metal-Organic Frameworks in Water at Room Temperature: Salts as Linker Sources. *Green Chem.* **2015**, *17*, 1500–1509.
- (26) Garzon-Tovar, L.; Carne-Sanchez, A.; Carbonell, C.; Imaz, I.; Maspocho, D. Optimised Room Temperature, Water-Based Synthesis of CPO-27-M Metal-Organic Frameworks with High Space-Time Yields. *J. Mater. Chem. A* **2015**, *3*, 20819–20826.
- (27) Hu, Z.; Peng, Y.; Kang, Z.; Qian, Y.; Zhao, D. A Modulated Hydrothermal (MHT) Approach for the Facile Synthesis of UiO-66-Type MOFs. *Inorg. Chem.* **2015**, *54*, 4862–4868.
- (28) Avci-Camur, C.; Troyano, J.; Perez-Carvajal, J.; Legrand, A.; Farrusseng, D.; Imaz, I.; Maspocho, D. Aqueous Production of Spherical Zr-MOF Beads via Continuous-Flow Spray-Drying. *Green Chem.* **2018**, *20*, 873–878.
- (29) Ragon, F.; Campo, B.; Yang, Q.; Martineau, C.; Wiersum, A. D.; Lago, A.; Guillerm, V.; Hemsley, C.; Eubank, J. F.; Vishnuvarthan, M.; Taudelle, F.; Horcajada, P.; Vimont, A.; Llewellyn, P. L.; Daturi, M.; Devautour-Vinot, S.; Maurin, G.; Serre, C.; Devic, T.; Clet, G. Acid-Functionalized UiO-66(Zr) MOFs and their Evolution After Intra-Framework Cross-Linking: Structural Features and Sorption Properties. *J. Mater. Chem. A* **2015**, *3*, 3294–3309.
- (30) Wang, J.; Wan, J.; Ma, Y.; Wang, Y.; Pu, M.; Guan, Z. Metal-Organic Frameworks MIL-88A with Suitable Synthesis Conditions and Optimal Dosage for Effective Catalytic Degradation of Orange G Through Persulfate Activation. *RSC Adv.* **2016**, *6*, 112502–112511.
- (31) (a) Llewellyn, P.; Maurin, G.; Rouquerol, J. *Adsorption by Powders and Porous Solids*, 2nd ed.; Academic Press: Poland, 2012. (b) Gomez-Gualdrón, D. A.; Moghadam, P. Z.; Hupp, J. T.; Farha, O. K.; Snurr, K. Q. Application of Consistency Criteria To Calculate BET Areas of Micro- And Mesoporous Metal–Organic Frameworks. *J. Am. Chem. Soc.* **2016**, *138*, 215–224.
- (32) (a) Cavka, J. H.; Jakobsen, S.; Olsbye, U.; Guillou, N.; Lamberti, C.; Bordiga, S.; Lillerud, K. P. A New Zirconium Inorganic Building Brick Forming Metal Organic Frameworks with Exceptional Stability. *J. Am. Chem. Soc.* **2008**, *130*, 13850–13851. (b) Bai, Y.; Dou, Y.; Xie, L. H.; Rutledge, W.; Li, J. R.; Zhou, H. C. Zr-based Metal–Organic Frameworks: Design, Synthesis, Structure, and Applications. *Chem. Soc. Rev.* **2016**, *45*, 2327–2367. (c) Han, Y.; Li, J.-R.; Xie, Y.; Guo, G. Substitution Reactions in Metal–Organic Frameworks and Metal–Organic Polyhedra. *Chem. Soc. Rev.* **2014**, *43*, 5952–5981.
- (33) Liu, X.; Demir, N. K.; Wu, Z.; Li, K. Highly Water-Stable Zirconium Metal–Organic Framework UiO-66 Membranes Supported on Alumina Hollow Fibers for Desalination. *J. Am. Chem. Soc.* **2015**, *137*, 6999–7002.
- (34) (a) Kim, H.; Yang, S.; Rao, S. R.; Narayanan, S.; Kapustin, E. A.; Furukawa, H.; Umans, A. S.; Yaghi, O. M.; Wang, E. N. Water Harvesting from Air with Metal-Organic Frameworks Powered by Natural Sunlight. *Science* **2017**, *356*, 430–434. (b) Garzon-Tovar, L.; Pérez-Carvajal, J.; Imaz, I.; Maspocho, D. Composite Salt in Porous Metal-Organic Frameworks for Adsorption Heat Transformation. *Adv. Funct. Mater.* **2017**, *27*, 1606424.
- (35) Jeremias, F.; Lozan, V.; Henninger, S. K.; Janiak, C. Programming MOFs for Water Sorption: Amino-Functionalized MIL-125 and UiO-66 for Heat Transformation and Heat Storage Applications. *Dalton Trans.* **2013**, *42*, 15967–15973.
- (36) DeStefano, M. R.; Islamoglu, T.; Garibay, S. J.; Hupp, J. T.; Farha, O. K. Room-Temperature Synthesis of UiO-66 and Thermal Modulation of Densities of Defect Sites. *Chem. Mater.* **2017**, *29*, 1357–1361.
- (37) Furukawa, H.; Gándara, F.; Zhang, Y.-B.; Jiang, J.; Queen, W. L.; Hudson, M. R.; Yaghi, O. M. Water Adsorption in Porous Metal–Organic Frameworks and Related Materials. *J. Am. Chem. Soc.* **2014**, *136*, 4369–4381.
- (38) Canivet, J.; Bonnefoy, J.; Daniel, C.; Legrand, A.; Coasne, B.; Farrusseng, D. Structure-Property Relationships of Water Adsorption in Metal-Organic Frameworks. *New J. Chem.* **2014**, *38*, 3102–3111.
- (39) Hu, Z.; Castano, I.; Wang, S.; Wang, Y.; Peng, Y.; Qian, Y.; Chi, C.; Wang, X.; Zhao, D. Modulator Effects on the Water-Based Synthesis of Zr/Hf Metal–Organic Frameworks: Quantitative Relationship Studies between Modulator, Synthetic Condition, and Performance. *Cryst. Growth Des.* **2016**, *16*, 2295–2301.

(40) Yang, H.; Zhu, H.; Hendrix, M. M. R. M.; Lousberg, N. J. H. G. M.; de With, G.; Esteves, A. C. C.; Xin, J. H. Temperature Triggered Collection and Release of Water from Fogs by a Sponge Like Cotton Fabric. *Adv. Mater.* **2013**, *25*, 1150–1154.

(41) Kalmutzki, M. J.; Diercks, C. S.; Yaghi, O. M. Metal–Organic Frameworks for Water Harvesting from Air. *Adv. Mater.* **2018**, *30*, 1704304.

(42) Rada, Z. H.; Abid, H. R.; Shang, J.; Sun, H.; He, Y.; Webley, P.; Liu, S.; Wang, S. Functionalized UiO-66 by Single and Binary (OH)₂ and NO₂ Groups for Uptake of CO₂ and CH₄. *Ind. Eng. Chem. Res.* **2016**, *55*, 7924–7932.

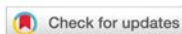
(43) Biswas, S.; Zhang, J.; Li, Z.; Liu, Y.-Y.; Grzywa, M.; Sun, L.; Volkmer, D.; Van Der Voort, P. Enhanced Selectivity of CO₂ over CH₄ in Sulphonate-, Carboxylate- and Iodo-Functionalized UiO-66 Frameworks. *Dalton Trans.* **2013**, *42*, 4730–4737.

(44) Ferey, G.; Serre, C. Large Breathing Effects in Three-Dimensional Porous Hybrid Matter: Facts, Analyses, Rules and Consequences. *Chem. Soc. Rev.* **2009**, *38*, 1380–1399.

(45) de Lange, M. F.; Zeng, T.; Vlugt, T. J. H.; Gascon, J.; Kapteijn, F. Manufacture of Dense CAU-10-H Coatings for Application in Adsorption Driven Heat Pumps: Optimization and Characterization. *CrystEngComm* **2015**, *17*, 5911–5920.

Aqueous Production of Spherical Zr-MOF Beads via Continuous-Flow Spray-Drying





Cite this: *Green Chem.*, 2018, 20, 873

Received 18th October 2017,
Accepted 10th January 2018
DOI: 10.1039/c7gc03132g
rsc.li/greenchem

Aqueous production of spherical Zr-MOF beads via continuous-flow spray-drying†

Ceren Avci-Camur,^a Javier Troyano,^a Javier Pérez-Carvajal,^a Alexandre Legrand,^a David Farrusseng,^b Inhar Imaz^{b,*} and Daniel Maspocho^{b,*,c}

Porous metal-organic frameworks (MOFs) are attracting great attention from industry, thanks to their myriad potential applications in areas such as catalysis and gas storage. Zr-MOFs (also known as UiO-type MOFs) are especially promising, owing to their large surface areas, high chemical versatility and remarkable hydrothermal, chemical and thermal stabilities. However, among the challenges currently precluding the industrial exploitation of MOFs is the lack of green methods for their synthesis. Herein we describe a continuous-flow spray-drying method for the simultaneous synthesis and shaping of spherical MOF microbeads in a mixture of water and acetic acid. We used this approach to build two archetypal Zr-MOFs: UiO-66-NH₂ and Zr-fumarate. By tuning the concentration of acetic acid in water, we were able to produce, by a scalable process, UiO-66-NH₂ and Zr-fumarate beads with S_{BET} and water-sorption values comparable to the literature values obtained with other methods.

Introduction

Metal-organic frameworks (MOFs) are an emerging class of porous materials with industrial relevance in many fields, including gas storage and separation,^{1–3} catalysis,^{4,5} adsorption heat transformations (AHTs),^{6–9} and contaminant sequestration.^{10,11} However, industry and academic experts widely agree that the effective exploitation and commercialisation of MOFs depend on the development of scalable, sustainable and cost-effective fabrication processes.^{12–16} Ideally, such green processes should enable continuous manufacturing of MOFs from non-toxic reagents in an energy-efficient way. Additionally, they should be specific for each targeted MOF, as small variations in process parameters can have structural and functional (e.g. stability, adsorption, etc.) consequences.^{17–19}

Green methods for MOF synthesis should be aqueous, as water is safer and cheaper than using organic solvents. However, this is not trivial, as most organic linkers are poorly soluble in water and most MOFs are not stable in water.^{20–22} This drawback is even more pronounced for continuous-fabrication methods, whereby the reaction time between organic

linkers and metal ions is significantly lower compared to that in batch methods. However, to date, major advances have been made in the aqueous synthesis of MOFs using continuous-flow chemistry. In these methods, water-solubility issues have been mitigated mainly by using sodium salts of the organic linkers and by increasing the length of the tubing systems to increase the reaction time. For example, Schröder and Poliakoff *et al.* reported a continuous-flow aqueous synthesis of MIL-53-Al ($S_{\text{BET}} = 1010 \text{ m}^2 \text{ g}^{-1}$) based on the reaction of $\text{Al}(\text{NO}_3)_3 \cdot 9\text{H}_2\text{O}$ with sodium terephthalate for 10 min at 250 °C.²³ Similarly, Blom *et al.* showed that CPO-27-Ni ($S_{\text{BET}} = 1085 \text{ m}^2 \text{ g}^{-1}$) could be synthesised in water by reacting $\text{Ni}(\text{OAc})_2 \cdot 2\text{H}_2\text{O}$ with sodium 2,5-dihydroxyterephthalate for 20 min at 90 °C.²⁴ Also, Stock *et al.* produced UiO-66-NH₂ ($S_{\text{BET}} = 1150 \text{ m}^2 \text{ g}^{-1}$) by reacting $\text{ZrOCl}_2 \cdot 8\text{H}_2\text{O}$ and 2-aminoterephthalic acid and Zr-fumarate ($S_{\text{BET}} = 1200 \text{ m}^2 \text{ g}^{-1}$) and by reacting $\text{ZrOCl}_2 \cdot 8\text{H}_2\text{O}$ with fumaric acid for 22 min at 85 °C in the presence of acetic acid.²⁵ Interestingly, Lester *et al.* recently demonstrated the large-scale aqueous fabrication of ZIF-8 (810 g h^{-1}) by reacting $\text{Zn}(\text{OAc})_2 \cdot 2\text{H}_2\text{O}$ and 2-methylimidazole with a base for 5 min in a pilot-scale, continuous counter-current reactor.²⁶

Another approach to the continuous fabrication of MOFs is spray-drying,^{27–30} a mature technology that has been widely deployed in many industrial sectors. Existing lab-scale spray-drying processes can easily be scaled-up to the pilot scale, including for tonne-scale production. Briefly, this technique entails the transformation of a liquid stream (solution, suspension or emulsion) into a dried powder upon rapid evaporation of the solvent using a hot gas. In 2013 we demonstrated that, when the liquid stream contains metal ions and organic

^aCatalan Institute of Nanoscience and Nanotechnology (ICN2), CSIC and The Barcelona Institute of Science and Technology, Campus UAB, Bellaterra, 08193 Barcelona, Spain. E-mail: inhar.imaz@icn2.cat, daniel.maspocho@icn2.cat

^bUniversité de Lyon, Université Claude Bernard Lyon 1, CNRS, IRCÉLYON - UMR 5256, 2 Avenue Albert Einstein, 69626 Villeurbanne Cedex, France

^cICREA, Pg. Lluis Companys 23, 08010 Barcelona, Spain

† Electronic supplementary information (ESI) available. See DOI: 10.1039/c7gc03132g

linkers, spray-drying can also be used to simultaneously synthesise and shape MOFs in the form of hollow or compact microscale spheres or beads.^{28,29,31} More recently, we showed that high-nuclearity MOF (*e.g.* UiO-type family) beads can also be produced by employing a continuous-flow process at the entrance to the spray-drier.²⁹ However, to date, all spray-drying syntheses of MOFs have involved organic solvents such as *N,N'*-dimethylformamide (DMF).^{32–35}

Zr-Type MOFs are characterised by their large surface areas, chemical versatility and remarkably high hydrothermal, chemical and thermal stabilities, making them promising for catalysis, gas and pollutant capture and adsorption, heat transformation and separation processes.^{31,36–38} Synthesis of this MOF family can be improved through the use of acids. Moreover, acetic acid can also be incorporated into UiO-type structures, leading to networks that contain missing-linker defects and that usually exhibit higher uptake capacities.^{18,39}

Here, we demonstrate the utility of continuous-flow spray-drying for aqueous fabrication and shaping of spherical Zr-MOF microbeads. This rapid technique uses reaction times of only 60 to 90 seconds. The ability to synthesise and shape MOFs in a single step is important for industrial applications, most of which demand specific shapes (*e.g.* tablets, extrudates, granulates or monoliths).^{40–43} As a proof of concept, we prepared two water-stable members of the UiO-type family: UiO-66-NH₂ and Zr-fumarate (also known as MOF-801). We then evaluated the BET surface areas (S_{BET}) from N₂ sorption and the water sorption properties of these beads.

Results and discussion

Aqueous synthesis of UiO-66-NH₂ beads

A schematic illustration of the aqueous continuous-flow spray-drying set-up is shown in Fig. 1. In a typical synthesis, an equimolar mixture of ZrOCl₂·8H₂O and 2-aminoterephthalic acid

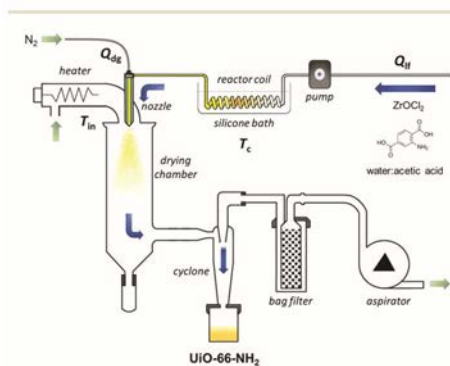


Fig. 1 Schematic illustration of the set-up for the aqueous continuous-flow spray-drying synthesis of UiO-66-NH₂.

(BDC-NH₂) in a mixture of water and acetic acid was injected into a coil-flow reactor (i.d. 3 mm), which was placed into a silicone bath. The reaction was run using a specific coil-flow reactor temperature (T_{c} ; in °C) and a liquid-feed rate (Q_{lf} ; in mL min⁻¹). The resulting yellow slurry was then spray-dried at a specific inlet temperature (T_{in} ; in °C) and a drying-gas (N₂) flow rate (Q_{dg} ; in mL min⁻¹) using a B-290 Mini Spray Dryer (BUCHI Labortechnik). The beads were collected, washed with ethanol and acetone, and then dried at 75 °C in air.

In addition to the optimisation of standard synthetic parameters (*e.g.* stoichiometry), our continuous-flow spray-drying method also demands the evaluation of T_{c} , T_{in} , Q_{lf} and Q_{dg} . Using this method, we initially produced UiO-66-NH₂ beads using a 0.05 M solution of ZrOCl₂·8H₂O and a 1 : 1 stoichiometric ratio of ZrOCl₂·8H₂O and BDC-NH₂. The total molar ratio of Zr/BDC-NH₂/acetic acid was defined as 1 : 1 : 50, which corresponds to an acetic acid concentration of 14% (v/v) in water. The optimal T_{c} was found to be 90 °C, as using lower values led to UiO-66-NH₂ with smaller S_{BET} values (Table S1, ESI†). The optimal Q_{lf} was defined as 2.4 mL min⁻¹, as higher values led to incomplete drying of the droplets. The residence time inside the coil-flow reactor was 63 s. As an additional green measure, we sought to minimise T_{in} , as this would translate to lower energy use and cost. Thus, T_{in} was set to 150 °C, which was the lowest temperature at which the solvent fully evaporated inside the spray-drier. Finally, a Q_{dg} of 336 mL min⁻¹ was used, based on earlier findings that it enables optimal nebulisation for MOF synthesis.^{28,29} The resulting yellow powder (yield: 70%) was characterised by X-ray powder diffraction (XRPD), which confirmed the formation of crystalline UiO-66-NH₂ (Fig. S1a, ESI†). The microporosity of this sample was analysed by N₂ adsorption measurements at 77 K (Fig. S1b, ESI†), giving an estimated BET surface area (S_{BET}) of 840 m² g⁻¹. This S_{BET} value is within the range reported for UiO-66-NH₂ synthesised in DMF.^{29,44,45}

To explore the synergic effects of coupling spray-drying to continuous-flow, we synthesised UiO-66-NH₂ using each of these techniques separately. Spray-drying alone provided a non-porous amorphous product, whereas continuous-flow synthesis alone afforded UiO-66-NH₂ as a crystalline solid but in a much lower yield (6%) than that obtained with the coupled method.

Having successfully produced UiO-66-NH₂ by continuous-flow spray-drying, we then sought to increase the yield by optimising the reagent concentrations. There are two main factors that limit the usable amounts of reagents in this reaction: the solubility of the organic ligand in water; and the blockage of the reaction coil during synthesis, due to the accumulation of precipitates. The maximum useable concentration of ZrOCl₂·8H₂O and BDC-NH₂ that we identified was 0.2 M for each reagent (Table S2, ESI†). Since the total molar ratio of Zr/BDC-NH₂/acetic acid was kept at 1 : 1 : 50, the concentration of acetic acid in water was 56% (v/v). These conditions afforded compact spherical UiO-66-NH₂ beads (size: 2–12 μm) in high yield (72%) and with a larger S_{BET} (1036 m² g⁻¹) than that obtained previously (Fig. 2). Thermogravimetric analysis (TGA) revealed that these UiO-66-NH₂ beads are stable up to near 400 °C, as depicted in Fig. S2 (ESI†).

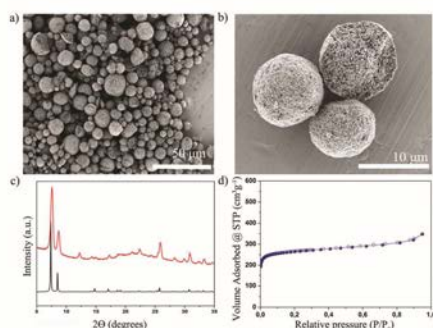


Fig. 2 Characterisation of UiO-66-NH₂ produced under optimised synthetic conditions ($[Zr] = 0.2 \text{ M}$; 3.2 mL of acetic acid (56% v/v in water); $Q_d = 2.4 \text{ mL min}^{-1}$; $T_c = 90 \text{ }^\circ\text{C}$). (a, b) Representative FESEM images showing the compact microspherical beads of UiO-66-NH₂. (c) XRPD diffractogram (red) compared to the simulated powder pattern for UiO-66 (black). (d) N₂ adsorption (filled dots) desorption (empty dots) isotherm at 77 K.

Modulator effects on the synthesis of UiO-66-NH₂ beads

We attributed the gain in the S_{BET} value in the synthesised UiO-66-NH₂ beads to the increased concentration of acetic acid. Given that the addition of acids (e.g. hydrochloric or acetic acid) can improve the formation and the crystallinity of UiO-type materials^{46–48} and that they can be incorporated into the structures leading usually to higher uptake capacities,^{18,43} we reasoned that this effect could depend on the concentration. Thus, we studied the influence of the modulator in the continuous-flow spray-drying synthesis of UiO-66-NH₂ beads by systematically increasing the concentration of acetic acid from 10% to 70% (v/v) under the optimised synthetic conditions (*vide supra*). To assess the reproducibility of the chemistry, each concentration was tested in triplicate. The resulting powders were characterised by FESEM, which revealed the formation of microscale structures ranging in shape from donut-like (at acetic acid concentrations [v/v] of 10% and 20%) to a more spherical shape (at concentrations $\geq 30\%$; Fig. S3, ESI†). XRPD confirmed that all these powders were crystalline UiO-66-NH₂ (Fig. 3a). However, UiO-66-NH₂ beads synthesised using acetic acid at concentrations from 30% to 60% exhibited better crystallinity, as evidenced by the calculated full width at half maximum (FWHM) values and average crystallite sizes (Table S3, ESI†). Remarkably, a similar trend had already been reported in the modulated hydrothermal batch synthesis of Zr-MOFs,^{49,50} whereby crystallinity was optimised by increasing the modulator up to a certain point, above which was observed a loss in crystallinity. For these more crystalline samples, the molar ratio of acetate/BDC-NH₂ in the structure determined by ¹H-NMR ranged from 0.03 to 0.13, the values that agree with those reported in the literature for samples of UiO-66 syn-

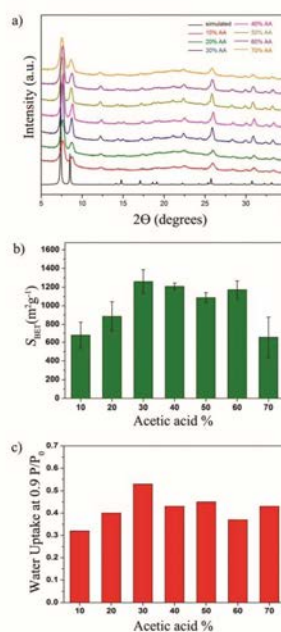


Fig. 3 (a) XRPD diffractograms of UiO-66-NH₂ synthesised using different concentrations of acetic acid (v/v, in water) compared to the simulated powder pattern for UiO-66 (black). (b, c) S_{BET} values (b) and maximum water uptake values (c) for UiO-66-NH₂ samples prepared using different concentrations of acetic acid.

thesised in the presence of acids at high temperatures (Fig. S4 and S5, ESI†).⁵¹

We measured the N₂ adsorption isotherms on all synthesised UiO-66-NH₂ (Fig. S6–12, ESI†). We found that, when using acetic acid at concentrations from 30% to 60%, the synthesised UiO-66-NH₂ beads exhibited the greatest mean values for S_{BET} (Fig. 3b), consistent with their greater crystallinity. In this range, the maximum mean S_{BET} was $1261 \text{ m}^2 \text{ g}^{-1}$ at an acetic acid concentration of 30%, which is within the range reported for UiO-66-NH₂ samples synthesised in DMF or water using acids such as HCl.^{25,52} Likewise, the water sorption isotherms revealed that this range of acetic acid concentrations provided the greatest water uptake, with the highest value ($0.57 \text{ g}_{\text{water}} \text{ g}^{-1}$) seen also at an acetic acid concentration of 30%, as well as the expected S-type trend, centred at $0.2P/P_0$ (Fig. 3c, Fig. S13, ESI†).⁵³

Modulated aqueous synthesis of Zr-fumarate beads

Encouraged by our results, we extended our aqueous continuous-flow spray-drying method to the synthesis of Zr-fumarate

beads.^{38,54} We followed a synthetic protocol analogous to that which we had earlier used for UiO-66-NH₂, and studied the influence of the concentration of acetic acid on the production of Zr-fumarate beads. In this case, acetic acid concentration values of 10% and 60% both led to quasi-amorphous materials (Fig. 4a). However, concentrations from 20% to 50% provided Zr-fumarate, as evidenced by XRPD (Fig. 4a). Here, FESEM revealed the formation of micron-sized spherical beads comprising nanoparticles of Zr-fumarate (Fig. 4b and Fig. S14,

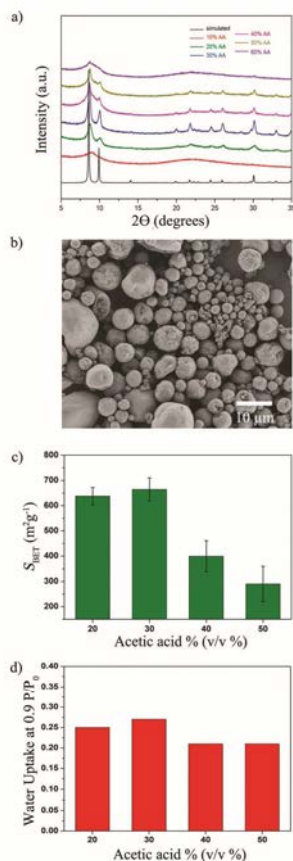


Fig. 4 (a) XRPD diffractograms of Zr-fumarate synthesised using different amounts of acetic acid compared to the simulated powder pattern for Zr-fumarate (black). (b) Representative FESEM images of Zr-fumarate beads synthesised using a 30% of acetic acid. (c, d) S_{BET} values (c) and maximum water uptakes (d) of Zr-fumarate samples prepared using different amounts of acetic acid.

ESI†). In this range, an acetic acid concentration of 30% provided optimal crystallinity (Table S4, ESI†). All synthesised samples contained an acetate/fumarate molar ratio between 0.2–0.3, which perfectly agrees with those previously reported for this MOF (Fig. S15, ESI†).⁵⁰

The N₂ and water sorption isotherms showed that the quality of the synthesised Zr-fumarate beads correlated to their crystallinity (Fig. S16–20, ESI†). In fact, the maximum mean S_{BET} value (664 m² g⁻¹) was obtained at an acetic acid concentration of 30% (Fig. 4c). This value was comparable to that previously reported for a water-batch synthesis,⁵⁰ but lower than that reported for an aqueous continuous-flow synthesis (ca. 1000 m² g⁻¹).⁴⁸ Water-sorption studies revealed similar behaviour, with a maximum water uptake of 0.27 g_{water} g⁻¹ at an acetic acid concentration of 30% (Fig. 4d). This value is slightly lower than that achieved for Zr-fumarate synthesised under hydrothermal conditions and a reaction time of 16 h (0.36 g_{water} g⁻¹).⁵⁵

Multi-gram synthesis of UiO-66-NH₂ beads

We next demonstrated the scalability of this aqueous synthesis by fabricating UiO-66-NH₂ beads on the multigram-scale (40 g; Fig S21, ESI†). To this end, we employed the optimised conditions described above. Thus, 792 mL of a 0.2 M equimolar mixture of ZrOCl₂·8H₂O and BDC-NH₂ in acetic acid in water (30% v/v) were injected into the coil-flow reactor (T_c: 90 °C) at a liquid-feed rate (Q_{lf}) of 2.4 mL min⁻¹, and then spray-dried at a flow rate (Q_{dg}) of 336 mL min⁻¹ and an inlet temperature (T_{in}) of 150 °C for 5.5 h. After washing and drying, the resulting UiO-66-NH₂ beads (40 g; yield: 85%; Fig S22, ESI†) showed an S_{BET} value of 1270 m² g⁻¹ and a total water uptake of 0.49 g_{water} g⁻¹ (Fig. S23 and 24, ESI†). These values are similar to those obtained in the milligram-scale synthesis. Additionally, we confirmed the long-term stability of the fabricated beads by comparing the XRPD patterns and S_{BET} values of a freshly prepared sample and a 1-year-old sample. We did not observe any significant differences between the two samples (Fig. S25, ESI†).

Conclusions

We have reported a continuous-flow spray-drying method for aqueous production of two representative Zr-MOFs: UiO-66-NH₂ and Zr-fumarate. For both Zr-MOFs, a modulator (acetic acid) concentration of 30% (v/v in water) was found to be optimum, as it yielded microbeads whose S_{BET} and water-uptake values were comparable to the literature values obtained using other methods. In addition, our method obviates post-synthetic shaping methods, which usually reduce the porosity of MOFs. Lastly, as a proof-of-concept on the scalability of our spray-drying approach, we used it to fabricate several grams of UiO-66-NH₂ beads. Thus, this work opens the possibility of using spray-drying, a mature process already integrated in many industrial sectors, as a green method for the continuous one-step fabrication of shaped MOF microbeads.

Experimental section

Materials and methods

Zirconium oxychloride octahydrate, 2-aminoterephthalic acid, fumaric acid and acetic acid were purchased from Sigma-Aldrich. All reagents were used without further purification. All reactions were performed using deionised water, obtained from a Milli-Q system (18.2 MΩ cm).

X-ray powder diffraction patterns were collected on an X'Pert PRO MPDP analytical diffractometer (Panalytical) at 40 kV and 40 mA using CuKα radiation ($\lambda = 1.5419 \text{ \AA}$). Nitrogen adsorption and desorption measurements were performed at 77 K using an Autosorb-IQ-AG analyser (Quantachrome Instruments). The specific surface area (S_{BET}) was determined by applying the BET equation to the adequate region of the nitrogen isotherms. The pore volume was determined from the adsorbed volume at P/P_0 0.3 of each isotherm. Prior to the measurements, the samples were degassed inside the cell under primary vacuum at 200 °C for 6 h (UiO-66-NH₂) or at 150 °C for 12 h (Zr-fumarate). Gravimetric water vapour sorption isotherms were measured using a DVS vacuum instrument (Surface Measurement Systems Ltd). The weight of the dried powder ($\approx 20 \text{ mg}$) was constantly monitored with a high-resolution microbalance ($\pm 0.1 \text{ \mu g}$) and recorded at 25 °C ($\pm 0.2 \text{ °C}$) under pure water vapour pressures. Field-emission scanning electron microscopy (FESEM) images were collected on an FEI Magellan 400 L scanning electron microscope at an acceleration voltage of 2.0 kV, and on an FEI Quanta 650F scanning electron microscope at an acceleration voltage of 20.0 kV, using aluminium as a support. The degree of insertion of acetate inside the UiO-66-NH₂ and Zr-fumarate frameworks was analysed by first digesting the samples, and then studying the resulting solutions by ¹H-NMR. For UiO-66-NH₂, the acetate/BDC-NH₂ molar ratio was calculated by comparison of the integration of a doublet at 7.75 ppm corresponding to NH₂-BDC and a singlet at 1.9 ppm corresponding to acetate. In the case of Zr-fumarate, the acetate/fumarate molar ratio was calculated by comparison of the integration of a singlet at 6.64 ppm corresponding to fumarate and a singlet at 1.9 ppm corresponding to acetate. ¹H-NMR spectra were collected on a Bruker AVANCE III 400 MHz spectrometer. Thermogravimetric analyses were performed on a PerkinElmer TGA 8000 thermogravimetric analyser. A heating rate of 10 °C min⁻¹ was used from room temperature up to 700 °C.

Optimised aqueous synthesis of UiO-66-NH₂ by continuous-flow spray-drying

ZrOCl₂·8H₂O (773 mg, 2.4 mmol) and 2-aminoterephthalic acid (435 mg, 2.4 mmol) were mixed under stirring in 12 mL of a 30% (v/v) solution of acetic acid in water. The resulting mixture was injected, with agitation maintained, into a coil-flow reactor (Pyrex; 3 mm, inner diameter) at a feed rate (Q_{f}) of 2.4 mL min⁻¹ and a bath temperature (T_{c}) of 90 °C. The preheated yellow slurry was then spray-dried at a flow rate (Q_{dg}) of 336 mL min⁻¹ (spray-cap hole diameter: 0.5 mm) and an inlet temperature (T_{in}) of 150 °C, using a B-290 Mini Spray Dryer

(BUCHI Labortechnik). The resulting yellow powder was collected, dispersed in ethanol at room temperature, precipitated by centrifugation three times, left to stand in ethanol overnight, and washed twice with acetone. The solid was dried for 12 h at 75 °C in a conventional oven to afford the final product (yield: 64%).

Optimised aqueous synthesis of Zr-fumarate by continuous-flow spray-drying

ZrOCl₂·8H₂O (644 mg, 2.0 mmol) and fumaric acid (232 mg, 2.0 mmol) were mixed under stirring in 10 mL of a 30% (v/v) solution of acetic acid in water. The resulting mixture was injected into a coil-flow reactor (Pyrex; 3 mm, inner diameter), with agitation maintained, at a feed rate of 2.4 mL min⁻¹ and bath temperature (T_{c}) of 90 °C. The resulting white slurry was spray-dried at a flow rate Q_{dg} of 336 mL min⁻¹ and an inlet temperature (T_{in}) of 140 °C. The resulting white powder was collected, dispersed in water at room temperature, left to stand overnight, and precipitated by centrifugation twice. This process was then repeated with ethanol instead of water. The solid was dried for 12 h at 75 °C in a conventional oven to afford the final product (yield: 58%).

Conflicts of interest

There are no conflicts to declare.

Acknowledgements

This work was supported by the Spanish MINECO (projects PN MAT2015-65354-C2-1-R), the Catalan AGAUR (project 2014 SGR 80), the ERC under the EU-FP7 (ERC-Co 615954), and the EU Horizon 2020 Research and Innovation Programme PRODIA (grant agreement #685727). It was also funded by the CERCA Programme/Generalitat de Catalunya. ICN2 acknowledges the support of the Spanish MINECO through the Severo Ochoa Centres of Excellence Programme, under Grant SEV-2013-0295.

Notes and references

- 1 A. D. Wiersum, E. Soubeyrand-Lenoir, Q. Yang, B. Moulin, V. Guillermin, M. B. Yahia, S. Bourrelly, A. Vimont, S. Miller, C. Vagner, M. Daturi, G. Clet, C. Serre, G. Maurin and P. L. Llewellyn, *Chem. – Asian J.*, 2011, **6**, 3270–3280.
- 2 J. A. Mason, M. Veenstra and J. R. Long, *Chem. Sci.*, 2014, **5**, 32–51.
- 3 J. Yu, L.-H. Xie, J.-R. Li, Y. Ma, J. M. Seminario and P. B. Balbuena, *Chem. Rev.*, 2017, **117**, 9674–9754.
- 4 F. G. Cirujano, A. Leyva-Pérez, A. Corma and F. X. Llabrés i Xamena, *ChemCatChem*, 2013, **5**, 538–549.
- 5 J. Lee, O. K. Farha, J. Roberts, K. A. Scheidt, S. T. Nguyen and J. T. Hupp, *Chem. Soc. Rev.*, 2009, **38**, 1450–1459.

- 6 F. Jeremias, D. Fröhlich, C. Janiak and S. K. Henninger, *New J. Chem.*, 2014, **38**, 1846–1852.
- 7 S. K. Henninger, F. Jeremias, H. Kummer and C. Janiak, *Eur. J. Inorg. Chem.*, 2012, **2012**, 2625–2634.
- 8 M. F. de Lange, B. L. van Velzen, C. P. Ottevanger, K. J. F. M. Verouden, L.-C. Lin, T. J. H. Vlugt, J. Gascon and F. Kapteijn, *Langmuir*, 2015, **31**, 12783–12796.
- 9 M. F. de Lange, K. J. F. M. Verouden, T. J. H. Vlugt, J. Gascon and F. Kapteijn, *Chem. Rev.*, 2015, **115**, 12205–12250.
- 10 A. V. Desai, B. Manna, A. Karmakar, A. Sahu and S. K. Ghosh, *Angew. Chem., Int. Ed.*, 2016, **55**, 7811–7815.
- 11 R. Ricco, K. Konstas, M. J. Styles, J. J. Richardson, R. Babarao, K. Suzuki, P. Scopecce and P. Falcaro, *J. Mater. Chem. A*, 2015, **3**, 19822–19831.
- 12 P. A. Julien, C. Mottillo and T. Friscic, *Green Chem.*, 2017, **19**, 2729–2747.
- 13 H. Reinsch, B. Bueken, F. Vermoortele, I. Stassen, A. Lieb, K.-P. Lillerud and D. De Vos, *CrystEngComm*, 2015, **17**, 4070–4074.
- 14 H. Reinsch, *Eur. J. Inorg. Chem.*, 2016, **27**, 4290–4299.
- 15 M. Rubio-Martinez, C. Avci-Camur, A. W. Thornton, I. Imaz, D. Maspocho and M. R. Hill, *Chem. Soc. Rev.*, 2017, **46**, 3453–3480.
- 16 H. Reinsch and N. Stock, *Dalton Trans.*, 2017, **46**, 8339–8349.
- 17 M. Taddei, *Coord. Chem. Rev.*, 2017, **343**, 1–24.
- 18 H. Wu, Y. S. Chua, V. Krungleviciute, M. Tyagi, P. Chen, T. Yildirim and W. Zhou, *J. Am. Chem. Soc.*, 2013, **135**, 10525–10532.
- 19 A. W. Thornton, R. Babarao, A. Jain, F. Trouselet and F. X. Coudert, *Dalton Trans.*, 2016, **45**, 4352–4359.
- 20 N. C. Burtch, H. Jasuja and K. S. Walton, *Chem. Rev.*, 2014, **114**, 10575–10612.
- 21 B. S. Gelfand and G. K. H. Shimizu, *Dalton Trans.*, 2016, **45**, 3668–3678.
- 22 Y.-H. Shih, Y.-C. Kuo, S. Lirio, K.-Y. Wang, C.-H. Lin and H.-Y. Huang, *Chem. – Eur. J.*, 2017, **23**, 42–46.
- 23 P. A. Bayliss, I. A. Ibarra, E. Perez, S. Yang, C. C. Tang, M. Poliakoff and M. Schröder, *Green Chem.*, 2014, **16**, 3796–3802.
- 24 T. Didriksen, A. I. Spjelkavik and R. Blom, *J. Flow Chem.*, 2017, **7**, 13–17.
- 25 H. Reinsch, S. Waitschat, S. M. Chavan, K. P. Lillerud and N. Stock, *Eur. J. Inorg. Chem.*, 2016, **27**, 4490–4498.
- 26 A. S. Munn, P. W. Dunne, S. V. Y. Tang and E. H. Lester, *Chem. Commun.*, 2015, **51**, 12811–12814.
- 27 A. Garcia Marquez, P. Horcajada, D. Grosso, G. Ferey, C. Serre, C. Sanchez and C. Boissiere, *Chem. Commun.*, 2013, **49**, 3848–3850.
- 28 A. Carné-Sánchez, I. Imaz, M. Cano-Sarabia and D. Maspocho, *Nat. Chem.*, 2013, **5**, 203–211.
- 29 L. Garzon-Tovar, M. Cano-Sarabia, A. Carne-Sanchez, C. Carbonell, I. Imaz and D. Maspocho, *React. Chem. Eng.*, 2016, **1**, 533–539.
- 30 V. Guillermin, L. Garzon-Tovar, A. Yazdi, I. Imaz, J. Juanhuix and D. Maspocho, *Chem. – Eur. J.*, 2017, **23**, 6829–6835.
- 31 L. Garzón-Tovar, J. Pérez-Carvajal, I. Imaz and D. Maspocho, *Adv. Funct. Mater.*, 2017, **27**, 1606424.
- 32 T. H. Kim and S. G. Kim, *Saf. Health Work*, 2011, **2**, 97–104.
- 33 K.-W. Kim and Y. H. Chung, *Toxicol. Res.*, 2013, **29**, 187–193.
- 34 K. C. A. Bromley-Challenor, N. Caggiano and J. S. Knapp, *J. Ind. Microbiol. Biotechnol.*, 2000, **25**, 8–16.
- 35 C. A. Redlich, W. S. Beckett, J. Sparer, *et al.*, *Ann. Intern. Med.*, 1988, **108**, 680–686.
- 36 J. H. Cavka, S. Jakobsen, U. Olsbye, N. Guillou, C. Lamberti, S. Bordiga and K. P. Lillerud, *J. Am. Chem. Soc.*, 2008, **130**, 13850–13851.
- 37 X. Liu, N. K. Demir, Z. Wu and K. Li, *J. Am. Chem. Soc.*, 2015, **137**, 6999–7002.
- 38 H. Kim, S. Yang, S. R. Rao, S. Narayanan, E. A. Kapustin, H. Furukawa, A. S. Umans, O. M. Yaghi and E. N. Wang, *Science*, 2017, **356**, 430–434.
- 39 G. C. Shearer, S. Chavan, S. Bordiga, S. Svelle, U. Olsbye and K. P. Lillerud, *Chem. Mater.*, 2016, **28**, 3749–3761.
- 40 T. Tian, J. Velazquez-Garcia, T. D. Bennett and D. Fairen-Jimenez, *J. Mater. Chem. A*, 2015, **3**, 2999–3005.
- 41 J. Dhainaut, C. Avci-Camur, J. Troyano, A. Legrand, J. Canivet, I. Imaz, D. Maspocho, H. Reinsch and D. Farrusseng, *CrystEngComm*, 2017, **19**, 4211–4218.
- 42 D. Crawford, J. Casaban, R. Haydon, N. Giri, T. McNally and S. L. James, *Chem. Sci.*, 2015, **6**, 1645–1649.
- 43 I. Stassen, M. Styles, T. Van Assche, N. Campagnol, J. Franssaer, J. Denayer, J.-C. Tan, P. Falcaro, D. De Vos and R. Ameloot, *Chem. Mater.*, 2015, **27**, 1801–1807.
- 44 P. M. Schoenecker, G. A. Belancik, B. E. Grabicka and K. S. Walton, *AIChE J.*, 2013, **59**, 1255–1262.
- 45 O. G. Nik, X. Y. Chen and S. Kaliaguine, *J. Membr. Sci.*, 2012, **413**, 48–61.
- 46 S. Diring, S. Furukawa, Y. Takashima, T. Tsuruoka and S. Kitagawa, *Chem. Mater.*, 2010, **22**, 4531–4538.
- 47 T. Tsuruoka, S. Furukawa, Y. Takashima, K. Yoshida, S. Isoda and S. Kitagawa, *Angew. Chem., Int. Ed.*, 2009, **121**, 4833–4837.
- 48 H. Reinsch, S. Waitschat, S. M. Chavan, K. P. Lillerud and N. Stock, *Eur. J. Inorg. Chem.*, 2016, **27**, 4490–4498.
- 49 S. Waitschat, H. Reinsch and N. Stock, *Chem. Commun.*, 2016, **52**, 12698–12701.
- 50 Z. Hu, I. Castano, S. Wang, Y. Wang, Y. Peng, Y. Qian, C. Chi, X. Wang and D. Zhao, *Cryst. Growth Des.*, 2016, **16**, 2295–2301.
- 51 M. R. DeStefano, T. Islamoglu, S. J. Garibay, J. T. Hupp and O. K. Farha, *Chem. Mater.*, 2017, **29**, 1357–1361.
- 52 F. Jeremias, V. Lozan, S. K. Henninger and C. Janiak, *Dalton Trans.*, 2013, **42**, 15967–15973.
- 53 J. Canivet, J. Bonnefoy, C. Daniel, A. Legrand, B. Coasne and D. Farrusseng, *New J. Chem.*, 2014, **38**, 3102–3111.
- 54 J. Ren, N. M. Musyoka, H. W. Langmi, B. C. North, M. Mathe, X. Kang and S. Liao, *Int. J. Hydrogen Energy*, 2015, **40**, 10542–10546.
- 55 Y. J. Bae, E. S. Cho, F. Qiu, D. T. Sun, T. E. Williams, J. J. Urban and W. L. Queen, *ACS Appl. Mater. Interfaces*, 2016, **8**, 10098–10103.

Systematic Study of the Impact of MOF Densification into Tablets on Textural and Mechanical Properties





Cite this: *CrystEngComm*, 2017, 19, 4211

Systematic study of the impact of MOF densification into tablets on textural and mechanical properties†

J. Dhainaut,^a C. Avci-Camur,^b J. Troyano,^b A. Legrand,^b J. Canivet,^a I. Imaz,^b D. Maspoch,^{b,c} H. Reinsch^d and D. Farrusseng^a

Received 17th February 2017
Accepted 16th May 2017

DOI: 10.1039/c7ce00338b

rsc.li/crystengcomm

Four different metal-organic framework powders (UiO-66, UiO-66-NH₂, UiO-67, and HKUST-1) were shaped into tablets. The effect of the applied pressure on porous properties, mechanical resistance and tablet bulk density is reported. We observe a linear relationship between densification and tensile strength for all four studied MOFs, with the slope being MOF-dependent. We also report conditions for improving significantly the volumetric uptake. Finally, we evaluated our tablets' stability over time in the presence of moisture.

1. Introduction

Less than 20 years after their discovery, commercial applications of metal-organic frameworks (MOFs) have been recently announced.¹ We have also acknowledged in the very last few years the development of pilot lines, either batch processes under hydrothermal conditions,² or continuous flow processes using water as solvent,³ and even solvent-free continuous processes.⁴ Thanks to the demonstration of these scalable pilot lines, the commercial applications of MOF will expand without any doubts.

Typically, synthesis processes lead to the production of MOFs as loose powders. However and except in very rare cases, their applications require bodies with a specific shape such as tablets, extrudates, granulates, monoliths or coatings to cite only the most common forms. For example, in catalysis, one of the usual forms is tablets which are obtained by pressing powders. Such bodies shall present mechanical resistance to attrition and hydrostatic pressure, while preserving as much as possible the original pore structure. Bazer-Bachi *et al.* reported the catalytic conversion of vegetable oil using ZIF-8 tablets which were as active as loose ZIF-8 powders, paving the way for further application of shaped MOFs

in catalysis.⁵ On the other hand, for gas storage, it is of utmost importance to fill the storage tanks with the largest amount of adsorbents. The void fraction within the adsorbent bed is a critical factor to control in the design of an adsorbent independently of its composition or structure.^{6,7} Therefore, MOFs should be pressed into solids of high density such as tablets in order to maximize their volumetric uptake.

Despite important efforts for the development of shaping processes suitable for MOFs, challenges linked to their intrinsic fragility remain.⁸ Limitations can be listed into three categories: (i) relatively low thermal stability with respect to oxides, impeding the use of classical shaping processes which are based on firing a binder-containing formulation after pelletization;⁹ (ii) relatively low chemical stability in the presence of solvents, including water, making extrusion processes not generalisable;¹⁰ and (iii) relatively low mechanical stability owing to their very high porosity and flexibility, leading to structural collapse when the applied pressure exceeds a given threshold.¹¹

When taking these limitations into account, mild pelletisation by compression appears to be a practical solution for MOFs as it overcomes firing issues and the use of solvent while limiting the structural collapse. Two review articles dealing with MOF densification have made a quite exhaustive inventory in the field, which will not be discussed here.¹² Nevertheless, it was concluded that tablets could be obtained by compressing binderless, pure MOF powders.¹³ The use of binders such as alumina, silica, graphite, or polyvinyl alcohol was also reported to reduce the structure degradation observed when even moderate strength is applied, but they also decrease the tablets' overall porosity proportionally.

The optimisation of MOF densification consists of finding a compromise between a gain in mechanical stability of their

^a Université de Lyon, Université Claude Bernard Lyon 1, CNRS, IRCELYON - UMR 5256, 2 Avenue Albert Einstein, 69626 Villeurbanne Cedex, France.

E-mail: jeremy.dhainaut@univ-lille1.fr

^b Catalan Institute of Nanoscience and Nanotechnology (ICN2), CSIC and the Barcelona Institute of Science and Technology, Campus UAB, Bellaterra, 08193 Barcelona, Spain

^c ICREA, Pg. Lluís Companys 23, 08010 Barcelona, Spain

^d MOFapps AS, c/o Smidig Regnskapservice ANS, P. Box 24 Tåsen, 0801 Oslo, Norway

† Electronic supplementary information (ESI) available: Data of all tablets, TG analyses, XRD. See DOI: 10.1039/c7ce00338b

‡ Present address: Univ. Lille, CNRS, ENSCL, Centrale Lille, Univ. Artois, UMR 8181 - UCSC - Unité de Catalyse et de Chimie du Solide, F-59000 Lille, France.

body and a loss of their initial properties. Ideally, the structural and textural properties of the MOF crystals should be preserved while the tablet density should be as high as possible. For example, Nandasiri *et al.* proposed an optimal tablet density of about 0.5 g cm^{-3} for MOF-5 and MIL-101(Cr) while maintaining their initial porosity.¹⁴ Similar binderless densification of other MOFs among the most studied, namely ZIF-8,⁵ UiO-66,¹⁰ UiO-66-NH₂,^{11,15} and HKUST-1,^{5,16} has already been reported. However, the tablet density increase comes with lower textural properties. This is especially the case of HKUST-1, which already collapses at modest applied pressure.

While those works pave the way for the further development of MOFs, parameters related to the shaping itself, such as the compression ramp speed and dwell time are rarely reported, although they can have tremendous importance for the final tablet properties. More surprisingly, very few mechanical tests were made although the tablets were usually reported as robust. As a result, the lack of standardization in densification studies prevents comparing mechanical stability and textural properties from one MOF to another. In addition, we may wonder whether conclusions of MOF structural stability drawn from densification data can be given when an all-or-nothing compression type is applied.

Herein, we report a systematic study based on quantitative descriptors for the densification of UiO-66, UiO-67, UiO-66-NH₂ and HKUST-1 using a R&D tableting machine. We measured the impact of the compression step on the textural properties (namely the specific surface area and the micropore volume), the bulk density and the mechanical resistance of the resulting tablets. In contrast to the general statement claiming that HKUST-1 can hardly be densified, we show here that robust tablets of HKUST-1 can be obtained without significant degradation of its microporous structure. In addition, we have investigated the use of a low content of expanded natural graphite (ENG) as a dried binder. Finally, we investigated the stability of our tablets after four months in the presence of moisture.

2. Experimental section

2.1. Synthesis of MOF powders

UiO-66 was prepared based on a protocol proposed by Kim *et al.*¹⁷ A DMF solution with a molar composition of zirconium chloride : terephthalic acid : hydrochloric acid = 1 : 1 : 1 was heated at 120 °C for 24 h under stirring. The solid product was recovered by filtration and washed twice with DMF. The remaining solvent entrapped inside the powder was exchanged first with ethanol and then with acetone, using Soxhlet extraction. Finally, UiO-66 was activated under vacuum at 150 °C for 12 h.

UiO-67 was prepared based on a protocol proposed by Shearer *et al.*¹⁸ A DMF solution with a molar composition of zirconium chloride : 4,4'-biphenyldicarboxylic acid : water : benzoic acid = 1 : 1 : 1.3 : 5 was heated at 120 °C for 24 h under stirring. The solid product was recovered by centrifuga-

tion and washed three times with DMF, three times with ethanol, and three times with acetone. Finally, UiO-67 was activated under vacuum at 60 °C for 12 h.

UiO-66-NH₂ was synthesized using a spray-drying continuous flow method.¹⁹ A precursor suspension of 0.22 M ZrOCl₂·8H₂O and 0.20 M 2-aminoterephthalic acid in a 24 mL mixture of water and acetic acid (1 : 1) was injected into a coil flow reactor at a feed rate of 2.4 mL min⁻¹ and at a temperature of 90 °C. The residence time inside the coil flow reactor was 63 s. The resulting pre-heated solution was then spray-dried in a Mini Spray Dryer B-290 (Büchi Labortechnik) at a flow rate of 336 mL min⁻¹ and an inlet air temperature of 150 °C, using a spray cap with a 0.5 mm-diameter hole, affording a yellow powder. This powder was then redispersed in ethanol and collected by centrifugation. The two-step washing process was repeated with acetone. The final product was dried for 12 h at 60 °C in air. This dried powder was finally activated under vacuum at 200 °C for 6 h (temperature slope of 4 °C min⁻¹).

HKUST-1 was prepared using the spray-drying technology.²⁰ A solution of 0.90 M Cu(NO₃)₂·2.5H₂O and 0.60 M 1,3,5-benzenetricarboxylic acid in 135 mL of a mixture of DMF, ethanol and water (1 : 1 : 1) was spray-dried in a Mini Spray Dryer B-290 (Büchi Labortechnik) at a feed rate of 4.5 mL min⁻¹, a flow rate of 336 mL min⁻¹ and an inlet air temperature of 180 °C, using a spray cap with a 0.5 mm-diameter hole, affording a blue powder. This powder was then redispersed in ethanol and precipitated by centrifugation. The two-step washing process was repeated with acetone. The final product was dried for 12 h at 60 °C in air. This dried powder was finally activated under vacuum at 150 °C for 12 h (temperature slope of 4 °C min⁻¹).

2.2. Densification method and body characterization

A Medel'Pharm STYL'ONE Evolution tableting instrument was used for the shaping purpose. Prior to compression, the powders were deagglomerated by grinding. The die was then filled at constant volume with 150 mg (UiO-67), 200 mg (UiO-66) or 300 mg (HKUST-1, UiO-66-NH₂) of the MOF powder. A punch diameter of 1.128 cm was used, allowing a tableting surface of 1.00 cm². Asymmetric compression, where the penetration of the upper punch was fixed at 2 mm, was used. From the moment the punches reached the powder filling height (h_0), a compression time of about 4 s was applied to reach a specified thickness following a constant displacement rate. This displacement rate is thickness-dependent. Then the compression was held for 400 ms, before the punches went back to h_0 within 4 s. To avoid any residue on the internal die surface, some cellulose was pressed between two MOF tablets.

After shaping, physical parameters of MOF tablets were measured using a Pharmatron SmartTest 50. These parameters include the weight, thickness, and diameter, allowing to calculate the tablet bulk density. The same apparatus was also used to evaluate the tensile strength, by pressing the side of the tablets at a constant 1 mm s⁻¹ displacement rate until a first load drop was detected. Such pressed tablets were usually

split into two halves. The degree of densification is reported here as a percentage of the crystal density which is in theory the highest density that can be achieved for a crystal. Similarly, we express the specific surface area (SSA) of the tablet as a percentage of the initial powder. The SSA is a relevant quantitative indicator, as a loss of SSA after compression indicates a partial collapse of the porous structure. Alternatively, the micropore volume can be used equally as a quantitative descriptor of the degradation of the porous networks (see Table S1†).

The main advantage in using these indicators is that they are non dimensional, bounded between 0 and 100% and hence can be used to compare MOFs regardless of their intrinsic properties. We also provide a novel descriptor called volumetric capacity (V_{cap}), which shall be relevant especially for gas storage applications. The positive effect of the shaping method is characterized by a higher volumetric capacity as compared to that of the initial powder. Moreover, the higher this descriptor is, the better the tablets shall perform for gas storage applications, until an optimum value is reached.

2.3. Structure and porosity characterization

Powder X-ray diffraction (PXRD) patterns were recorded on a Bruker D8 advance diffractometer using a CuK α radiation source and a Lynx-Eye detector. Nitrogen adsorption isotherms were measured at 77 K on a BELSORP-mini device from BEL Japan. The samples were outgassed at 150 °C overnight prior to measurement. Specific surface areas (SSAs) were determined using the BET method. The micropore volume (V_{micro}) was evaluated from the adsorbed volume of N₂ at $P/P_0 = 0.3$. In order to calculate the bulk density of the tablets, dry masses were estimated from thermogravimetric (TG) analyses measured on a Mettler Toledo TGA-DSC1 using reconstituted air (Fig. S1 and Table S2†). Linker defects were also evaluated from TGA, assuming that the remaining weight at 800 °C corresponds to the metal oxide, namely ZrO₂ (UiO-) or CuO (HKUST-1). This allows to determine directly the theoretical weight of a dehydroxylated MOF structure Zr₆O₆(linker)₆ and Cu₃BTC₂, which is compared to the experimental remaining weight after solvent loss and dehydroxylation (taking metal oxidation into account). The weight difference is thus attributed to linker defects. This method doesn't take possible cluster defects into account. Powder bulk density, also called tap density, was determined by adding a known mass of deagglomerated MOF powder into a vial with a high height/diameter ratio. Then, the vial was repetitively hit on a hard surface until no more volume change could be observed – generally a few hundred times, thus allowing to measure the packed bed dimensions. Scanning electron microscopy (SEM) was performed on a Hitachi S-4800.

3. Results and discussion

3.1. Influence of compression on MOF tablet properties

The impact of the densification step on the final tablet properties including density, SSA and tensile strength is presented

in Fig. 1. First, we can see that the tap densities of MOF powders are very low with respect to their corresponding crystal density: it is only 14% for UiO-66, and the highest value is obtained for HKUST-1 with a relative density of 40%. We can also note that while being isostructural to UiO-66, the UiO-66-NH₂ tap density reaches 32% of its crystal density. Here, the difference between these two isostructural MOFs is partly due to the synthesis protocol.

The MOF tablets were observed by SEM and the images are presented in the ESI†. Small and rounded crystals of HKUST-1 (Fig. S2†) and UiO-66-NH₂ (Fig. S3†) are observed. No large agglomerate usually produced by spray-drying can be seen,^{19,20} meaning that grinding was successful at deagglomerating. UiO-67 prepared by a solvothermal method leads to micrometric crystals with a bipyramidal shape (Fig. S4†). The latter is typical of the isostructural Zr-based series. While also being a part of this series, UiO-66 crystals are small and rounded (Fig. S5†). This is however in accordance with previous results.¹⁷ Moreover, the SEM images reveal that densification occurs more notably at the surface in contact with the punches.

For all studied MOFs, compression can yield tablets with twice higher density than their corresponding powders, while preserving more than 70% of their initial SSA. For instance HKUST-1, which has a reputation of being fragile, was densified to 75% of its crystal density while preserving 80% of its initial textural properties when pressed at 121 MPa. One may note that the densest random packing of spheres is about 64 to 74% of their three-dimensional volume.²¹ Surprisingly, we achieved here comparable values while limiting the loss of textural properties.

As expected, the higher the applied pressure, the higher the achieved densification. More interestingly, we observe a linear relationship between densification and tensile strength for all four studied MOFs below 80% relative density, with a slope being MOF-dependent. To the best of our knowledge, it is the first time that this behaviour is reported.

Obviously the densification level or the tensile strength cannot be enhanced by an ever increasing applied pressure without leading to porous structure collapse. When the highest density is sought, the loss of microporosity should be as reduced as possible; otherwise, it will affect the tablets' ultimate performances. For UiO-66, no loss of SSA has been observed until 40% relative density which is the highest level we have investigated as the aim was to reach a mechanical resistance high enough for further production of grains. This does not imply that a higher level of densification cannot be obtained without damaging the porous structure. For other studied MOFs, a modest but somehow linear decrease can be observed with increasing densification. Again, the decreasing rate is MOF-dependent.

Zr-based MOFs are known for their high mechanical and thermal stabilities owing to their 12-fold connected clusters in the three spatial directions.^{22,23} These stabilities can be compromised by the number of missing linkers per node – usually about 2;^{24,25} however, the addition of monocarboxylic

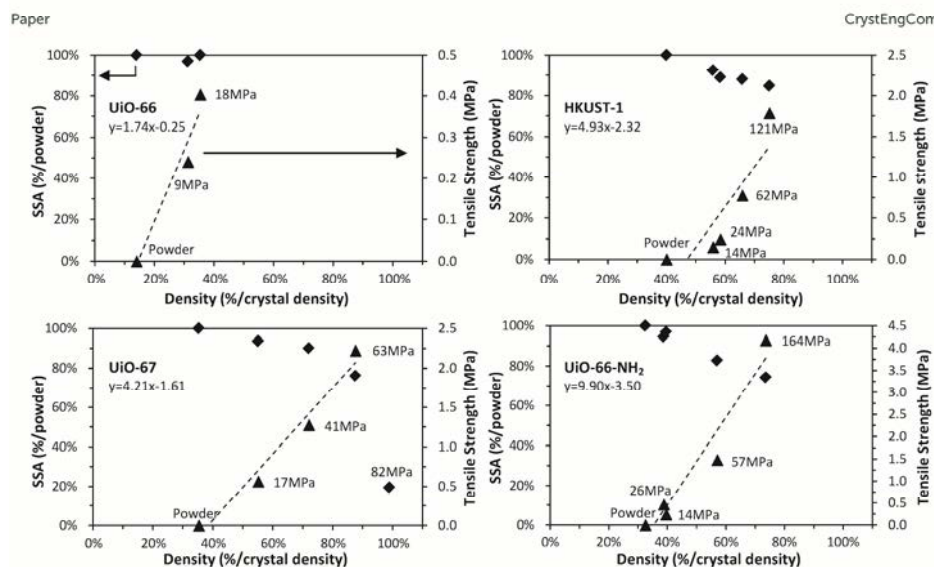


Fig. 1 Impact of the degree of compression on the textural properties (rhombus) and mechanical strength (triangle) for tablets of UiO-66, HKUST-1, UiO-67 and UiO-66-NH₂. Applied pressures are indicated for each tablet, and the linear relationship tensile strength = $f(\text{relative density})$ is reported. For UiO-67, the tensile strength was not measured above 63 MPa as the structure collapsed.

acids during the synthesis of UiO-66 proved to enhance its stability.²⁶ UiO-66 and UiO-67 powders prepared by solvothermal synthesis present 17% missing linkers per node (2 out of 12), which is comparable to the literature data.^{25,27} Although UiO-67 possesses the same topology as UiO-66 and the same degree of defects, its mechanical stability under compression is relatively modest as the porous structure collapses between 63 and 82 MPa (SSA loss of about 80%). This is in line with prior studies.^{25,28} Here, we can safely assume that the reason for this collapsing is due to the very high densification degree already reached, beyond 90%, coupled with the very low flexibility of the framework.²⁹

In summary, when MOF powders are pressed into tablets, up to a two-fold bulk density can be achieved at the expense of slightly reduced textural properties. For the production of MOF solids for catalysis, one may press a tablet only to reach an industrially-relevant tensile strength above 0.1 MPa,³⁰ thus limiting the impact of shaping on the gravimetric uptake.

In the case of gas storage and without precluding neither a specific gas nor application conditions, we can foresee that the densification level which would offer the greatest micropore volume per unit of volume should perform better assuming that the interaction is mainly van der Waals. We have calculated the volumetric capacity descriptor by multiplying the tablet microporous volume by their bulk density. This descriptor $V_{\text{cap},t}$ presented in Table 1, is expressed in cubic centimetre of pore volume per cubic centimetre of tablet

(cm^3/cm^3). It can be pointed out that the micropore volume is correlated to the specific surface area and as a consequence, either one or the other can be used as descriptors (Fig. S6[†]). Detailed inputs for all tablets can be found in Table S2.[†] One may note that in most cases (HKUST-1, UiO-66, UiO-66-NH₂), the “optimized” tablet is the one compressed at the highest pressure, meaning that the optimal pressure might not have been reached here and the volumetric capacity could still be increased. This is especially the case of UiO-66, which is likely to resist compression pressures up to 2.500 MPa with 50% of the initial SSA maintained.¹⁰ Nevertheless, a remarkable increase of tablet volumetric capacity can already be observed as compared to their powder counterparts, from 1.5 to 2.6-fold. For example, the volumetric capacity of HKUST-1 can be increased from 0.24 to 0.36 cm^3/cm^3 . According to calculations made by Dailly *et al.*,⁷ such densified HKUST-1 tablets could result in an outperforming adsorbed natural gas (ANG) adsorbent.

3.2. Comparison with literature data

Our results were further compared to the state-of-the-art literature in Fig. 2. For UiO-66 and UiO-66-NH₂, we can see that the loss of SSA as a function of the applied pressure is well in line with the literature data.^{12,13}

However, important discrepancies are observed in the case of HKUST-1. Herein, up to 85% of the original SSA of the

Table 1 Textural properties and resulting volumetric capacity of optimized MOF tablets

MOF	Form	Applied pressure (MPa)	SSA ($\text{m}^2 \text{g}^{-1}$)	V_{micro} ($\text{cm}^3 \text{g}^{-1}$)	Crystal density (g cm^{-3})	Bulk density (g cm^{-3})	Tensile strength (MPa)	V_{cap} (cm^3/cm^3)
UiO-66	Powder	—	1426	0.54	1.21	0.17	—	0.09
	Tablet	18	1459	0.54	—	0.43	0.40	0.23
UiO-66-NH ₂	Powder	—	839	0.34	1.26	0.41	—	0.14
	Tablet	164	625	0.25	—	0.93	4.18	0.23
UiO-67	Powder	—	2034	0.90	0.71	0.25	—	0.23
	Tablet	63	1549	0.70	—	0.62	2.22	0.43
HKUST-1	Powder	—	1288	0.49	1.20	0.48	—	0.24
	Tablet	121	1091	0.40	—	0.90	1.78	0.36

powder was preserved at a moderate pressure of 120 MPa, while about 50% SSA loss was reported at lower pressures of 10 and 70 MPa elsewhere.¹⁶ This could arise from several factors: (1) we used a relatively slow rate of pressure increase, which could allow HKUST-1 crystals to rearrange during compression; (2) as shown in Fig. 3, the solvent presence within the framework during compression allows maintaining its integrity, while in the literature, HKUST-1 powders are typically activated prior to compression; and (3) the presence of defects within the MOF structure is likely to lower its resistance during compression. Here, assuming that there is no cluster defect, the HKUST-1 powder used only presents 10% linker defects as shown in Table S2.† The latter assumption can hardly be verified as it would require shaping exactly the same powders that were used elsewhere. One may note that in the literature, the mechanical resilience of zeolitic MOF single crystals was greatly improved using common solvents, namely ethanol and butanol.³¹

3.3. Addition of expanded natural graphite as the binder for HKUST-1 powder

Graphite is generally used as an additive for improving materials' thermal conductivity.³² Graphite was also applied as a mineral binder with UiO-66.³³ Herein, up to 2 wt% expanded natural graphite was mixed with the HKUST-1 powder prior to compression, and its impact on both the textural proper-

ties and the tensile strength of the resulting tablet was investigated and presented in Fig. 4.

No measurable impact on the SSA could be observed at any of the applied pressure, while a minor enhancement of the tensile strength can be noted for 2 wt% ENG, almost independent of the applied pressure. This latter observation is particularly interesting for shaping MOFs at low pressure, thus maximizing the textural properties while reaching robustness high enough for applications.

3.4. Overtime ageing of tablets in polyethylene bags

After characterization, each tablet was sealed in a small polyethylene (PE) bag and left on a shelf under room conditions. It should be pointed out that PE bags are not impermeable. Indeed, their permeability to water vapor is $8.6 \times 10^{-4} \text{ cm}^3(\text{STP}) \text{ cm}^{-1} \text{ cmHg}^{-1}$ per day.³⁴ The packaging in PE bags thus limits but does not prevent the water vapor exchange. The tablets with optimised volumetric capacity were then characterized again four months later in order to check their stability in the presence of moisture. The nitrogen adsorption isotherms of the different tablets are shown in Fig. 5 and their textural properties are summarized in Table 2. In the case of UiO-66 and UiO-66-NH₂, only a slight decrease of SSA and micropore volume was observed (−9 to −11%), while the PXRD was unchanged as shown in Fig. S7.†

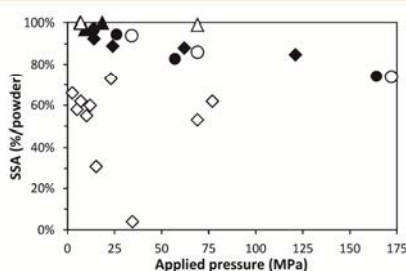


Fig. 2 SSA loss during compression observed in this work (black) and reported in the literature (white), using UiO-66 (triangle), UiO-66-NH₂ (round) and HKUST-1 (rhombus) powders.^{10,15,16}

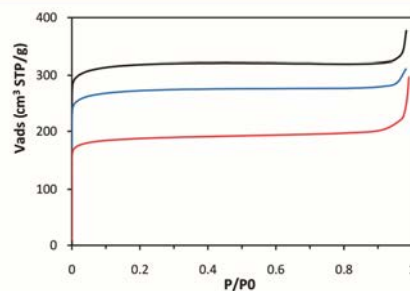


Fig. 3 Nitrogen adsorption isotherms of the as-made HKUST-1 powder (black/top) and HKUST-1 tablets pressed at 62 MPa with the as-made powder (blue/middle) or with powder fully activated prior to compression (red/bottom).

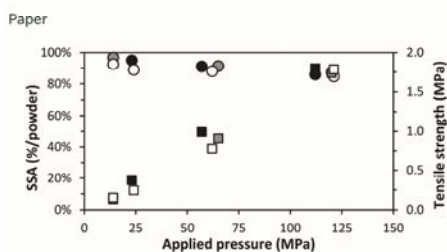


Fig. 4 Impact of compression on SSA (according to initial powder) and tensile strength of pure HKUST-1 tablets (white) or HKUST-1 mixed with 1 wt% graphite (grey) and 2 wt% graphite (black). Circles represent the SSA (according to initial powder), and squares represent the tensile strength.

In contrast, for UiO-67 tablets, 96% of their initial SSA was lost after 4 months. Notably, the PXRD patterns shown in Fig. S8† confirm a drastic loss of crystallinity. It was shown that UiO-67 is poorly stable under humid conditions.³⁵ However, unlike what was published by DeCoste *et al.*,³⁵ no monoclinic zirconia diffraction peak could be observed; the degraded product can still be identified as pure UiO-67. This result confirms that UiO-67 cannot be used in processes where even traces of water are present.

The HKUST-1 stability over time was extensively studied as it is one of the best candidates for gas storage and chromatography stationary phase.³⁶ Todaro *et al.* investigated the HKUST-1 decomposition process with air moisture.³⁷ They concluded that Cu–O bond hydrolysis is driven by the accumulation of water molecules during exposure. This phenomenon is reversible for short exposure times, up to 20 days, following a simple vacuum treatment. For longer exposure

Table 2 Textural properties and resulting volumetric capacity of optimized MOF tablets after ageing for four months in the presence of moisture

MOF	SSA ($\text{m}^2 \text{g}^{-1}$)	V_{micro} ($\text{cm}^3 \text{g}^{-1}$)
UiO-66	1295	0.49
UiO-66-NH ₂	570	0.24
UiO-67	55	0.02
HKUST-1	580	0.23

times, irreversible hydrolysis occurs, but up to 60% of the initial SSA is still preserved after 6 months.³⁷ Interestingly, our HKUST-1 tablets aged similarly, with 53% of their initial SSA retained after 4 months. We can deduce that irreversible hydrolysis also occurred after tableting. Therefore, shaping MOF powders into dense tablets does not improve significantly their resistance toward air moisture. One can suppose that the formation of a dense crust of MOFs during tableting slows down the diffusion of moisture within the tablets at first, but does not prevent the degradation.

Conclusions

We present here a general methodology for comparing the impact of MOF powder compression on the textural and mechanical properties using non dimensional indicators. By compression, the tablet bulk density can be increased by 1.8 to 3.4-fold while the specific surface area decreased between 0 and 30% for all MOFs studied here. We report here for the first time that the mechanical stability, deduced from tensile strength tests, is proportional to the bulk density. Both are MOF-dependent.

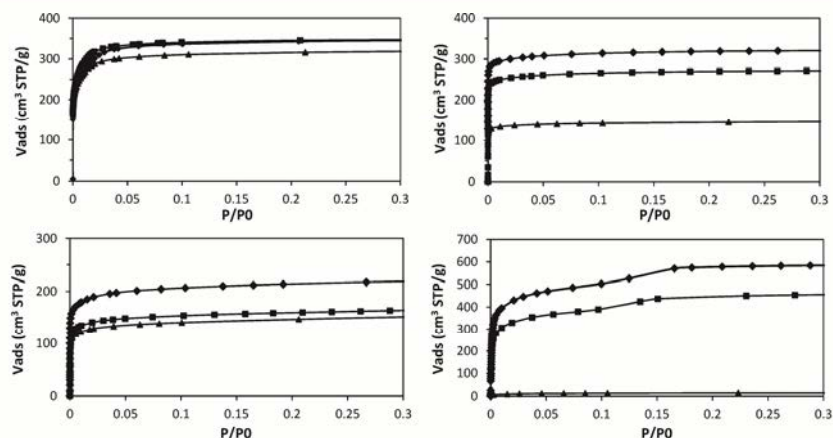


Fig. 5 Nitrogen adsorption isotherms measured for UiO-66 (top-left), UiO-66-NH₂ (bottom-left), HKUST-1 (top-right) and UiO-67 (bottom-right): activated powders (rhombus), as-made tablets (square) and tablets aged for 4 months under standard room conditions (triangle).

In contrast to all past densification studies carried out on HKUST-1, we demonstrated that robust tablets presenting only limited textural degradation can be obtained. We believe that it arises at least partly from our compression protocol, in which the compression rate and dwell time are thoroughly controlled. As a consequence, densification results obtained in an uncontrolled or poorly-controlled manner such as when using a manual press should be interpreted with care. Moreover, as reported in the case of zeolitic MOF single crystals, the presence of solvent traces within the pores of HKUST-1 seems beneficial during compression.

We underline here that depending on the final application, namely catalysis or gas storage, a different strategy can be used. For catalysis, a mild pressure, usually around 20 MPa, seems enough to produce tough and highly porous tablets that can then be grinded and sieved. The use of graphite up to 2 wt% can also be beneficial as it lowers the pressure required to reach certain robustness, thus maximizing the retained textural properties. For gas storage, the maximum volumetric capacity was obtained at the highest applied pressure, except for UiO-67 which collapses at 82 MPa. However, only UiO-66 and UiO-66-NH₂ proved to be stable overtime in the presence of moisture, making them highly attractive for further production and applications.

Acknowledgements

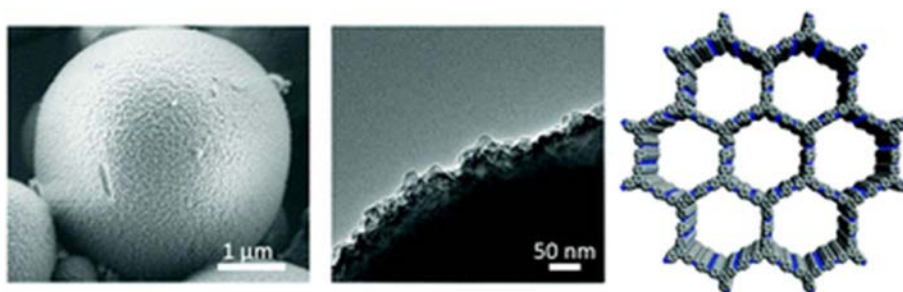
This work has been carried out within the ProDIA project that has received funding from the European Union's Horizon 2020 research and innovation programme under grant agreement No 685727. We would like to thank S. Nieto Bobadilla and T. Menard from Medel'Pharm (FR) for providing their expertise, D. Cot (IEM, FR) for the SEM images, and Coldway (FR) for providing enhanced natural graphite.

References

- 1 Editorial, *Nat. Chem.*, 2016, 8, 987.
- 2 A. S. Munn, P. W. Dunne, S. V. Y. Tang and E. H. Lester, *Chem. Commun.*, 2015, 51, 12811.
- 3 M. Rubio-Martinez, T. D. Hadley, M. P. Batten, K.-C. Carey, T. Barton, D. Marley, A. Mönch, K.-S. Lim and M. R. Hill, *ChemSusChem*, 2016, 9, 1; H. Reinsch, S. Waitschat, S. M. Chavan, K. P. Lillerud and N. Stock, *Eur. J. Inorg. Chem.*, 2016, 27, 4490.
- 4 D. Crawford, J. Casaban, R. Haydon, N. Giri, T. McNally and S. L. James, *Chem. Sci.*, 2015, 6, 1645.
- 5 D. Bazer-Bachi, L. Assié, V. Lecocq, B. Harbuzaru and V. Falk, *Powder Technol.*, 2014, 255, 52.
- 6 H. C. Foley and A. Qajar, *Ind. Eng. Chem. Res.*, 2014, 53, 19649.
- 7 M. Beckner and A. Dailly, *Appl. Energy*, 2015, 149, 69; M. Beckner and A. Dailly, *Appl. Energy*, 2016, 162, 506.
- 8 A. I. Spjelkavik, A. Sevilime, S. Divekar, T. Didriksen and R. Blom, *Chem. - Eur. J.*, 2014, 20, 8973; B. Böhlinger, R. Fischer, M. R. Lohe, M. Rose, S. Kaskel and P. Kösgens, *MOF Shaping and Immobilization, in Metal-Organic Frameworks: Applications from Catalysis to Gas Storage*, ed. D. Farrusseng, Wiley-VCH Verlag GmbH & Co. KGaA, Weinheim, Germany, 2011.
- 9 S. Mitchell, N.-L. Michels and J. Pérez-Ramírez, *Chem. Soc. Rev.*, 2013, 42, 6094; G. T. Whiting, A. D. Chowdhury, R. Oord, P. Paalanan and B. M. Weckhuysen, *Faraday Discuss.*, 2016, 188, 369.
- 10 P. S. Bácia, D. Guimarães, P. A. P. Mendes, J. A. C. Silva, V. Guillerm, H. Chevreau, C. Serre and A. E. Rodrigues, *Microporous Mesoporous Mater.*, 2011, 139, 67; G. W. Peterson, J. B. DeCoste, T. G. Glover, Y. Huang, H. Jasuja and K. S. Walton, *Microporous Mesoporous Mater.*, 2013, 179, 48.
- 11 P. G. Yot, K. Yang, F. Ragon, V. Dmitriev, T. Devic, P. Horcajada, C. Serre and G. Maurin, *Dalton Trans.*, 2016, 45, 4283.
- 12 F. Akhtar, L. Andersson, S. Ogunwumi, N. Hedin and L. Bergström, *J. Eur. Ceram. Soc.*, 2014, 34, 1643; S. C. McKellar and S. A. Moggach, *Acta Crystallogr., Sect. B: Struct. Sci., Cryst. Eng. Mater.*, 2015, B71, 587.
- 13 K. W. Chapman, G. J. Halder and P. J. Chupas, *J. Am. Chem. Soc.*, 2009, 131, 17546; M. A. Moreira, J. C. Santos, A. F. P. Ferreira, J. M. Loureiro, F. Ragon, P. Horcajada, K.-E. Shim, Y.-K. Hwang, U.-H. Lee, J.-S. Chang, C. Serre and A. E. Rodrigues, *Langmuir*, 2012, 28, 5715; D. Peralta, G. Chaplais, A. Simon-Masseron, K. Barthelet and G. D. Pirngruber, *Ind. Eng. Chem. Res.*, 2012, 51, 4692; R. Zacharia, D. Cossement, L. Lafi and R. Chahine, *J. Mater. Chem.*, 2010, 20, 2145.
- 14 M. I. Nandasiri, S. R. Jambovane, B. P. McGrail, H. T. Schaeff and S. K. Nune, *Coord. Chem. Rev.*, 2016, 311, 38.
- 15 G. W. Peterson, J. B. DeCoste, F. Fatollahi-Fard and D. K. Britt, *Ind. Eng. Chem. Res.*, 2014, 53, 701.
- 16 J. Kim, S.-H. Kim, S.-T. Yang and W.-S. Ahn, *Microporous Mesoporous Mater.*, 2012, 161, 48; J. Liu, P. K. Thallapally and D. Strachan, *Langmuir*, 2012, 28, 11584.
- 17 S.-N. Kim, Y.-R. Lee, S.-H. Hong, M.-S. Jang and W.-S. Ahn, *Catal. Today*, 2015, 245, 54.
- 18 G. C. Shearer, S. Forselv, S. Chavan, S. Bordiga, K. Mathisen, M. Bjørgen, S. Svelle and K.-P. Lillerud, *Top. Catal.*, 2013, 56, 770.
- 19 L. Garzón-Tovar, M. Cano-Sarabia, A. Carné-Sánchez, C. Carbonell, I. Imaz and D. Maspoch, *React. Chem. Eng.*, 2016, 1, 533.
- 20 A. Carné-Sánchez, I. Imaz, M. Cano-Sarabia and D. Maspoch, *Nat. Chem.*, 2013, 5, 203.
- 21 J. R. Parrish, *Nature*, 1961, 190, 800.
- 22 L. Valenzano, B. Civalieri, S. Chavan, S. Bordiga, M. H. Nilsen, S. Jakobsen, K. P. Lillerud and C. Lamberti, *Chem. Mater.*, 2011, 23, 1700.
- 23 M. Kandiah, M. H. Nilsen, S. Usseglio, S. Jakobsen, U. Olsbye, M. Tilset, C. Larabi, E. A. Quadrelli, F. Bonino and K.-P. Lillerud, *Chem. Mater.*, 2010, 22, 6632; Y. Bai, Y. Dou, L.-H. Xie, W. Rutledge, J.-R. Li and H.-C. Zhou, *Chem. Soc. Rev.*, 2016, 45, 2327.

- 24 G. C. Shearer, S. Chavan, J. Ethiraj, J. G. Vitillo, S. Svelle, U. Olsbye, C. Lamberti, S. Bordiga and K. P. Lillerud, *Chem. Mater.*, 2014, 26, 4068.
- 25 S. M. J. Rogge, J. Wieme, L. Vanduyfhuys, S. Vandenbrande, G. Maurin, T. Verstraelen, M. Waroquier and V. Speybroeck, *Chem. Mater.*, 2016, 28, 5721.
- 26 B. Van de Voorde, I. Stassen, B. Bueken, F. Vermoortele, D. De Vos, R. Ameloot, J.-C. Tan and T. D. Bennett, *J. Mater. Chem. A*, 2015, 3, 1737.
- 27 M. J. Katz, Z. J. Brown, Y. J. Colón, P. W. Siu, K. A. Scheidt, R. Q. Snurr, J. Hupp and O. Farha, *Chem. Commun.*, 2013, 49, 9449.
- 28 H. Wu, T. Yildirim and W. Zhou, *J. Phys. Chem. Lett.*, 2013, 4, 925.
- 29 C. L. Hobday, R. J. Marshall, C. F. Murphie, J. Sotelo, T. Richards, D. R. Allan, T. Düren, F.-X. Coudert, R. S. Forgan, C. A. Morrison and S. A. Moggach, *Angew. Chem., Int. Ed.*, 2016, 55, 2401.
- 30 S. Yamadaya, M. Oba, T. Hasegawa, K. Ogawa and Y. Kotera, *J. Catal.*, 1970, 19, 264.
- 31 T. D. Bennett, J. Sotelo, J.-C. Tan and S. A. Moggach, *CrystEngComm*, 2015, 17, 286.
- 32 D. Liu, J. J. Purewal, J. Yang, A. Sudik, S. Maurer, U. Mueller, J. Ni and D. J. Siegel, *Int. J. Hydrogen Energy*, 2012, 37, 6109.
- 33 M. A. Moreira, J. C. Santos, A. F. P. Ferreira, J. M. Loureiro, F. Ragon, P. Horcajda, K.-E. Shim, Y.-K. Hwang, U.-H. Lee, J.-S. Chang, C. Serre and A. E. Rodrigues, *Langmuir*, 2012, 28, 5715.
- 34 R. L. Hamilton, *Bell Labs Tech. J.*, 1967, 46, 391.
- 35 J. B. DeCoste, G. W. Peterson, H. Jasuja, T. G. Glover, Y.-G. Huang and K. S. Walton, *J. Mater. Chem. A*, 2013, 1, 5642.
- 36 M. S. Singh, N. R. Dhumal, H. J. Kim, J. Kiefer and J. A. Anderson, *J. Phys. Chem. C*, 2016, 120, 17323.
- 37 M. Todaro, G. Buscarino, L. Sciortino, A. Alessi, F. Messina, M. Taddei, M. Ranocchiarri, M. Cannas and F. M. Gelardi, *J. Phys. Chem. C*, 2016, 120, 12879.

Spray Drying for Making Covalent Chemistry II: Synthesis of Covalent– Organic Framework Superstructures and Related Composites





Cite this: *Chem. Commun.*, 2017, 53, 11372

Received 8th September 2017.
Accepted 25th September 2017

DOI: 10.1039/c7cc07052g

rsc.li/chemcomm

Spray drying for making covalent chemistry II: synthesis of covalent–organic framework superstructures and related composites†

Luis Garzón-Tovar,^a Ceren Avcı-Camur,^a David Rodríguez-San-Miguel,^b Inhar Imaz,^a Félix Zamora^{b,c} and Daniel Maspocho^{a,d}

Here we report a method that combines the spray-drying technique with a dynamic covalent chemistry process to synthesize zero-dimensional, spherical and microscale superstructures made from the assembly of imine-based COF nanocrystals. This methodology also enables the integration of other functional materials into these superstructures forming COF-based composites.

Covalent organic frameworks (COFs) are an emerging class of crystalline porous materials, where two-dimensional (2D) or three-dimensional (3D) architectures are formed from organic building blocks linked by dynamic covalent bonds (e.g. imine, boroxine, β -keto-enamine and azine).^{1–3} These materials are characterized by their high porosity, high thermal stability and low mass density, which confer them potential for myriad applications, such as gas sorption and storage,^{4–7} catalysis,^{8–10} sensors^{11–13} and optoelectronics.^{14,15} Seeking to exploit these possibilities, researchers have developed several fabrication methods for COFs, including not only the traditional solvothermal synthesis but also microwave,¹⁶ microfluidic,¹⁷ mechanochemical,¹⁸ ionothermal,¹⁹ and continuous-flow synthesis.^{20,21}

While many efforts have been devoted to the synthesis of new COFs and to their production methods, there is a growing interest in structuring these COFs at the micro/macroscale forming more complex, high-order super- or mesostructures from the assembly of COF nanoparticles. As their metal–organic framework (MOF) counterparts,^{22,23} these types of structures made

from COF nanocrystals are especially attractive due to the possibility of (i) controlling the shape and size of COFs at the micro/macroscale, two parameters that are very important to control for many applications; (ii) enhancing the initial performance *via* the design of their morphology; and (iii) combining COFs with other materials to create functional composites, which can further expand the scope for applications.^{24–27}

To date, there have been a few studies based on the creation of COF superstructures. For example, Banerjee *et al.* synthesized a highly crystalline and porous COF in the form of hollow spheres that were used for immobilizing the enzyme trypsin.²⁸ In a more recent study, core-shell microspheres containing Fe₃O₄ nanoclusters were synthesized using a template assisted route. The resulting hybrid microspheres showed a photothermal conversion ability after exposing them to near infrared light.²⁵

Despite these advances, the synthesis of higher-order COF superstructures is still challenging mainly due to the harsh conditions usually needed to synthesize highly crystalline COF nanoparticles. In this sense, we have recently reported that the spray drying method can be used to synthesize MOFs in the form of spherical hollow or compact superstructures made from the assembly of MOF nanoparticles.^{29–32} Additionally, we have recently reported that spray drying is also an effective methodology to perform Schiff-base condensation reactions, either between discrete organic molecules or on the pore surfaces of MOFs.³³ Herein, we combine both achievements and extend the applicability of spray drying to synthesize imine-based COF nanocrystals while structuring them into spherical hollow superstructures. This strategy consists of a two-step process. In the first step, the spray drying allows the formation and shaping of amorphous imine-based polymer spheres. Then, in a second step, these spheres are subjected to a dynamic covalent chemistry process to crystallize them under similar conditions to those reported by Dichtel *et al.*³⁴ Remarkably, after the crystallization step, the resulting superstructures preserve the initial size and morphology of the amorphous spheres. Further, we show that this strategy enables integrating

^a Catalan Institute of Nanoscience and Nanotechnology (ICN2), CSIC and The Barcelona Institute of Science and Technology, Campus UAB, Bellaterra, 08193, Barcelona, Spain. E-mail: daniel.maspocho@icn2.cat

^b Departamento de Química Inorgánica and Institute for Advanced Research in Chemical Sciences (IAdChem), Universidad Autónoma de Madrid, Madrid, 28049, Spain. E-mail: felix.zamora@uam.es

^c Instituto Madrileño de Estudios Avanzados en Nanociencia (IMDEA Nanociencia), Cantoblanco, 28049, Madrid, Spain

^d ICREA, Pg. Lluís Companys 23, 08010, Barcelona, Spain

† Electronic supplementary information (ESI) available: Experimental procedures and additional characterization of the synthesized COFs. See DOI: 10.1039/c7cc07052g

guest functional materials, either molecules or other nano-materials, in these COF superstructures.

Initially, we began with the synthesis of superstructures of COF-TAPB-BTCA, a two-dimensional COF assembled from two trigonal building blocks, 1,3,5-benzenetricarbaldehyde (BTCA) and 1,3,5-tris-(4-aminophenyl)benzene (TAPB).³⁵ In a typical first step, a 0.03 mol L⁻¹ solution of BTCA in a mixture of DMSO and acetic acid (9:1 v/v) and a 0.03 mol L⁻¹ solution of TAPB in DMSO were independently atomized using a three-fluid nozzle at a feed rate of 3.0 mL min⁻¹, a flow rate of 336 mL min⁻¹ and an inlet temperature of 200 °C, using a B-290 Mini Spray Dryer (BÜCHI Labortechnik). This atomization immediately afforded a yellow powder (Fig. 1a). Note here that the use of the three-fluid nozzle ensured that the two reactants only come in contact inside the drying chamber avoiding the clogging of the nozzle.

Field-emission scanning electron microscopy (FESEM) images and X-ray powder diffraction (XRPD) performed on the intermediate solid collected revealed the homogeneous formation of amorphous spheres with an average size of 2.2 ± 1.1 μm (Fig. 1b and Fig. S1, ESI†). Since the spray-drying method is based on the fast evaporation of the solvent, we reasoned that the kinetic product was obtained instead of the thermodynamic one. The formation of the imine-based polymer was confirmed by FT-IR spectroscopy and solid-state ¹³C magic angle spinning nuclear magnetic resonance (MAS NMR) spectroscopy. The FT-IR spectrum showed the presence of the typical imine (C=N) band at 1633 cm⁻¹ and the absence of the band corresponding to free -NH₂ between 3300 and 3500 cm⁻¹, indicating the absence of unreacted TAPB. The imine formation was further corroborated by the appearance of a signal at 158 ppm in the ¹³C MAS NMR spectrum, which was attributed to the carbon atom of the C=N

imine group (Fig. S2, ESI†). These results are in agreement with those previously reported for COF-TAPB-BTCA.³⁵ In a second step, this imine-based polymer was subjected to a dynamic covalent chemistry process. Thus, the amorphous spheres were dispersed in a mixture of 1,4-dioxane/mesitylene/water/acetic acid and heated at 80 °C for 192 h. The isolated material did not show significant spectroscopic changes in both FT-IR and ¹³C MAS NMR spectra (Fig. S3, ESI†). However, the FESEM and high-resolution transmission electron microscopy (HR-TEM) images displayed the formation of hollow superstructures in which their walls are created by the close packing of COF nanoparticles (Fig. 1c, d and Fig. S4, ESI†). Remarkably, these superstructures retained both the shape and size of the amorphous spheres (Fig. S5, ESI†). The XRPD pattern of these superstructures showed the most intense peak at 5.5°, which properly matches with the simulated COF-TAPB-BTCA structure (Fig. 1e and Fig. S6, ESI†). The microporosity of the COF-TAPB-BTCA superstructures was confirmed by N₂ adsorption measurements, which gave a BET surface area of 911 m² g⁻¹. This value is consistent with that previously reported for COF-TAPB-BTCA (Fig. 1f).³⁰ Finally, thermogravimetric analysis (TGA) revealed the high thermal stability of the COF-TAPB-BTCA superstructures (up to 500 °C), following by a weight loss due to the decomposition of the framework (Fig. S7, ESI†).

To demonstrate the generality of our approach, we used similar synthetic conditions to synthesize other imine-based COF superstructures. To this end, we selected the recently discovered COF-LZU1⁸ and COF-TAPB-PDA.³⁴ COF-LZU1 was synthesized by the condensation of BTCA and *p*-phenylenediamine (PPD), whereas COF-TAPB-PDA was synthesized from TAPB and terephthalaldehyde (PDA). In both cases, after the two-step process,

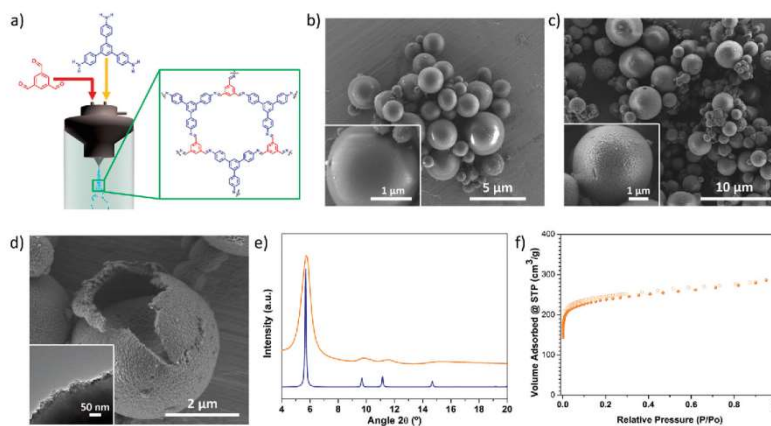


Fig. 1 (a) Schematic representation of the spray drying synthesis of COF-TAPB-BTCA. (b) Representative FESEM images of amorphous COF-TAPB-BTCA spheres. (c) Representative FESEM images of microspherical COF-TAPB-BTCA superstructures. (d) FESEM and HRTEM images of a mechanically broken superstructure, revealing the hollow cavity and that they are formed by COF nanocrystals. (e) XRPD diffractogram of COF-TAPB-BTCA (orange), compared with the simulated powder pattern (blue). (f) N₂ adsorption isotherm of COF-TAPB-BTCA.

ChemComm

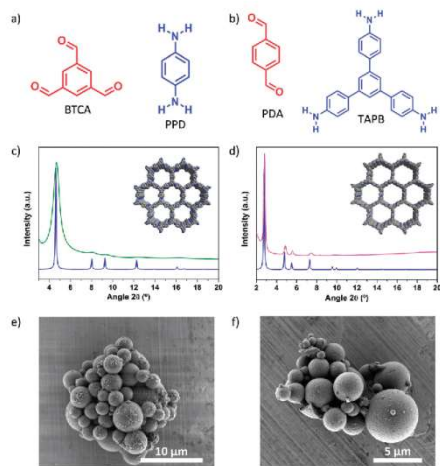


Fig. 2 (a and b) Representation of the building blocks used to synthesize (a) **COF-LZU1** and (b) **COF-TAPB-PDA**. (c) XRPD diffractogram of the obtained **COF-LZU1** (green) compared with the simulated powder pattern (blue). (d) XRPD diffractogram of the obtained **COF-TAPB-PDA** (pink) compared with the simulated powder pattern (blue). (e and f) FESEM images showing the general view of the microspherical (e) **COF-LZU1** and (f) **COF-TAPB-PDA** superstructures.

FESEM and HR-TEM images and XRPD of the resulting solids revealed the formation of crystalline microspherical superstructures of the desired COFs (Fig. 2 and Fig. S8, S9, ESI†). FT-IR spectra of **COF-LZU1** and **COF-TAPB-PDA** showed the presence of the characteristic C=N stretching band at 1618 and 1628 cm^{-1} , respectively. Moreover, the formation of imine was further corroborated by the peaks observed in the ^{13}C MAS NMR spectra at 157 ppm for **COF-LZU1** and 158 ppm for **COF-TAPB-PDA** (Fig. S10 and S11, ESI†). Additionally, the microporosity of the COFs was confirmed by N_2 adsorption analysis, from which the BET surface areas of 319 $\text{m}^2 \text{g}^{-1}$ for **COF-LZU1** and 1162 $\text{m}^2 \text{g}^{-1}$ for **COF-TAPB-PDA** were calculated (Fig. S12, ESI†). These values are consistent with those previously reported.^{8,34}

Having demonstrated that our spray-drying methodology enables the formation of hollow COF superstructures, we envisioned to use it as a simple method for integrating other functional substances to these superstructures and thus, create COF-based composites.^{36–38} To explore this possibility, we synthesized **Rose-bengal@COF-TAPB-BTCA** superstructures by reproducing the formation of **COF-TAPB-BTCA** superstructures but dissolving Rose bengal in the initial precursor solution. FESEM images and XRPD patterns revealed the formation of crystalline microspherical superstructures of **COF-TAPB-BTCA**, confirming that their synthesis was not affected by the presence of the dye (Fig. S13, ESI†). The presence of Rose bengal was confirmed by elemental mapping with energy dispersive X-ray spectrometry (EDX) performed on a single superstructure, which revealed a

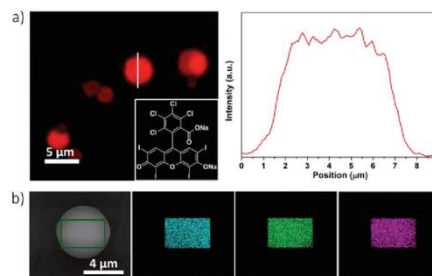


Fig. 3 (a) Confocal fluorescence image of **Rose-bengal@COF-TAPB-BTCA** superstructures and their fluorescence intensity profile. Inset: Chemical structure of Rose bengal. (b) Elemental mapping with EDX performed on a single spherical superstructure of **Rose-bengal@COF-TAPB-BTCA** showing the homogeneous distribution Na (cyan), Cl (green) and I (pink).

highly uniform distribution of Cl, I, and Na atoms (Fig. 3b). Additionally, the successful encapsulation of this dye was visualized by confocal images, where the intensity profile and the confocal image taken on a single sphere revealed the homogeneous distribution of Rose bengal (Fig. 3a). Finally, to evaluate the possibility to release the encapsulated molecules from these COF superstructures, the **Rose-bengal@COF-TAPB-BTCA** composite was incubated in ethanol for different periods of time, and the dye released was quantified by fluorescence spectroscopy (Fig. S14, ESI†). Notably, a dye release of 32% was observed for the first day, achieving a dye release of 56% after 8 days. This slow release suggests that the dye is in fact located on the pores of the COF nanocrystals rather than on their crystal surface.

To further explore the formation of COF-based composites using this strategy, we incorporated magnetic Fe_3O_4 nanoparticles dispersed in the precursor solution. Under the same conditions, Fe_3O_4 nanoparticles (8 nm diameter) were encapsulated

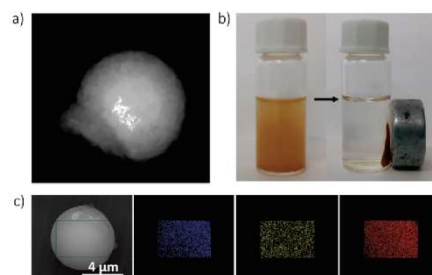


Fig. 4 (a) HAADF-STEM image of a single **Fe₃O₄@COF-TAPB-BTCA** superstructure. (b) Photographs of the dispersion of **Fe₃O₄@COF-TAPB-BTCA** superstructures before and after exposure to a magnet. (c) Elemental mapping with EDX performed on a single spherical superstructure of **Fe₃O₄@COF-TAPB-BTCA**, showing the homogeneous distribution of N (blue), Fe (yellow) and O (red).

into the COF-TAPB-BTCA superstructures, as confirmed by HAADF-STEM and HR-TEM images and XRPD (Fig. 4a and Fig. S15, S16, ESI†). The content of Fe in the composite was estimated using inductively coupled plasma-mass spectrometry (ICP-MS), from which a Fe₃O₄ content of 2.8% w/w in the composite was determined. EDX mapping performed on a single superstructure showed the distribution of N, Fe and O atoms, confirming the presence of Fe₃O₄ into the superstructures (Fig. 4c). Also, as an indication of the encapsulation, a colloidal suspension of the composite was exposed to a magnet and rapidly attracted to it (Fig. 4b). Similarly, magnetic measurements performed on the composite confirmed its magnetic character, exhibiting a characteristic hysteresis loop with a coercive field of 240 Oe at 10 K (Fig. S17, ESI†).

In summary, we have reported a highly versatile and effective methodology to simultaneously synthesize and shape microspherical hollow imine-based COF superstructures. This method also enables making COF-based composites by simply adding the selected functional materials during the spray-drying synthesis.

This work was supported by the Spanish MINECO (project PN MAT2015-65354-C2-1-R), the Catalan AGAUR (project 2014 SGR 80), and the ERC under the EU FP7 (ERC-Co 615954). It was also funded by the CERCA Programme/Generalitat de Catalunya. ICN2 acknowledges the support of the Spanish MINECO through the Severo Ochoa Centers of Excellence Program under Grant SEV-2013-0295.

Conflicts of interest

There are no conflicts to declare.

Notes and references

- P. J. Waller, F. Gándara and O. M. Yaghi, *Acc. Chem. Res.*, 2015, **48**, 3053–3063.
- S.-Y. Ding and W. Wang, *Chem. Soc. Rev.*, 2013, **42**, 548–568.
- J. Thote, H. Barik Aiyappa, R. Rahul Kumar, S. Kandambeth, B. P. Biswal, D. Balaji Shinde, N. Chaki Roy and R. Banerjee, *IUCr*, 2016, **3**, 402–407.
- H. Furukawa and O. M. Yaghi, *J. Am. Chem. Soc.*, 2009, **131**, 8875–8883.
- C. J. Doonan, D. J. Tranchemontagne, T. G. Glover, J. R. Hunt and O. M. Yaghi, *Nat. Chem.*, 2010, **2**, 235–238.
- M. G. Rabbani, A. K. Sekizkardes, Z. Kalivceci, T. E. Reich, R. Ding and H. M. El-Kaderi, *Chem. – Eur. J.*, 2013, **19**, 3324–3328.
- S. S. Han, H. Furukawa, O. M. Yaghi and W. A. Goddard, *J. Am. Chem. Soc.*, 2008, **130**, 11580–11581.
- S.-Y. Ding, J. Gao, Q. Wang, Y. Zhang, W.-G. Song, C.-Y. Su and W. Wang, *J. Am. Chem. Soc.*, 2011, **133**, 19816–19822.
- H. Li, Q. Y. Pan, Y. C. Ma, X. Y. Guan, M. Xue, Q. R. Fang, Y. S. Yan, V. Valtchev and S. L. Qiu, *J. Am. Chem. Soc.*, 2016, **138**, 14783–14788.
- Q. R. Fang, S. Gu, J. Zheng, Z. B. Zhuang, S. L. Qiu and Y. S. Yan, *Angew. Chem., Int. Ed.*, 2014, **53**, 2878–2882.
- G. Das, B. P. Biswal, S. Kandambeth, V. Venkatesh, G. Kaur, M. Addicoat, T. Heine, S. Verma and R. Banerjee, *Chem. Sci.*, 2015, **6**, 3931–3939.
- Y. Yuan, H. Ren, F. X. Sun, X. F. Jing, K. Cai, X. J. Zhao, Y. Wang, Y. Wei and G. S. Zhu, *J. Mater. Chem.*, 2012, **22**, 24558–24562.
- S.-Y. Ding, M. Dong, Y.-W. Wang, Y.-T. Chen, H.-Z. Wang, C.-Y. Su and W. Wang, *J. Am. Chem. Soc.*, 2016, **138**, 3031–3037.
- S. Wan, J. Guo, J. Kim, H. Ihee and D. Jiang, *Angew. Chem.*, 2008, **120**, 8958–8962.
- J. Mahmood, E. K. Lee, M. Jung, D. Shin, I.-Y. Jeon, S.-M. Jung, H.-J. Choi, J.-M. Seo, S.-Y. Bae, S.-D. Sohn, N. Park, J. H. Oh, H.-J. Shin and J.-B. Baek, *Nat. Commun.*, 2015, **6**, 6486.
- H. Wei, S. Chai, N. Hu, Z. Yang, L. Wei and L. Wang, *Chem. Commun.*, 2015, **51**, 12178–12181.
- D. Rodríguez-San-Miguel, A. Abrishamkar, J. A. R. Navarro, R. Rodríguez-Trujillo, D. B. Amabilino, R. Mas-Balleste, F. Zamora and J. Puigmarti-Luis, *Chem. Commun.*, 2016, **52**, 9212–9215.
- B. P. Biswal, S. Chandra, S. Kandambeth, B. Lukose, T. Heine and R. Banerjee, *J. Am. Chem. Soc.*, 2013, **135**, 5328–5331.
- P. Kuhn, M. Antonietti and A. Thomas, *Angew. Chem., Int. Ed.*, 2008, **47**, 3450–3453.
- S. Karak, S. Kandambeth, B. P. Biswal, H. S. Sasmal, S. Kumar, P. Pachfule and R. Banerjee, *J. Am. Chem. Soc.*, 2017, **139**, 1856–1862.
- Y. Peng, W. K. Wong, Z. Hu, Y. Cheng, D. Yuan, S. A. Khan and D. Zhao, *Chem. Mater.*, 2016, **28**, 5095–5101.
- S. Furukawa, J. Reboul, S. Diring, K. Sumida and S. Kitagawa, *Chem. Soc. Rev.*, 2014, **43**, 5700–5734.
- A. Carné-Sánchez, I. Imaz, K. C. Stylianou and D. Maspoch, *Chem. – Eur. J.*, 2014, **20**, 5192–5201.
- D. Rodríguez-San-Miguel, J. J. Corral-Perez, E. Gil-Gonzalez, D. Cuellas, J. Arauzo, V. M. Monsalvo, V. Carcelen and F. Zamora, *CrystEngComm*, 2017, **19**, 4872–4876.
- J. Tan, S. Nambuankur, W. Kong, N. Kungwan, J. Guo and C. Wang, *Angew. Chem., Int. Ed.*, 2016, **55**, 13979–13984.
- X. Shi, Y. Yao, Y. Xu, K. Liu, G. Zhu, L. Chi and G. Lu, *ACS Appl. Mater. Interfaces*, 2017, **9**, 7481–7488.
- A. Halder, S. Kandambeth, B. P. Biswal, G. Kaur, N. C. Roy, M. Addicoat, J. K. Salunke, S. Banerjee, K. Vanka, T. Heine, S. Verma and R. Banerjee, *Angew. Chem., Int. Ed.*, 2016, **55**, 7806–7810.
- S. Kandambeth, V. Venkatesh, D. B. Shinde, S. Kumari, A. Halder, S. Verma and R. Banerjee, *Nat. Commun.*, 2015, **6**, 6786.
- A. Carné-Sánchez, I. Imaz, M. Cano-Sarabia and D. Maspoch, *Nat. Chem.*, 2013, **5**, 203–211.
- L. Garzon-Tovar, M. Cano-Sarabia, A. Carne-Sanchez, C. Carbonell, I. Imaz and D. Maspoch, *React. Chem. Eng.*, 2016, **1**, 533–539.
- V. Guillerme, L. Garzon-Tovar, A. Yazdi, I. Imaz, J. Juanhuix and D. Maspoch, *Chem. – Eur. J.*, 2017, **23**, 6829–6835.
- L. Garzon-Tovar, J. Pérez-Carvajal, I. Imaz and D. Maspoch, *Adv. Funct. Mater.*, 2017, **27**, 1606424.
- L. Garzon-Tovar, S. Rodríguez-Hermida, I. Imaz and D. Maspoch, *J. Am. Chem. Soc.*, 2017, **139**, 897–903.
- B. J. Smith, A. C. Overholts, N. Hwang and W. R. Dichtel, *Chem. Commun.*, 2016, **52**, 3690–3693.
- A. de la Pena Ruizgomez, D. Rodríguez-San-Miguel, K. C. Stylianou, M. Cavallini, D. Gentili, F. Liscio, S. Milita, O. M. Roscioni, M. L. Ruiz-Gonzalez, C. Carbonell, D. Maspoch, R. Mas-Balleste, J. L. Segura and F. Zamora, *Chem. – Eur. J.*, 2015, **21**, 10666–10670.
- D. Mullangi, S. Nandi, S. Shalini, S. Sreedhala, C. P. Vinod and R. Vaidhyanathan, *Sci. Rep.*, 2015, **5**, 10876.
- D. Mullangi, S. Shalini, S. Nandi, B. Choksi and R. Vaidhyanathan, *J. Mater. Chem. A*, 2017, **5**, 8376–8384.
- P. Wang, Q. Wu, L. Han, S. Wang, S. Fang, Z. Zhang and S. Sun, *RSC Adv.*, 2015, **5**, 27290–27294.